Molecular Dynamics of Ice-Solid Bi-material Interfaces

by

Nishikant Sonwalkar

Submitted to the Interdepartmental Program in Interface Mechanics
in partial fulfillment of the requirements for the degree of

DOCTOR OF SCIENCE

at the

MASSACHUSETTS INSTITUTE OF TECHNOLOGY

August 1992

Author .....
Interdepartmental Program in Interface Mechanics
August, 1992

Certified by .....
Dr. S. Shyam Sunder
Thesis Supervisor

Certified by .....
Professor Sidney Yip
Thesis Supervisor

Accepted by .....
Eduardo A. Kausel
Chairman, Departmental Committee on Graduate Students

Molecular Dynamics of Ice-Solid Bi-material Interfaces

by

Nishikant Sonwalkar

Submitted to the Interdepartmental Program in Interface Mechanics
on August, 1992, in partial fulfillment of the
requirements for the degree of
DOCTOR OF SCIENCE

Abstract

The goal of this dissertation is to gain fundamental understanding of the formation and growth of ice-solid interface bonds. This is obtained by an investigation of the molecular dynamics involved in the formation and the stability of ice-solid bi-material interfaces. The results of the investigation provide a rational basis for the design of deicing coatings that will prevent and/or disrupt the formation of ice on solid surfaces.

To achieve this objective, this research involved both experimental and computational studies. In the experimental studies, the structure of ice layers forming on solid surfaces has been studied with laser Raman microprobe spectroscopy. The phenomena of the nucleation and the growth of ice on solid surfaces are investigated using both *in-situ* video and confocal microscopy. The mechanisms of adhesion have been studied using a laser Raman microprobe shear apparatus. In the computational studies, using molecular dynamics (MD) simulations, the instability of cubic ice induced by heating, under constant pressure and constant volume conditions, has been investigated. The temperature induced variations in the structural and dynamical properties are calculated in the range of 70K to 300K. The emphasis of the study is on the dynamical (vibrational) properties, which can be compared with the Raman experiments.

An ice-copper interface has been simulated to obtain the geometry and binding energy of the interface. The interface is studied layer-by-layer to investigate local variations in the dynamical properties. The O-H stretching peaks of the computed vibrational spectra of cubic ice are compared with the the O-H stretching peaks obtained from the Raman spectroscopy of ice layers on the copper substrate.

The variations in the vibrational spectrum of the ice layers, in the O-H stretching and the lattice vibrational regions, are determined by using *in-situ* laser Raman microprobe spectroscopy on several metal surfaces and electrical transmission line samples. The temperature variations of the peak positions and band widths between 30K and 180K are observed in steps of 10K and their comparison with the variations reported for the bulk polycrystalline and amorphous ice shows that the vapor deposited ice layer that forms initially on the cold metal substrate (below 150K) possesses a low-density amorphous structure. The temperature variation of the half-power band width of the in-phase O-H stretching peak indicates that the ice layer changes into

a high defect density polycrystalline ice above a temperature of 150K. The broken network structure of the high defect density polycrystalline ice is responsible for the lower shear strength than tensile strength of the ice-solid bond.

A laser Raman microprobe shear apparatus was designed and fabricated to perform pure shear experiment on an ice-solid interface while simultaneously making Raman spectroscopic and video microscopic observations. The video and confocal microscopy provides a clear visual record of the nucleation and growth of ice formed by the condensation of atmospheric vapor on solid surfaces (titanium, copper, aluminum, stainless, steel, glass and teflon) maintained at -20 °C. An icing chamber was designed and fabricated for recording the nucleation and growth of ice on solid surfaces under controlled environmental conditions. The frame-by-frame analysis of the video images shows that the phase transition on the high energy surfaces is dominated by dropwise condensation, while on the low energy surface it proceeds by sheet-like condensation. The smaller embryo size and the larger triple line density per unit area result in higher adhesive strength for these surfaces. The microscopic observations of the ice-solid bond before and after failure, obtained by adhesion tests conducted under pure shear, show that the condensate region and the faceted cross-link region primarily govern the adhesive strength of the interface.

The variations in the Raman spectra of the ice layer before and after the shearing event, based on the peak positions of the O-H stretching frequencies and band widths, show that the out-of-phase stretching frequency (ν_3) has larger shift resulting from the disorder in the ice that can only result from the breakage of the hydrogen bond after the shearing event. The in-phase vibrational frequency (ν_1) remains unchanged. The increase in the band width of the (ν_3) frequency shows a disorder in the unbonded hydrogen atoms. These observations indicate that an adhesive bond is formed by the adsorption of hydroxil group on the metal surface. The oxygen atoms are adsorbed primarily on the atomic sites of the metal surface. As a result, the ice-solid bond is strong for solids surfaces which have good match with the lattice of ice (commensurate interface) but the bond is weak for mis-matched surfaces (incommensurate interfaces).

The MD simulation results, from the isochoric and isobaric melting of the cubic simple point charge (SPC) ice, show considerable shift (about 40% increase from the original 600 cm^{-1}) and spread (about 100% increase from the original 500 cm^{-1}) in the calculated rotational vibrations towards bending vibrations (located about 1700 cm^{-1} frequency) at 240K temperature. The normal mode analysis made on a nine atom tetrahedral configuration of a distorted ice crystal at this temperature obtained at the end of the simulation run, shows variations in the eigenvectors of the bending and torsional vibrations. These variations demonstrate that the increase in the rotational vibrations is caused by the coupling and mixing of the rotational (torsional) vibrations with the bending vibrations. This coupling and mixing is a precursor to melting, and is a mechanism that is responsible for disintegration of the crystalline SPC ice. The sudden change in the coordination number, the reduction in the potential energy, and the increase in the O-H stretching frequency at 240K, are found to correlate with the vibrational coupling mechanism.

A first attempt to simulate an ice-copper interface using a cross-interaction potential has been made. The cross-interaction potential was obtained by fitting ex-

ponential functions to the electronic cluster calculation. The simulation results are found to be reasonable in describing the ice-copper interface geometry as well as the binding energy known from experiments. The computed vibrational spectra of the interface ice layers at 70K on a copper surface, based on the layer-by-layer variation of the O-H stretching frequency band-width, show a larger disorder in the ice layer adjacent to the copper surface as compared to bulk ice. This observation agrees with our experimental Raman measurements for thick and thin ice layers. The geometry of the ice-copper interface, obtained by plotting the time-averaged particle positions, shows that the adsorption of the oxygen atom occurs at the atomic sites of the copper lattice. This observation supports our experimental finding that the adsorption of the hydroxil group is commensurate with the lattice structure of the substrate.

The experimental and computational studies constitute a complementary approach that provides valuable atomistic information on ice-solid bi-material interfaces. The implications of these findings for prevention and or disruption of icing on solids are discussed and recommendations for a rational design of de-icing coating have been made.

Thesis Supervisor: Dr. S. Shyam Sunder
Title: Principal Research Scientist

Thesis Supervisor: Professor Sidney Yip
Title: Professor of Nuclear Engineering

Acknowledgments

I would like to thank the members of my thesis committee, Dr. S. Shyam Sunder, Professor Sidney Yip, Professor Ali S. Argon, Professor J. J. Connor and Professor D. Blankschtein for agreeing to serve on the interdepartmental program in the field of "interface mechanics".

I am grateful to Dr. S. Shyam Sunder for his strong support and belief in my educational and research aspirations. It was because of his strong support and belief in me that I could, not only get all the funding for the thesis research, but also have an interdepartmental thesis program. His supervision and advice has always brought focus and direction in my thesis research. I have learned much from him, regarding the professional and personal aspects of a research career.

Professor Sidney Yip has been a constant source of encouragement to me for acquiring sincere attitude for the research and breaking new grounds. I always looked up to him for advice throughout my thesis research and he has always given me his best. He has always challenged me to give my best to the research endeavors. Association with him will have a long lasting impression on my research career. He has been my mentor in the field of atomistic simulation.

My association with Dr. Shiv K. Sharma has been extremely fruitful in the experimental work at spectroscopy laboratory of Hawaii Institute of Geophysics (HIG). It was through his collaboration, that we were able to conduct experimental work efficiently and without any obstacles. I would also like to thank Dr. Tom Cooney for his help in carrying out the experiments at HIG.

During the course of my thesis research, I had opportunity to visit several agencies and expand my research horizon. I wish to extend my gratitude to Dr. Dieter Wolf of Argonne National Laboratory, Dr. M. Bailey of San Diago Super Computing Center and Dr. John F. Rabolt of IBM, Almaden Research Center, San Jose, for providing me with the access, facilities and expertise during my stay at respective agencies.

The research reported in this thesis was supported by National Science Foundation and the Electric Power Research Institute at MIT (Grant No. CES-8815942 and

RP23567-2). It would have been impossible for me to pursue this research without the financial support.

Throughout my stay at MIT I have benefited from association with numerous friends and colleagues, I wish to thank them all for being so wonderful to me. I am indebted to my family for supporting all my imaginations and aspirations throughout my life, and encouraging me to become what I am today.

Nishikant Sonwalkar

July, 1992

Contents

List of Figures

List of Tables

Chapter 1

Introduction

1.1 Problem Definition and Literature Review

The mechanical behavior of a bi-material composite is highly dependent on the molecular bond strength of the interface region. In many bi-material applications, e.g., packaging of integrated circuits, the goal is to maximize adhesion and toughness. However, in other cases, e.g., adhesion of ice on solid surfaces, the lack of adhesion is desirable.

Excessive build-up of ice on structures and cables can cause severe damage and even disaster. Icing, therefore, represents an important problem area where the goal is to minimize interface adhesion [1, 2, 3, 4, 5]. For example, studies by the Federal Highway Administration indicate that snow and ice control is the single most expensive maintenance function performed by the northern states and cities [6]. Estimates by Minsk [7] show that the cost of maintenance is reaching $ 1.4 billion annually for the northern states alone. The use of road-salt (NaCl, $MgCl_2$) for the disruption of ice-substrate bond costs an additional $3 billion in environmental and economic damage each year (Massachusetts Audubon Society, 1986). In the case of transmission cables, icing is responsible for frequent disruption of electrical and communication systems as well as an annual repair and maintenance cost of approximately $5-10 million in the United States [8, 9]. The phenomenon is also a matter of concern to aircraft and ship structures [5].

Ice develops strong adhesive bonds with most materials. Hydrophobic coatings are often used to reduce adhesion of ice on solids (e.g., several materials reduce the adhesive strength to less than 15 psi), but such coatings suffer from serious durability problems due to freeze-release cycles and exposure to rain [7]. Most de-icing chemicals are costlier and less effective in terms of spatial coverage and rate of under-cut to ice when compared with sodium chloride (rock-salt), a highly corrosive material [10].

The principal factor preventing progress in solving the icing problem is the lack of fundamental understanding concerning the processes governing the formation of ice-solid interface bonds. This understanding is crucial for the development of (a) de-icing coatings with low adhesion and high durability, and (b) de-icing chemicals that are non-corrosive, effective and inexpensive.

Studies conducted on ice-substrate interface behavior indicate that both physical properties (e.g., surface roughness and surface energy of the substrate) and chemical properties (e.g., chemical composition of the substrate material) influence the resulting adhesive bond [1, 3]. Experiments also show that the adhesive bond strength in shear is considerably smaller than that in tension, although the cause for this atypical behavior is not understood.

Jellinek [1, 11, 12] proposed that the observed interface behavior is due to the presence of a liquid-like layer at the interface. The thickness of this liquid-like layer depends on the roughness of the substrate surface. Bascom et al. [2] found that the lower shear strength could not be attributed to the surface energy of the substrate. Instead, their microscopic observations showed the existence of a defective lattice structure at the interface. Itagaki [13] found that the bond strength depends on the surface energy of the substrate, the area of wetting, and on the duration of contact between the supercooled droplets and the substrate surface before freezing. Past research, as indicated here has tended to be empirical and its focus generally has been on isolated, and sometimes contradictory, mechanisms to explain the observed macroscopic phenomenon.

General theories of adhesion [14, 15, 16] currently point towards four distinct mechanisms to explain the adhesion process. These are: (a) mechanical interlocking

induced by the roughness of the substrate, (b) diffusion of the absorbent on the substrate surface, (c) electronic interaction between the adsorbent and the substrate, and (d) adsorption of the chemical species on the surface. In a particular situation, such as the adhesion of ice on a surface, several of these mechanisms can be activated simultaneously. The overall adhesive strength is postulated to be the additive sum of the various dominant and secondary mechanisms. This classical approach, however, only considers the macroscopic mechanisms that become active once the interface bond is formed. The approach is limited in scope for understanding the role of microscopic parameters, such as the lattice structure of the interface, the molecular structure of the ice at the interface and the adsorption preference of a chemical group on the surface, on the adhesion process. Before research can progress to develop better de-icing coatings and chemicals it is essential that the physical process ocurring well-understood on a more fundamental basis.

1.2 Research Goals

The primary objective of this dissertation is to gain a fundamental understanding of the processes involved in the formation and growth of ice-solid interface bonds. In this regard, the research goals of this dissertation are: (a) to investigate the influence of the microscopic physical-chemical parameters on the adhesion of ice, (b) to investigate the physical mechanisms responsible for the lower adhesive shear strength of an ice-solid bond compared to its tensile strength and (c) to develop criteria that can be used in the rational design of de-icing coatings and materials.

In contrast to previous theories of adhesion and empirical ice adhesion studies, the approach adopted here considers the role of microscopic factors on the macroscopic processes of adhesion. More specifically, the research investigates the molecular dynamics involved in the formation and stability of ice-solid bi-material interfaces.

The process of adhesive bond formation of ice is postulated to consist of three stages [17, 18]: (a) the adsorption of water molecules on the solid surface; (b) the nucleation of ice and the formation of stable ice embryos; and (c) the sintering of

ice clusters under the externally imposed temperature and pressure environment. Ultimately, the research seeks to shed light on how these physical stages can be controlled to minimize ice adhesion.

The results of this study will provide a rational basis for the design of de-icing coatings and materials to prevent and/or disrupt the formation of ice on solid surfaces. In this regard, the research approach consists of both experimental and computational methods that yield complementary information towards a new understanding of the icing problem.

1.3 Research Methodology

The experimental methods employ laser Raman microprobe spectroscopy as a tool for the investigation of intramolecular and intermolecular activities in the ice layers formed on solid surfaces. The computational approach uses molecular dynamics (MD) simulations of the ice and an ice-metal interface.

Raman spectroscopy provides *in-situ* information on the vibrational modes of the ice layers at a resolution of several microns. The MD simulation provides an atomistic picture of a few layers (about 20 angstroms) of ice forming on the solid surface. The combination of Raman spectroscopy and MD simulations together yield sufficient information to draw useful conclusions regarding the icing process.

The Raman spectroscopy is used to study the *structure* of the ice layers on solid surfaces. However, for understanding the mechanisms that are involved in the the formation of ice-solid interface bonds, it is also necessary to examine the process of *nucleation* and *growth* of ice on solids. This is studied using the video and confocal microscopy.

1.3.1 Rationale for Raman Spectroscopy

For the icing problem, the transient process of bond formation starts as an unstable state where ice crystals nucleate from the adsorbed water. Since the ice molecules at the interface reflect the geometry and the binding energy of the ice-solid bi-material

interface, the variation in the angle bending and bond stretching vibrational frequencies can be used as an indicator of the local atomistic environment. The vibrational frequencies in the O-H stretching mode of the ice molecule at the interface are representative of variations in intramolecular O-H bond length. The intermolecular activities at the interface can be quantified with data on the lattice vibrational frequencies. A branch of spectroscopy, known as vibrational spectroscopy, provides direct information regarding the molecular structure of a material, irrespective of its state of aggregation (e.g., vapor, liquid and/or solid).

Among the vibrational spectroscopic techniques (i.e., infrared, Raman, neutron scattering, and nuclear magnetic resonance), infrared spectroscopy uses the infrared part of the spectrum, Raman spectroscopy uses the visible part of the electromagnetic spectrum (laser beam), NMR uses variations in the magnetic field, and neutron spectroscopy uses the neutron beam as the source of excitation.

Raman spectroscopy has several experimental advantages that makes it favorable for ice-solid interface problem. Unlike NMR and neutron scattering, Raman spectroscopy does not need sample preparation and can be used for the *in-situ* analysis of submicron size samples. This feature makes it most suitable for the interface analysis. The Raman spectroscopy, being in the visible part of the electromagnetic spectrum, does not get absorbed due to the presence of water vapor (which is observed in the case of infrared spectroscopy) and, therefore, it provides a sharp spectrum of ice with little background noise in the optical signals. The vibrational sensitivity and the low signal-to-noise ratio makes Raman spectroscopy an excellent tool for studying the structure of ice at the interface [19].

Raman spectroscopy is based on inelastic scattering of the incident radiation as a result of interaction with the polarizability tensor of the sample material. This technique provides direct information on the intramolecular covalent (O-H) bond [20] and the weaker intermolecular hydrogen bond [21]. The difference in the band positions and the widths yields information about the hydrogen bonding and the crystalline structure [22].

The applications of the micro-Raman spectroscopy to thin films and interfaces

has gained momentum in recent years. They include research on the characterization of semi-conductors [23, 24, 25], stress determination in semiconductor films [26, 27], recrystallization of glass [28] and interface studies on carbon-carbon composites and monolayer assemblies [29, 30, 31].

1.3.2 Rationale for Video and Confocal Microscopy

The process of icing involves several stages as described in our three-stage model, i.e., adsorption of water molecules, growth of microcrystallites at the nucleation sites, and sintering of the crystals to form an interface ice layer. The effect of the various stages of icing on the adhesive strength is of primary importance to identify the important parameters that govern the ice adhesion process. In this dissertation, we begin from a controlled experiment in which mirror polished surfaces are first studied under the video microscope to study the process of nucleation and growth of ice. The same samples are then sheared in a laser Raman microprobe shear apparatus. Further studies on the nucleation and growth are conducted on the same sample surfaces using high resolution laser confocal microscope. The laser confocal microscope provides a unique capability for obtaining detailed scanned images of the flourecent samples layer-by-layer in three-dimensions that may not be possible with other optical microscopic techniques [32, 33].

1.3.3 Rationale for Molecular Dynamics Studies

Among the particle simulation methods, such as, Monte Carlo (MC) and molecular dynamics (MD) simulations [34], the MC method primarily deals with the equilibrium state satisfying to the minimum energy criterion. Unlike MC methods,the "molecular dynamics" (MD) approach (Alder and Wainwright, 1959) also provides complete information on the transient (dynamic) processes prior to achieving a stable equilibrium state.

In an MD simulation, the Newtonian equations of motions of a set of N particles in a volume V are solved numerically. The total energy E of the system is conserved as

the system moves along its trajectory. The model system evolves in time according to the interatomic force exerted by particles on each other and to the prescribed boundary conditions. For a complete description of the MD techniques and details of property calculations the reader may refer to the text by Allen and Tildesley [34].

Investigations involving the MD approach on water molecules were initially conducted by Rahman and Stillinger (1971) [35] who studied both static and dynamic behavior of water molecules based on a rigid tetrahedral model of the individual molecules. Numerous studies on water molecules and microclusters have since appeared (see, e.g., Rahman and Stillinger, 1971 [35], Briant and Burton, 1975 [36]; Berendsen et al. 1981[37]; Toukan and Rahman, 1985 [38]; Anderson et al. 1987 [39].

The structure of the water molecule is responsible for the unusual properties of water and ice [40]. The attribute of the water molecule giving rise to many physical peculiarities primarily originates from its polar character derived highly directional hydrogen bonds [41]. The triangular shape of the water molecule with a permanent dipole moment gives rise to a high dielectric constant, high specific heat and low diffusion coefficient.

A factor which complicates the simulation of molecular polar fluids and ionic solids is the long-range Coulomb interaction. All these complications lead to significant coupling between the intermolecular and intramolecular interactions. As a result, the analytical treatment becomes extremely intractable. In such situations, the molecular dynamics technique offers a unique capability to probe complex molecular interactions. Within the framework of MD simulations, it is possible to model long-range interactions in polyatomic molecules where the intermolecular and intramolecular interactions are explicitly defined. The MD approach is based on classical mechanics and the atomic motions arising from both the strong valence forces and weak dispersion forces without making any compromising assumptions.

More recently, an approach for modeling the potential function of metals, termed as embedded atom method, has been proposed by Daw and Baskes (1984) [42]. In this approach, the cohesive energy of metals is represented as the sum of the embedding energy, which is a function of electron density and the 2-body interactions. The

embedded atom method has been found particularly suitable for simulating metals and alloys of structural interest.

The availability of the potential functions for ice and metals makes it possible to undertake a study that involves an ice-metal interface. The atomistic information provided by such a system can be used to understand the mechanisms involved in the formation of the ice-metal interfaces and to predict the mechanical behavior of the interface.

1.4 Organization of Dissertation

Following the introduction in chapter-I, Chapter-II describes the Raman spectroscopic studies conducted on copper and aluminum surfaces and on electrical transmission line samples. The studies conducted in this chapter investigate the structure of ice layers forming on metal surfaces.

In Chapter-III we describe the design and fabrication of an optical cell (icing chamber) used for the study of nucleation and growth of ice on several metal surfaces. The nucleation is studied first using video microscopy and then in more detail using confocal microscopy. The results from the Raman microprobe shear apparatus built in the icing chamber indicate the role of the hydroxil group in the adhesion of ice.

In Chapter-IV, a molecular dynamics methodology involving simulation of bulk cubic ice and FCC copper has been discussed. This chapter primarily deals with the validation of the potential functions for the simulation of ice and copper. Having validated a potential model for cubic ice in chapter-IV, a few important MD experiments are carried out on bulk simple cubic ice and diamond cubic ice. The results of these molecular dynamics experiments are discussed in Chapter-V. In Chapter-VI, the simulation of an ice-copper bi-material is considered. Also, potential function for ice-copper interface is derived and a few preliminary results from the MD simulation are discussed.

Chapter-VII, finally reports the conclusions of both the experimental and molecular dynamics studies conducted. This chapter also summarizes the implications of

the research findings for the design of de-icing coatings and materials and identifies future research initiatives.

Chapter 2

Raman Microprobe Spectroscopy of Icing on Metal Surfaces and Cables

The primary focus of this chapter is to identify the structure (e.g., polycrystalline or amorphous) of ice layers on metal surfaces. *In-situ* laser Raman microprobe spectroscopy is used to probe molecular vibrations of ice layers at micron scale. Features of the Raman spectra of the thin and thick ice layers is compared with the Raman spectra of bulk crystalline and amorphous ice to identify structure.

2.1 Icing on Metal Surfaces

The adhesive strength of ice on solids has been studied in such occurrences as icing of electrical transmission cables, highways and bridges, and aircraft and ship-decks[1, 43, 3, 4, 5, 11]. These studies indicate that both physical properties (e.g., surface roughness, surface energy, substrate temperature, droplet size in vapor, etc.) and chemical properties (e.g., chemical composition of surface, trace species present at the surface, etc.) influence the resulting adhesive strength of atmospheric ice on a solid surface.

The process of icing often involves freezing of atmospheric vapor on a cold metallic

surface. The ice layer which forms initially at the interface influences the growth rate, physical properties and microstructural characteristics (defect density, porosity, crystallinity, morphology, etc.) of the subsequent layers. Therefore, the microstructural properties of the ice layers at the interface can provide fundamental information on the physics of the processes involved during ice adhesion.

In-situ vibrational information on the intramolecular covalent (O-H) bond and the weaker intermolecular hydrogen bond in an ice sample can be obtained via laser Raman spectroscopy. Since the vibrational signatures differ for each metamorphic phase of ice, Raman spectroscopy is used typically to identify the metamorphic phases of ice I to IX. With the development of the Raman microprobe and optical multichannel analyzer, it is now possible to obtain the in-situ Raman spectra from sub-micron size samples. As a result, application of the Raman microprobe to thin films and interfaces has gained momentum in recent years, e.g., in the chemical characterization of semiconductor films[23, 24, 25], determination of local stress in semiconductor thin film devicesNishioka, Atwater, recrystallization of glass [28], and interface studies on carbon-carbon composite and monolayer assemblies [31, 29, 30, 31].

This paper is concerned with the structural characterization of vapor deposited ice on cold metallic substrates using the Raman microprobe.*In-situ* Raman spectra of the interface ice layer are obtained in the translational vibrational (lattice frequency) region, i.e., 100-400 cm^{-1} and the O-H stretching region, i.e., 2800-3600 cm^{-1}. For purposes of comparison, the spectra of bulk water and bulk ice are also obtained. The process of ice formation on solid surfaces has been observed by recording time-resolved Raman spectra. The variations in the Raman peak positions and half power bandwidth are investigated to study the structure of both thin and thick interface ice layers.

2.1.1 Low Temperature Optical Cell using Liquid Nitrogen Bath

To record the low temperature *in-situ* spectra of vapor-deposited ice on a cold metallic substrate, an optical liquid nitrogen cell has been fabricated. Figure 2-1 shows a schematic of the cell and the optical path accessible to the Raman microprobe. The liquid nitrogen cell is fabricated with a clear laboratory grade glass with a glass-to-metal seal for achieving effective thermal cooling. A metal finger protruding from the glass-metal seal thermally connects a copper extension to the liquid nitrogen bath. The cold copper extension acts as a flat surface for the nucleation and growth of the vapor-deposited ice layer. The substrate assembly is kept in a glass capsule. The copper substrate extension is exposed to the microprobe through a flat quartz window. To measure the temperature of the cold surface, two copper-constantan thermocouples are brazed on the lower side of the metal extension. The thermocouples are placed below the spot where the optical observations are made. The accuracy of the temperature measurements was found to be $\pm$ 0.2 K.

The low temperature cell is evacuated to (a pressure of 0.5 to one Torr) to prevent frosting of the observation window. Liquid nitrogen is supplied to the cell, and the temperature is observed to ensure a steady state condition in the metallic substrate. Saturated vapor is supplied through a bleed valve, and the flow rate of the vapor is measured by a sensitive rotameter (Omega Inc.).

2.1.2 Spectroscopy on the Metal Surfaces

A Leitz-Ortholux microscope is used for the *in-situ* probing of the interface ice layer deposited on the cold substrate. The microscope is optically coupled to the spectrometer (Spex Triplimate). Details of the spectroscopic and optical multichannel analyzer are given by Sharma et al.[44]. The Raman spectra are recorded at both back scattering (180°) and 135° geometries as shown in Figure 2-2. A 10X objective with a focal length of 15 mm is used to focus the laser beam as well as to collect the scattered radiation from the sampling area. The collected scattered light is subsequently

focused through a 200 μm pin-hole to the monochromator entrance slit.

The sample is excited by an Argon ion laser (Spectra Physics 2020) with an average power of 30-50 mW at a wavelength of 4880 angstrom. The scattered light is detected by an optical multichannel analyzer (EG&G Princeton Applied Research, OMA-III). The data are scanned and analyzed by a dedicated computer (EG&G Model-1460).

The O-H stretching and translational vibrational regions of the Raman spectra were calibrated with the plasma lines of an $r^{(+)}$ ion laser. The optical alignment of the monochromator was verified using the Raman spectra of a standard Mercury lamp. The wavenumber calibration was accurate to within $\pm$ 1.4 cm^{-1} when the optical signals in the monochromator were resolved by a 1200 grooves/mm grating.

2.1.3 Growth of Ice on Metal Surfaces

In the present study, ice is formed by the condensation of saturated vapor on the cold substrate. The metal surface provides the necessary nucleation sites for the vapor-to-solid phase transition. The growth of ice layer formed in this manner closely resembles the process of ice accretion on aircraft wings, overhead transmission cables, etc.

The thickness of the ice layer was measured with the microscopic focusing capability of the Leitz-Ortholux microscope. The vertical movement of the microscope stage was calibrated by focusing on the two surfaces of a thin glass slide of a known thickness. The least count of the macrometer screw was found to be 1.5 $\pm$ 0.4 μm.

It is important to note that because of the sharp focusing capability of the microscope used in micro-Raman spectroscopy the scattered radiation is collected primarily from the focusing volume with a vertical resolution of about 7.5 μm (see Figure 2-2). The space-resolved Raman spectrum of the thick ice layer is obtained by focusing the microscope on the top surface and this spectrum has minimum distortion due to contribution from the lower lying ice interfac.

The visual and video observations through microscope show that the vapor droplets condensing on the metallic substrates typically range in 25-35 μm diameter. These droplets grow gradually to 60-70 μm size by coalescence. At this size they stop grow-

ing and through surface diffusion form an interface ice layer. Using this observation as a reference, we have defined an ice layer less than 35 μm (the thickness before coalescence) as a 'thin interface ice layer' and the ice layer greater than about 70 μm (the thickness after coalescence) as a 'thick ice layer'. This definition can be used to differentiate between the structures of the initial ice layer from the subsequent ice layers. It is important to note here that the thickness of interface also depends on the surface texture i.e. average size of pits on the metal surface. A detailed scanning electron microscope (SEM) study on the effect of surface texture and surface energy on ice accretion process will be published elsewhere.

Procedure

In order to conduct repeatable experiments and clearly establish the characteristics of both the thin and the thick interface ice layers, the following procedure has been adopted:

1. The surface of the substrate metal is thoroughly cleaned with a solvent (Acetone).

2. Liquid nitrogen is poured into the cell and the vacuum is turned on to evacuate the complete assembly. Sufficient time is allowed for the temperature to reach a constant value, typically in the range of $\pm$ 0.5 K, and the vacuum pressure to stabilize at about one Torr.

3. A spectroscopic observation of the cleaned surface is made to ensure that there are no external artifacts present on the surface.

4. The monochromator is set to the lattice frequency region (505 nm). The region is calibrated with Argon plasma lines.

5. Vapor is introduced through a bleed valve at a rate of about 10 $\pm$ 1 ml/min for about 2 minutes. The bleed valve is closed and no observation is made until the temperature and pressure are restored to steady state. Typically, vacuum pressure returns to about one Torr value within two minutes, while the temperature takes about five minutes to settle back to a constant value.

6. The vapor deposited thin film of ice is observed through the microscope and the spectroscopic observations are made in the lattice frequency region. The observations are repeated at least five times at a given interface thickness to ensure the repeatability and stability of the observed spectra. However, only the best reproducible spectra are reported. The thickness of the interface layer is measured by the microscope.

7. The monochromator is now set to the O-H stretching region (581 nm) and spectroscopic observations are repeated for the same thin ice layer. The spectral observations are calibrated by recording the Argon plasma lines in the same region.

8. The monochromator is set back to the lattice frequency region. The vapor is introduced again, and time-resolved spectroscopic observations are made while the initial thin ice layer is growing in thickness. A flow rate of 80 ± 2 ml/min is maintained for about five minutes. The Raman spectra are recorded at a rate of one spectrum per 0.5 minute. For the measurement of growing layer thickness same experiment is repeated in O-H stretching region.

9. The thick ice layer formed at the end of the ice growth process is then observed in the O-H stretching region. The spectra are calibrated by recording Argon plasma lines. Once again sufficient number of spectra are collected to ensure repeatability of the results.

The thickness of the thin interface ice layer was measured to be 30 ± 1.5 μm for the copper surface and 20 ± 1.5 μm for the aluminum surface. The thick ice layer was found to be 90 ± 1.5 μm on the copper surface and 80 ± 1.5 μm on the aluminum surface. The Raman spectra of both the thin and the thick ice layers were observed at a temperature of 120 ± 2 K. The variation in the Raman bands with temperature was also recorded. A temperature of 120 K was selected to ensure the existence of a sufficiently thick and stable interface layer. At higher temperatures, due to thermal agitations, the interface layer is expected to become smaller than the resolution of the present experimental set-up.

Measurement of the interface thickness at different temperatures will be useful data in characterizing the growth mechanism. However, the present experimental set-up is inadequate to make this measurement with necessary accuracy and the task is left for future research. The conclusions in the present paper are not dependent on this information.

2.1.4 Results of Spectroscopy on Metal Surfaces

The interface ice layers are characterized on the basis of the Raman spectra in the translational vibration and the O-H stretching regions. The crystalline phase is represented by a sharp peak in the lattice vibration region in the Raman spectrum. The parameters which are important in characterizing the structure of the interface ice phase are the band frequencies, the half power bandwidth (HPBW), and the relative positions of the bands in the O-H stretching region.

Bulk Water and Ice

To understand the important features of the Raman spectra of the water molecule, we start with the spectra of bulk water and bulk ice. Figures 2-3A and 2-3B show the spectra of bulk water at room temperature (295 K), at the freezing temperature (273 K), and of ice below the freezing temperature (263 K) in the lattice and O-H stretching frequency regions, respectively. The spectra show that the liquid and solid states have distinct features. In the lattice frequency region, the peak frequency increases as a result of the strengthening of the hydrogen bond in the solid phase [45]. In the O-H stretching region, water has a broad peak which is replaced by a distinct symmetric peak in the solid phase. The O-H stretch frequency decreases in the solid phase and this reduction is attributed to the lengthening of the O-H covalent bonds (see Figure 2-3B) [20].

In the case of bulk ice, a single sharp peak at 214.2 cm^{-1} in the lattice frequency region has been assigned to the transverse optic (TO) translational vibration by Bertie and Whalley [45]. The shoulder at 165.5 cm^{-1} is assigned to the longitudinal acoustic (LA) branch of the translational vibrations of the lattice. Due to the anharmonicity of the lattice structure of ice, the sharp peak of the lattice frequency becomes temper-

ature and stress sensitive. With a decrease in temperature, the TO peak is expected to move towards higher frequencies (see Figure 2-3A).

In the O-H stretching region, the strong symmetric peak at 3185 cm^{-1} in the case of ice-Ih is assigned [20, 46] to the in-phase stretching vibration, $nu_(1)$, and the broad symmetric peak at 3456 cm^{-1} is assigned to the out-of-phase stretching vibrations, $nu_(3)$. Tables 2.1 and 2.1 show that the observed lattice and O-H stretching Raman bands are in excellent agreement with data in the literature [20, 47, 21]. The intensity peak assignments in the O-H stretching region were made with the aid of a Lorentzian line shape fit to the raw data. These fits are not included in the figures for the sake of clarity.

Ice on Metal Surfaces

Ice formation at the interface is investigated by comparing the structural characteristics of the thin and the thick ice layers. The most important features, as stated earlier, are the bandwidths and the peak positions of the Raman bands in the lattice mode and O-H stretching modes.

The bandwidth in the lattice region indicates the degree of order in a crystalline system. A sharp peak represents an ordered state, as in the case of bulk ice, while a broad peak shows loss of crystalline order, as in the case of bulk water (Figure 2-3A). According to Brueck et al.[48], an increased disorder in the lattice structure leads to broadening of the TO branch. Kakimoto and Katoda [49] showed that *stress-induced* disorder affects the LO branch of the crystal force field. An increase in the shear stress at the interface is expected, therefore, to increase the bandwidth of the LO branch. These studies suggest that the peak in the lattice mode is sensitive to the state of order and the local stress environment.

Figure 2-4 shows the sequence of spectral measurements using time-resolved Raman spectroscopy. As previously mentioned, first a stable thin interface ice layer is produced by introducing vapor at slow flow rate. The microscope is used to measure the thickness of this layer. The growth of the stable thin interface ice layer into a thick ice layer is observed via time-resolved Raman measurements. The thickness of the ice layer increases gradually from its initial value of 30 μm, as depicted in Figure

2-4, and reaches a final value of 90 μm over a duration of 300 seconds. The intermediate layer thicknesses in Figure 2-4 are estimated approximately by an interpolation of the Raman peak intensities in the O-H stretching region which vary with growing thickness of the layer. The intensity of the O-H stretching peak for initial and final layers are used as the initial and final data points and the intermediate data are interpolated using the intensities for the intermediate layers. The intermediate thickness measurements, are accurate to within about ($\pm$ 10%), although the microscopic observations made for the initial and final layer thickness are significantly more accurate (to about $\pm$ 2%). In spite of this limitation, the time-resolved measurements provide useful qualitative information on the growth process.

Spectroscopic observations at the interface (Fig. 2-4) show that the thin ice layer has an extremely broad spectrum in the lattice region. This indicates either that the interface layer is not sufficient to generate a Raman spectrum, or that it is extremely disordered in nature. To check on the accuracy of the spectral observations of the thin ice layer, the spectrum of the same layer is obtained in the O-H stretching region. The spectrum shows a symmetric intense broad peak near 3100 cm^{-1} (see curve I in Figure 2-5). From these observations, it is possible to infer that the thin layer is indeed a layer of ice sufficient to generate a Raman spectrum. Therefore, the broad spectrum observed in the lattice region is most likely representative of an extremely disordered state.

Further deposition of vapor on the thin ice layer, as observed in the time-resolved Raman spectra, shows the gradual development of a sharp peak in the lattice region. The spectrum of the thick ice layer (as shown in Figure 2-5) has an intense sharp peak, which has been clearly associated with the crystalline ice phase by Johari and Sivakumar [21]. These observations suggest that the ice-solid interface may not be crystalline initially and that it transforms from a highly disordered state to an ordered state as the layer thickness increases.

The band positions and the band shapes in the O-H stretching region are known to be sensitive to intramolecular interactions. The factors strongly influencing the bandwidths in the stretching region as discussed by Sivakumar et al.[19] are: (a) the

configuration of the near neighbors and, (b) the variation in the O-H bond length. These parameters (neighbor configuration and bond length) provide useful information about the structural order in the local environment.

The Raman spectra of ice layers on a copper substrate in the O-H stretching region are shown in Figure 2-5. The figure shows that the 3100 cm^{-1} peak is sharp and symmetric for the thick ice layer while it is broader for the thin ice layer. The peak positions and the respective bandwidths of the thin ice layer show good agreement with the spectrum of *low density amorphous solid water* reported by Venkatesh et al. [50] and Sivakumar et al.[19]. These observations suggest that the water molecules condensing on top of the cold substrate experience rapid cooling and do not get enough time to form an ordered structure. The subsequent layers of ice experience relatively slower cooling because of the low thermal conductivity of the thin ice layer already existing on the copper substrate and, as such, form an increasingly ordered structure. The differential thermal expansion of the metal and the ice can induce local stresses at the interface that, in turn, contribute to the disorder in the interface region. These stresses are non-existent in subsequent layers and, hence, permit the formation of an ordered structure as the thickness of the ice layer increases.

Several interpretations have been offered in previous studies[50, 19, 51, 22]to explain the band broadening of the O-H stretching peaks for amorphous solid water (also denoted as *low density amorphous ice*[52] and high density amorphous ice. In general, the coupling between the O-H and O-O oscillators, caused by the redistribution of the O..O..O angles, has been suggested as the possible mechanism responsible for the broadening of the peak at 3100 cm^{-1}.

The Raman spectra of the thin and the thick ice layers on an aluminum surface are shown in Figure 2-6. The features observed in these spectra are similar to those observed in the case of copper. In the O-H stretching region, the symmetric peak is broader for the thin interface ice layer while the same peak is sharp in the case of the thick ice layer. These observations suggest that the ice growth phenomenon is relatively independent of the type of metal used as the substrate. However, it would be necessary to make similar observations on other metallic surfaces before the

generality of this result can be fully accepted.

The symmetric stretching mode of crystalline ice, nu_1, is sensitive to temperature variations because of the coupling between the O-H stretching and lattice vibrations caused by the hydrogen bonding. Figure 2-7 shows the temperature variation of the nu_1 mode for both the thick and thin ice layers. The variation of nu_1 for crystalline ice as reported by Sivakumar et al.[19], Gabrichidze[53], and Cross et al.[54] and that for amorphous solid water reported by Sivakumar et al.[51] are also plotted in Figure 2-7. The thin ice layer follows the trend of amorphous solid water while the thick ice layer closely follows the trend of crystalline ice. These observations clearly suggest that the thin ice is primarily disordered in nature, with a possible resemblence to low density amorphous ice, and the thick ice layer resembles crystalline ice.

The half power bandwidth (HPBW) of the Raman peaks is also related to the degree of order in a crystalline solid[51, 22]. As shown in Figure 2-8, the HPBW of the ν_1 peak for the thin interface ice layer is larger than that for the thick ice layer suggesting that the interface ice layer is disordered. The temperature variations of the HPBW for the thin and thick ice layers are also compared with the HPBW variations for bulk polycrystalline ice and bulk amorphous ice as reported by Sivakumar et al.[51]. The comparisons show that the temperature variation of the thin interface ice layer follows the trend of low density amorphous solid water, while the variation for the thick ice layer closely resembles that of polycrystalline ice.

In Figure 2-7 we observe that the ν_1 frequencies for interface ice layers are, in general, lower than that observed by others[51, 53, 54] On the other hand, figure 2-8 shows that the HPBW for the thin ice layer is marginally smaller than that for bulk amorphous ice[51] while the HPBW for thick ice is larger than that for bulk crystalline ice[51]. These observations suggest that the ν_1 vibrations in the interface ice layers are restrained as compared to bulk samples and that the thick ice layer is more disordered than the bulk crystalline samples.

The reduction in ν_1 frequencies and increase in the disorder in the thick ice layer can be attributed to: (a) the presence of the solid substrate which provides an additional restraint to the vibrational motions of the ice molecules in the interface ice

layers; and (b) to the intermixing of disordered and ordered layers. The random vibration of the disordered structure is likely to reduce the ν_1 frequencies and increase disorder in the thick ice layer. It is important to note that the polycrystalline and amorphous ice samples grown by Sivakumar et al. are as much as a few millimeters in thickness and are representative of the pure bulk phase without surface effects.

The broad spectra in the lattice region, similarity of the stretching peak to amorphous ice, and temperature variations of the ν_1 peak frequency and half power bandwidth strongly suggest a disordered structure for the thin interface ice layer. However, the distinction between the disordered structures obtained in a high defect density crystalline solid and an amorphous ice phase needs further high resolution microprobe investigation[51]. Also, investigation of icing on non-metallic substrates will be useful in understanding the effect of surface energy on the ice formation process.

2.1.5 Conclusions of the icing on metal surfaces

The Raman microprobe multichannel spectroscopy has been used successfully for the *in-situ* microprobing of interface ice layers. Both time-resolved and steady state observation in the O-H stretching and lattice vibrational regions have been obtained.

The results strongly suggest disorder in the interface ice layer which forms initially on a cold metal substrate. The disordered structure has spectral similarity with that of low density amorphous ice. Ice layers forming subsequently become ordered and their spectral features resemble that of polycrystalline ice. The transition from a disordered structure to an ordered structure occurs in a gradual manner. The disorder in the interface ice layers seems to be caused primarily by rapid thermal cooling, and appears to be independent of the type of metallic substrate used.

At a given temperature, the profile of the ice-solid bond consists of an initial disordered layer which behaves like low density amorphous solid water and subsequent layers that gradually turn into a dense crystalline phase. The presence of the low density water (liquid) like interface may be responsible for the low shear strengthin the case of ice-solid adfreeze bonds.

NOMENCLATURE

ν_1 = in-phase O-H stretching Raman frequency, cm^{-1}

ν_3 = out-of-phase O-H stretching Raman frequency, cm^{-1}

ω = lattice vibrational Raman frequency, cm^{-1}

HPBW = half power band width, cm^{-1}

TH = thickness of an ice layer on the substrate, μm

Table 2.1: Temperature Variation of Vibrational Frequency in the O-H Stretching Region for Bulk Samples.

Temperature (K)	ν_1 (cm^{-1})	ν_3 (cm^{-1})	HPBW (ν_1) (cm^{-1})	HPBW (ν_3) (cm^{-1})	Sample Ref.
295	3185	3456	240	470	water
295	3188	3420			Scherer et al. [20]
273	3185	3417	213	560	water
273	3180				Scherer et al. [20]
263	3140	3390	155	280	ice
263	3144				Scherer and Snyder [47]

Table 2.2: Temperature Variation of the Vibrational Frequency in the Lattice Mode for Bulk Samples.

Temperature (K)	ω (cm^{-1})	HPBW (ω) (cm^{-1})	Sample Ref.
295	165.5	103	water
295	165		Scherer et al. [20]
273	176	70	water
273	177		Scherer et al. [20]
263	214.3	40	ice
263	214		Johari and Sivakumar[21]

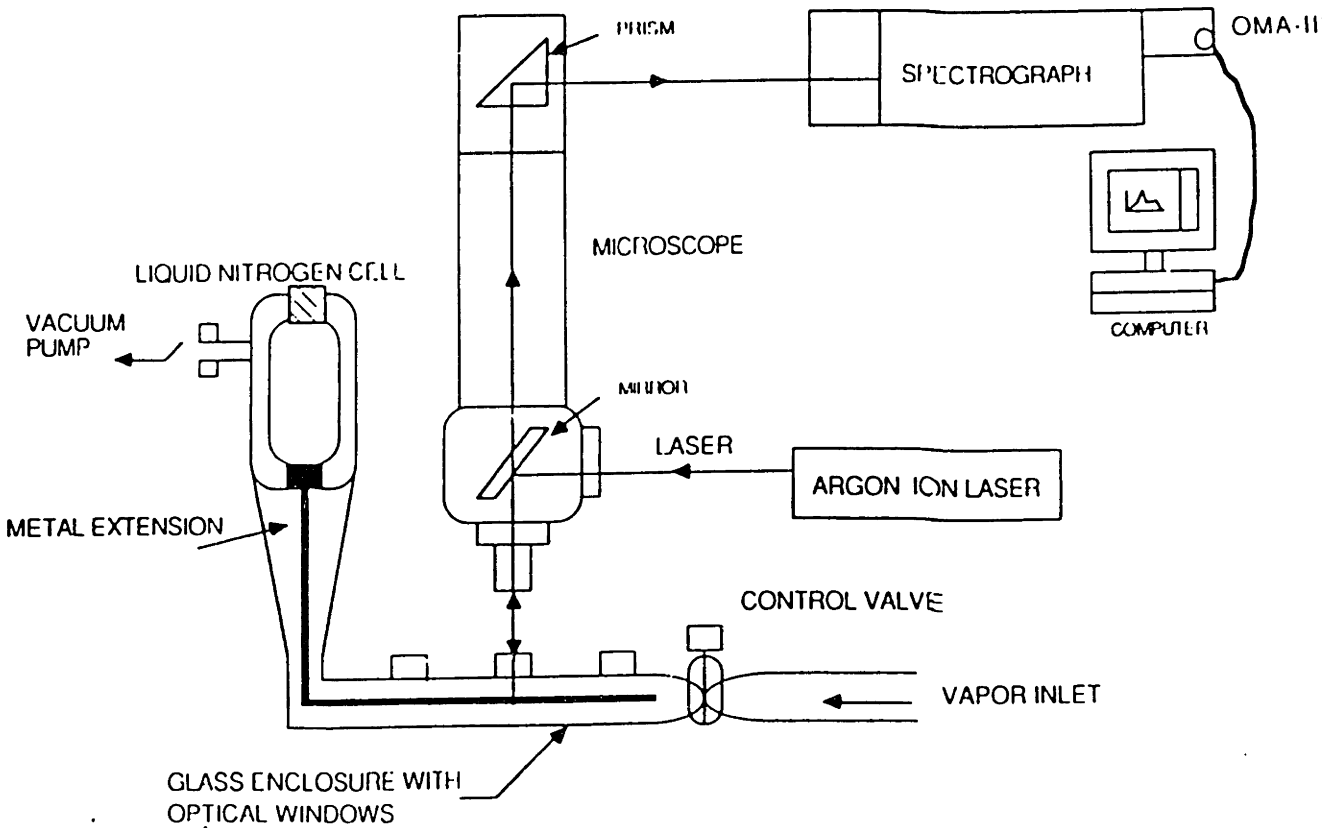

Figure 2-1: Schematic diagram of the liquid nitrogen experimental set-up.

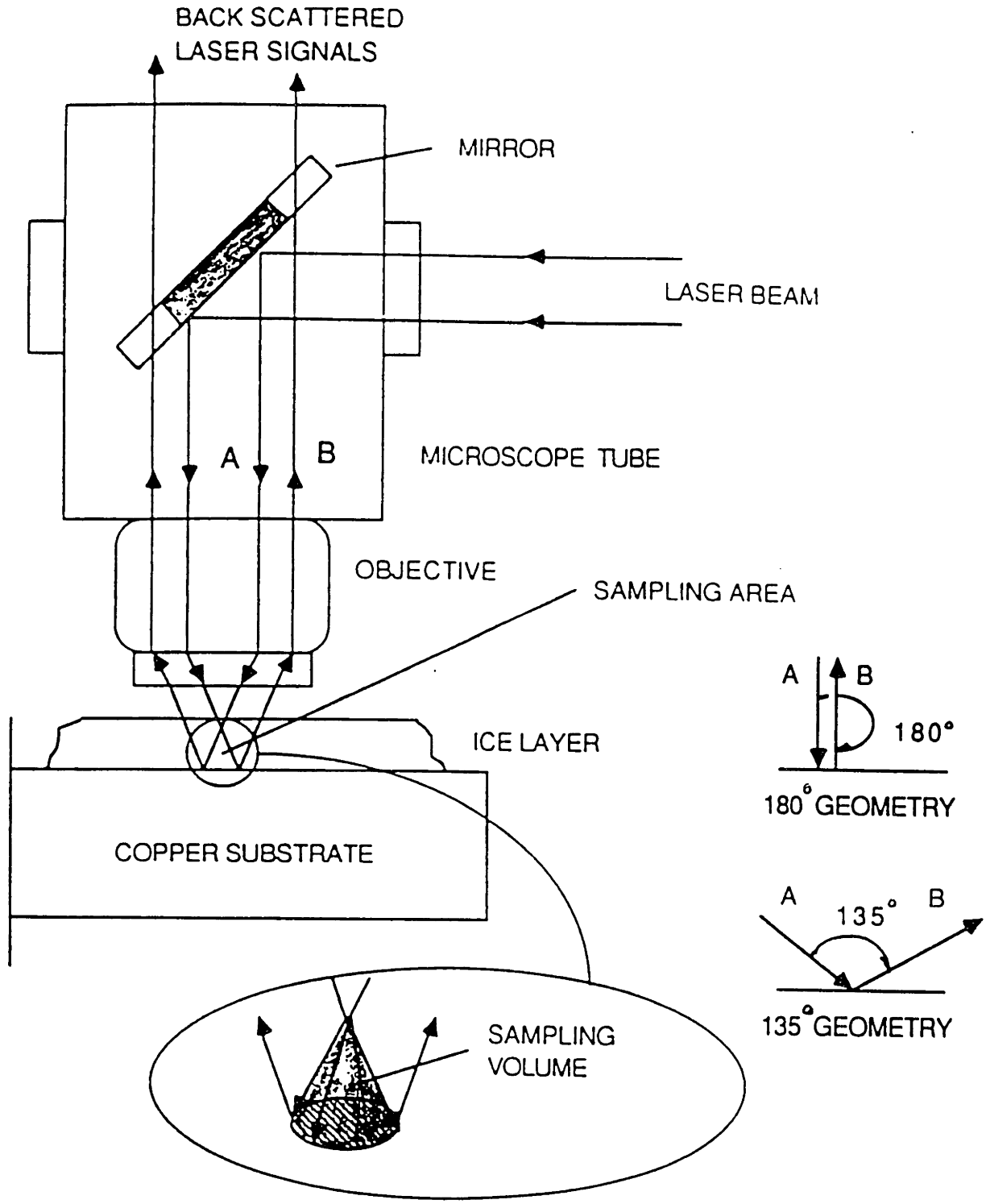

Figure 2-2: Schematic diagram of the microprobe laser pathe. A incident beam direction; B. scattered beam direction.

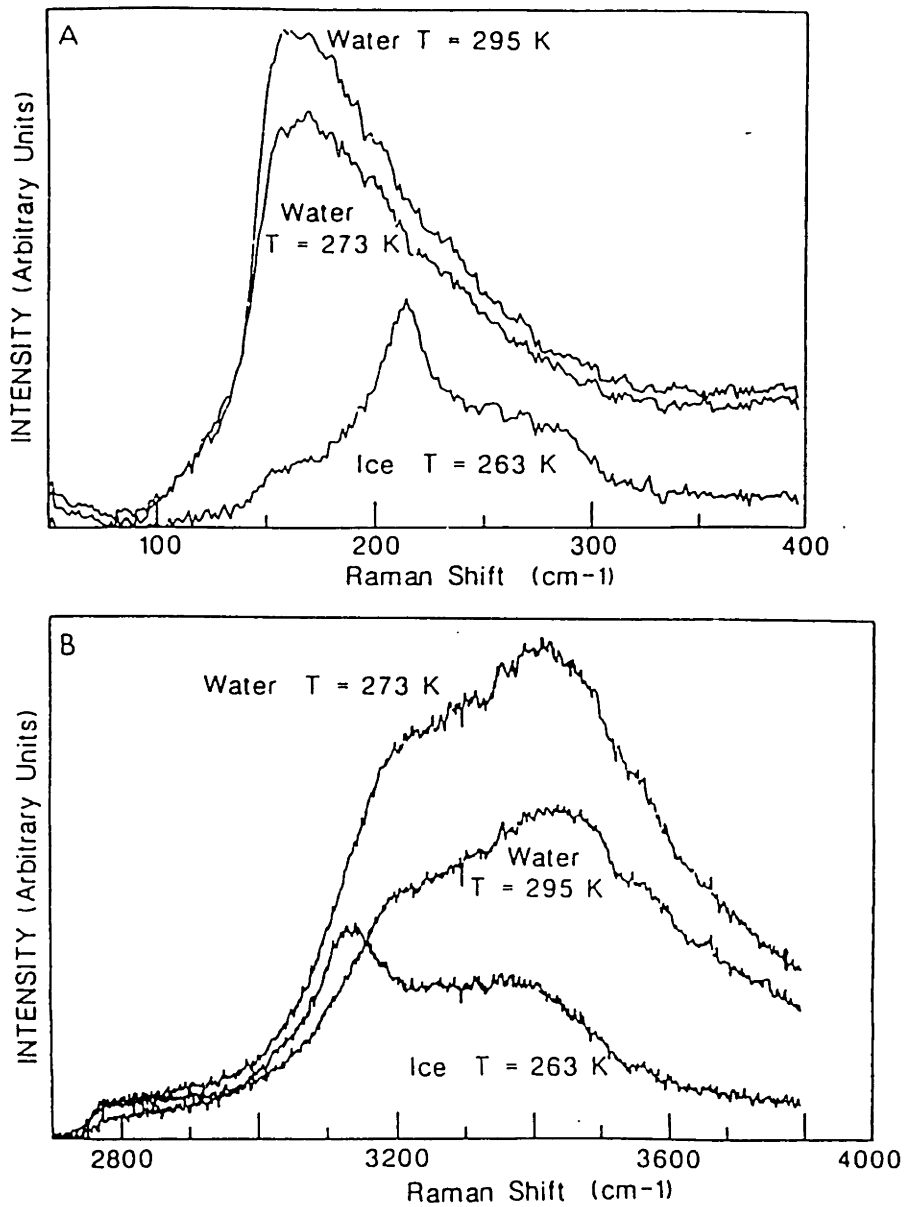

Figure 2-3: Phase transition from water to ic. (A) Lattice frequency region; (B) O-H stretching region.

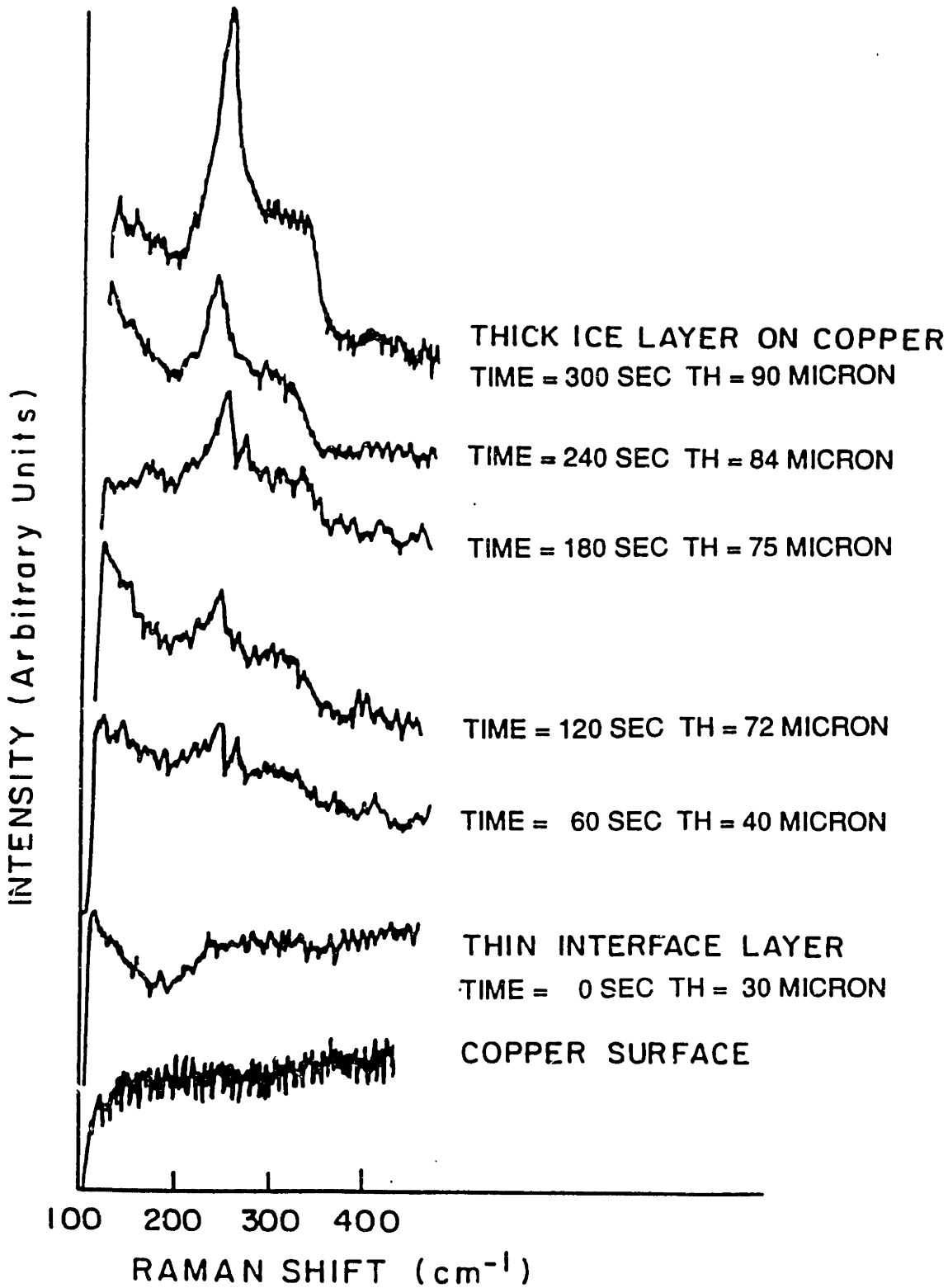

Figure 2-4: Time-resolved Raman spectra in lattice frequency region.

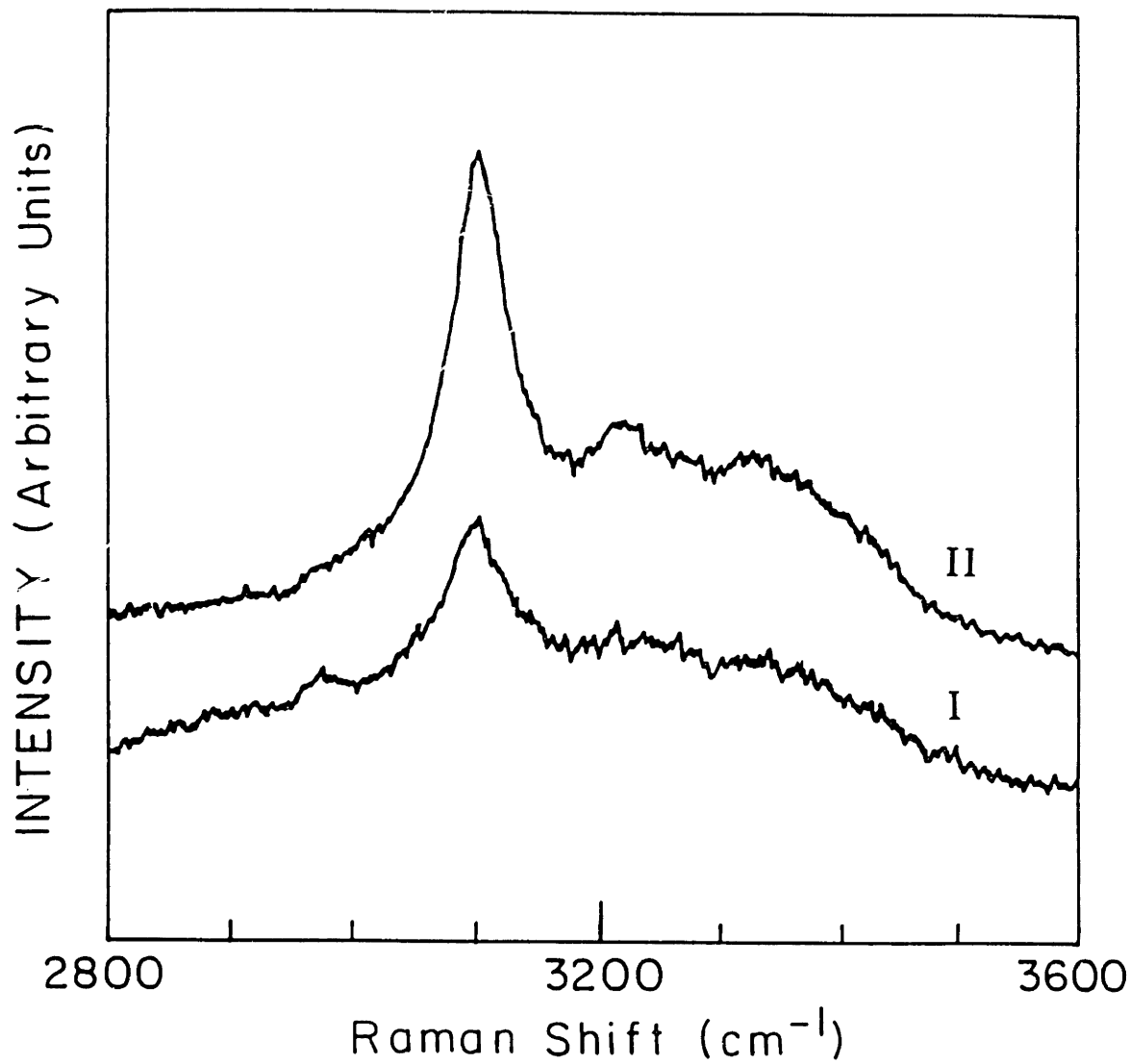

Figure 2-5: Raman spectra of ice layers on copper at 120K in O-H stretching region. (I), Thin ice layer; II, Thick ice layer.

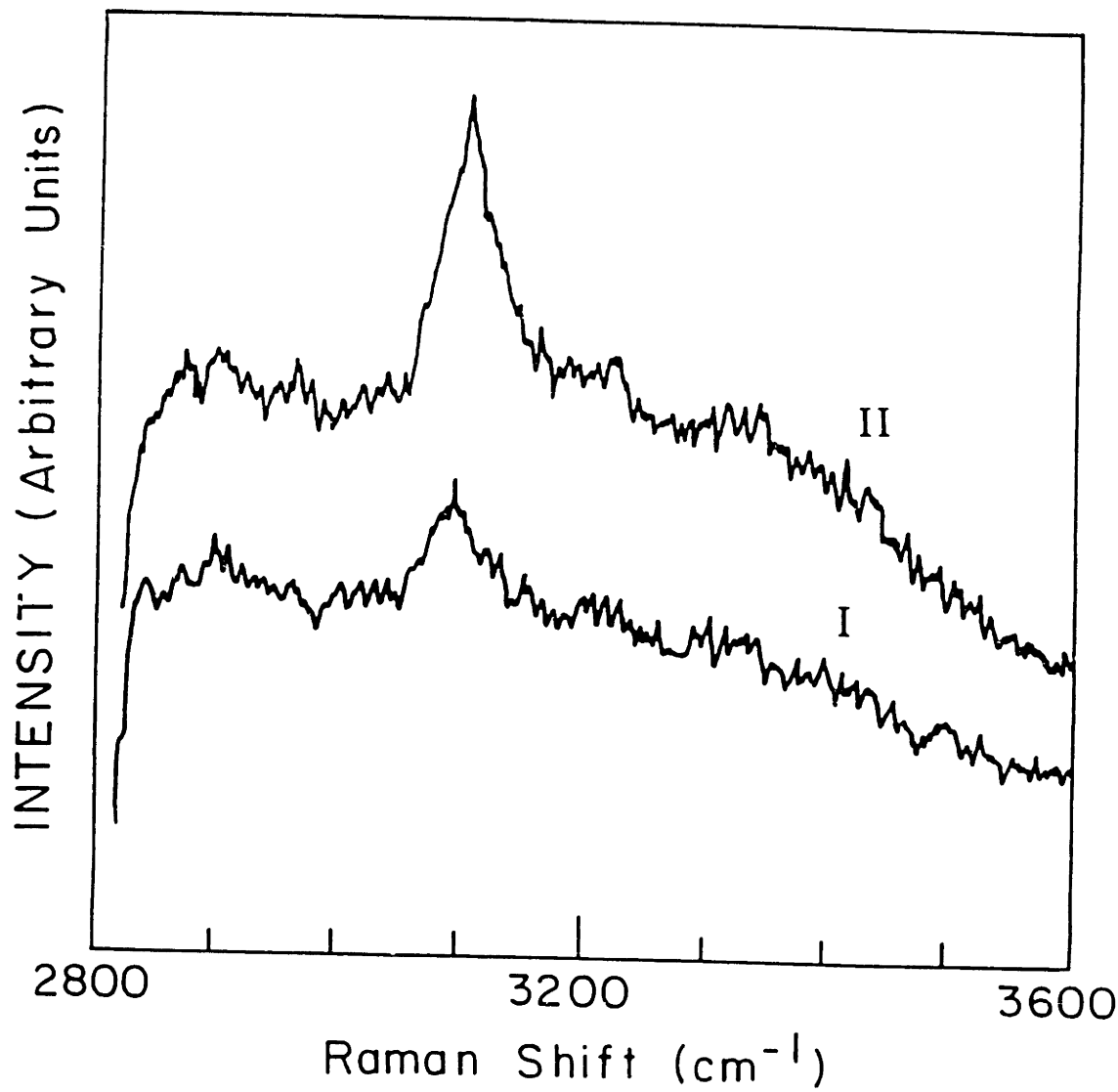

Figure 2-6: Raman spectra of ice layers on aluminum at 120K in O-H stretching region. (I), Thin ice layer; II, Thick ice layer

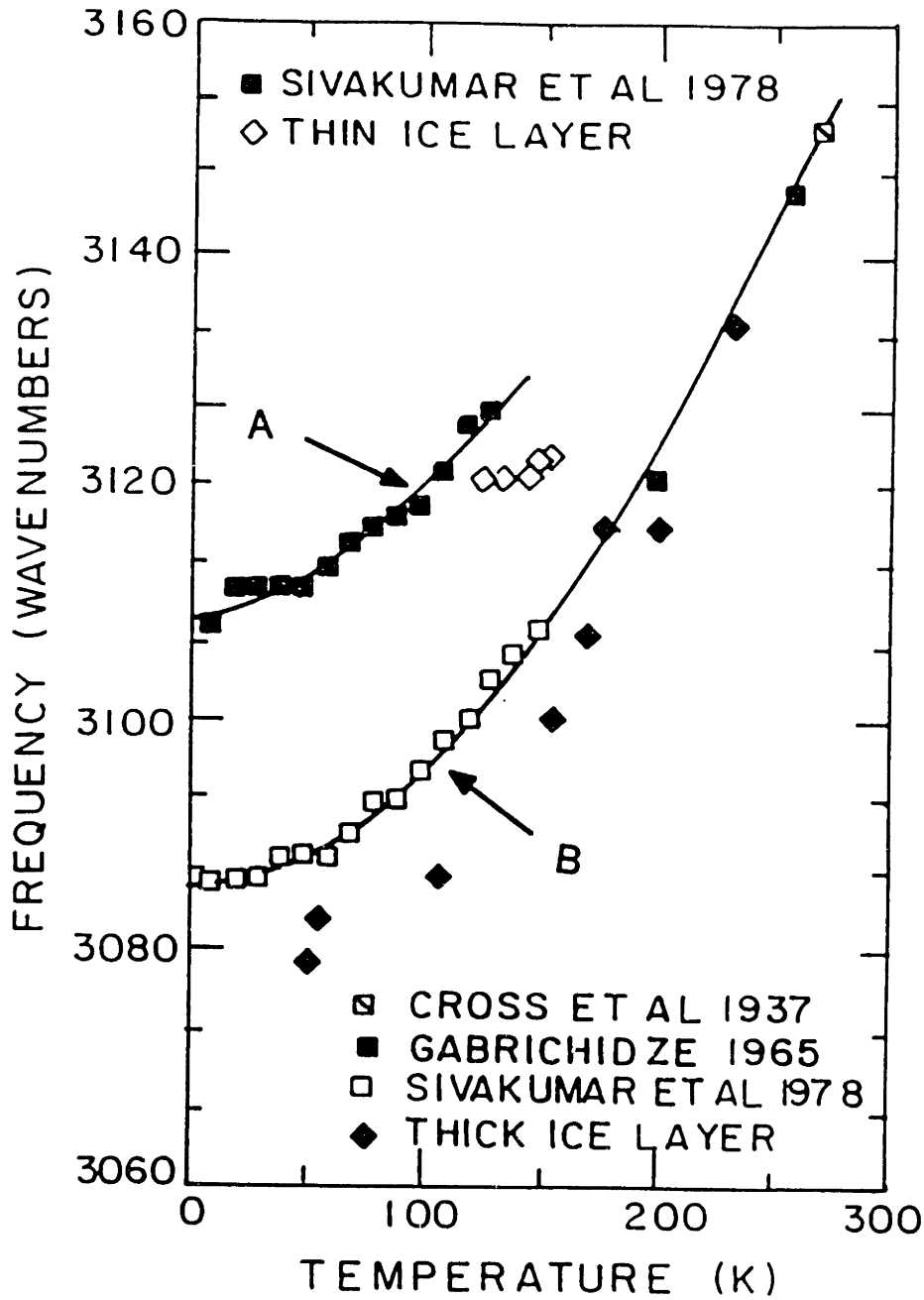

Figure 2-7: Variations of symmetric stretching frequency with temperature. A, Amorphous ice; B, crystalline ice

2.2 Structure of Ice Layers on Transmission Line Samples

At high latitudes and during severe winter, freezing rain and supercooled fog can unpredictably cause excessive accretion of ice on the surface of electrical transmission cables and support towers [4]. The excessive buildup of ice on long-span, flexible structures such as transmission cables may lead, in turn, to the collapse of tension towers, short circuiting, flashovers, conductor failures, and galloping. As a result, research activities have been initialted to reduce transmission cable icing. These studies include development of computer models to predict rate and shape of ice accretion, mechanical devices to shed ice from cables, and deicing coatings and chemicals to reduce adhesion of ice on the cables [4, 55, 56, 57, 58, 59]. However, fundamental physical understanding of the molecular structure of the ice layers responsible for the large scale accretion is still lacking.

In order to understand the fundamental process involved in ice nucleation, bond formation and growth, it is important to identify the molecular structure of the ice layers deposited on the cold cable surface. Laser micro-Raman spectroscopy provides an effective means to record the *in-situ* vibrational spectrum and to identify the layer-by-layer molecular structure of ice [29, 31, 60].

We have fabricated an icing chamber using a closed-cycle helium cryostat that allows the *in-situ* vibrational spectrum to be measured when ice is deposited on samples from an electrical transmission cable. The *in-situ* Raman spectra of the ice layers are recorded in the O-H stretching region (2800-3400 cm^{-1}). The temperature of the cable sample is varied from 30K to 180K in steps of 10K. A comparison of the temperature variations in the band position and the half power band width (HPBW) of the thinning ice layer has been made with both polycrystalline and low density amorphous ice to identify the layer-by-layer structure.

The variations in the O-H stretching peak positions and the the half power band width indicate the existence of polycrystalline ice layers that become extremely defective as we probe closer to the metal surface. We postulate that the excessive

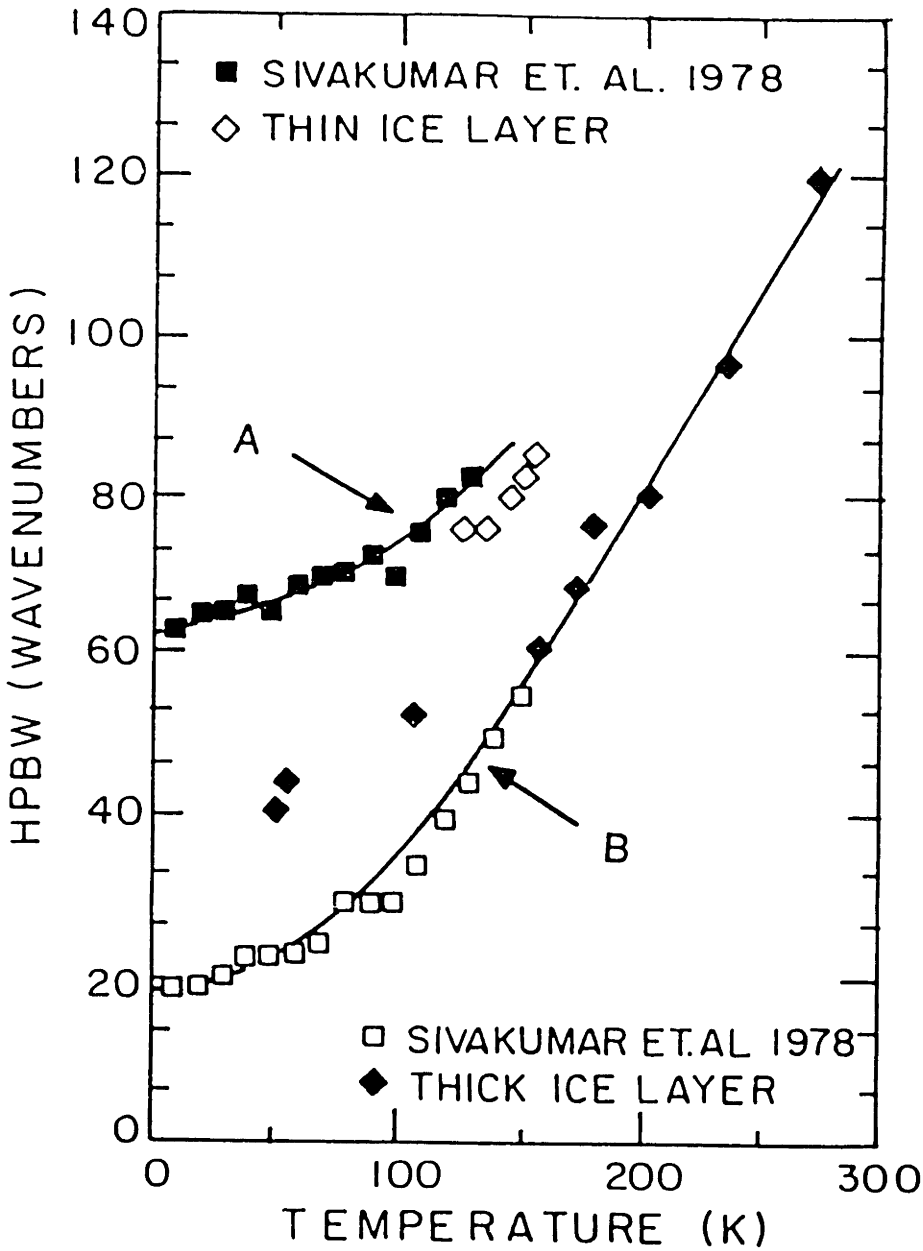

Figure 2-8: Variations of the half power band width (HPBW) with temperature for symmetric stretching frequency. A, Amorphous ice; B, crystalline ice

disorder in the ice layers close to the metal is inherited from the low density amorphous phase which exists prior to the phase transition to polycrystalline ice at about 150K temperature.

2.2.1 Helium Cryostat Icing Chamber

A closed cycle He cryostate (CTI Cryogenics) is used to cool the transmission cable samples to extremely cold temperatures (30 K). A He cryostate is ideal for extremely low temperature applications (as low as 10 K). As shown in Figure 1, a copper holder is fabricated to mount the 125 mm cable samples on the cooling spot of the He cryostate. The copper holder ensures good thermal contact between the cooling element and the cable samples. The holder along with the samples is put under moderate vacuum (5-10 milli-Torr) by providing an aluminum enclosure on top of the cryostate cooling element. This enclosure forms an evacuated icing chamber around the cooling element to prevent frosting of the optical windows. The aluminum enclosure has 2.54 cm diameter optical quartz windows on the four sides to facilitate optical excess to the cable samples. The vapor is introduced through a needle valve connected to a mass flow controller. A heating coil is wound around the cooling element of the cryostate. The temperature at the sample holder is measured using flat shaped thin platinum resistance temperature detector (RTD). A microprocessor based temperature controller is connected to a gold-bismuth thermocouple to sense the temperature at the cold finger. The temperature controller adjusts the heating load to maintain the desired temperature at the cold finger.

The cryostate with aluminum icing chamber is mounted on a three-axis translation stage close to the focus of the microscope which is optically connected to the spectrometer.

2.2.2 Spectroscopy on Cable Samples

A Leitz-Ortholux microscope is used for the *in-situ* probing of the interface ice layers deposited on the cold substrate. The microscope is coupled optically to the spectrometer (Spex Triplimate). Details of the spectroscopy and optical multichannel analyzer have been given by Sharma et al.[44]. The Raman spectra are recorded using the back scattering (180°) geometry. A 10X objective with a focal length of 15 mm both focuses the laser beam and collects the scattered radiation from the sampling area. The collected scattered light is subsequently focused through a 200 μm pin-hole and transmitted to the monochromator entrance slit.

An argon ion laser (Spectra Physics 2020) excites the sample with an average power of 30-50 mW at a wavelength of 488 nm. The scattered light is detected by an optical multichannel analyzer (EG&G Princeton Applied Research, OMA-III). The data are scanned and analyzed with a dedicated computer (EG&G Model-1460).

The O-H stretching region (2800-3800 cm^{-1}) and the low frequency region (50-400 cm^{-1}) of the Raman spectra were calibrated with the plasma lines of an Ar^{+} ion laser. The optical alignment of the monochromator is verified using the Raman spectra of a standard mercury lamp. The wavenumber calibration is accurate to within $\pm$ 0.7 cm^{-1} when the optical signals in the monochromator are resolved by a 1200 grooves/mm grating.

2.2.3 Growth of Ice on Cable Samples

In the present study, ice forms by the condensation of saturated vapor on the cold cable samples. The cold surface of the samples mounted on the cryostat cooling element provides the necessary nucleation sites for the vapor-to-solid phase transition. The growth of the ice layer formed in this manner closely simulates the process of atmospheric ice accretion on overhead transmission cables.

The thickness of the ice layer is measured with the microscopic focusing capability

of the Leitz-Ortholux microscope. The vertical movement of the microscope stage is calibrated by focusing on the opposite surfaces of a thin glass slide of a known thickness. The least count of the macrometer screw is 1.5 ± 0.4 μm.

The space-resolved Raman spectrum of the thick ice layer is obtained by focusing the microscope on the top surface, this spectrum has a minimum of distortion from the underlying layers. It is important to note that because of the sharp focusing capability of the microscope used in micro-Raman spectroscopy, the scattered radiation is collected primarily from the focusing volume, which in our case has a vertical resolution of about 7.5 μm, as calculated by assuming conical shape of the focussed laser beam [60].

The results of our previous study [60] has shown that Raman spectra of the initial ice layer of thickness 30 μm deposited at 120K shows characteristics of a disordered phase resembling a low-density amorphous ice, therefore, a vertical resolution less than 30 μm will be sufficient to distinguish the spatial variations in the ice layer that is vapor deposited on a cold metal surface. In the present case, we observe not only the variations caused by the temperature but also the spatial variation in the structure of the ice as the thick ice layer grdually evaporates under vacuum pressure.

Procedure

The focus of the present study is to investigate the structure of the ice layers close to the metal surface. To achieve this objective, we first deposit a thick layer of ice on an extremely cold substrate and then gradually evaporate the thick layer into a thin layer of ice by increasing the temperature of the substrate under a vacuum pressure of about 5-10 millitorr. The recorded Raman spectra of the gradually thinning layers reveal the layer-by-layer structure of the ice.

The ice layers deposited at extremely low temperatures provide an amplified and stable view of the initial layers forming on the metal surface, that is otherwise extremely thin and difficult to investigate at high temperatures (owing to the resolution of the current experimental set-up). Moreover, as we approach the melting temperature (273 K), ice layers near the metal surface become thermally agitated and

fundamental structure of the ice formation is lost due to inter-mixing. We have, therefore, adopted the following procedure for making Raman measurements.

A chemically clean cable sample (aluminum alloy) is mounted on the cryostat cooling element using a copper holder (see Figure 2-9). The top concentric aluminum cover with the quartz windows is closed and the vacuum pump is switched on to obtain a moderate vacuum in the icing chamber (about 5-10 millitorr). The temperature controller is set to the required temperature and all the measuring instruments are activated. The cryostat assembly is allowed to reach a steady state. The steady state is monitored by measuring the temperature (stable within $\pm$ 0.5K) and pressure (stable within $\pm$ 5 millitorr) data.

Vapor is introduced through a bleed valve at a rate of about 10 $\pm$ 1 ml/min for about 2 minutes. The bleed valve is closed and no observation is made until the temperature and pressure are restored to steady state. A video monitor is used to visually align the microscope and observe the nature of ice accretion on the sample surface. The thinning layers of ice are observed through the microscope and the spectroscopic observations are made in the O-H stretching frequency region by setting the monochromator at 581 nm. The observations are repeated at least five times at a given layer thickness to ensure the repeatability and stability of the observed spectra. However, only the best reproducible spectra are reported here. The thickness of an ice layer is measured by the macrometer focusing capability of the microscope. The temperature setting of the controller is then changed and the procedure mentioned above is repeated for the next higher temperature setting. The spectral observations are calibrated by recording the argon plasma lines in the same region.

The Raman spectra are recorded for 16 temperature settings in the range from 30K to 180K, at intervals of 10 K. The fluctuation in the temperature control is within $\pm$ 4K. The thickness of the layer initially deposited on the cable is found to be 80 μm $\pm$ 1.5 μm. The thickness of subsequent layers was measured by the microscopic focusing capability. The thickness (TH) data reported for nine of the 16 recorded spectrum on Figure 2-10 are an average of the several thickness measurements.

2.2.4 Results of the Investigation on Cable Samples

According to the band assignment of the Raman spectra of ice-Ih [61], the sharp peak at 3100 cm^{-1} is assigned to the symmetric O-H stretching vibrations (ν_1) and the broad band at about 3220 cm^{-1} to the out-of-phase stretching vibrations (ν_3). The frequency and the band shape of the ν_1 mode are known to be sensitive to the intramolecular interactions. The primary factors responsible for the variation in the ν_1 peak are (a) the configuration and number of near neighbors at an oxygen atom site and (b) the variation in the O-H bond length [20, 50]. The variation in the neighbor configuration is sensitive to the network ot atoms that defines a structure as being polycrystalline or amorphous. An increase in the temperature causes a reduction in the intermolecular coupling that results in an increase of the ν_1 frequency [51]. The band width of ν_1 depends on the in-phase vibrations. A narrow band width represents the presence of structural order leading to a maximum in the in-phase vibrations, while the broadening of the band indicates disorder. The disorder in an ice sample may originate either from changes in the near neighbor configuration for the random network structure of amorphous ice or from a large number of defects in a polycrystalline lattice [60, 20, 50].

Figure 2-10 shows the Raman spectra in O-H stretching region (2800-3400 cm^{-1}) at various temperatures and thicknesses. As mentioned earlier, we recognize the strong and sharp peak at 3100 cm^{-1} as representing the in-phase stretching vibrations and the broad and weak band at about 3200 as representing the out-of-phase stretching vibrations (ν_3). The ν_1 and ν_3 bands overlap because of intramolecular coupling. With the increase in temperature from 30K to 180K the peak frequency increases from 3084 cm^{-1} to 3117 cm^{-1} and the HPBW increases from 27 cm^{-1} to 117 cm^{-1}. The observations are made in steps of 10 K. Table 2.3 reports the variation in the ν_1 peak for all 16 temperature steps between 30K and 180K along with the thickness of the layer.

Interpretation of the variations in the Raman spectra is based on the band position and HPBW of the ν_1 peak. The ν_3 peak is broad and insensitive to temperature and,

hence, is not useful in the present analysis. In order to understand the features observed in the vibrational spectrum, it is important to keep in mind the sequence of the experiment. Initially, a thick layer of ice is vapor deposited on the cable sample (about 80 μm), subsequently the temperature of the sample is increased in steps of 10 K and the spectrum is recorded. The ice layer depletes as a result of heating under low pressure (10 millitorr). Thus, as the temperature is increased and time progresses, thinner layers of the ice are exposed for Raman observation.

In order to assess the layer-by-layer structure of the ice exposed by gradual evaporation, the temperature variation of the ν_1 frequency is plotted along with the data of Sivakumar et al. [51] for polycrystalline and low density amorphous ice (Figure 2-11). The variation of ν_1 coincides with the variation of polycrystalline ice. Similarly, temperature variation in the HPBW for the ice on cable is plotted along with the data for polycrystalline and amorphous ice. As shown in Figure 2-12, the HPBW of the ice on cable is initially closer to the values for polycrystalline ice but moves closer to the values for amorphous ice as temperature increases. At 130K, the HPBW values match the values for HPBW(as) and continue to do so upto 170K. At 180K we observe a jump in the HPBW, indicating increased disorder in the ice layer closer to the metal surface.

The observations plotted in Figures 2-11 and 2-12 and the features of the Raman spectra (e.g., see spectra obtained by Sivakumar et al. [51]. indicate that the outermost thick layer of ice is polycrystalline. This polycrystalline ice, however, has a much broader band width than the band width reported[15] in the literature for bulk samples, which indicates that the ice layer on the metal surface has a larger number of defects. These defects may be induced by several possible mechanisms, such as orientational disorder caused by thermal agitation or disorder caused by the random network structure of the amorphous layer deposited at low temperature (30K). The orientational disorder is caused by the vacancies occurring as a result of rotation of water molecules within the tetrahedral coordination. The disorder in the case of amorphous ice is caused by the freezing of randomly oriented water molecules forming a network structure, i.e., the ice clusters form a layer on metal surface that are not in

registry (i.e., match between the lattice of copper and ice) with the crystal structure of the metal and undergo differential thermal contraction, causing disruption in the crystal structure of ice molecules.

As we explore the vibrational spectrum closer to the metal surface, ice layers become progressively more disordered. The increased HPBW cannot be explained only on the basis of orientational disorder caused by thermal agitation because the band width is too large at 170K, (93 cm^{-1}) and at 180K (117 cm^{-1}) as compared to the band width of bulk polycrystalline ice at the same temperatures (see Figure 2-12). However, the band widths are comparable to those reported for the bulk amorphous ice. This observation suggests that the defects may be originating from the parent amorphous phase of ice before the amorphous-to-crystalline phase transition occurs at about 150K as reported by Klug et al. [22]. At higher temperatures, i.e., above 150K the amorphous ice turns into polycrystalline ice [22, 62]. Hence even for the thin layer at 170 and 180K, the ν_1 frequency follows the polycrystalline curve. However, the excessive disorder in the thin layers can only be explained by the existence of a random network structure similar to low density amorphous ice.

To explain the excessive disorder in the thin ice layer we refer to Table 2.1, which reports the results obtained from the evaporation experiment at 16 temperatures. It is important to note here that the measurements are made at the top surface of the sample. The microscopic observations show that the ice layer formed is milky and opaque. The temperature reported in the table refers to the substrate temperature. However, ice, being an extremely poor conductor of heat, will have a large thermal gradient between the layer in contact with solid surface and the top surface (about 120K for a thermal conductivity of 0.002 W/mK at 30K). This temperature gradient, resulting from thermal softening of bonds, causes the top surface of the thick ice layer to crystallize. The band frequency and the features of the Raman spectrum at the 80 μm thickness definitely resemble polycrystalline ice [51].

The temperature of the substrate is then raised and the thickness of the ice layer gradually decreases as a result of temperature induced evaporation. The layer temperature and the low thermal conductivity provide the necessary thermal mobility for

these subsequent layers to crystallize. Therefore, the ν_1 frequency always follows the curve representing polycrystalline ice. The ice layers adjacent to the metal surface are expected to be amorphous because of rapid cooling and local stresses caused by differential thermal expansion at the surface. As indicated in our previous study [60], the initial ice layers less than 30 μm thickness are amorphous in nature upto 120K temperature. Therefore, ice layers closer to the cold surface are expected to sustain a low density amorphous structure up to 120K. This amorphous layer turns in to crystalline cubic ice-Ic at 150K [62] but because of the disorder existing in the amorphous phase adsorbed on the metal surface, a larger number of defects result in the polycrystalline phase. Therefore, although the peak frequency follows the polycrystalline curve, the band width shows excessive disorder that is inherited from the parent low density amorphous phase.

As reported in Table 2.1, the δ(HPBW) shows a larger (9 cm^{-1}) increment at a thickness of 38 μm, indicating a jump in the disorder of the layers below 38 μm. Our previous study [60] indicates that ice layers less than 30 μm may be amorphous. However, temperature at which we reach this thickness is 180K, that is well above the amorphous-to-crystal transition temperature of 150K [22, 62]. As a result, the HPBWs of polycrystalline ice layer less than 38 μthickness exhibit memory of the disorder inherited from the parent amorphous phase. The disorder increases rapidly as the thinner layers are revealed. At 30 μm the increase in the HPBW is quite large, indicating a strong possibility of the existence of the parent low density amorphous phase prior to the present crystalline phase. This inference is consistent with the results of our previous study [60] on the structure of thin and thick ice layers on metal surfaces. Thus, the parent low density amorphous solid layer turns into a high defect density polycrystalline solid above 150K.

Low density amorphous ice is a loosely connected network of ice molecules [51]. Therefore, we suggest that the initial layers of ice formed at low temperatures are in the low density amorphous phase of ice, which gradually crystallize into a high defect density polycrystalline ice at about 150K. The broken network structure of ice molecules closer to the metal surface may be attributed to the low shear strength

(liquid-like behavior) of the ice/cable interface bonding.

The atmospheric icing on electrical transmission cables in reality occurs in the temperature range of 233K to 263K. At this temperature the condensed vapor has sufficient mobility to form a polycrystalline ice structure, however, the mismatch (disregistry) between the crystal structure of ice and metal (that causes random network structure of ice at low temperatures) will lead to significant defects and disorder in the ice layer, similar to that observed in the present study.

2.2.5 Conclusions of Investigation on Cable Samples

The observations based on the O-H stretching peak positions and the HPBW obtained in the ice layer evaporation experiment on aluminum alloy cable samples suggest the existence of polycrystalline ice layers that progressively become more defective closer to the metal surface. The excessive defect density near the metal surface (30 μm) is evidenced in by a large value for the band width. The larger number of defects in the polycrystalline ice indicates that the defects may be originating from the random network structure inherited from the parent low density amorphous ice that is formed initially by the condensation of vapor on the cold metal surface.

The low density amorphous ice layer adjoining the metal surface changes into a high defect density polycrystalline ice above temperatures 150K. The structural features of the ice layer closest to the metal surface support the notion that the low density amorphous (broken network) structure may be the primary reason for the liquid-like behavior of the ice-solid bond.

Table 2.3: Variations of O-H Stretching Frequency Peak for Ice Layers as a function of Temperature and Thickness

Temp	ν_1	HPBW	δHPBW	Thickness
	K	cm^{-1}	cm^{-1}	μm
4 30	3084	27	-	80
40	3085	30	3	72
50	3087	33	3	63
60	3088	36	3	60
70	3090	42	6	52
80	3092	45	3	48
90	3095	54	9	44
100	3097	60	6	40
110	3099	63	3	40
120	3100	66	3	38
130	3102	75	9	38
140	3104	84	9	37
150	3108	85	1	37
160	3111	90	5	34
170	3114	93	3	32
180	3117	117	24	30

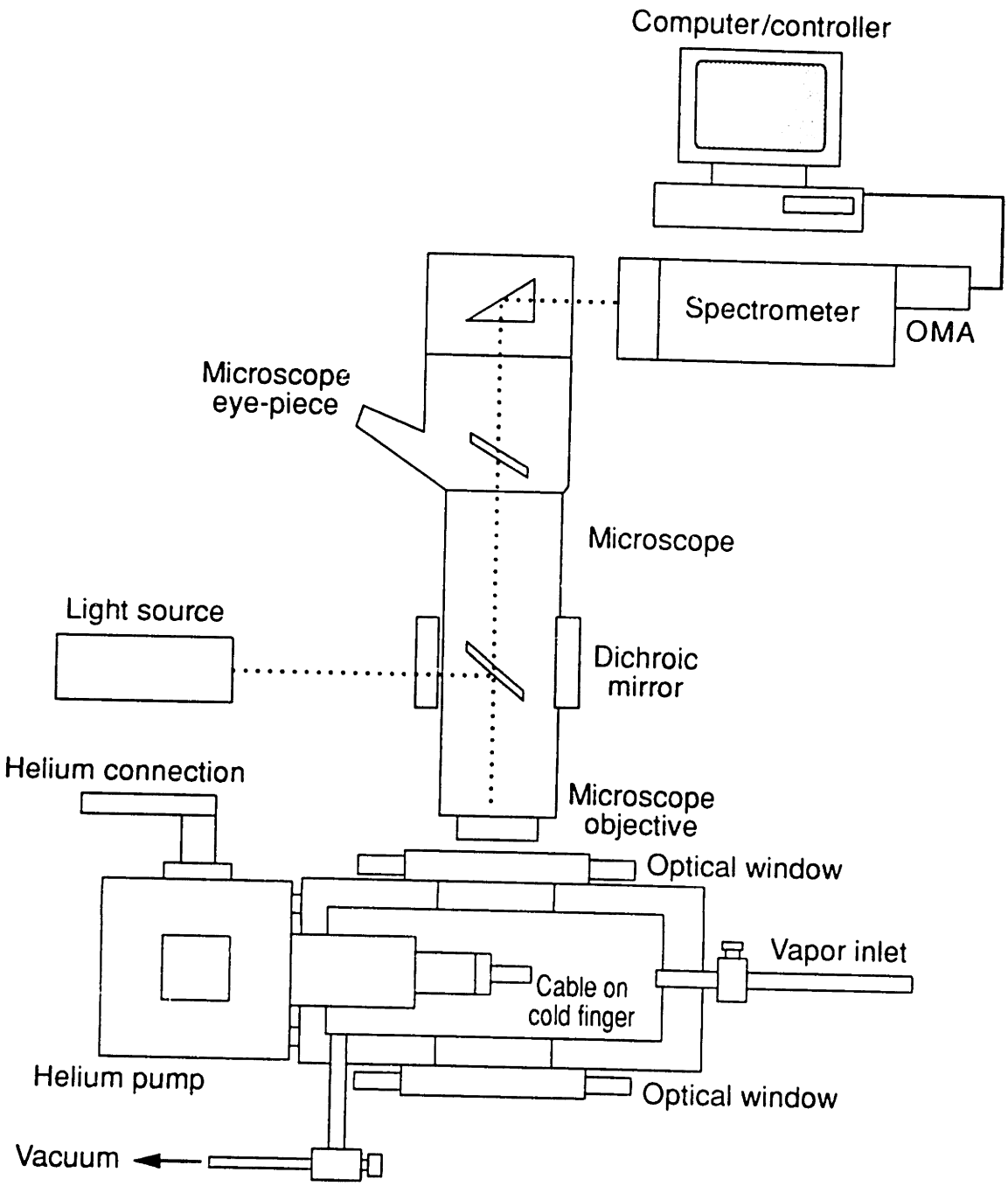

Figure 2-9: Schematic diagram of the helium cryostat experimental set-up.

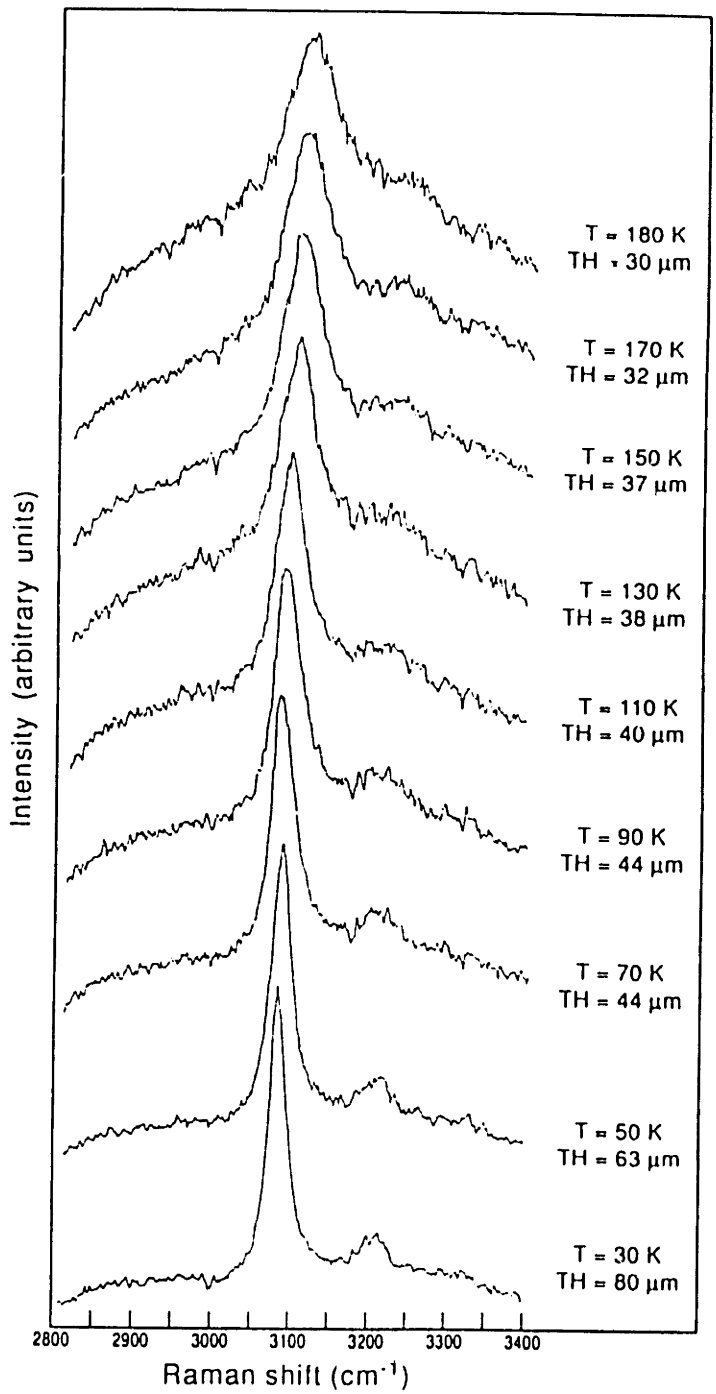

Figure 2-10: Variation of Raman spectra in O-H stretching frequency region with temperature.

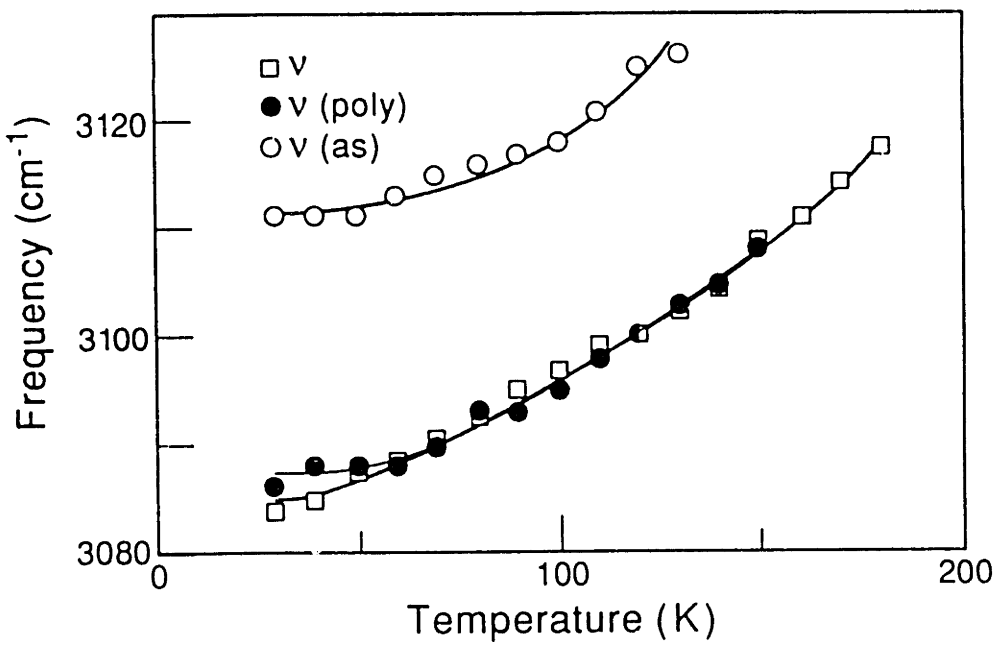

Figure 2-11: Variation of ν_1 frequency with temperature for ice on cable: ν_1(poly) represents temperature variation for polycrystalline ice; ν_1(as) represents temperature variation for amorphous ice.

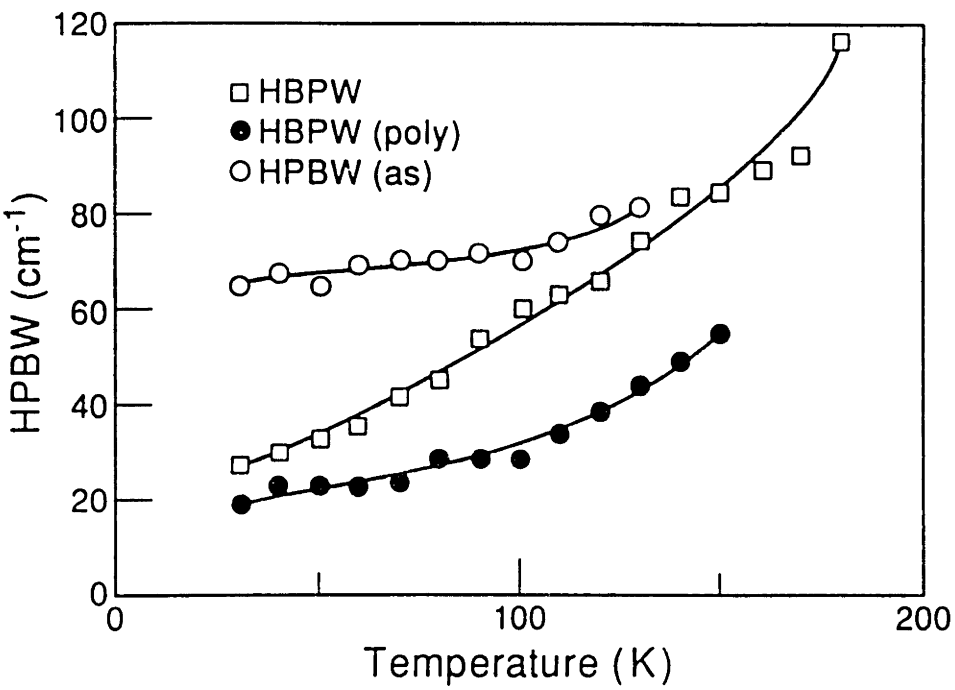

Figure 2-12: variation of HPBW for ice on cable: HPBW(poly) represents temperature variation for polycrystalline ice; HPBW(as) represent temperature variation for the amorphous ice .

Chapter 3

Nucleation, Growth and Adhesion of Ice on Solid Surfaces

The process of icing involves several stages as described in our three stage model, i.e., adsorption of water molecules, growth of microcrystallites at the nucleation sites and the sintering of crystals to form an interface ice layer. The effect of the various stages of icing on the adhesive strength is of primary importance to identify the important parameters that govern the ice adhesion process. In this chapter we start from a controlled experiment, where mirror polished surfaces are first studied under a video microscope for the nucleation and growth of the ice. The same samples are then subjected to shear decohesion in a laser Raman microprobe shear apparatus. Further studies on the nucleation and growth are conducted on the sample surfaces using a high resolution laser confocal microscope. This integrated approach provides a connection between the microscopic and macroscopic behavior of the ice-solid interface bond.

3.1 Nucleation of Ice on Solid Surfaces

Atmospheric icing is a problem of significant engineering concern for electrical cables, highways and bridges, aircraft wings, and ship decks [1, 43, 3, 4, 5, 11]. The pro-

cess of icing generally involves the freezing of saturated and supercooled atmospheric water vapor on cold, typically, metallic surfaces. Physical, not chemical, adhesion mechanisms dominate this icing process.

Theoretical models have been developed in recent years [55, 56, 57, 58] to predict the accretion of ice on solid surfaces. These thermodynamically-based models predict the rate and shape of the accreting ice using macroscopic parameters that characterize the environmental conditions and heat transfer mechanisms involved. They, however, provide little or no information concerning the underlying physical micro-mechanisms of ice adhesions that is essential in the development of effective methods for both prevention and disruption of ice-solid bonds.

Research in related areas, viz., growth of thin films by physical vapor deposition [63, 16] shows that in general three distinct processes contribute to the formation of adhesional bonds involving ice. These are, wetting, nucleation, and sintering. *Wetting* involves the adsorption of molecules of water vapor on the solid surface under short range surface energetic forces (secondary bonds, e.g., due to van der Waal's forces and hydrogen bonds) and the possible formation of local microclusters [64]. *Nucleation* of ice and the formation of ice microcrystals (embryos) involves phase change from vapor to solid as well as the autohesive bonding or self-adhesion of the adsorbed water molecules [36]. Finally, *sintering* involves the formation of a thermodynamically stable interface layer by the growth and coalescence of critical-sized ice embryos under favorable temperature and pressure conditions [65, 66].

The phenomenon of wetting or adsorption has been studied extensively by Zisman [67] (see Cazabat [68] for a recent review). This work has established the central role of the solid-vapor surface energy (contact angle) in the wetting process, including the effect of surface roughness. Klier and Zettlemoyer [64] studied the problem of water vapor adsorption on solids and quantified the extent of the spatial coverage of the adsorbed layer. This study showed that the water molecules adsorbed on the surface undergo an irreversible and complete reorientation by the virtue of the rotational degree of freedom. The hydroxil (O-H) groups stick to the favorable surface sites and form an embryo for ice nucleation. However, this study did not provide information

on the effect of embryo characteristics (size, shape, rate of formation) on the adhesive strength of the resulting ice-metal interface.

The nucleation and precipitation of atmospheric ice in the presence of a solid surface has also been studied. Nakaya [69] was among the first to investigate the effect of temperature and degree of supersaturation on the shape and size of (fully grown) ice crystals nucleated on solid surfaces by vapor deposition. These experiments were improved later by Hallet and Mason [70], who used a diffusion chamber to define the crystal growth environment more precisely. The results of such studies are reported in form of Nakaya diagrams which map the occurrence of different crystal habits. There is now an extensive literature on habits of macroscopic ice crystals formed on solid surfaces (see, e.g., Hobbs [17] for a summary).

In spite of this progress, the surface phenomenon governing the nucleation and growth of ice crystals on solid surfaces are not yet well understood [18, 71]. Among the areas that remain to be investigated are the heterogeneous nucleation of the ice embryos on solid surfaces, the strength of the resulting embryo-solid adhesive bond, and the effect of surface properties on nucleation and adhesion. Information concerning these phenomenon will aid the development of methods that retard and, possibly, even prevent ice from nucleating on and adhering to solid surfaces.

The phenomenon of sintering has been studied extensively in the field of material science. In the case of heterogeneous interfaces, surface diffusion along with evaporation, condensation and volume diffusion have been identified as major factors causing mass transfer. The mass transfer phenomenon is responsible for the sintering of ice on solid surface [13, 66].

The objective of this paper is to study the formation of ice embryos on a solid surface using video microscopy for real-time *in-situ* monitoring of the nucleation process. The attachment of a Charged Coupled Device (CCD) camera in the optical path of a microscope makes possible the complete visualization and frame-by-frame analysis of fast processes such as growth of layers [72], recrystallization [73], and nucleation. An optical chamber, with facilities for simulating atmospheric icing by physical vapor deposition on a thermoelectrically-cooled solid surface, has been fabricated for use in

the video-microscopy work.

Experiments are performed on mirror polished surfaces at a temperature of -20°C. The effect of surface properties is studied by considering five distinct materials for the solid surface; these are titanium, copper, aluminum, stainless steel and PTFE (polytetrafloroethylene, also known as teflon). The first four solids represent a broad range of metals that possess high surface energy. In contrast, PTFE is low energy surface with strong hydrophobic properties.

The critical size of an ice embryo necessary to initiate crystal growth on the solid surface is determined from experimental observations. The data are then compared with predictions from the classical theory of heterogeneous nucleation (see, e.g., Hirth and Mozed [74]). The size of the critical ice embryo is correlated with theoretical estimates of the Gibbs free energy barrier for nucleation and the reversible work of adhesion between the embryo and the solid surface.

3.1.1 Design and Fabrication of Icing Chamber

The primary objective of the icing chamber is to be able to simulate atmospheric icing under controlled environmental conditions and to provide optical access for the video microscopy apparatus. The chamber assembly is contained in an aluminum box of dimension 15 cm x 15 cm x 3.8 cm shown schematically in Figure 3-1. Instrumentation within the icing chamber can record physical parameters such as temperature, vapor flow rate, water content of vapor, and the pressure in the chamber.

A micro-flow controller (Tylon, model 0.02-15 SCCM) measures the flow of vapor into the icing chamber in the range of 0.02-15 cc/min to an accuracy of $\pm$ 0.005 cc/min. A humidity sensor (Vaisala, model HPM113Y) measures the water content of the vapor being introduced to an accuracy of one percent in relative humidity.

A square annular holder protrudes at the center of the aluminum box. The cooling elements of a thermoelectric cooling device (Melcor, model CP1 4-124-06L) are mounted on top of this holder. A v-notched aluminum substrate holder is thermally

attached to the cooling element by means of screws. The solid substrate to be tested is slipped into the sample groove made on the substrate holder. The substrate holder moves through the v-notch which acts as a guide allowing only horizontal linear movement. Test samples can be cooled to an accuracy of $\pm$ 0.5°C and down to temperature of -30°C in the chamber. Temperature measurement and control on the surface of the test specimen is achieved using platinum resistance temperature detectors or RTD's (Omega, model DP2000) that are accurate to within $\pm$0.005°C. All measuring devices are placed inside the icing chamber box and electrical connections are made through two vacuum feed-throughs.

A transparent, circular fused-quartz window allows optical access for the video microscopy. An O-ring is used in the joint between the icing chamber and cover plate to ensure that the assembly is vacuum tight.

All measuring instruments are monitored through an 8-channel analog-to-digital converter which is connected to a dedicated IBM-PC controller. A data acquisition and control software with color graphical display of major experimental parameters, i.e., temperature, humidity, and mass flow rate of vapor has been developed and implemented. This facilitates complete on-line control of experimental conditions and recording of the test data on hard disk.

3.1.2 Laboratory Simulation of Atmospheric Icing

In the present study, the nucleation of ice occurs by the condensation of saturated and supercooled water vapor on the surface of the test specimen. The saturated water vapor is made by bubbling air through de-ionized and triple-distilled water. The vapor is then cooled by passing it through a thermoelectric element. The cold solid surface provides the necessary nucleation sites for the phase transition from vapor to ice. The ice layer formed in this manner closely resembles the process of atmospheric ice accretion in engineering applications.

The five solid surfaces tested in the experiment include four high energy surfaces

(titanium, copper, aluminum, and stainless steel) and one low energy surface (PTFE). The test specimens are made in the form of coupons of size 48 mm x 12 mm x 12 mm. To eliminate any effects in the test results due to variations in surface roughness, the test specimens are polished to ensure an optically flat and mirror finished surface.

The polishing procedure involves six steps which utilizes two grades of SiC sandpaper (600 and 1000 grit), diamond polishing compound (3 and 1 μm) and alumina micropolish (0.3 and 0.05 μm). The coarse grinding is performed on a Longitech LP30 semi-automatic grinding wheel, while the fine diamond polishing is performed on a Longitech WG-2 polishing equipment and Longitech polishing fluid.A nylon membrane is used with the 0.3 μm alumina micropolish and a polishing cloth with 0.05 μm alumina micropolish. Distilled water is used in conjunction with the alumina micropolish to reduce contamination. The aluminum coupon is polished with a bronze wheel, while low energy PTFE surface does not use the 600 grit coarse grinding. After polishing, the coupons are sonicated in deionized-distilled water and kept in solvent (100% ethanol) bottle to prevent chemical contamination prior to testing.

Contact angle measurements are made on each of the polished surfaces prior to testing using a telescope fitted with a goniometer eyepiece. A separate sealed chamber is used for these measurements. The polished specimen is mounted in the center of the chamber and a water droplet is placed on the solid surface with a micro syringe needle. The contact angle of the stationary droplet is observed from the protractor in the goniometer eyepiece.

The procedure used to simulate atmospheric icing in the laboratory consists of the following steps:

1. The polished and chemically clean test specimen is mounted in the icing chamber.

2. The top aluminum cover plate with the quartz window is secured and a moderate vacuum (about 10 millitorr) is created in the icing chamber by evacuating the assembly.

3. The thermoelectric cooler is set to the required test temperature (-20°C) and all

the monitoring instruments are activated via the computer controller. The data acquisition system is set to record the temperature, chamber pressure, humidity and flow controller readings at specified intervals (10-30 seconds) throughout the experiment.

4. The icing-chamber assembly is allowed to reach a steady state by continuously monitoring the temperature and pressure data. The temperature is held constant to within $\pm$ 0.5°C and the vacuum pressure stabilizes at about 1 torr.

5. Water vapor is introduced through a bleed valve at a rate of 10 $\pm$ 1 ml/min for about 2 minutes and then shut-off.

6. The nucleation of the condensing vapor droplets is recorded by the video microscopy from the instant vapor is introduced into the icing chamber up until the nucleated ice embryos attain an equilibrium size (typically not more than 3-5 minutes).

3.1.3 Video Microscopy of Ice Nucleation

The icing chamber assembly is placed below a modified Leitz-Ortholux microscope that is used for the *in-situ* monitoring of ice nucleation. The microscope is optically coupled to a CCD camera to record the nucleation of vapor deposited ice in real time (Figure 3-1). A television monitor is also used to visually align the test set-up and observe the nucleation process in real-time. The linear scale of the recordings is calibrated by observing a microscope optical slide (with graduation markings at an interval of 1μm) through the video microscope.

A similar test set-up has been adapted by authors to obtain the vibrational (Raman) spectra of ice layers forming on solid surfaces by coupling a spectrometer to the optical microscope [60].

After the test, observations from the video microscope are analyzed frame-by-frame to determine the size of the droplet condensing on the solid surface. All video

observations are made in the 180° back-scattering geometry. The droplets condensing on the surface, in general, do not possess an exactly symmetric and spherical shape. Consequently, a statistical average value for the radius of the ice embryo is estimated from the experimental measurements (see, e.g. [75]). This involves considering all the droplets in each frame and determining the area of each droplet in the plane of the solid surface. The area measurement is accomplished with the help of a planimeter. The equivalent radius of a spherical, cap-shaped droplet, r_{eq}, is computed from the average droplet area, A, using the following relation:

$$r_{eq} = (A/\pi)^2/f(\theta) \tag{3.1}$$

where θ is the water-solid contact angle and the function f(θ) is defined in the following section. The radius may be estimated as a function of time and its critical value corresponds to the maximum size attained prior to coalescence of the droplets.

3.1.4 Theory of Nucleation on Solid Surfaces

Hirth and Moazed [74] have summarized the classical development of the theory of heterogeneous nucleation on solid surfaces. Their work is based on a spherical cap-shaped nucleus or embryo formed by molecules impinging from the vapor and subsequent phase change and equilibration on the solid surface. The amount of the sphere of radius of curvature intersected on the solid surface is determined by the equilibrium contact angle θ. These modeling assumptions are justified when dropwise condensation is the mechanism dominating the nucleation process.

The total Gibbs free energy of formation of a single spherical, cap-shaped droplet can be expressed as the sum of the volume and the surface energies.

$$\Delta G = \frac{4}{3}\pi r^3 f(\theta)\Delta G_v + \pi r^2 \gamma_{lv} f(\theta) + \pi r^2(\gamma_{sl} - \gamma_{sv}) \tag{3.2}$$

where γ_{lv}, γ_{sl}, and γ_{sv} are the surface free energies for liquid-vapor, solid-liquid and

solid-vapor interfaces, and f(θ) is a geometric quantity expressing the fraction of the total sphere intersected by the solid surface which may be expressed as:

$$f(\theta) = (2 - 3\cos\theta + \cos\theta^3)/4 \tag{3.3}$$

and ΔG_v is the thermodynamic driving force for nucleation which depends on the ratio of the actual and the equilibrated vapor pressure or (supersaturation ratio). Equation (2) can be used to predict the variation of the total free energy as a function of r. In the typical case, the free energy first increases from zero to a maximum positive value and then continuously decreases and becomes negative as r is increased.

The thermodynamic driving force can be expressed as the product of the average entropy of fusion, $< \Delta S >$, which considers the effect of a phase change from liquid to ice, and the degree of supercooling of vapor prior to phase change, $\Delta T = [T - T_m]$, where T_m is the melting temperature, i.e.

$$\Delta G_v =< \Delta S > \Delta T \tag{3.4}$$

Fletcher [18] has presented am empirical equation that describes experimental data on the entropy of fusion for water which is given by:

$$< \Delta S >= (1.13 - 0.004|\Delta T|).10^9 mJ/m^3/^oC \tag{3.5}$$

The critical embryo size necessary for initiating crystal gr... , r_c, corresponds to the value of r at which the total free energy given by Eq. (2) is maximized. This yields a modified form of the Gibbs-Thomson relation for the present case:

$$r_c = \frac{\gamma_{lv}(1 - cos\theta)}{2\Delta G_v} \tag{3.6}$$

The maximum Gibbs free energy corresponding to the formation of a critical-sized embryo is obtained by substituting Eq. (6) in Eq. (2), i.e.:

$$\Delta G_{crit} = 5\pi\gamma_{lv}^3(1 - cos\theta)^3 f(\theta)/6\Delta G_v^2 \tag{3.7}$$

The experimentally determined values of the critical embryo size are compared with predictions given by Eq. (6) while the Gibbs free energy for nucleation, a barrier that must be overcome for the subsequent growth and coalescence, is estimated from Eq. (7).

The critical embryo size can also be compared with the reversible work of adhesion between the embryo and the solid surface to discern any trend between the two sets of variables. The work of adhesion required to separate a unit area of the condensed phase, i.e., ice, and the solid surface forming an interface across which secondary forces are acting may be expressed in terms of the Dupre equation as [67, 15, 14]:

$$W_a = \gamma_{sv} + \gamma_{ice,v} - \gamma_{s,ice} \tag{3.8}$$

where subscripts s and v refer to the solid surface and vapor, respectively. This equation assumes that after separation the solid is still covered with a layer of vapor. The solid-ice interfacial energy may be obtained from the Young equation given by:

$$\gamma_{s,ice} = \gamma_{sv} - \gamma_{ice,v} \cos\theta \tag{3.9}$$

and this may be substituted into Eq. (8) to yield:

$$W_a = \gamma_{ice,v}[1 + \cos\theta] \tag{3.10}$$

The work of adhesion given by Eq. (10) is considered to be adequate for the purposes of this study. The two parameters in the equation, $\gamma_{ice,v}$ and the contact angle θ may be determined directly from standard experiments. Ketcham and Hobbs [76] have estimated the ice-vapor surface energy to be 109 ± 3 mJ/m^2 at a temperature of 0°C. This value is relatively insensitive to temperature variations down to -50°C. Contact angle measurements are generally made at a solid-water interface but, by assuming that contact angle does not change significantly when the water droplet solidifies isothermally and ignoring expansion stresses, such measurements may be applied, albeit in an approximate manner an ice-solid interface.

To investigate the sensitivity of the work of adhesion to variations in the surface energy of the condensed phase, i.e., ice, it becomes convenient to express the contact angle in terms of the following empirical equation:

$$\cos\theta = 1 - b(\gamma_{lv} - \gamma_c) + c(\gamma_{lv} - \gamma_c) \tag{3.11}$$

where b and c are empirical constants, and γ_c is defined as the critical surface tension of wetting and is the value to which γ_{lv} extrapolates as $\cos\theta$ tends to unity or $\theta = 0^o$. Numerical estimates for γ_c are strong function of the solid surface (being almost identical to γ_s for many materials), though also mildly sensitive to solid-liquid surface energy, and can be found in literature (see, e.g., [67, 14]).

Experiments show that for may homologous (and even non-homologous) series of liquid compounds and for all values of γ_{lv} greater than γ_c, a linear relationship is valid and Eq. (11) may be used with a value of c = 0 [67, 15, 14]. The value of b lies in the range of 0.03 to 0.04 for many solid surfaces with a value closer to 0.04 for low energy surfaces. This paper assumes b = 0.03 for the metallic surfaces. Certain low energy surfaces such as PTFE exhibit a small curvature in the data for values of γ_{lv} above 50 mJ/m^2 and it is more accurate to use the full parabolic relationship given in Eq. (11). A fit of the experimental data for PTFE reported in Zisman [67] yields b = 0.042 and c = 3.28x10^{-4}.

3.1.5 Results of Video Microscopy Experiments

The measured values of the equilibrium contact angles for each surface at room temperature (24°C) are listed in Table 3.1. Since θ is greater than 0^o in all cases, water does not wet the surfaces completely nor does it spontaneously spread freely on the surface. At the same time, θ is always less than 180^o as a result of which water will always wet (and adhere to) the surface to some extant. The high surface energy metallic surface possess a contact angle less then 90^o while the low energy PTFE surface possesses a contact angle greater than 90^o characterizing a hydrophobic surface.

Adhesive forces exceed the cohesive forces for $0^c \leq \theta \leq 180^o$ and the reverse is true for $90^o \leq \theta \leq 180^o$.

The values of the critical surface tension of wetting, γ_c, for each solid surface, determined from comprehensive contact angle analysis at room temperature (24°C), are also listed in Table 3.1. The surface free energy of solids (γ_s) are provided for reference.

The results from the video microscopy of the nucleation process of ice on the five solid surfaces are presented in what follows. The general observations show that in the case of the high energy metallic surfaces (i.e., titanium, copper, aluminum, and stainless steel) the condensation of the vapor is dropwise. The vapor condenses initially as liquid droplets of very small diameter. These droplets then grow to a certain critical diameter where they stop growing further and wait for coalescence to occur. This limiting drop size yields the critical radius of the ice embryo, r_c, for the phase transformation from liquid to solid.

The video microscopy shows that the nucleation process for titanium, copper and aluminum are similar in many respects. Numerous embryos form on the surface of these metals; Figures 3-2a-d show photographs from the video microscope taken at four different instants of time in the nucleation process for copper. In contrast, stainless steel displays the well-known "cauliflower" type of condensation characteristic of very high energy surfaces [14] as shown in the photo-micrograph sequence in Figures 3-3a-d. These grow rapidly into ice crystals of cylidrical shape.

The nucleation of ice on PTFE is very different from that on metallic surfaces. The surface is hydrophobic and has a high contact angle of 108°. The nucleation process is observed to retain the shape of the droplet to large diameters and the coalescence is very slow even after the droplet has condensed. The growth rate is very slow, the initial growth is plate-like, and the subsequent growth is columnar in the form of hollow prisms (Figures 3-4a-b).

The critical embryo radius for each of the metallic surfaces, determined from the video observations using the procedure previously described, are listed in Table 3.2. In all cases, this radius lies between 10 to 20 μm being largest for titanium and smallest

for stainless steel. The radius for copper is almost identical to that for titanium while the value for aluminum is less than that for copper. No value is reported for PTFE because nucleation takes a long time and the condensed radius is extremely large.

Theoretical predictions of the critical embryo radius using Eq. (6), in conjunction with Eqs. (4) and (5), are also listed in Table 3.2 . The predictions are based on γ_{lv} = 72.88 mJ/m^2 [15] and the degree of supercooling $\Delta T = 20°$. Since the nucleation theory is based on the assumption of dropwise condensation, its application in case of PTFE, may not be realistic because of the large size of the embryo necessary for nucleation. For all the other materials, the predictions provide a good match to the experimental observations. The difference between the prediction and the observation may be attributed to assumptions in the model, such as the ideal spherical shape assumed for the embryo and neglecting the existence of surface diffusion and coalescence processes.

The growth of the ice embryo on the stainless steel surface as a function of time is plotted in figure 3-5. The equivalent embryo radius computed from experimental observations increases with time to its critical value of 10 μm. The total process takes place less then 1.5 minutes. For the other metallic surfaces, the embryo radius shows considerable oscillations prior to attaining the stable critical value. This is because, at any given instant of time, the degree of heterogeneity in the size of embryos is much greater for these materials. This greater heterogeneity may relate to the fact that their contact angles are about 7-10 degrees larger than that for stainless steel. The variation of the Gibbs free energy as a function of the embryo radius as predicted by Eq. (2) is plotted in Figures 3-6a-e for each of the five surfaces. The metallic surfaces display the classic behavior with a peak value of the barrier corresponding to the critical embryo radius. The energy barrier for the nucleation of the droplet is greatest for titanium followed by copper, aluminum and stainless steel in descending order. In contrast, the free energy shows a continuously increasing trend with embryo radius for PTFE. Stainless steel offers the least resistance to nucleation and as a result should display rapid embryo growth as is observed in the experiments.

The work of adhesion for each of the five solid surfaces is estimated from Eq. (10),

in conjunction with the contact angle information in Table 3.1 and listed in Table 3.2. The results show that the work of adhesion is greatest for stainless steel, followed in decreasing order by aluminum, copper, titanium, and PTFE. The value for PTFE is about one half that for stainless steel. The work of adhesion is greater than the ice-vapor surface energy, except in the case of PTFE where it is lower. Note that according to Eq. (10), its value cannot exceed twice the ice-vapor surface energy.

To investigate sensitivity of the work of adhesion to variations in the surface energy of the condensed phase, Equ. (10) and (11) are used to plot the work of adhesion as a function of the surface energy of the condensed phase (Figures 3-7a-e). For purposes of this discussion, the liquid-vapor surface energy (γ_{lv}) is used in both equations and no distinction is made between surface energy values for the solid and liquid phase. The results show that for all the metallic surfaces, the work of adhesion is a maximum for water $\gamma_{lv} = 72.88$ mJ/m^2. The work of adhesion is close to the maximum even for PTFE. Consequently, it is possible to infer that the work of adhesion of water on all the solid surfaces considered in this study is almost optimal, i.e., other liquids with both higher and lower surface energies will tend to have lower values for the work of adhesion.

Finally, a comparison of the critical embryo radius, maximum free energy, and the work of adhesion shows that the embryo radius is proportional to the free energy barrier but inversely proportional to the work of adhesion, at least for the mirror polished surfaces that were tested. The surface with the lowest free energy barrier, i.e., stainless steel, has smallest critical embryo radius and the ice crystals form with the least amount of resistance and grow rapidly into large crystals. The resulting work of adhesion is highest for such a surface.

Conclusions from Video Microscopy Experiment

The nucleation of ice on solid surfaces has been studied in this paper using *in-situ* video microscopy. An optical chamber, with facilities for simulating atmospheric icing by physical vapor deposition on a thermoelectrically-cooled solid surface, has

been designed and fabricated. Experiments performed on five mirror polished solid surfaces (titanium, copper, aluminum, stainless steel and PTFE) at a temperature of -20°C and comparison with theoretical predictions resulted in following specific conclusions.

1. The phase transition from vapor to solid occurs by dropwise condensations for high energy energy surfaces and by sheet-like condensation for the low energy PTFE surface. Stainless steel displays a "cauliflower" type of condensation that is characteristic of very high energy surfaces and nucleates crystals that have a cylindrical shape. In contrast, the nucleated crystals for PTFE show a plate-like structure in form of hollow prisms.

2. The very small water droplets condensing on metallic surfaces form ice embryos that grow to a critical radius and wait for coalescence to occur. Experimental observations of the critical embryo radius are in excellent agreement with predictions from the classical theory of heterogeneous nucleation. The agreement is within 15% for metallic surfaces.

3. The critical embryo radius is proportional to the theoretically predicted Gibbs free energy barrier for nucleation and inversely proportional to the predicted work of adhesion. For the metallic surfaces which follow the dropwise condensation model, the critical radius and energy barrier is greatest for titanium, followed by copper, aluminum and stainless steel in descending order. The work of adhesion, in contrast, is greatest for stainless steel, followed in decreasing order by aluminum, copper and titanium. Ice crystals form with least resistance and grow rapidly into large crystals on the surface of stainless steel which has the lowest Gibbs free energy and smallest critical embryo radius. The work of adhesion is highest for this surface.

4. A sensitivity analysis of the work of adhesion to variations in the surface energy of the condensed phase shows that the work of adhesion of water on all the solid surfaces is almost optimal, i.e., other liquids with both lower and higher surface energies will tend to have lower values of work of adhesion.

In summary, this study has established the importance of surface phenomena in the nucleation and growth of ice crystals on smooth solid surfaces. The nucleation characteristics are of critical importance in determining the resulting adhesional strength. Thus, it is clear that in order to develop effective ice phobic coatings it is necessary to control the nucleation characteristics of the coatings.

Table 3.1: Contact angle (θ), critical surface tension (γ_c), and solid surface energy (γ_s) for each of five solid surfaces investigated

Material	θ (°)	γ_c (mJ/m^2)	γ_s (mJ/m^2)
Titanium	76.98	31.2	49.1
Copper	76.52	33.3	43.4
Aluminum	73.28	36.8	45.4
Stainless Steel	66.94	40.9	57.1
PTFE	108.71	18.4	22.2

Table 3.2: Contact angle (θ), exprimentally determined critical embryo size (r_{eq}), theoretically predicted critical embryo size (r_c), maximum Gibbs free energy (ΔG_{crit}) and work of adhesion (W_a) for ice nucleation on five solid surfaces.

Material	Contact Angle (°)	r_{eq} (μm)	r_{cal} (μm)	ΔG_{crit} 10^{-9} mJ	W_a mJ/m^2
Titanium	76.98	17	15.050	0.20	93.48
Copper	76.52	16	15.045	0.28	93.94
Aluminum	73.28	12	14.590	0.21	97.25
Stainless Steel	66.94	10	11.409	0.08	103.72
PTFE	108.71	-	-	-	63.60

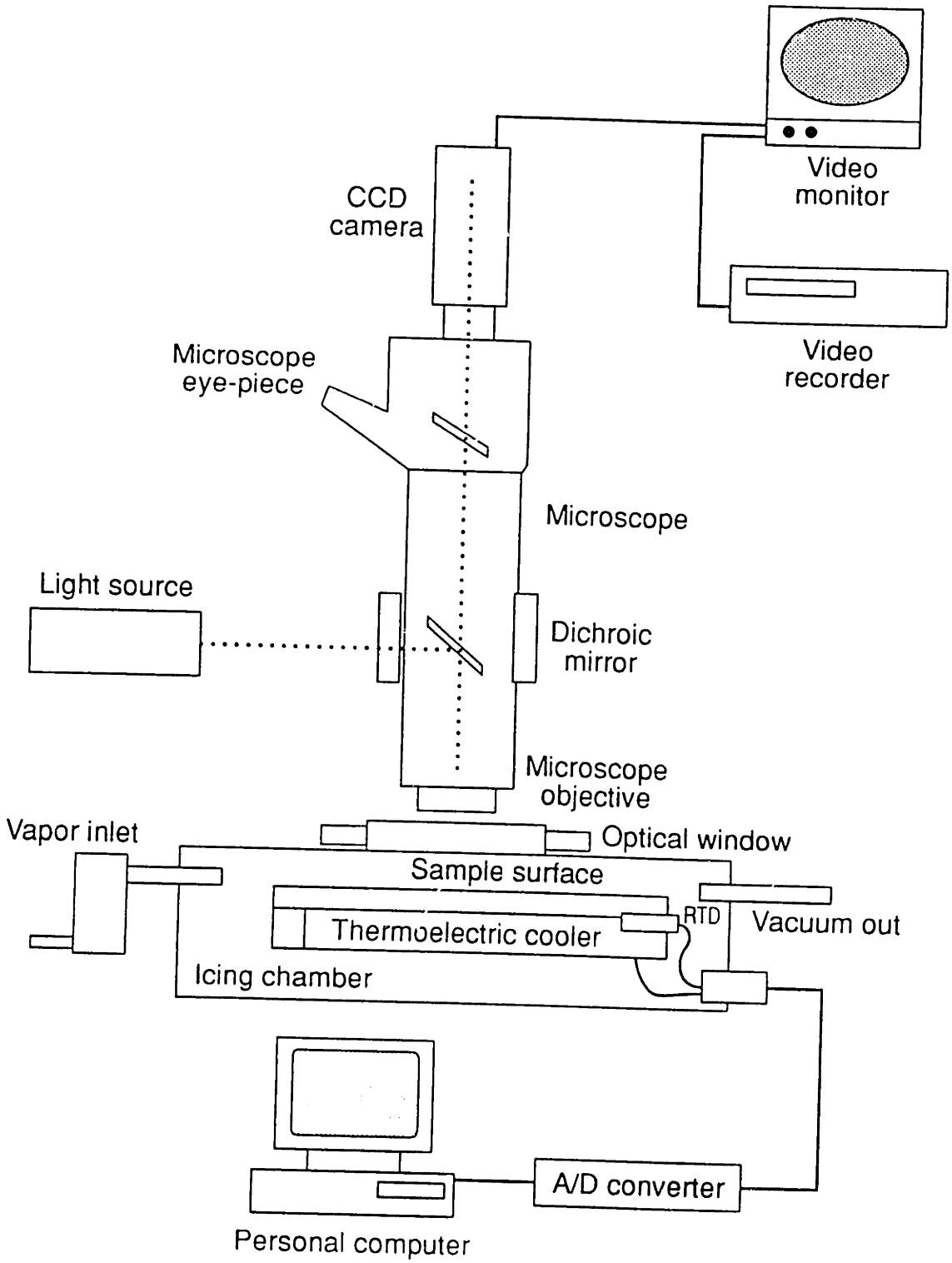

Figure 3-1: Schematic diagram of the video microscopy experimental set up.

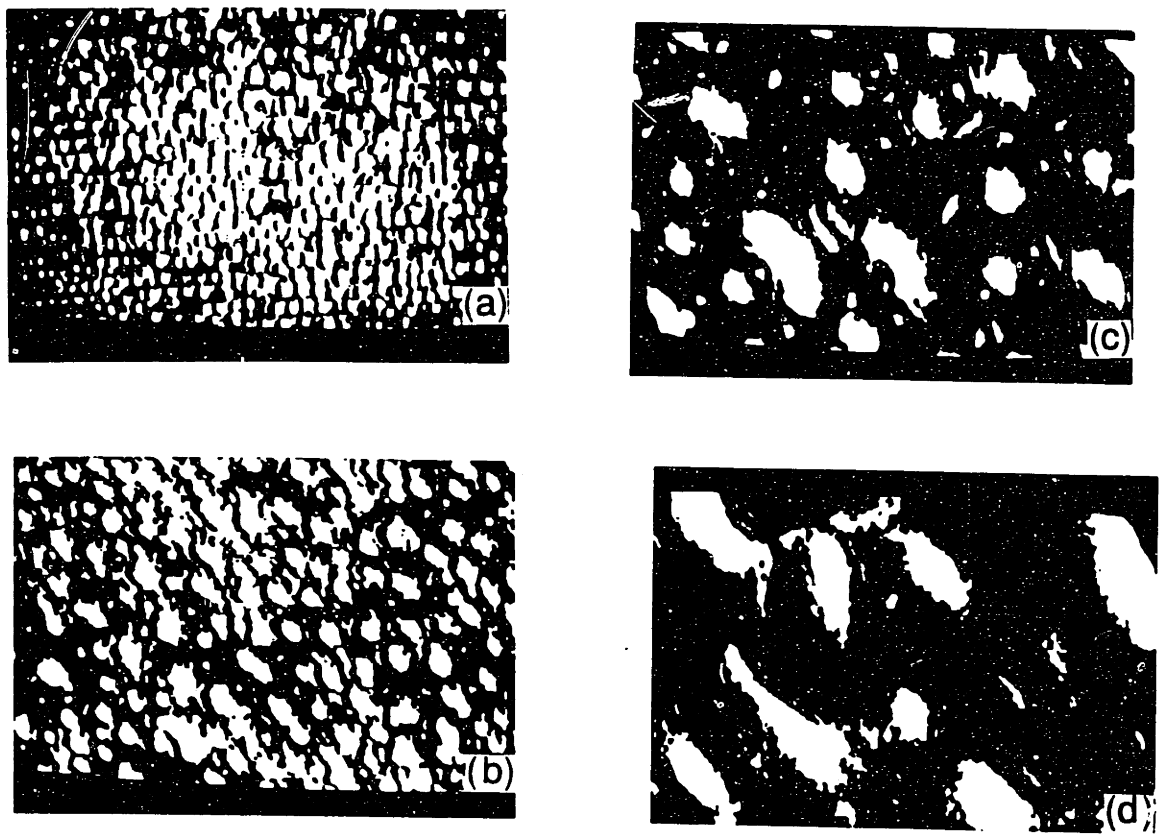

Figure 3-2: Photographs from recording of video microscope showing dropwise nucleation of ice embryos on copper surface. A,B,C,D show droplets at different times intervals

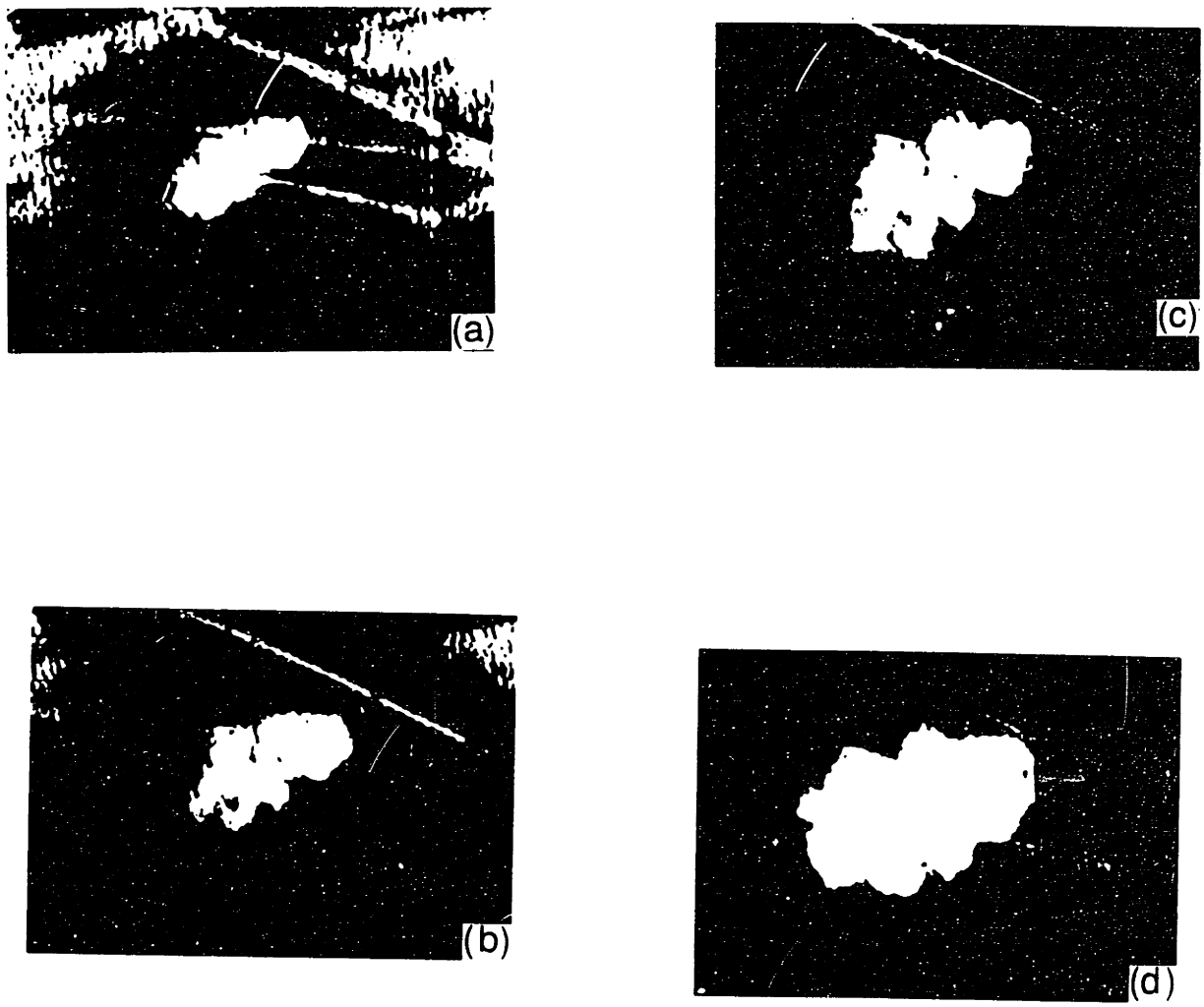

Figure 3-3: Photograpsh from recording of video microscope showing the nucleation of ice embryos on stainless steel surface. A,B,C,D show droplets at different times intervals

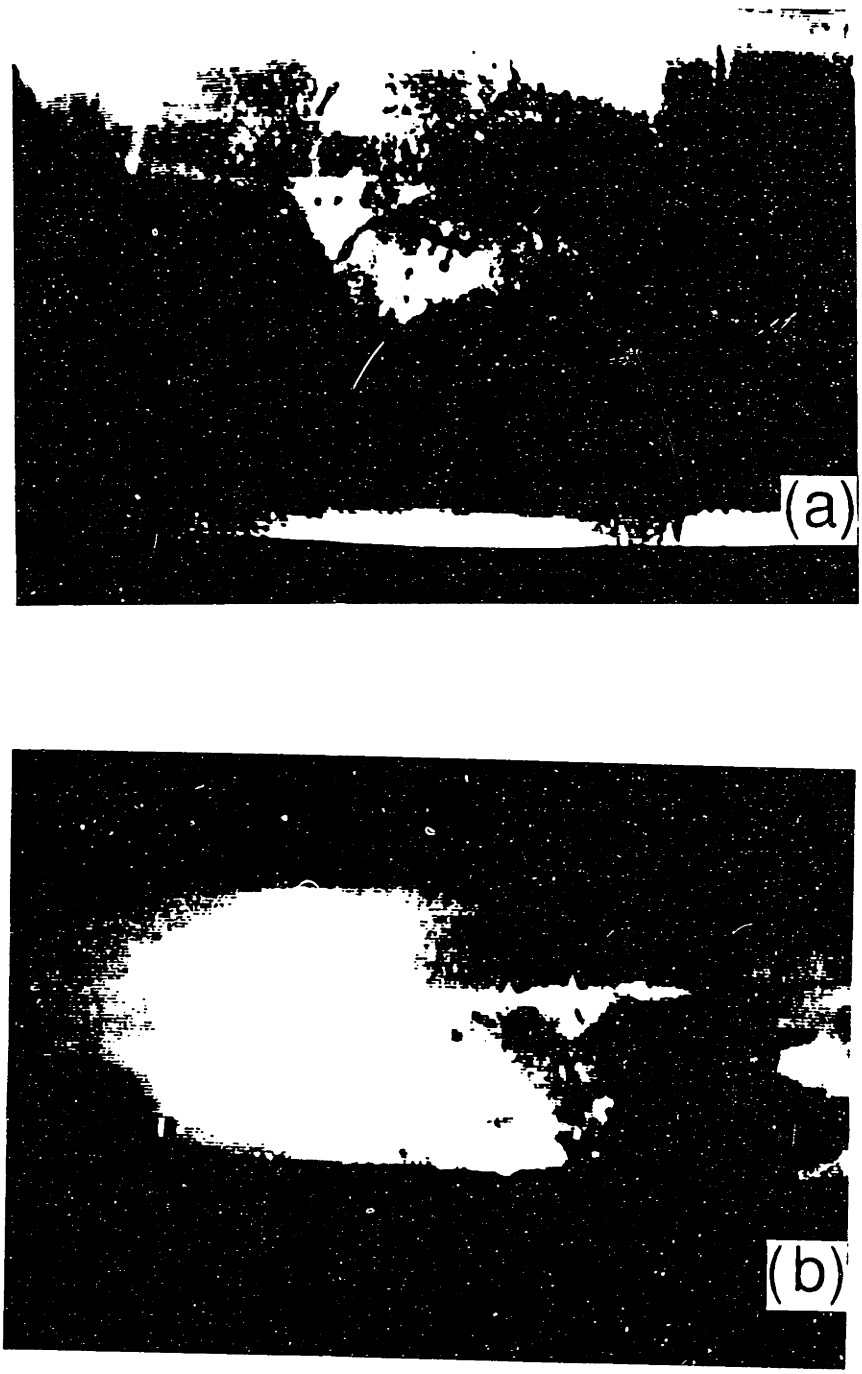

Figure 3-4: Photographs from recording of video microscope showing the nucleation of ice embryos on PTFE surface. A,B show droplets at different times intervals

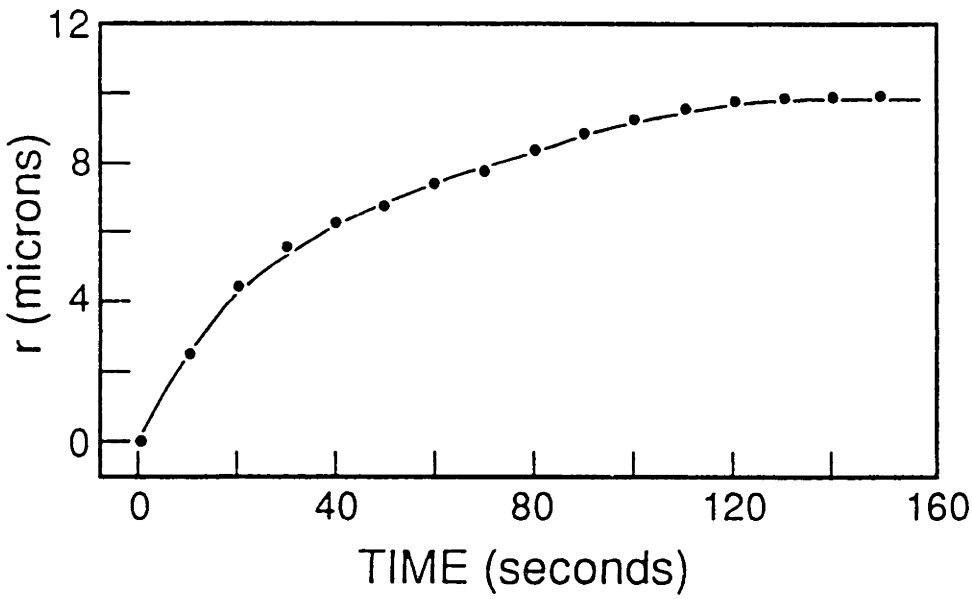

Figure 3-5: Evolution of the embryos radius with time for nucleation of ice on a stainless steel surface.

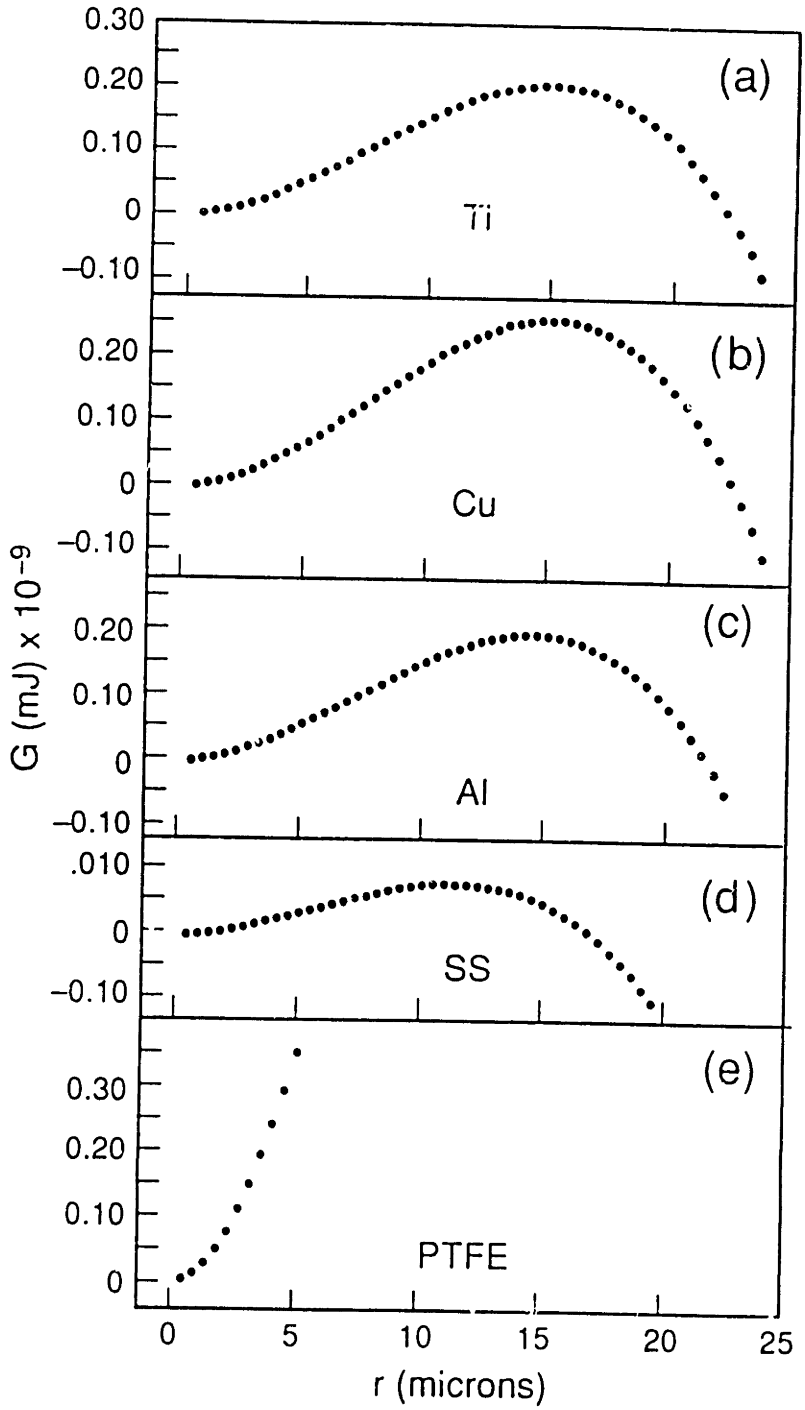

Figure 3-6: Variation of Gibbs free energy, ΔG, as a function of embryo radius, r, on solid surfaces; A. Titanium, B. Copper, C. Aluminum, D. Stainless Steel, and E. PTFE.

3.2 Adhesion of Ice on Solid Surfaces

The icing of structures and cables represents an important problem area where the goal is to minimize adhesion [1, 43, 3, 4, 5, 11]. Studies conducted on ice-solid interface behavior indicate that both physical properties (surface roughness and surface energy of the substrate material) and chemical properties (e.g., chemical composition of substrate material) influence the resulting adhesive bond. Smith-Johannsan [77] studied the effect of impurities (salt) present in water on adhesive strength of the ice resulting from freezing water over different substrates. Jellinek [12], referring to the data of Smith-Johannsen, proposed that the significant difference between tensile and shear strength of ice-solid bond is primarily caused by the presence of a liquid-like (amorphous) layer at the interface. Based on energy balance calculations performed at the grain boundary of the theoretical ice structure, Jellinek [78] concluded that the thickness of the liquid like layer depends on the roughness of the solid surface.

Bascom et al. [2] carried out careful measurements on the contact angle of water droplets over hydrophobic and hydrophilic substrates to determine the effect of the surface energy of the substrate material on the adhesive bond strength. The reduction in the shear strength of the bond could not be related to the surface energy. However, microscopic observations of the separated ice surface samples showed that the lattice structure of the ice at the interface was highly defective. On the basis of this observation, Bascom et al.[2] attributed the reduction in shear strength of the bond to an increase in the defect density of the crystalline interface. Andrews and Lockington [79] on the basis of plain-strain fracture tests observed the effect of temperature on the cohesive to adhesive strength transition in the interface layer.

In order to better understand the molecular mechanics of the ice-solid adhesive bond, it is important to probe the molecular structure of the ice layers condensing on the metal surfaces and to then relate this structure to the resulting adhesive strength of the ice-solid adhesive bond.

The strength of the ice-solid bond may be measured in several ways. A common

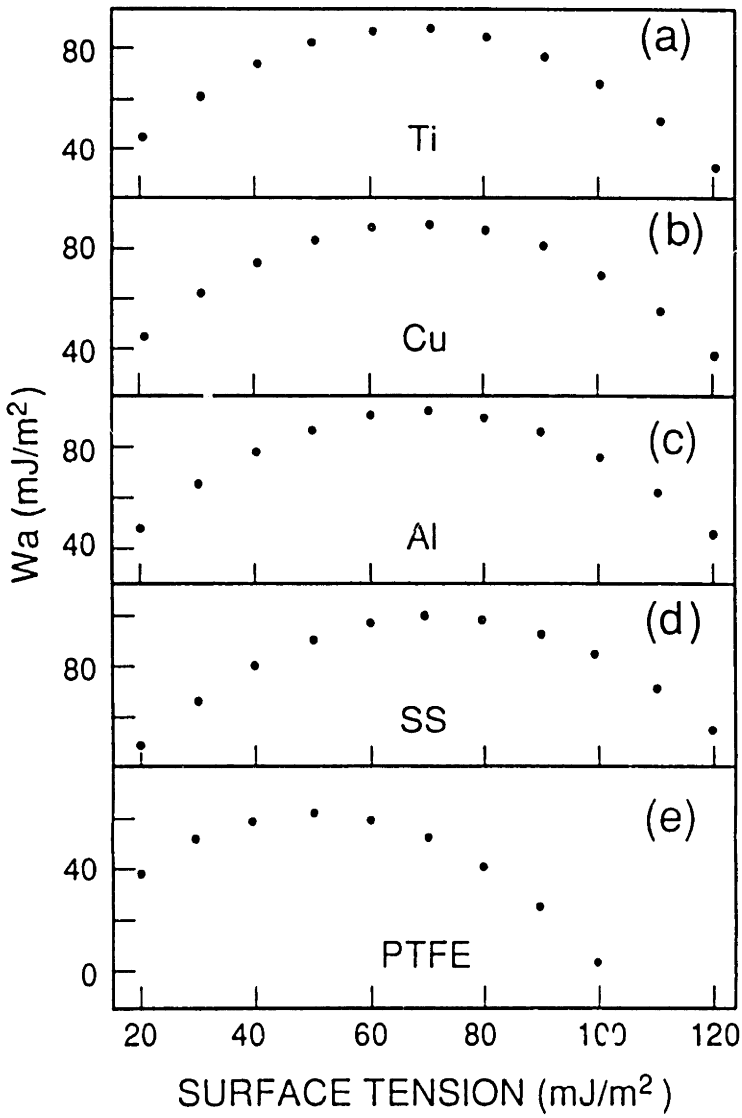

Figure 3-7: Sensitivity of the work of adhesion, W_a, to the variation in the surface energy of the condensed phase, γ_{lv}, for five solid surfaces; A. Titanium, B. Copper, C. Aluminum, D. Stainless Steel, and E. Teflon.

and standard method is to determine the shear adhesive strength as the force parallel to the surface that is needed to break the joint. This pure shear experiment has been used as a measure of the adhesive strength of ice-solid joint by several researchers [80, 72]. However, these tests have been performed at a macroscopic scale without any reference to the microscopic information about the interface.

The phenomenon of adhesion is described in terms of four mechanisms: mechanical interlocking, diffusion, electronic interaction and adsorption. The most dominant mechanisms are adsorption and mechanical interlocking. The microscopic theory of adhesion favors the adsorption mechanism for explaining the process of adhesion. According to this theory, wetting of the substrate surface and subsequent sintering of the ice crystals is primarily responsible for the development of the adhesive bond between ice and solid substrates [66, 17]. Wetting creates a molecular interfacial contact between ice crystals and the solid surface, while the subsequent sintering between ice crystals leads to the most stable configuration in equilibrium. The molecular forces and the conformal energy (i.e., energy due to the relative placement of ice molecules on the atoms of solid surface) at a surface diff. from that for the bulk phase since molecules at the surface have a larger number of broken bonds. The surface energy is therefore higher than the energy of the bulk phase. The excess free energy available at the solid surface provides the necessary driving force for the adhesive bond to form [14].

The transient process of the bond formation starts as a metastable state when ice crystals nucleate and reaches a stable state when the bond is completely formed as a result of sintering, which is essentially a process of restructuring of the neighboring molecules to obtain a minimum energy configuration. The process of stable bond formation is, therefore, a complicated process which involves both intra and inter molecular bond structures.

The changes in ice molecules owing to the local forces at the surface can be probed by obtaining the in-situ vibrational spectra of a microscopic sample of ice. These surface effects can be further quantified by comparing the microscopic results at the surface to the adhesive strength obtained for a bulk sample.

Raman spectroscopy is a well established technique to probe the molecular structure of material interfaces [31, 29, 24, 25, 28]. Recently, this technique has been used to identify the characteristics of the ice layers forming on metal surfaces [60]. The study has revealed that the initial layer of ice at a temperature of 120K is amorphous which turns into a high defect density polycrystalline layer at about 150K [81]. Also, the video microscopy of the nucleation event on five solid surfaces (titanium, copper, aluminum, iron, and PTFE) has shown that the work of adhesion is inversely proportional to the radius of the nucleus forming on the solid surface [82].

In this section, we describe the pure shear experiments that are performed on the four metal surfaces (titanium, copper, aluminum, iron) and one polymer polytetrafluoroethelene (PTFE) surface as described in our previous study [82]. The temperature variation of the adhesive strength in pure shear is recorded and the activation energy for decohesion is calculated. All the five solid surfaces are mirror polished. We have also obtained scanning electron micrograph (SEM) of the surfaces to assess the effect of the surface texture on the adhesive strength of the ice. Changes in the molecular structure of the ice caused by the shearing event have been quantified by monitoring the Raman spectra of ice layers developing on the solid surfaces before and after the shearing event.

The results indicate that, at -20°C, titanium has the maximum adhesive strength followed by copper, iron, aluminum and PTFE. This is in fair agreement with our previous work of adhesion calculations based on the surface energy criteria. It is foune that mechanical interlocking and the secondary hydrogen bonds are two dominant contributors to the total adhesive strength.

3.2.1 Design and Fabrication of Microprobe Shear Apparatus

The primary objective of the icing chamber is to be able to simulate atmospheric icing under controlled environmental conditions, perform a pure shear experiment on

the ice layers deposited on the metal surface, and to provide optical access for the Raman micropscopy apparatus.

The pure shear experiment is performed in a single lap joint geometry. The ice vapor deposited on the solid surface is put between two solid substrates forming a lap joint. The ice acts as an adhesive substance that breaks under the pure shear force applied on the metal plates.

The chamber assembly is contained in an aluminum box of dimension 15 cm x 15 cm x 3.8 cm shown schematically in Figure 3-8. Instrumentation within the icing chamber can record physical parameters such as temperature, vapor flow rate, water content of vapor, and the pressure in the chamber, stress applied on the shearing substrate plate, and the displacement of the shearing plate.

The shear mechanism consists of an assembly of compressed air driven pulling cylinder (Bimba, model FOS-04-0.250-3-MT) and a load cell (Interface Inc, model SSM50) that are connected to the opposite sides of a moving substrate plate holder. The ice is formed on the moving substrate plate by vapor deposition. An identical substrate plate is placed on top of the ice layers. A knife edge scraper on top of the moving substrate plate to subject the ice formed between two substrate plates to a pure shear stress. As shown in Figure 3-8, the substrate plate moves through a v-notched guide rail to obtain a linear movement. The force is applied on the bottom substrate plate by allowing the compressed air into the pulling cylinder through a needle valve and pressure gauge assembly. The pressure exerted on the plate via the pulling cylinder is measured by the load cell which is connected to the other end of the moving plate. The movement of the solid plate is measured by a linear variable differential transformer (LVDT) transducer (Shavitz Engg., model 009SX-B) attached at the bottom of the moving plate. This assembly allows an accurate measurement of the load-displacement data for the failure of an ice-metal interface under pure shear.

A micro-flow controller (Tylon, model 0.02-15 SCCM) measures the flow of vapor into the icing chamber in the range of 0.02-15 cc/min to an accuracy of $\pm$ 0.005 cc/min. A humidity sensor (Vaisala, model HPM113Y) measures the water content of the vapor being introduced to an accuracy of one percent in relative humidity.

A square annular holder protrudes at the center of the aluminum box. The cooling elements of a thermoelectric cooling device (Melcor, model CP1 4-124-06L) are mounted on top of this holder. A v-notched aluminum substrate holder is thermally attached to the cooling element by means of screws. The solid substrate to be tested is slipped into the sample groove made on the substrate holder. The substrate holder moves through the v-notch which acts as a guide allowing only horizontal linear movement. Test samples can be cooled to an accuracy of $\pm$ 0.5°C and down to temperature of -30°C in the chamber. Temperature measurement and control on the surface of the test specimen is achieved using platinum resistance temperature detectors or RTD's (Omega, model DP2000) that are accurate to within $\pm$0.005°C. All measuring devices are placed inside the icing chamber box and electrical connections are made through two vacuum feed-throughs.

A transparent, circular fused-quartz window allows optical access for the video microscopy. An O-ring is used in the joint between the icing chamber and cover plate to ensure that the assembly is vacuum tight.

All measuring instruments are monitored through an 8-channel analog-to-digital converter which is connected to a dedicated IBM-PC controller. A data acquisition and control software with color graphical display of major experimental parameters, i.e., temperature, load, displacement, humidity, and mass flow rate of vapor has been developed and implemented. This facilitates complete on-line control of experimental conditions and recording of the test data on hard disk.

The Raman spectroscopy apparatus and the formation procedure of the ice on the solid surfaces are identical to those described in the previous sections.

3.2.2 Substrate Preparation for SEM Studies

In order to control the surface texture effects, all the solid surfaces were mirror polished. The samples obtained after the elaborate polishing procedure were used to make contact angle measurements. Five solid surfaces have been used in the current study, namely, copper, aluminum, titanium, stainless steel and teflon. The results of the contact angle measurements and the surface energy are listed in Table 3.3. Iden-

tically polished samples of 10x10 mm surface area were used to obtain the scanning electron micrographs.

E. Procedure

To obtain the structure-property relationship between the structure of the ice layers and the resulting adhesive strength of the ice-solid bond the following procedure is followed. The details of the nucleation process observed on the solid substrates is described elsewhere [81]. Ice layers of about 100-200 micron thickness are grown on the solid substrate by vapor deposition. The Raman measurements are done both before and after shearing the ice layer on the solid surface.

1. The polished and chemically clean substrate plate is mounted on the substrate slot on the micro-shear assembly.

2. The top cover with the quartz window is closed and the vacuum pump is switched on to obtain a moderate vacuum in the icing chamber (about 1-2 Torr).

3. The thermoelectric cooler is set to the required temperature and all the measuring instrument are switched on via the computer controller. The data acquisition program is set to record the temperature, vacuum gauge, humidity and flow controller readings at preset intervals throughout the experiment.

4. The icing-chamber assembly is allowed to reach a steady state. The steady state is monitored by the graphical display of the temperature and pressure data on the data-acquisition computer.

5. Vapor is introduced through a bleed valve at a rate of about 10 ± 1 ml/min for about 2 minutes. The nucleation of the condensing vapor droplets is recorded on the video-recorder for the nucleation study. The bleed valve is closed and no spectroscopic observation is made until the temperature and pressure are restored to steady state. Typically, vacuum pressure returns to the atmospheric

value within two minutes while the temperature takes about five minutes to settle back to a constant value.

6. The vapor deposited thin film of ice is observed through the microscope and the spectroscopic observations are made in the O-H stretching frequency region (581 nm).

7. The monochromator is now set to the lattice frequency region (505 nm) and spectroscopic observations are repeated for the same thin ice layer. The spectral observations are calibrated by recording the Argon plasma lines in the same region.

8. The sufficiently thick ice layer is then subjected to a pure shear test. The load-displacement data is obtained and the stress upto the point of abhesion of ice-surface bond is recorded.

9. The Raman spectra of the sheared layer of the ice at the knief edge is obtained in O-H stretching frequency region.

3.2.3 Results of Raman microprobe shear experiments

A. SEM Micrographs

The scanning electron micrographs of the five metal surfaces are reported in Figures 3-9A-E. The figures indicate that among all the high energy surfaces stainless steel has the largest pit-size and a rough surface followed by copper, aluminum and titanium. The surface texture of titanium, copper and stainless steel show similar characteristics, i.e., surface with occasional pits. However, in the case of aluminum the surface morphology shows linear scratches every where that is caused by the polishing. In the case of the low energy PTFE, the surface shows a clean smooth pattern with the absence of deep pits.

B. Adhesive Strength and Activation Energy

The data on the adhesive strength (load/unit-area required to break the ice-solid bond) at -20°C along with the surface energy parameters are reported in Table 3.3. The adhesive strength of ice on the titanium surface is the largest followed in order by copper, iron, aluminum and PTFE. These results do not correlate to the calculated work of adhesion and as such indicate that the adhesive strength for the layers of ice on a solid surface (not the bulk) is not related only to the surface energy. There may be several competing factors, such as, the spreading of the droplets on the surface, the surface morphology and the lattice matching between ice and solid substrate, that contribute to the resulting strength in a complex fashion.

In the present case, with the error bars of about $\pm$ 8%, the metals have a higher adhesive strength than the polymer surface. This is partly because of mechanical interlocking that is achieved due to the presence of a large number of etch pits on the surface of metals, a low contact angle causing spreading of the droplets, and a large number of small diameter ice embryos that occur as a result of the lower Gibbs free energy barrier offered to the nucleation [82]. The reduced adhesive strength on the PTFE surface originates from the smoothness of the surface and absence of deep pits. The low surface energy prevents the droplets from spreading and this results in the larger embryo sizes necessary for the condensation of adsorbed molecules.

The temperature variation of the adhesive strength, σ, over the range 0 to -30°C are reported in Figures 3-10A-E. The trends on the metal surfaces show a change in the slope of σ verses temperature plot at about -10 to -15°C and adhesive strength after this temperature region increases almost linearly with the temperature. This increase in adhesive strength with the reduction in the temperature can be attributed partly to the sintering process. Below -10 to -15°C temperature the spherical ice embryos come close together to form a sintered layer of ice and as a result the strength of the ice-metal bond increases linearly with the temperature. This process will be same for aluminum but the surface texture does not have sufficient mechanical interlocking and consequently yields lower adhesive strengths. The observations on the fracture of the ice-metal bond indicate that failure always occurs in the ice layer and there remains a thin layer of ice sticking to the metal surface even after the complete abhesion of

the metal from ice. This observation suggests that the interface strength is greater than the cohesive strength of ice.

In the case of PTFE the adhesive strength becomes almost constant below -18°C. This observation has been reported in earlier studies [3, 83]. In the case of PTFE, the contact angle is very large (108°) as is the diameter of the resulting embryo. The condensation essentially takes much longer and is predominantly sheet like [81]. The surface morphology does not help to produce mechanical interlocking. The failure in case of PTFE is observed at the interface. This indicates that the strength of an ice-PTFE interface is less than the cohesive strength of ice.

In the above shear experiments, the failure stress (adhesive strength) is obtained under a constant strain rate. For a constant rate condition, the strength may be expressed in the form of a power law [3]:

$$ln\sigma = \frac{Q}{nRT} + constant \tag{3.12}$$

where σ is adhesive strength of the ice-solid bond, Q is the activation energy, n is the power law exponent whose value is reported by Raraty and Tabor [3] to be equal to 4, R is the universal gas constant and T is the temperature in Kelvin.

The activation energy required for breaking the ice-solid bond can be calculated from the slope of the logarithm of the adhesive strength verses inverse temperature. Figures 3-11A-E show these plots for the five solid surfaces. The activation energies for titanium, copper, aluminum and stainless steel are 23.46, 18.64, 16.69 and 23.41 KJ/mol respectively. For PTFE, the activation energy is 6.03 KJ/mo; this is consistent with the low adhesive strength of ice on PTFE. The activation energies are for the *layers* of ice which are deposited on the solid surface, and not that for the bulk ice sample. These values indicate that failure on the metal is sensitive to strain rate while that on PTFE is relatively insensitive. The activation energy values also support a cohesive failure (in ice phase) mechanism in the case of metals and an interface failure mechanism in the case of PTFE.

C. Raman Spectra

The Raman spectra of the ice is recorded in the O-H stretching region for all five solid surfaces both after the formation stable bond and after the failure of the adhesive bond. Figures 3-12A-E show the Raman spectra taken at -20°C. In the O-H stretching region, the strong symmetric peak at 3100 cm^{-1} is assigned to the in-phase symmetric stretching vibrational mode (ν_1). The broad peak at 3300 is assigned to out-of-phase asymmetric stretching vibrational mode (ν_3) [61, 20].

All these spectra show that the ice is in the polycrystalline phase (for a detailed analysis see Sonwalkar et al. [60]). However, the positions of the O-H stretching frequencies and band width differ with the specific surface under consideration.

In general, for the metal surfaces, the spectrum of the bonded ice (before failure) shows an increase in the intensity of the (ν_3) peak as compared to that for bulk ice while that for the sheared ice (after failure of ice-solid bond) is similar to bulk ice. The band width of the sheared ice, however, is larger than that for the bulk ice; this is because the shearing event induces defects in the polycrystalline ice.

The variation in the O-H stretching peak frequencies and respective half-power band widths (HPBW) for the five solid surfaces are reported in Table 3.4. The ice layer which is adsorbed on the solid surface has fewer degrees of freedom for the hydroxil group in contact with the surface than bulk ice. The O-H stretching peaks for titanium show a reduction in the (ν_3) peak frequency, while for all the other solids an increase in (ν_3) frequency is observed. The cause of this difference in the case of titanium is not known. However, for all the other surfaces the probable interpretation can be made on the basis of the disregistry (mis-match) observed in the crystalline structures at the interface and the stress induced as a result of differential thermal expansion between ice and solid surfaces.

Ice has a very low coefficient of thermal expansion as compared to metals. Consequently, the ice layers on metal substrates are subjected to a tensile forces. On the other hand, PTFE has a thermal expansion coefficient which is lower than ice. As a result, the ice is under compression on the PTFE surface. These surface forces

act through the hydroxil group of the water molecule which is adsorbed on the solid surface [64]. The hydroxil group is attached to the surface via van der Waals type of short range weak interactions. The van der Waals attraction (or repulsion in some cases) modifies the coupling between ν_1 and ν_3. In the present case, the contribution of the differential thermal expansion may not be significant because we are operating at only -20° C. We expect the effect of the mis-match (disregistry) to be the dominant component.

Although it is not possible to draw conclusions regarding the nature of the forces, i.e., compressive or repulsive, based on the frequency of vibration, some inferences can be made on the basis of the variation of the uncoupled O-H stretching frequency with O-H bond length. The empirical relation obtained on the for the variation of O-H frequency with the O-H distance by Klug and Whalley[84], shows that the frequency is inversely proportional to the bonsd length. Considering the ν_1 frequency as a basis, the ice on titanium and iron is not subjected stress, i.e., the atoms of titanium (Ti) and stainless steel (Fe) are in registry with the lattice of ice. This is evident from the lattice constants of Ti and Fe, $2.95\dot{A}$ and $2.87\dot{A}$ respectively, which are close to $2.78\dot{A}$, the distance between two oxygen atoms. In the case of Cu and Al, the ν_1 frequency shows a slight reduction, corresponding to an increase in bond length, indicating that the ice layer is under tension. The lattice constant for Cu and Al are $3.61\dot{A}$ and $4.05\dot{A}$ respectively, which is much larger than O-O distance in the ice lattice. As a result the interface is subjected to significant mis-match. The coupling between ν_1 and ν_3 will cause a variation in the ν_3 frequency. In the case of Ti and Fe the effect on ν_3 frequency is minimal; while the coupling decreases in the case of Cu and Fe and causes the ν_3 frequency to increase.

In the case of PTFE the interatomic distance between C-C determines the nature of the forces on the O-H bond. The average C-C distance is $1.54\dot{A}$ and the length of polytetrafluroethylene is approximately $4\dot{A}$, which is greater than the O-O distance. As a result the O-H bond length increases, which is evident with the decrease in the ν_1 frequency. The corresponding increase in the coupled ν_3 frequency is also observed in the Raman spectra.

The interpretation of the HPBW is made on the basis of the disorder present in the ice layers. The HPBW(ν_1) for sheared ice shows an increase in disorder as a result of breakage in the bonds during the shearing event. In the case of Al, it remains constant but HPBW(ν_3) shows considerable disorder. For Fe, the HPBW(ν_1) shows increase in disorder while HPBW(ν_3) shows increase in order. These observations indicate that the shearing of the ice layers has a complex interaction with the O-H bond in the lattice. However, the net result is an increase in disorder for the metals. In the case of PTFE, HPBW(ν_1) is larger than that for metals, which can be attributed to the considerable mis-match between the backbone carbon chain of the polymer and O-O positions in the ice lattice. The disorder is further enhanced as a result of the shearing event.

Conclusions of Raman microprobe shear experiments

In general, adhesive strength of the ice-solid bond is found to be proportional to the mechanical interlocking caused by surface pits, while it is found to be inversely proportional to the size of the embryo. However, assuming that both mechanisms are active the total adhesive strength can be obtained by the superposition of strength provided by the mechanical interlocking and the anchorage provided by the ice embryos formed at the ice-solid interface. In the case of metal surfaces, deep pits at the surface and the large number of ice embryos formed in the nucleation event lead to a high adhesive strength. In the case of PTFE, the absence of the deep pits reduces the mechanical interlocking contribution and the smaller number of ice embryo result in the low value of adhesive strength for the ice-PTFE bond.

The activation energy analysis of the ice-solid bond shows that the ice-metal bond is rate sensitive while the ice-PTFE bond is relatively insensitive to strain rate. The failure of the ice-metal bonds is cohesive in the ice phase and the failure of the ice-PTFE bond occurs at the interface. All the ice-solid bonds fail in a brittle fracture mode.

The bonded ice possesses significant order that is induced by the order in the

substrate, while the sheared ice is characterized by increased disorder due to the shearing event and the loss of bond with the substrate surface. The structure of the ice remains polycrystalline. Although, the defect density of the sheared ice is larger than that for the bulk ice.

The adhesive bond is primarily formed between the oxygen atoms of ice and the atoms of the solid surfaces. The bond, therefore, is strong in the case of metals (such as Ti and Fe) that have a good match with the lattice of the ice while it is relatively weak for metals that are mis-matched with ice lattice. The extreme mis-match of ice lattice with the carbon chain, may be a dominant reason for the low adhesive strength of ice on PTFE.

Table 3.3: Contact angle (θ), exprimentally determined critical embryo size (r_{eq}), theoretically predicted critical embryo size (r_c), maximum Gibbs free energy (ΔG_{crit}), work of adhesion (W_a) and adhesive strength σ for ice nucleation on five solid surfaces.

Material	Contact Angle (^{o})	r_{eq} (μm)	r_{cal} (μm)	ΔG_{crit} 10^{-9} mJ	W_a mJ/m^2	σ Kpa
Titanium	76.98	17	15.050	0.20	93.48	436.00
Copper	76.52	16	15.045	0.28	93.94	421.94
Aluminum	73.28	12	14.590	0.21	97.25	351.61
Stainless Steel	66.94	10	11.409	0.08	103.72	416.31
PTFE	108.71	-	-	-	63.60	175.80

Table 3.4: Variations of O-H stretching frequency peaks (ν_1, ν_3) and HPBW of ν_1 peak for ice on solid surfaces.

Material	ν_1 cm^{-1}	ν_3 cm^{-1}	HPBW (ν_1) cm^{-1}	HPBW (ν_1) cm^{-1}	Type
Bulk Ice	3140.0	3390.0	155	280	Bulk
Titanium	3153.6	3386.9	274	295	Bonded
Titanium	3153.6	3369.1	337	315	Sheared
Copper	3140.9	3331.8	232	358	Bonded
Copper	3139.7	3360.4	336	421	Sheared
Aluminum	3144.6	3331.6	315	368	Bonded
Aluminum	3143.4	3400.8	315	380	Sheared
Stainless Steel	3145.1	3335.7	358	463	Bonded
Stainless Steel	3145.1	3355.1	410	368	Sheared
PTFE	3153.1	3324.6	368	189	Bonded
PTFE	3149.9	3369.1	452	400	Sheared

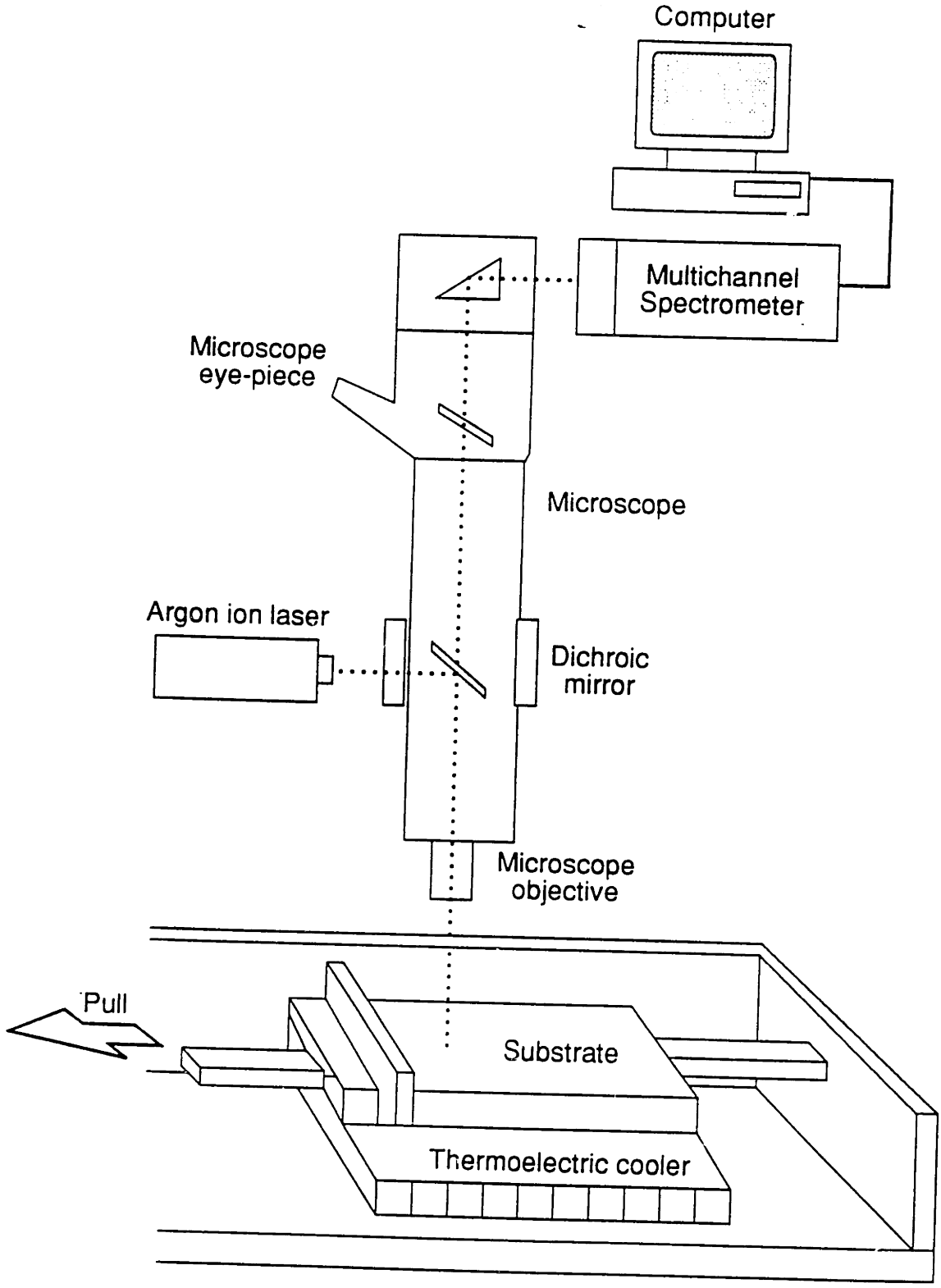

Figure 3-8: Schematic diagram of the Raman microprobe shear experimental set up

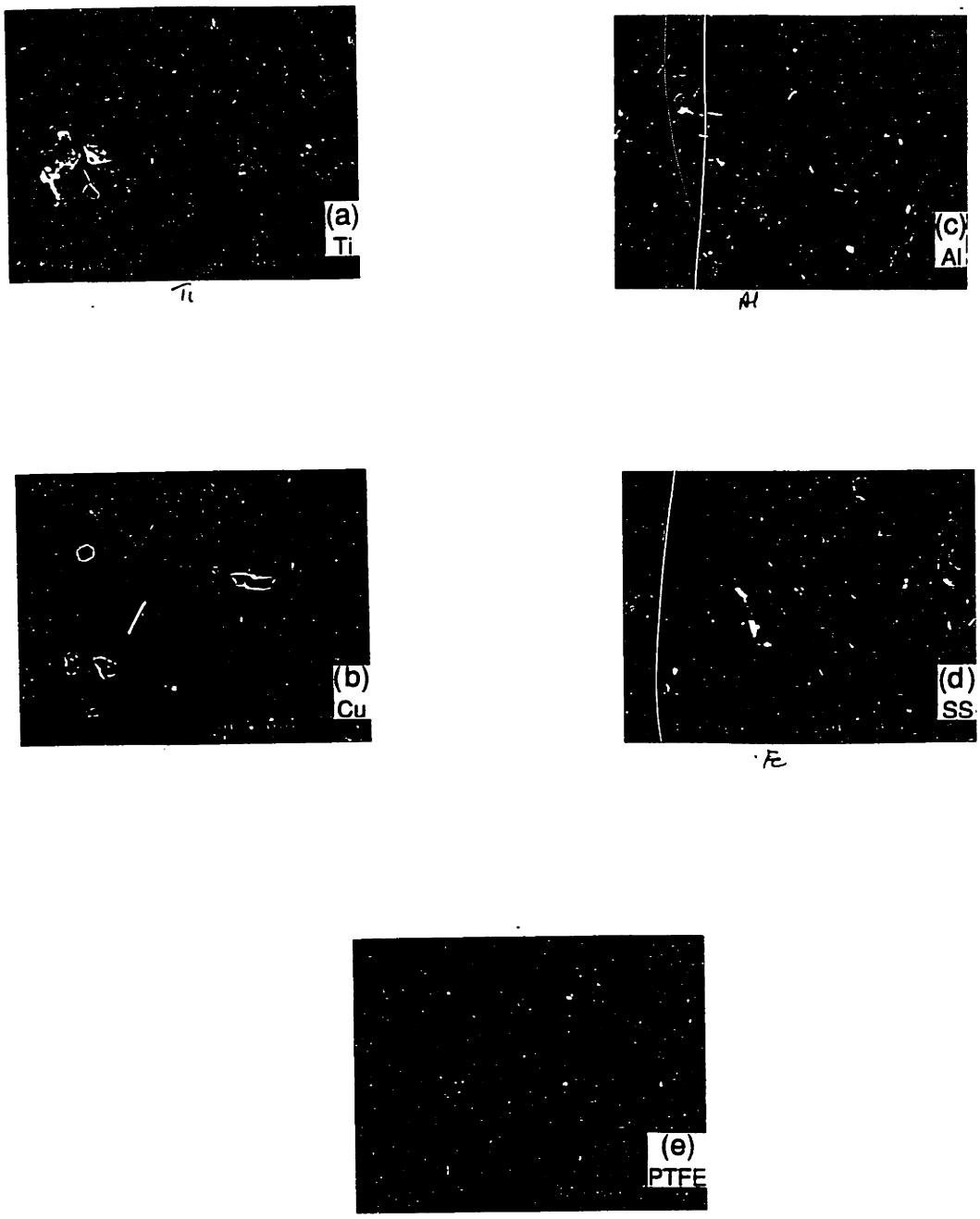

Figure 3-9: Scanning Electron Micrographs of five solid surfaces; A. Titanium, B. Copper, C. Aluminum, D. Stainless Steel, and E. PTFE.

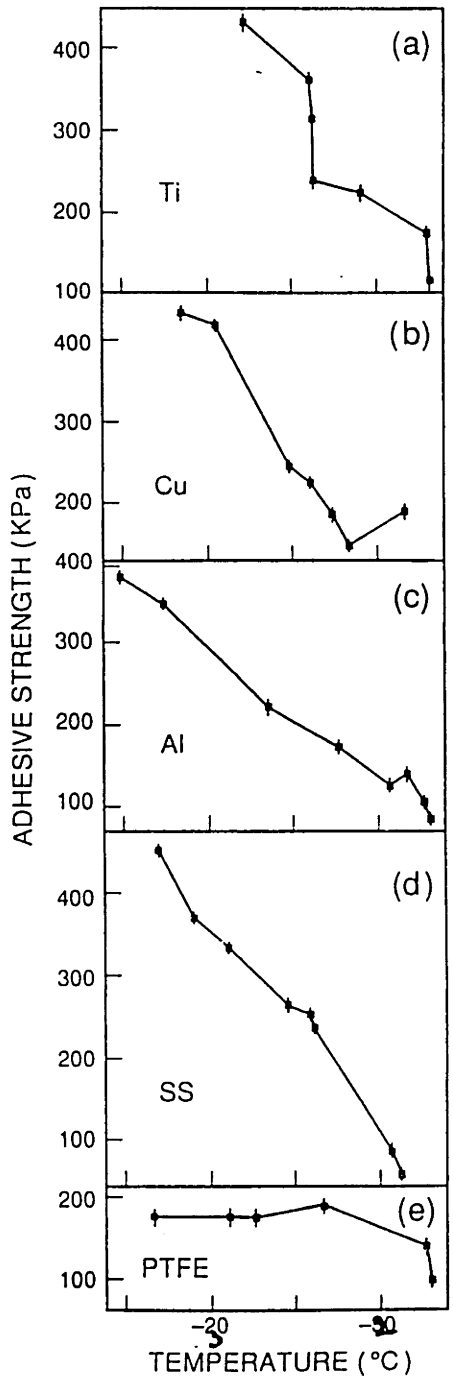

Figure 3-10: Temperature Variation of the adhesive strength (σ) for five solid surfaces; A. Titanium, B. Copper, C. Aluminum, D. Stainless Steel, and E. PTFE.

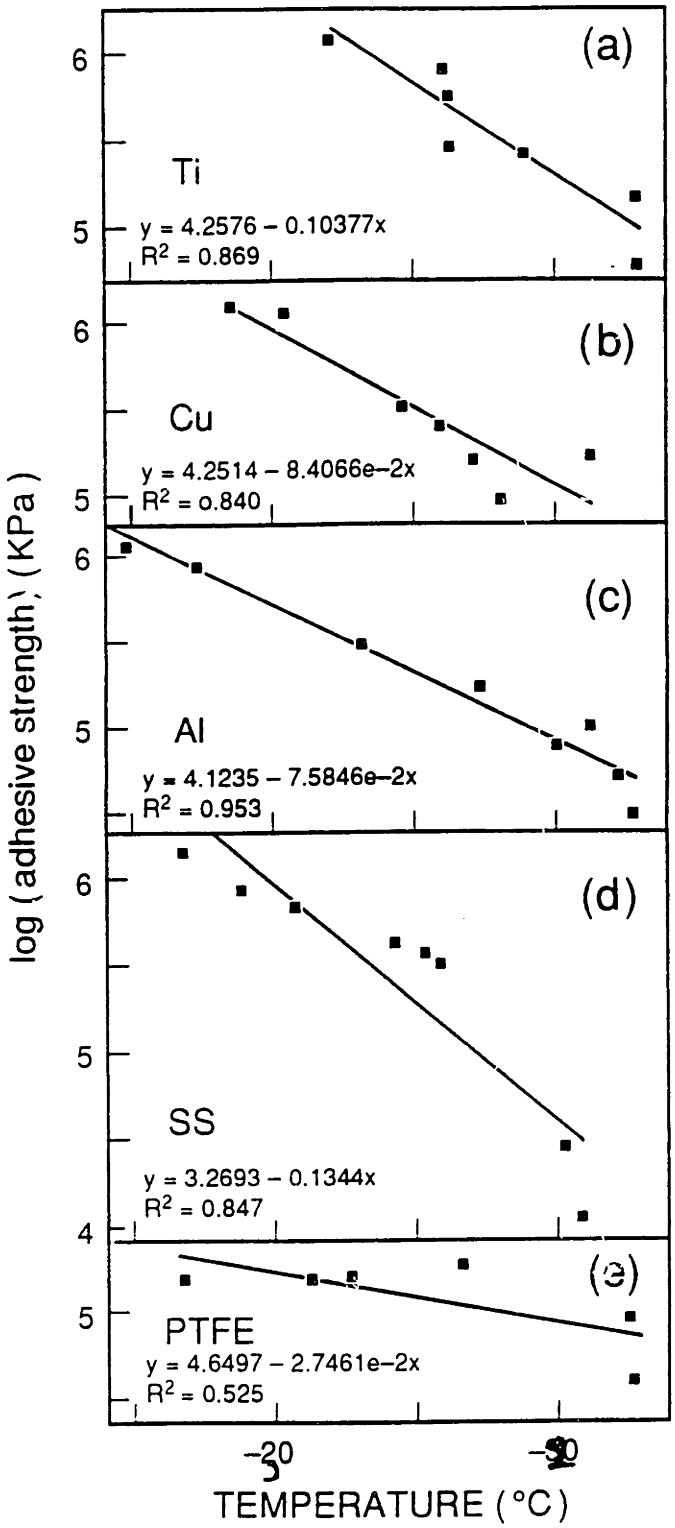

Figure 3-11: Temperature Variation of log(adhesive strength) for five solid surfaces A. Titanium, B. Copper, C. Aluminum, D. Stainless Steel, and E. PTFE.

3.3 Confocal Microscopy of Icing on Metal Surfaces

The adhesion of ice on solid surfaces is an important phenomenon in several engineering applications, such as, failure of electrical transmission cables, performace and safety of aircraft, detoriation of highways and bridges[1, 43, 3, 4, 5, 11]. In all of the above instances, atmospheric icing occurs primarily as a result of the condensation of supercooled water droplets on the solid surfaces. The process of droplet nucleation and coalescence are fundamental phenomenon that have a strong influence on the adhesive strength of ice-solid interface bond, and on the resulting habit of the subsequent crystal growth. The importance of this physical mechanism has not been included in existing theories of adhesion [15, 14, 85].

The laser confocal microscope provides a unique capability for obtaining scanned images of flourecent samples in three-dimensions. The uniqueness of the confocal images is derived from their ability to obtain optical information from only the focal plane, thereby, observing a two-dimensional slice in sample space. A group of such slices can results into a complete three-dimensional reconstruction of the sample space [32, 33].

In our previous studies [81, 82] on the nucleation and growth of ice layers on solid surfaces, the importance of the nucleation process on the resulting adhesive strength of ice-solid bonds has been recognized. However, the role of the liquid droplet formation, prior to its phase transition to ice, may have much more physical significance than is conceived at present. Recently, Steyer et al.[14] have reported spontaneous jumps in the condensing droplets that cause rapid coalescence to an equilibrium radius which then undergoes the phase transition. To understand the effect of the droplet formation and coalescence on the adhesion of the ice-solid interface and its influence on the habit of the crystal growth on a given surface, confocal microscopic observations of the liquid droplet condensation, ice embryo formation and the growth of a crystalline ice layer have been made. The complete record of the nucleation event and the microtomoscopy (i.e., slice-by-slice reconstruction) of the ice formation has been performed on the three

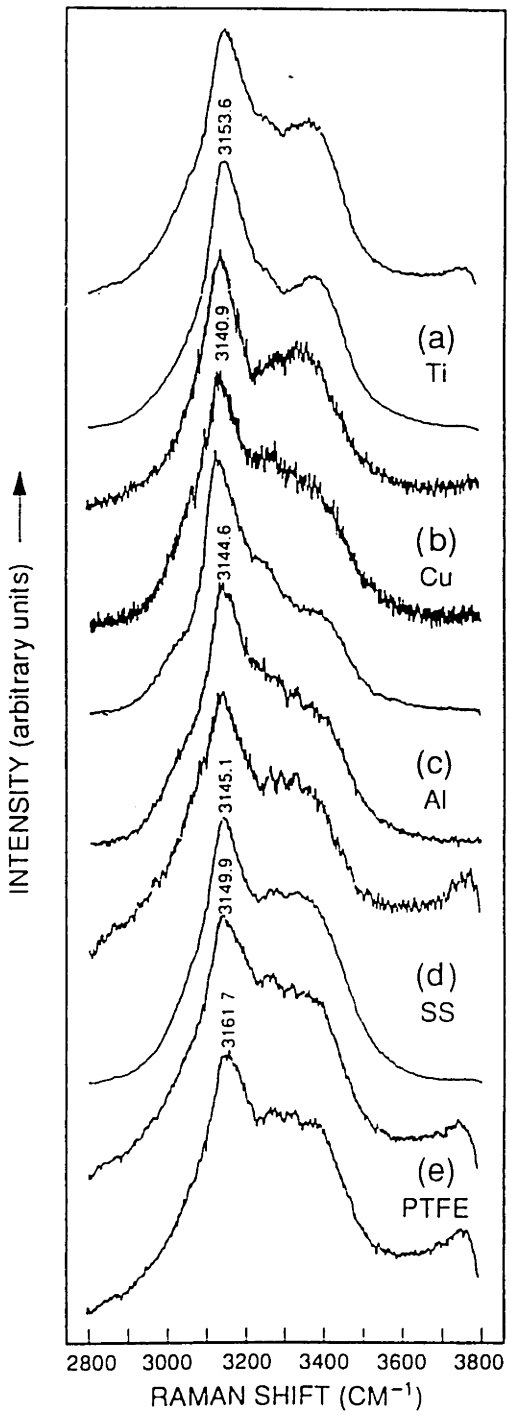

Figure 3-12: Raman spectra of bonded and sheared ice on five solid surfaces A. Titanium, B. Copper, C. Aluminum, D. Stainless Steel, and E. PTFE.

high energy surface (copper, aluminum, glass) and one low energy polymer surface (polytetraflourourethene, known as teflon).

3.3.1 Cooling Stage for Confocal Microscopy

An icing platform is designed and fabricated to simulate atmospheric icing under normal atmospheric conditions and to provide an optical access for the confocal microscopy apparatus. The experimental set-up consists of a thermoelectric cooler (120 mm diameter) that maintains the solid samples at a temperature of -20°C by adjusting the electrical voltage across the thermopile. The polished metal substrate is attached on the thermoelectric cooler with a thermal grease and held in position with the help of masking tape at the two ends. The cooler (with controller) is mounted on the microscopic stage of the confocal assembly, such that it faces the laser scanning head. The surface is scanned by a laser beam (Figure 1).

In the present study, the nucleation of ice occurs by the condensation of a saturated and supercooled water vapor on the surface of a test specimen. The saturated water vapor is made by bubbling air through the de-ionized and triple-distilled water. The vapor is then cooled by passing it through the thermoelectric element. The cold solid surface provides the necessary nucleation sites for the phase transition from vapor to ice. The ice layer formed in this manner closely resembles the process of atmospheric ice accretion in engineering applications.

The four solid surfaces tested in the experiment include three high energy surfaces (copper, aluminum, glass) and one low energy polymer surface (PTFE). The test specimens are made in the form of coupons of size 48 mm x 12 mm x 12 mm. To eliminate any effects in the test results due to variations in surface roughness, the test specimens are polished to ensure an optically flat and mirror finished surface. The details of the sample preparation and characterization (i.e., contact angle measurements) are described in the previous sections.

In summary, the procedure used to simulate atmospheric icing in the laboratory consists of the following steps:

1. The polished and chemically clean test specimen is mounted on the icing platform.

2. The thermoelectric cooler is set to the required test temperature (-20°C) and all the monitoring instruments are activated via the computer controller.

3. The icing platform with sample glued on top is allowed to reach a steady state by continuously monitoring the temperature. The temperature is held constant to within $\pm$ 0.5°C.

4. The nucleation of the condensing vapor droplets is recorded by the digital imaging facility of the confocal microscope from the instant that the vapor starts to condense on the icing chamber until the nucleated ice embryos attain an equilibrium size (typically not more than 3-5 minutes).

D. Confocal Microtomy of Ice Nucleation

The icing chamber assembly is placed below a laser scanning confocal imaging system (Biored, MRC-600). Figure 1 shows the schematic of the confocal imaging system with an inverted microscope (Zeiss Axioplane). The sample is illuminated by an Argon ion laser (Spectra Physics 2020) with a laser line of 488.0 nm or 514.5 nm. A television monitor is used to visually align the test specimen and to observe the nucleation process in real-time. The linear scale of the recordings is calibrated by observing a microscope optical slide (with graduation markings at an interval of 1μm) through the video microscope. The main part of the instrument consists of a scanner head that optically scans the sample and a charged coupled device (CCD) detector collects photons from the scanned region. The light scattered from the sample is collected by the same objective through a pinhole that enables confocal detection. A pinhole of 100 μm diameter provides a depth resolution of 1.34 μm. The high quantum efficiency CCD detector provides almost noise-free signals.

Typically, a laser power of 20 mW is used. The calibration of the instrument for the vertical direction (z-direction) is done by measuring a glass slide of known

thickness. The scanner head is controlled by the computer keyboard. The image output is displayed at the video rate as RGB signals. The output is fed to a standard VHS video recording unit. The digital imges recorded in the frame buffer at a preset time intervals are stored in an optical disk (1GB) for later analysis. A 3-D image reconstruction software is used subsequently to reconstruct the nucleation event by performing a frame-by-frame analysis.

3.3.2 Results and Discussion on the Confocal Microscopy

The nucleation and growth of ice on four solid surfaces are analyzed on the basis of images collected with the confocal microscope. The confocal images are recorded throughout the icing process. Once a sufficiently thick layer of ice is formed on the surface, the layer is also imaged slice-by-slice, begining from the surface of the substrate through the crystal growth region. This visual data provides direct information on specific nucleation events that subsequently affect the growth of ice layers. The observations show different growth mechanisms for the different surfaces. Figures 3-14 through 3-17 are the collection of sequential images on copper, aluminum, glass and teflon obtained during the icing process. For purpose of reference the contact angles and the surface energies of the polished surfaces are reported in the Table 3.5.

In the case of the copper surface, as shown in Figure 3-13, the nucleation consists of small diameter droplets that grow to a certain equilibrium radius and condense to form ice embryos. The ice embryos grow further to form ice crystals of different shapes. The droplets condense in the shape of a sphere which then develop facets at the surfaces. The facets grow into crystal planes optimizing the local surface energy available for the growth. For copper, the facets form horizontal cylinders that produce a complicated network of cross-linked crystals. The microtomy on the copper surface (Figure 3-13 shows that the ice layer adjacent to the metal surface has a pattern of ice embryos that results from the droplet condensation. The anchorage of the first layers depends on the number of droplet rings that form on the surfaces.

For the aluminum surface, the ice embryos initially form faceted crystals from spherical droplets and later grow to discrete crystal facets (see Figure 3-15). The

growth of the crystals is in the horizontal direction. However, the morphology of the cross-linked connection between the crystals is different than on the copper surface. This difference can be attributed to the differences in surface energy and grain size of the ice crystals.

As shown in Figure 3-16, the icing on a glass surface has a different pattern of droplets. The droplets do not remain spherical, but change their shape by deformation in several ways. The oblong shapes form a network of droplets that have low contact angle which is expected due to the high surface energy of the glass surface. The of ice embryos condensed on the glass surface show a polycrystalline texture with multiple facets formed on the embryo surface. This unusual texture is associated with smaller grains that do not have a preferred orientation. The polycrystals with the random orientation strongly suggest that the ice formation has been influenced by the amorphous structure of the glass. The crystal growth also shows a cross-linking of the crystal facets among the condensed droplets. There is no spontaneous jumping (hopping) mechanism as result of the low contact angle [85]. The microtomy on the glass surface shows that the interface ice layer does retain the memory of the initial layer of droplets that condensed on the surfaces. The perimeter (triple line) of the droplets plays an important role in adhesion of ice. The crystals forming on the glass surface clearly show facets that form cleavage planes for the failure of the ice-glass interface.

The nucleation on the polymer (PTFE) surface is different from both the metal and glass surfaces (see the sequence in Figure 3-17). The surface has low energy and, hence, has a high contact angle (108 °) that makes condensation difficult on the teflon surface. The Gibbs free energy barrier requires a large droplet diameter before it reaches an equilibrium embryo size for the phase change to occur. The process of condensation is delayed for the droplet to attain a large diameter. The small droplets become grow through a hopping mechanism which induces coalescence. The hopping frequency decreases with time and reaches zero as droplets attains the equilibrium diameter. The droplets are completely spherical prior to condensation. The large diameter droplets condense and form small platelets at the surface that show a sheet-

like condensation. The droplets grow vertically to form columnar ice crystals. The cross-links between the columnar crystals are weak and not well-established to impart strength to the ice layer on the polymer surface.

The microtomy on the metal surface show three distinctive regions that constitute the initial growth of ice. The first region is the condensation region which shows memory of the droplets that condense on the surface prior to phase-transition (liquid-to-ice) process. The droplet shape is preserved in the form of a perimeter that is still visible on the surface layer. The droplet perimeter, being the region of stress concentration, provides an essential link between the metal and ice crystals. The second region originates due to the faceted growth between the ice embryos. This region has a number of horizontal small crystals originating from the droplets that form links between the crystals. The third region is made of large crystals that grow from the facets and form the distinctive crystal habits as recorded by Nakaya et al. [69]. The crystal habit, i.e., size and the shape of the crystals, depends significantly on the nucleation and initial pattern of facets that originate from the condensed droplets.

The three regions of ice growth are present in all the surfaces. However the morphological character and the thickness of the regions differ depending on the type of surface. The condensate region is very small on the metal and glass surfaces as compared to the PTFE surface. The cross-faceting region is more pronounced on the high energy surfaces, but is almost absent in case of the low energy surfaces. The crystal growth region on the metal surfaces show smaller crystals and short facets, while for PTFE this region shows long facets and big crystals. The smaller grain size is typical of the metal surfaces and big grain size is characteristic of the polymer surfaces.

Finally, a comparison of the critical embryo radius, maximum free energy, and the work of adhesion shows that the embryo radius is proportional to the free energy barrier but inversely proportional to the work of adhesion for the mirror polished surfaces that were tested in our previous studies [81, 82]. The surface with the lowest free energy barrier, i.e., stainless steel, has the smallest critical embryo radius and the ice crystals form with the least amount of resistance and grow rapidly into large

crystals. The resulting work of adhesion is highest for such a surface. These results support the hypothesis that the adhesive strength is proportional to the area of the droplet triple lines. Ice at the triple lines forms the strongest bond with the solid surface. This is because the mechanical interlocking mechanism and the adsorption of the hydroxil group is a maximum at the triple line due to the stress concentration. The results in Table 3.6 show that glass has the highest adhesive strength and the largest triple line density followed by copper and aluminum. In the case of PTFE, the density of triple lines is very low and so is the adhesive strength.

The adhesive strength of an ice-solid interface has contributions from several mechanisms, such as, mechanical interlockning, chemisorption of the hydroxil group on the metal surface, and van der Waals dispersion forces. However, results of the present study show that all these mechanism are pronounced at the triple lines of the droplets that become the ice embryo for nucleation process.

3.3.3 Conclusions of the Confocal Microscopic Studies

The microtomy of the ice nucleation and growth process was performed on several solid surfaces using a confocal microscope. These observations, which provide the complete picture of the nucleation and growth process, reveal the following findings:

1. The role of the nucleation process on the adhesive strength of ice-solid bonds depends on the droplet perimeter shape and area. The smaller droplets that have a large droplet perimeter and a circular shape, provide excellent anchorage of ice crystals on the solid surface at the perimeter rings, where the stress concentration is high.

2. The microtomy of the ice layers deposited on the solid surface show three distinctive regions. The first one is the condensate region resulting from the adsorption of water molecules; the second region is the crystal facet region, where facets grow from spherical ice embryos; and the third region consists of crystals

that grow from the facets in different shapes and form cross-links. The condensate and faceted cross-linked regions are responsible primarily for the resulting strength of the adhesive bond and the habit of the crystal structure.

3. The hopping mechanism is observed in the case of the smooth PTFE surface. On the high energy surfaces, the hopping of the droplets is suppressed due to wetting and the roughness of the surface. The stress concentration at the rim of the droplet condensing on the surface plays vital role in the adsorption of the water molecule on the solid surface. The anchorage provided at the droplet ring is stable and stays in the same pattern even after significant ice growth has taken place.

4. The low adhesive strength on the PTFE surface originates from the lack of both droplet perimeter area and cross-linking between columnar crystals in the faceted region of the ice growth. It is necessary to control the droplet formation mechanism and reduce the effective rim area on the surface to prevent icing on the solid surfaces. The hopping mechanism of the droplets that encourages coalescence of the small high contact angle droplets($\rangle$ 90°) into larger droplets helps in reducing the adhesive strength of the ice-solid bond involving ice.

In summary, this study has established that the droplet condensation characteristics have a major influence on the nucleation and growth of ice layers on solid surfaces. The triple line characteristics are of critical importance in determining the resulting adhesional strength. Thus, it is clear that in order to develop effective ice phobic coatings it is necessary to design them such that the formation of a large number of triple lines on the surface is prevented.

Table 3.5: Contact angle (θ), critical surface tension (γ_c), and solid surface energy (γ_s) for three solid surfaces investigated

Material	θ ($^\circ$)	γ_c (mJ/m^2)	γ_s (mJ/m^2)
Copper	76.52	33.3	43.4
Aluminum	73.28	36.8	45.4
Glass	79.89	30.3	56.3
PTFE	108.71	18.4	22.2

Table 3.6: Contact angle (θ), experimentally determined critical embryo size (r_{eq}), theoretically predicted critical embryo size (r_c), maximum Gibbs free energy (ΔG_{crit}), work of adhesion (W_a) and adhesive strength σ for ice nucleation on five solid surfaces.

Material	Contact Angle ($^\circ$)	r_{eq} (μm)	r_{cal} (μm)	ΔG_{crit} 10^{-9} mJ	W_a mJ/m^2	σ Kpa
Copper	76.52	16	15.045	0.28	93.94	421.94
Aluminum	73.28	12	14.590	0.21	97.25	351.61
PTFE	108.71	-	-	-	63.60	175.80
Glass	79.89	10	11.901		86.29	450.45

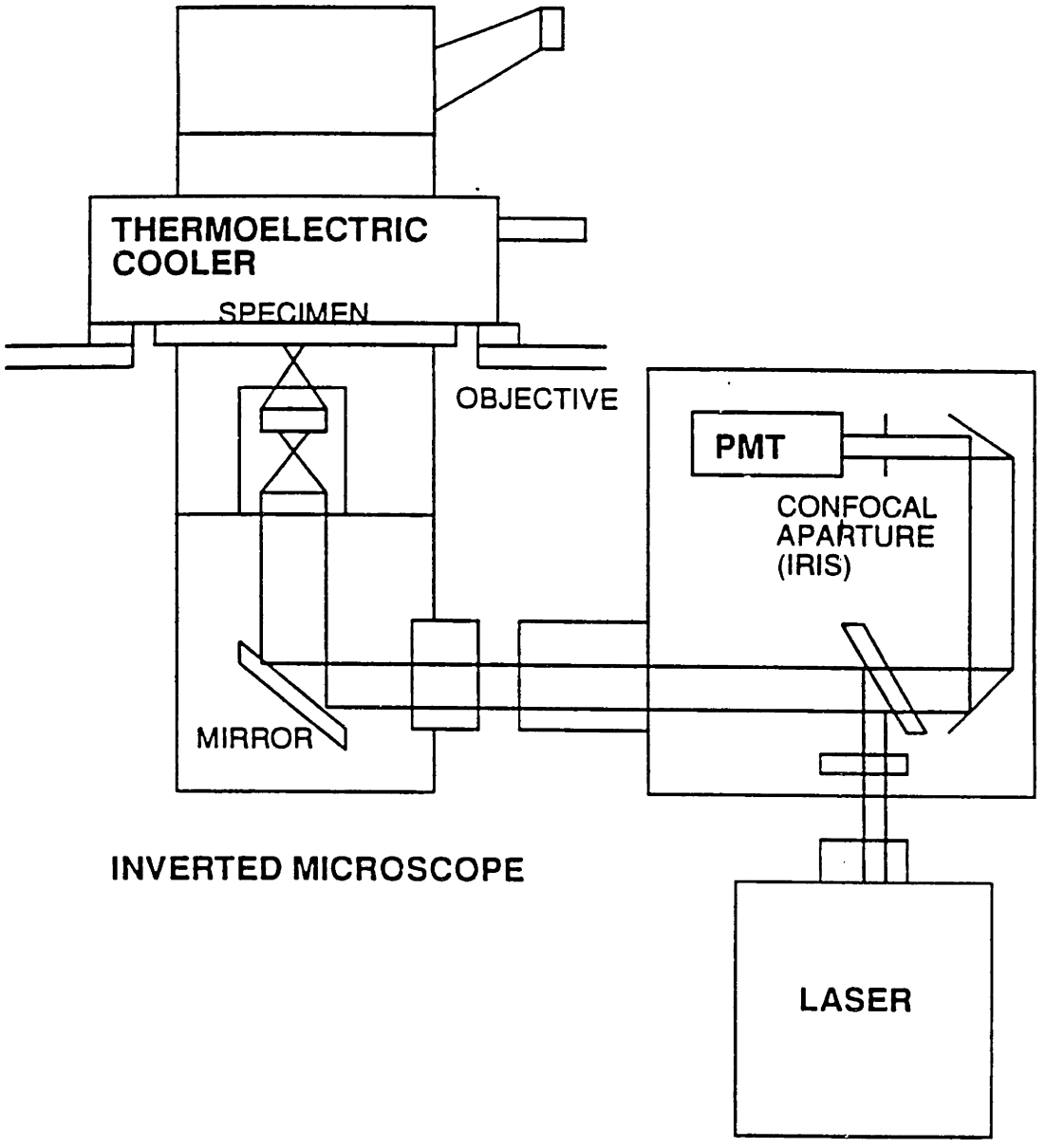

Figure 3-13: Schematic diagram of the confocal microscopy experimental set up.

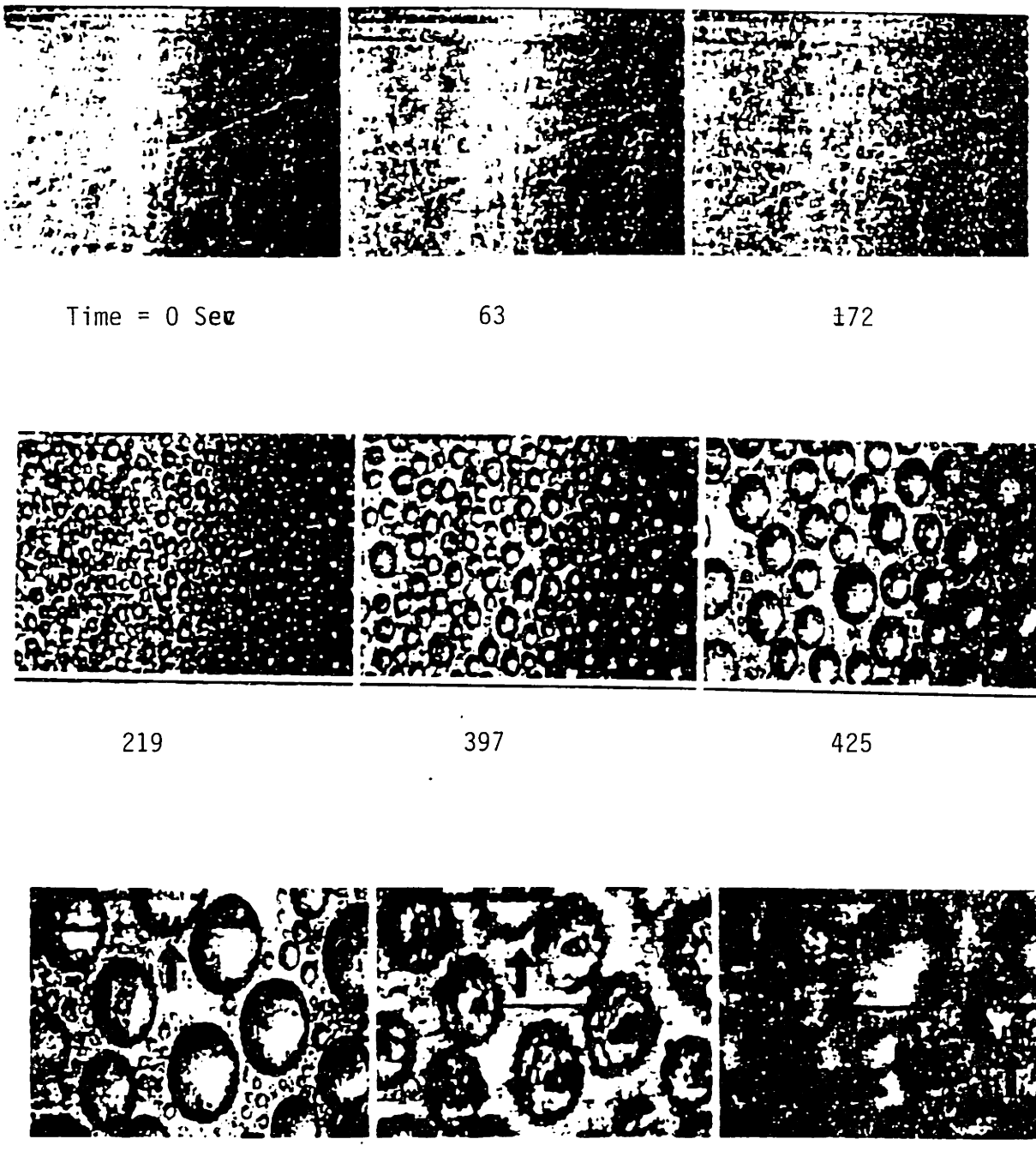

Figure 3-14: Photographs from recording of confocal microscope showing nucleation and growth of ice on copper surface.

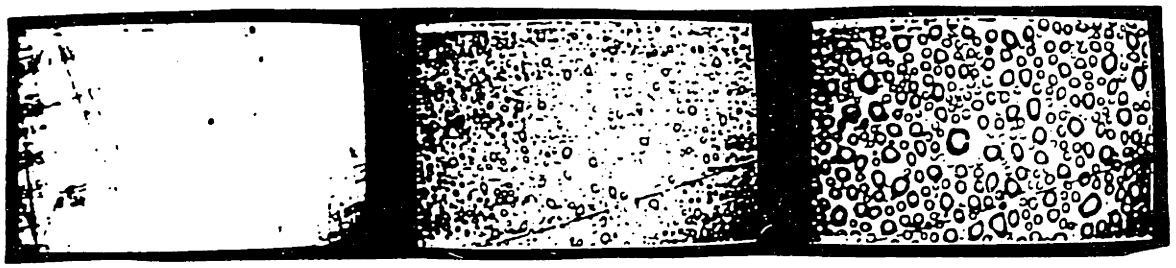

Time = 0 Sec 100 270

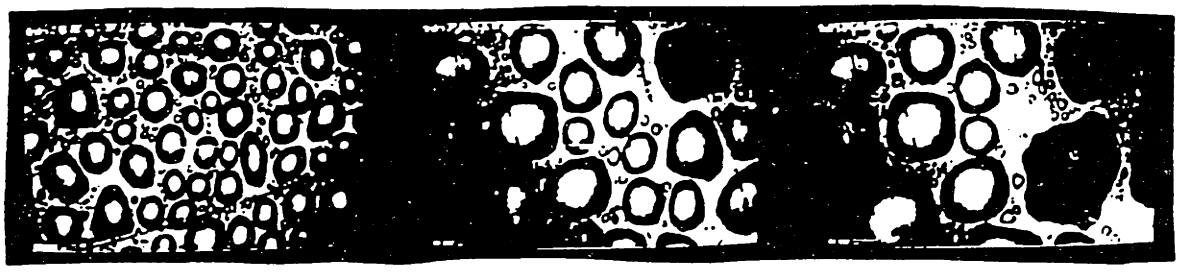

760 1397 1600

1910 2200 2300

Figure 3-15: Photographs from recording of confocal microscope showing nucleation and growth of ice on aluminum surface.

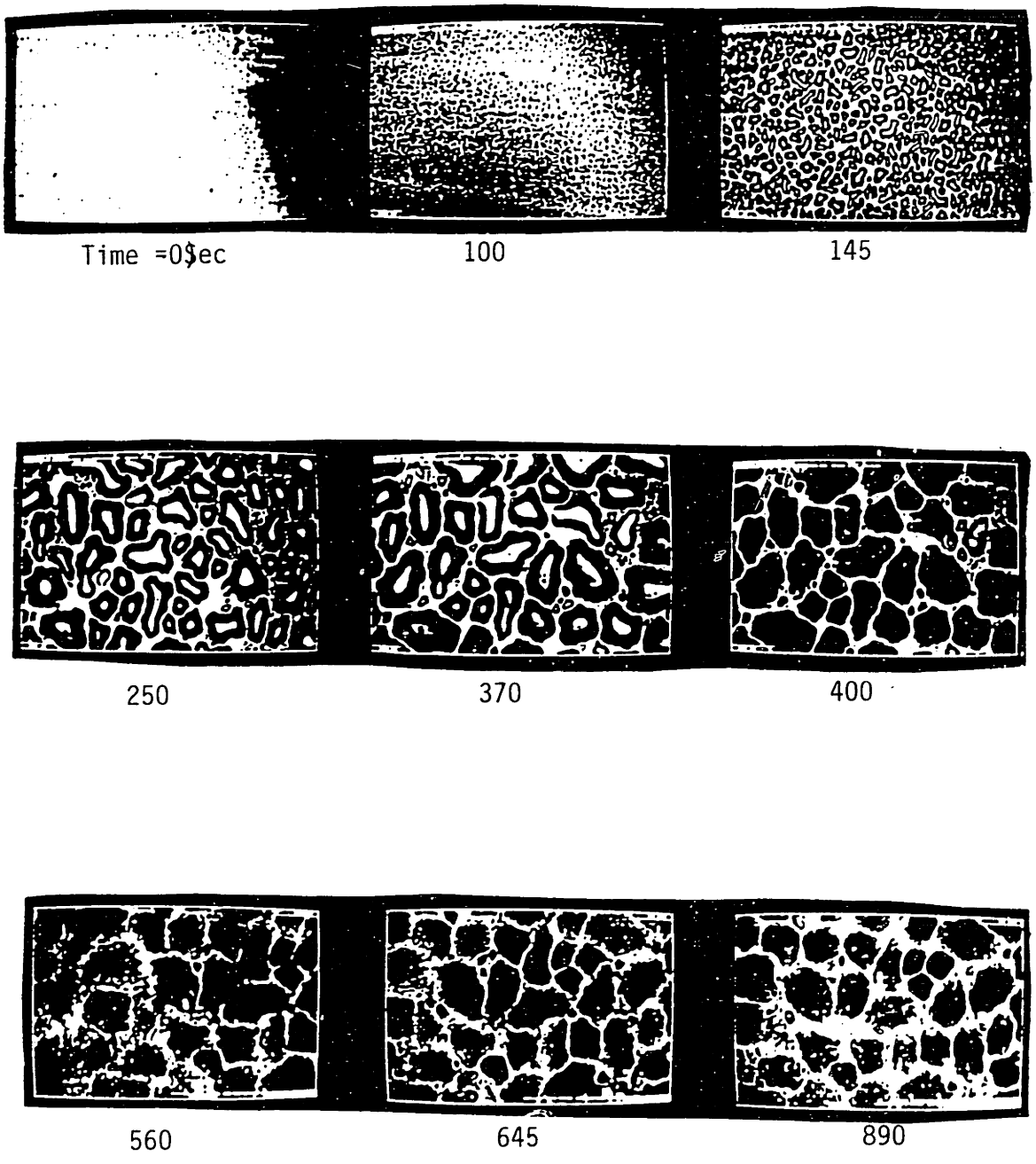

Figure 3-16: Photograpsh from recording of confocal microscope showing the nucleation and growth ice on glass surface.

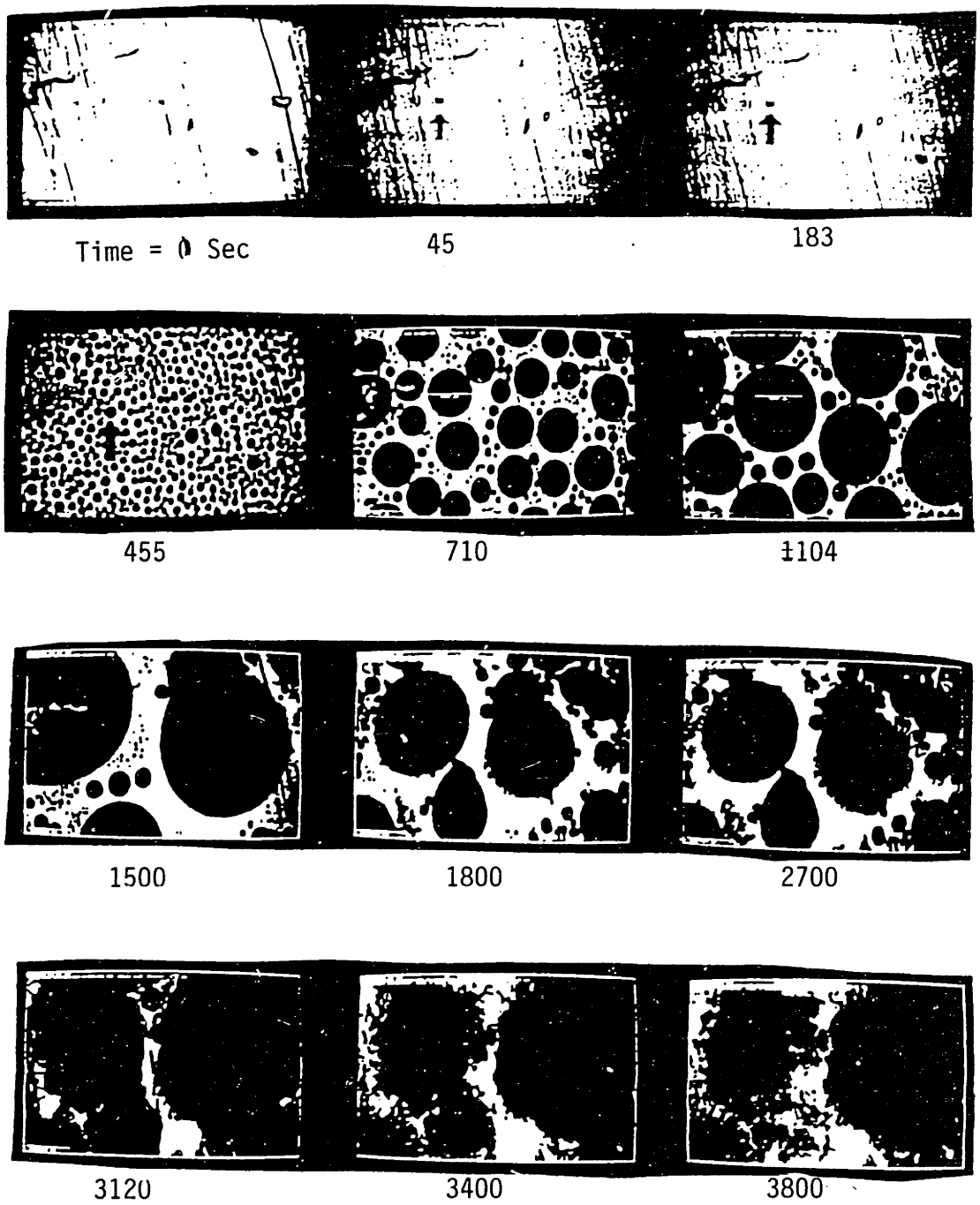

Figure 3-17: Photographs from recording of video microscope showing the nucleation and growth ice on PTFE surface.

Chapter 4

Molecular Dynamics Simulation of Ice and Copper

The validity of molecular dynamics simulations strongly depend on the characteristics of potential function that describe interaction between the atoms. Therefore, it is necessary to test the validity of the potential models against a given set of known experimental/theoretical information. This chapter focuses attention on the validation of simulation models for the bulk water/ice and the bulk copper. This chapter is an important step towards the simulation of an ice-copper bi-material interface.

4.1 The Potential Model for Water/Ice

The condensation of water droplets has been studied extensively by atmospheric scientists concerned with the formation of clouds. Investigations involving the MD approach were initially conducted by Rahman and Stillinger (1971,1974) [86, 87] who studied both static and dynamic behaviors of water molecules based on a rigid tetrahedral model of the individual molecules. Numerous studies on water molecules and microclusters have since appeared in the literature (see, e.g., Rahman and Stillinger, 1971 [86], Briant and Burton, 1975 [36]; Berendsen et al. 1981 [37]; Toukan and Rahman, 1985 [38]; Anderson et al. 1987 [88]; Berendsen et al. 1987 [89], Prevost et al.(1990) [90].

The structure of water molecule is primarily responsible for the unusual properties of water and ice [40]. The attribute of the water molecule giving rise to many physical peculiarities primarily originates from polar character of the water molecule forming highly directional hydrogen bonds [41]. The triangular shape of water molecule, having a permanent dipole moment, gives rise to a high dielectric constant, a high specific heat and a low diffusion coefficient. A factor, which complicates the simulation of molecular polar fluids and ionic solids, is the long-range Coulomb interaction. All these complications lead to a significant coupling between the intermolecular and intramolecular interactions. As a result, the analytical treatment becomes extremely intractable. In such situations Molecular Dynamics techniques (MD) offer unique capability to probe complex atomic/molecular interactions. Within the framework of MD simulation, it is possible to treat long-range interactions in polyatomic molecules where the intermoluecular and intramolecular interactions are explicitly defined. The MD approach is based on the classical mechanics. In this approach the atomic motions arising from both strong valence forces and weak dispersion forces are considered without making any compromising assumptions.

A few studies have been reported on the application of MD on ice (see, e.g., Weber and Stillinger, 1984 [91]; Tse et. al., 1984 [92]; Karim et al., 1987,1990 [93, 94]).

4.1.1 Potential Functions for Ice

As described in the previous sections, the molecular dynamics simulation of ice depends on the potential functions which have been either primarily constructed to simulate properties of liquid water or derived from the potential for simulation of water molecules. The methods that have been utilized to construct the potential function for water molecules can be broadly categorized into three groups: (a) two-body potentials obtained from the first principle *ab-initio* calculations, (e.g., MCY potential [95]) (b) effective pair potentials obtained by fitting empirical data for the condensed-phase of liquid water and ice, (e.g., SPC [89]), and (c) non-additive potentials in which non-additivity is explicitly represented by a polarization mode (e.g., Stillinger and Devid [96]).

In the case of water molecules, the historical development of potential models shows a trend from a rigid monomer model(e.g. Rowlinson, 1951 [97]) to a flexible water-water potential described by Matsuoka el al. (1986) [95]. The initial models, such as Rowlinson [97], ST2 [86], TIPS [98] and SPC [37], considered only a rigid nonomer with three, four or five point charge interactions along with a Lennard-Jones short range interaction model between oxygen atoms to describe the dimerization energy between two monomers.

With the exception of a few, all the potential models mentioned above, fall under the category of pairwise additive effective pair potentials. The rigid monomer model of SPC pair-potential was subsequently improved by incorporating flexibility to the molecule [38]. In the flexible model, the bond length and angle are allowed to change according to the local force field.

The interaction potentials that will be used for simulation of ice, need to be sensitive to the interaction of the covalently bonded O and H bonds, as well as to the interaction of the H-O-H dimers bonded via hydrogen bond. Besides, the heteropolar nature of the H-O-H molecule makes it also necessary to include long range Coulomb interaction between the point charges carried by the atoms. These requirements call for an explicit treatment of intra- and inter-molecular potential functions.

Lamberg and Stillinger [99] developed a central force model describing intra and inter atomic interaction, in terms if atom-atom interaction. This representation allowed calculation of dipole-dipole correlation function to obtain density of vibrational states for proton motions. However, this approach did not give satisfactory agreement with the experimental data and was not pursued further, but it did demonstrate the possibility of using effective pair potentials for such calculations. Later Stillinger and Rahman proposed modified effective pair potential ST2, which clearly demonstrated that a four point charge effective potential model can be successfully used to calculate the vibrational density of states.

Berendsen et at. (1981)[37], and Jorgensen (1981)[98] proposed effective pair potentials, where the point charges coincides with the positions of the atomic masses, these potentials are referred as SPC and TIPS respectively. The SPC potential was

derived and calibrated using MD simulation results while the TIPS was derived via MC simulation results. The SPC potential has been further modified by Berendsen et al.(1987) [89] to include the self energy correction to account for the average effect of the polarization, while Jorgensen (1988) [100] has modified the TIPS water model to more closely resemble the initial SPC model. These two, three-point-charge models have been quite often used to simulate ice and its high pressure phases.

Toukan and Rahman (1985) [38] modified the original rigid monomer model suggested by Berendsen et al. (1981) [37] by incorporating an anharmonic Morse term for the inter atomic interactions. The modified flexible-SPC model was used in the calculation of the proton density of states and proton velocity autocorrelation. The autocorrelation function showed good agreement with the experimental neutron scattering data.

The SPC model has been used to calculate the vibrational properties of the ice. Tse et al. [92] calculated the lattice vibrational spectra of ice Ih, VII and IX, which were found be in reasonable agreement with the Raman spectroscopic data of Wong and Whalley, (1975) [61]. Bansil et al. (1986) [101] used the flexible-SPC model to calculate inelastic neutron scattering, infrared and Raman spectra of water and supercooled water. Anderson et al. 1987 [88] showed the validity of flexible-SPC model in calculating the dielectric properties of the water and salt solutions.

Jorgensen et al. (1983) [98], Tse et al. (1984) [92], Impey et al.(1984) [102] and Prevost et al. (1990) [90] have compared the relative merit of the SPC, MCY and TIPS models in predicting thermodynamic, structural and dynamic properties of the water and ice. Tse et al. (1984) [92] have employed the SPC model to study the various high pressure structure of ice. This study showed that the interaction potential for water can be used to study the structural and thermodynamic properties of the ice polymorphs. They also showed that not all interaction potentials accounted for the pressure effects. Impey et. al.(1984) [102] have conducted a comparison of thermodynamic properties predicted by the competing interaction potentials for ice. This comparison indicates that SPC potential is as good as other potenttials in predicting thermodynamic properties. The SPC potential provides extremely convenient

functional form for the solution of the equation of motion as compared to other potential formulations. The SPC model has shown a marginal superiority in predicting structure of water, the vibrational properties of ice, and its high pressure phases.

4.1.2 Flexible SPC Potential Model

In the present simulation studies, the modified flexible SPC model proposed by Toukan and Rahman [38] has been used. In this model, the intermolecular interactions are modeled by the Lennard-Jones potential between oxygen atoms, and a Coulomb potential for the electrostatic interaction arising from the partial charges on oxygen and hydrogen. The intramolecular interactions are modeled by the interaction of the O-H bond stretching and the H-O-H bond bending along with the cross terms for the stretch-stretch and stretch-bend contributions. Harmonic potentials are used for modeling these interactions.

$$U = U_{inter} + U_{intra} \tag{4.1}$$

$$U_{inter} = \sum_{i=1}^{n}\sum_{j=1}^{m} q_i q_j r_{ij}^{-1} + A r_{OO}^{-12} - C r_{OO}^{-6} \tag{4.2}$$

$$\begin{aligned} U_{intra} = D_{OH}([1 - exp(-\alpha\Delta r_1)]^2 \\ +[1 - exp(-\alpha\Delta r_2)]^2) + \frac{1}{2}k_\theta(\Delta(r_3)^2 \\ +k_{r\theta}(\Delta r_3)(\Delta r_1 + \Delta r_2) \\ +k_{rr}(\Delta r_1 \Delta r_2) \end{aligned}$$

The potential parameters are listed as follows.

Parameters for Intermolecular Interaction

A = 629.4 x 10^3 $\dot{A}^{12}$ kcal mol^{-1}

$C = 625.46\ \dot{A}^6$ kcal mol^{-1}

q(O) = -0.82e

q(H) = +0.41e

Equilibrium Geometry

$r_e(OH) = 1.0\ \dot{A}$

$r_e(HH) = 1.6337\ \dot{A}$

$\theta(HOH) = 109.47^o$

Parameters for Intramolecular interaction

$D_{OH} = 0.708$ mdyn$\dot{A}^{-1}$

$\rho = 2.567\ \dot{A}^{-1}$

$k_{theta} = 2.283$ mdyn$\dot{A}^{-1}$

$k_{r\theta} =$ -1.460 mdyn$\dot{A}^{-1}$

$k_{rr} = 0.776$ mdyn$\dot{A}^{-1}$

and

$$\Delta r_1 = r_1 - r_{eOH}; \Delta r_2 = r_2 - r_{eOH}; \Delta r_3 = r_3 - r_{eHH} \tag{4.3}$$

4.1.3 Structure of Atmospheric Ice

It is well known that ice has a very rich phase diagram. Within the range of zero to 24 kilobar pressure and temperature between 160K to 380K nine polymorphs of ice can exist [18]. However, at atmospheric pressure (1 bar) only ice I exists. Interestingly, ice I is the only ice form which is less dense than liquid water and found in abundance in the atmosphere. We are concerned with the atmospheric icing on the structures and cables, consequently, we restrict our attention only to ice I.

Normally, ice I is hexagonal (referred as I_h) and has crystal structure, for oxygen positions, which can be considered as two interpenetrating hexagonal closed-packed structures. This geometry is similar to the zinc sulphide (ZnS) called wurtzite. There is a cubic analogue to this structure consisting of two interpenetrating face-centered

cubic lattices based on points (0,0,0) and (1/4,1/4/,1/4) which is similar to the structure taken by diamond cubic structure, referred to as ice I_c. The ice condensed on the metal surfaces at low temperatures (below 150K) has been found to have cubic structures.

As reviewed by Kamb (1969) [103], the existence of the cubic phase of ice is well confirmed. The lattice parameter of cubic ice at 150K has been reported as 6.350 $\pm$ 0.008 $\dot{A}$, which results in the same density as hexagonal ice. The nearest neighbor environments in both ice I_h and ice I_c are identical. These structures start to differ only after second neighbors. Infrared and Raman spectra of I_h and I_c are identical in the range of 350-4000 cm^{-1} [45]. Features in the H_2O -D_2O mixture show identical band broadening resulting from proton disorder. Electron diffraction of ice I_c by Honjo et al. (1956) [104] confirm the similarity in the disordered hydrogen positions between ice I_c and ice I_h. Fletcher [18] describes that due to these similarities the configurational entropy of ice I_c is the same as ice I_h and, therefore, the two forms are analogous. Owing to the simplicity and convenience of analysis offered by the cubic structure, we have used the cubic structure for the molecular dynamics studies on ice.

The location of the hydrogen atoms has been matter of debate owing to the lack of a direct experimental evidence. Only after the application of neutron diffraction by Peterson and Levy (1957) [105], some definitive conclusions have been obtained. Historically, Bernal and Fowler (1933) [106] and Pauling (1935) [107], proposed that the H_2O molecules remain intact in the ice lattice. These intact nonlinear H-O-H molecules, having one O-H bond pointing towards the other oxygen, can form six possible orientation for each H_2O molecule. This leads to a large number of probable geometries in which the hydrogen atoms can reside.

Arguing on the basis of equal probability, Pauling [107] proposed his conditions for hydrogen atom configuration. These conditions, listed below, are popularly known as ice-rules [107]:

1. H_2O molecules are intact neglecting small quantity of ionized molecules.

2. Each H_2O molecules is oriented such that its two O-H bonds are directed approximately towards two of the four nearest neighboring oxygen atoms.

3. Only one hydrogen atom lies between two adjacent water molecules.

Under these conditions the resulting crystal is proton disordered and, hence, possesses residual entropy at 0K.

In the present study, we generate ice geometry by loading eight oxygen atoms at the unit cell of a Bravais space lattice of face centered cubic type, with a basis of two atoms at (0,0,0) and (1/4,1/4,1/4). The eight particles, therefore, have positions (0,0,0); (1/2,1/2,0); (1/4, 1/4,1/4); (3/4,3/4,1/4); (0,1/2,1/2); (1/2,0,1/2); (1/4,3/4,3/4); (3/4,1/4,3/4). The lattice constant of the ice is taken as 6.35 $\dot{A}$. The hydrogen atoms are initially put pointing in the xy direction and with hydrogen sites making an angle of 109 degrees at the oxygen positions. Figure 4-1 shows the geometry of a cubic ice without the hydrogen positions. The proton positions are randomly distributed.

4.2 Calculation of Long Range Forces

The calculation of the trajectory of atomic movement is obtained by solving Newtons equation of motion in time domain. The integration of Newton's equation of motion requires accurate evaluation of the forces at each time step to describe correctly the properties of the simulated material. In the case of ionic molecular system, such as water/ice, the interaction potential can be divided into short range and long range interactions. The inter-moleccular part of the SPC potential consists of short range forces described by Lennard-Jones (6-12) functional form which includes both repulsion and attraction while the long range interactions are described by the Coulomb potential.

The calculation of the short range forces is straight forward, and is obtained within the truncation of the interaction by a sphere centered at the atom. However, the long range interactions calculated with the same procedure lead to a highly unphysical and orientationally distorted system. Therefore, the alternative methods, such as Ewald summation [108] and reaction field method [39], have been used to calculate long range forces in the case of a 3-D periodic MD system. We have employed the Ewald summation method for the calculation of the long range forces.

4.2.1 Implementation of Ewald Summation Procedure

Ewald summation procedure can be best described by an ionic system put in a cubic cell with N ions having volume $\omega = L^3$ where L is the side length of the simulation cell. We use a double index jn to express j^{th} particle in n^{th} image cell which is displaced from the original cell by an amount Ln, where n is the integer triplet describing the cell.

The total Coulomb energy of the N ions in the classical form is expressed as:

$$V^c = 0.5 \sum_{i=1}^{N} \sum_{j=1}^{N} \sum_{n}^{'} \frac{Z_i Z_j}{r_{i,jn}} \tag{4.4}$$

where $r_{i,jn}$ is the vector of the particle i from particle jn, Z_i, Z_j are charges on i

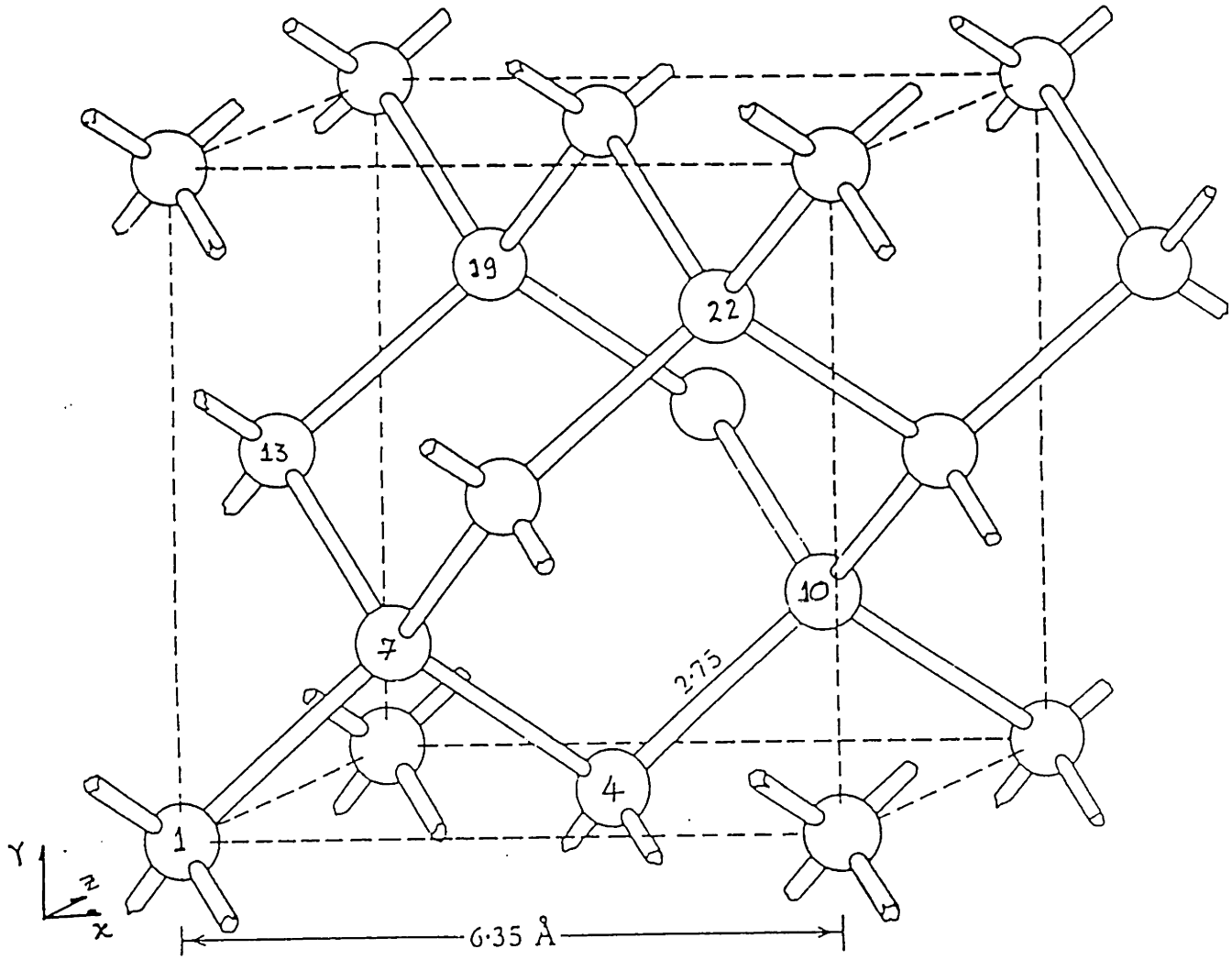

Figure 4-1: The diamond cubic structure of Ice-I

and j atoms and the ' on the third summation indicates a sum excluding real cell. This equation is a conditionally convergent series which converges very slowly for an infinite crystal.

This summation is replaced by two rapidly converging summations: one in real space and the other in reciprocal space with subtration of the self term due to charge themselves. Thus, the total electrostatic potential can be divided into three parts, namely real space V_1^c, self V_2^c and reciprocal space parts, V_3^c.

Hence,

$$V^c = V_1^c + V_2^c + V_3^c$$

(4.5)

The expressions for each contribution are given below (for derivation, see Born and Huang, 1964):

$$V_1^c = 0.5 \sum_{i=1}^{N} \sum_{j=1}^{N} \sum_{n}^{'} Z_i Z_j \frac{erfc(\alpha r_{i,jn})}{r_{i,jn}}$$

(4.6)

where $j \neq i$ when n = 0; α is an arbitrary convergence parameter and self term is expressed as:

V_2^c = - $\sum_{i=1}^{N} Z^2 \alpha \pi^{-1/2}$(4.7)

The reciprocal part of the electrostatic sum is expressed as:

$$V_3^c = \frac{1}{2\pi L} \sum_{i=1}^{N} \sum_{j=1}^{N} \sum_{|h|=0} Z_i Z_j exp \frac{-\pi^2 |\underline{h}|^2}{\alpha^2 L^2} h^{-2} cos \frac{2\pi . |\underline{h}| . \underline{r_{ij}}}{L}$$

where, erfc is the complimentary error function and $\underline{h}$ is the reciprocal lattice vector in units such that its components are integers; α is an arbitrary convergence parameter and the total electrostatic energy is independent of the the choice of α. Although, the accuracy of the V^c does not depend on α, but the rate of convergence of the summation V_1^c and V_3^c does depend on the choice of α.

$$\alpha = \sqrt{\frac{\pi}{L}} \tag{4.9}$$

where L is the side length of a cubic simulation cell.

There are several versions of the same Ewald summation formulations as applied to the MD simulation of the ionic solids (particularly in the case of alkali helides (e.g., see Sangster and Dixon, 1976 [109]).

4.2.2 Validation of the Ewald Sum Procedure

The reciprocal space summation can be made highly efficient to calculate, hence, an optimum choice of α will be one that leads to a large number of sums in reciprocal space and small number in the real space. A large value of α means a smaller number of lattice summation in real space and hence the cut-off distance for the electrostatic direct sum can be same as the cut-off for the short range interaction. However, it will also result in the larger number of the reciprocal lattice vectors to converge V_3^c summation. A parametric study with 216 NaCl particles put in FCC structure shows that for $\alpha = 2/\mathrm{L}$ the direct summation needs a cut of radius $r_c \leq 2.5\sigma$ with a reciprocal lattice extending upto to 35 lattice vectors $\underline{h}$; while a choice of $\alpha = 5/\mathrm{L}$ leads to $r_c \leq \mathrm{L}$ and a reciprocal space to extend upto $96\underline{h}$. Therefore, a value of α = 5.6, makes it possible to converge direct sum part of Ewald sumation to coincide with the short range cut-off distance L/2 with reciprocal space extending upto $100\underline{h}$. An appropriate choice α is the one that leads to simultaneous convergence of lattice sums in direct and reciprocal space with minimum computational expenditure.

The evaluation of the Madelung constant, which only depends on the geometry of the crystal lattice, serves as a useful benchmark to calibrate the validity of the the long range electrostatic interaction. The Madelung constant can be calculated by the Ewald summation method by the equations given above. The Madelung constant is a nondimensional parameter and hence does not depend on the electrostatic unit used in the calculations.

To validate the electrostatic calculation procedure used in the ice code, we have made two different evaluations. The first calculation is made on the NaCl, 216 particle FCC crystal. The calculations for NaCl crystal are done using BHM (Born-Higgins-Mayer) potential. The second comparison is made on the 192 atom diamond cubic SPC ice with the electrostatic Madelung constant obtained by Bjerrum (see Table 4.1. The results reported in Table 4.1 show excellent agreement with the data obtained by Evjan for NaCl and Bjerrum for the Ice lattice structure. This result indicates that the implementation of the Ewald sum procedure for the periodic boundary condition is correct.

Table 4.1: Calculation of Madelung Constant Using Ewald Summation

Type	M	r_{ij} $\dot{A}$	a $\dot{A}$	Method
NaCl	3.49513	2.82	5.63	Evjan [110]
NaCl	3.49512	2.82	5.63	Ewald [108]
Ice	14.90	2.76	6.35	Bjerrum [111]
Ice	14.902	2.78	6.35	Ewald

The Ewald method represents the electrostatic clculations implemented in the present code for a cubic ice.

4.3 Validation of SPC Model

The MD code developed originally by Anderson [39] has been vectorized and optimized for the simulation of water in liquid and solid state. To demonstrate the validity of MD code, an attempt is made to reproduce results obtained by Anderson (1986) [39] for bulk water. To keep the consistency of the comparison, identical runs have been made at 300K and 259K temperatures at 1 gm/cc density. For the simulation of water, the cell consists of 125 molecules in a cubic box of 15.521 $\dot{A}$ side length. The time step is 3.9188×10^{-4} ps. The simulation starts with the harmonic potential and the system is equilibrated for 10,000 time steps (3.9188 ps) while rescaling velocities at each time step. The anharmonic potential is implemented with velocity rescaling for 2000 time steps and then a run with property calculation is made for 10000 time steps. The total run amounts to 8.621 ps where properties are calculated for about 3.9183 ps. The details of the property calculations are given in appendix-A.

The energy conservation is a good test for the thermodynamic stability of the code. Pressure variation with time shows the consistency of the force calculations made by virial theorem. The mean squared displacement (MSD) represents dynamic property (relates the simulation data with the experimental observations of the self-diffusion coefficient). The radial distribution function , G(r), shows the density variation in the MD cell.

The evaluation of velocity autocorrelation function correlates the fluctuation in the

velocity of particles and provides information about the vibrational modes. Therefore, this can be used as an independent test for the validity of the SPC potential model for predicting vibrational spectrum of water and ice.

4.3.1 Thermodynamic Properties of Bulk Water

The results of the the simulation runs for the liquid water at 259 K and 300 K are reported in Table 4.2. The results also show comparison with the data obtained by Anderson (1987) [39]. The calculated potential energy is 20 percent lower than the experimental value of 41.5 KJ/mol. The potential energy variations with time typically shows that the energy is conserved up to the fourth decimal place. The values for the pressure are much higher in case of the SPC model, i.e., 11.3 Kbar as compared to 1 bar which corresponds to atmospheric pressure. The modified SPC model thus gives rather poor description of the thermodynamics properties of the water. The simulations made in the present study are done for shorter length of time as compared to the Anderson (1987). The agreement in bond length and self difffusion coefficient is within 2 %. The difference in case of bond angle (R_{OH}) and self diffusion (D) can be attributed to the slow convergence of the SPC model. In other words, SPC model takes longer simulation runs to converge (more than 50 ps).

The OH bond length and HOH bond angle do change with temperature and show a trend reaching towards the value for free molecule equilibrium value. The anharmonic intramolecular potential model in the present study shows better agreement than harmonic intramolecular potential with the referenced data in the case of HOH bond angle.

The self-diffusion coefficient reported in Table 4.2 is calculated from the slope of center-of-mass mean-squared displacement as function of time using the Einstein's relation. The calculated results at 300 K in the present study $2.66\text{x}10^{-5} cm^2/s$ with harmonic potential model and $2.69\text{x}10^{-5} cm^2/s$. These are in reasonable agreement with the value $2.53\text{x}10^{-5} cm^2/s$ obtained by Anderson [39]. However it is higher than the value $2.20\text{x}10^{-5} cm^2/s$ obtained by experiments by Krynicki et al. [112].

Table 4.2: Summary of Thermodynamic Properties of the Bulk Water

Time (ps)	T (K)	R_{OH} (A)	θ_{HOH} (deg)	-U (KJ/mol)	P (Kbar)	D $10^{-5}cm^2/s$
50	300	1.021	106.24	32.8	11.3	2.53[1]
8	300	1.0058	106.37	31.11	13.89	2.66[2a]
8	300	1.008	106.27	31.14	15.23	2.69[2b]
20	259	1.021	106.15	33.1	10.7	1.42[1]
4	259	1.0054	106.226	32.12	11.71	1.46[2a]
4	259	1.0072	106.181	32.16	14.42	1.43[2b]

Data obtained from present study is listed according to the intraatomic potential model used.[1]Anderson(1986) [2a]Harmonic potential; [2b]Anharmonic potential.

4.3.2 Structural Properties of Bulk Water

The atom-atom radial distribution functions $G_(r)_{\alpha\beta}$ for water at 259K and 300K are compared with the data obtained by the Anderson [39] and Toukan and Rahman [38] in Table 4.3 and Table 4.4. The $G(r)_{O-O}$ for oxygen-oxygen radial correlation show a prominent peak at 2.78 $\dot{A}$ at 300 K and at 2.76 At 259 K that corresponds to the nearest neighbor distance. The second neighbor peak is at 4.5 A. The plot of $G(r)_{O-O}$ as shown in Figure 4-2 shows that the structure beyond the first peak is quite diffuse.

The radial distribution for the oxygen-hydrogen pair shows the first prominent peak at 1.04 $\dot{A}$ corresponding to OH bond length. The second peak, representing the distance between an oxygen and hydrogen along a hydrogen bond, is observed at 1.75 $\dot{A}$. The third peak, representing the distance from an oxygen to a hydrogen of the neighboring water molecule, is at 3.24 $\dot{A}$.

The radial distribution for hydrogen-hydrogen pair atoms shows the first peak at 1.65 $\dot{A}$ which represents intramolecular separation of hydrogen atoms. The second and third peaks are at 2.35 $\dot{A}$ and 3.9 $\dot{A}$, representing the hydrogen atom positions in a water dimer.

The data obtained in the present study show excellent agreement with those of Anderson(1986) and Toukan and Rahman(1985), the difference between anharmonic and harmonic intramolecular models is not significant in calculation of structural properties.

The comparison of the intensities for $G(r)_{O-O}$, $G(r)_{O-H}$, $G(r)_{H-H}$ peaks at 300 K are reported in table 4.4. For both harmonic and anharmonic models the intensities show good agreement with the data of Toukan and Rahman (1985) [38]. However, the anharmonic model shows better agreement with the referenced data.

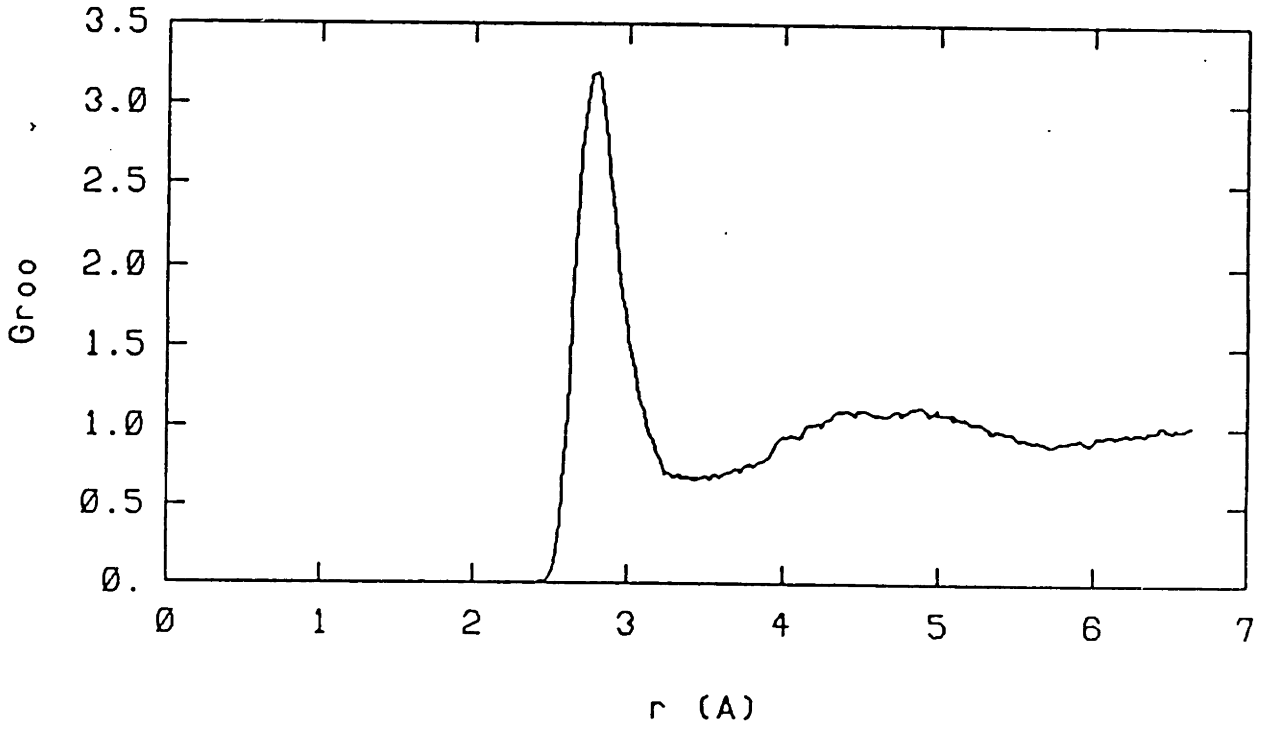

Figure 4-2: The O-O radial distribution fuction for water at 300K

4.3.3 Vibrational Properties of Water and Ice

The vibrational properties are important indicator of the atomic motions in the water. To obtain vibrational properties, the atom-atom velocity autocorrelation functions and their Fourier transforms, i.e., power spectra are used. Table 4.5 shows the comparison of the peak positions obtained from the vibrational spectrum of the hydrogen velocity autocorrelation function. This vibrational spectrum is known as the generalized vibrational frequency spectrum of hydrogen. The term "generalized" means that the density of states is weighted by the square of the vibrational amplitudes of the individual atoms [39]. The implicit assumption in this calculation is that all hydrogen atoms in the water network are dynamically equivalent, so that the calculation of velocity autocorrelation is averaged over all hydrogen atoms.

The hydrogen atom power spectrum has four prominent peaks, each representing a particular kind of vibrational motion that have been assigned by the classical lattice dynamics calculations and the Raman spectroscopic experiments [61, 45]. The first peak at about 50 cm^{-1} represents hindered translational motion. The second peak at 575 cm^{-1}, which is relatively broad, represents rotational (torsional) molecular vibrations. The third peak at 1850 is associated with the HOH bond bending vibrations and the fourth broad peak has two vibrational modes overlapping at 3450 cm^{-1} 3570 cm^{-1}, which represent symmetric and asymmetric O-H stretching vibrations.

The comparison of the power spectra obtained by the present study shows good agreement with the data of Anderson (1986) [39]. The difference in the frequency values for O-H stretching modes can be attributed to the lower temperature (252 K) and the shorter simulation run. The O-H stretching modes and H-O-H bending modes are compared with the experimental data obtained for the vapor phase using Raman spectroscopy [40].

Table 4.6 shows the calculation of the force constants K_r and K_{rr} made on the basis of a simple mechanistic model of vibrational modes derived by Landau and Lifshitz [113], a normal mode analysis for Raman frequencies, and by simulation of the SPC anharmonic potential model. The data are compared with the laser Raman experimental obtained by Sonwalkar et al.(1991) [60]. A glance through the

Table 4.3: Summary of G(r) Results (A) Peak Positions

Peak	I^{st} $\dot{A}$	II^{nd} $\dot{A}$	III^{rd} $\dot{A}$	T K
$G(r)_{O-O}$	2.8	4.55	-	300[3]
	2.78	4.54	-	300[2a]
	2.78	4.54	-	300[2b]
	2.76	4.5	-	259[1]
	2.76	4.58	-	259[2a]
	2.78	4.52	-	259[2b]
$G(r)_{O-H}$	1.035	1.75	3.25	300[3]
	1.040	1.76	3.24	300[2a]
	1.040	1.76	3.26	300[2b]
	1.02	1.75	3.24	259[1]
	1.04	1.78	3.32	259[2a]
	1.04	1.76	3.33	259[2b]
$G(r)_{H-H}$	1.66	2.28	3.8	300[3]
	1.64	2.40	3.90	300[2a]
	1.64	2.40		300[2b]
	1.65	2.35	3.90	259[1]
	1.64	2.40	3.92	259[2a]
	1.64	2.452	3.94	259[2b]

[1]Anderson [39], [3]Toukan and Rahman [38], Data obtained from present study are listed according to the intraatomic potential model used. [2a]Harmonic potential; [2b]Anharmonic potential.

Table 4.4: Summary of G(r) Results (B) Peak Intensity

Peak	I^{st} $\dot{A}$	II^{nd} $\dot{A}$	III^{rd} $\dot{A}$	T K
$G(r)_{O-O}$	2.80	1.05	-	300^{3}
	2.65	1.05	-	300^{2a}
	2.80	1.08	-	300^{2b}
$G(r)_{O-H}$	35	1.45	1.48	300^{3}
	37	1.42	1.45	300^{2a}
	35	1.45	1.48	300^{2b}
$G(r)_{H-H}$	3.3	1.25	1.18	300^{3}
	3.6	1.35	1.20	300^{2a}
	3.5	1.28	1.18	300^{2b}

[1]Anderson [39], [3]Toukan and Rahman [38], Data obtained from present study are listed according to the intraatomic potential model used. [2a]Harmonic potential; [2b]Anharmonic potential.

force constant values obtained for water and ice indicates that there is a need for modification in SPC model to take into account the phase transition from water to ice. The modifications in the force constant values will improve the temperature and pressure dependent shift in the vibrational frequency of the water and ice molecules.

Table 4.5: Comparison of Power Spectra: Peak Positions

Peak	I^{st}	II^{nd}	III^{rd} (all in cm^{-1})	IV^{th}	V^{th}	T K
	50	575	1850	3450	3570	259[1]
			1594	3676	3755	vapor[4]
	66	534	1804	3350	3480	252[2b]

Peak I: represents hindered translational vibrations; Peak II: represents hindered librational vibrations; Peak III: represents angle bending vibrations; Peak IV: represents O-H symmetric and asymmetric stretching vibrations. [1]Anderson (1987); [4] Eisenberg and Kauzmann (1969) (these are gas-phase Raman frequencies); [2b] Data obtained from present study using anharmonic potential.

4.3.4 Summary of Results on Validation of SPC Potential

The results reported on the thermodynamic, structural and dynamic properties of water show that the code developed for ice, based on the SPC potential model provides a reasonable description of water. The SPC model overpredicts the pressure and is not particularly good for the calculation of the potential energy. The structural and dynamical properties have good agreement with the experimental results and previous simulation results. These checks provide sufficient confidence in the use of SPC model for studying cubic ice.

4.4 Molecular Dynamics Simulation of Bulk Copper and (100) Surface

To understand the molecular dynamics involved with icing on structures and cables, we need to simulate solid surfaces that will serve as cold substrate for icing to occur. For this purpose, simulation of copper has been performed using MD technique.

As mentioned in the earlier sections, the most important issue in MD simulations is the choice of a potential function. We have seen in previous studies that most common potentials belong to a range of effective pair potentials that have demonstrated validity in the modeling of inert gases. For the simulation of metal surfaces, several

Table 4.6: Calculation of Force Constant

Sample	Temp K	ν_1 cm^{-1}	ν_3 cm^{-1}	K_r mdyn/A	K_{rr} mdyn/A	B_{HOH} deg
Normal[5]		3832	3942	8.454	-0.101	105
Model[6]		3832	3942	8.391	-0.046	109
Vapor[4]	373	3656	3755	8.454	-0.101	109
Model[6]		3656	3755	7.614	-0.053	109
Wate[7]	295	3184	3417	6.30	-0.020	105
Water[2b]	300	3350	3480	6.54	-0.023	106
Ice[7]	70	3090	3320	5.95	-0.020	109
Ice[2b]	70	3350	3472	6.51	-0.009	106

[2b] Data obtained from present study using anharmonic potential, [4] Eisenberg and Kauzmann (1969) (these are gas-phase Raman frequencies), [5]Results from normal mode analysis, [6]Nonlinear triatomic model, [7] Sonwalkar et al.(1991) [60] experimental Raman data.

empirical and semi-empirical potentials [114, 115, 116] have been designed by fitting experimental parameters. However, it is well known that the simulation of metals using empirically designed pair-potentials, automatically satisfy the Cauchy relation for the elastic constants ($C_{12} = C_{44}$) [116], which is not satisfied in the case of most real metals. The pairwise potentials also predict that the interplaner spacing will relax outward near the surface, which is in contradiction of experimental observation where interplaner spacing of most metal surfaces contract. This suggests that the effective pair potentials obtained by fitting study bulk properties may not be suitable for the study of materials at the surface or interface. Consequently, based on the density functional theory, Daw and Baskes [117, 42] have proposed an alternative approach, popularly known as 'embedded atom method' (EAM). This method has been proposed as a technique to construct many body potentials for metals. The application of this model to several metal and alloys has given result without having Cauchy's discrepancy and having contraction in the surface layers of metals [115, 118, 119].

In the EAM approach, the dominant energy of metals is considered as the amount of energy that is needed to embed an atom into local electron density that results from the remaining atoms [117]. This embedding energy with the short range core-core

repulsion energy determines the total energy of the system. The approach resulting from this formulation has the simplicity two-body interaction potentials to carry out complicated many body interactions, such as, metals with defects and amorphous structures. In our studies on copper as substrate material we have chosen an EAM potential developed by Foiles, Baskes and Daw [120]. For details of the EAM theory and application to metals we suggest reader to consult the paper by Foiles [119].

4.4.1 Embedded Atom Method Potential

In the case of EAM, the potential energy of the assembly of atoms is expressed in terms of embedding energy and pairwise core-core repulsion energy.

$$E_{tot} = \sum_i F_i(\rho_i) + \frac{1}{2}\sum_{j \neq i} \phi_{ij}(r_{ij}) \tag{4.10}$$

$$\rho_i = \sum_{j \neq i} f_j(r_{ij}) \tag{4.11}$$

where $F_i(\rho_i)$ represents the embedding energy for atom i, in the electron density of ρ_i; $f_j(r_{ij})$ is the electron density contribution to atom i from atom j at a distance r_{ij} apart, and the $\phi_{ij}(r_{ij})$ is the core-core repulsion energy between atoms i and j.

Foiles et al. (1986) [120] have obtained the embedding functions, pair repulsion and the atomic densities for the EAM potential model for several metals. They obtained atomic densities from the Hartree-Fock calculations, embedding function by empirically fitting the experimental parameters to get the effective charge that accurately describes the energetics of a metal. The empirical parameters used in the fitting are sublimation energy, lattice constant, elastic constants, vacancy formation energy, and internal energy of the FCC phase.

The pair repulsion term is obtained by assuming a simple parameterized form for effective charge Z(R) which is related with the core repulsion energy by the expression:

$$\phi_{ab}(R) = Z_a(R)Z_b(R)/R \tag{4.12}$$

Table 4.7: Thermodynamic properties of the Bulk EAM Copper

Time (ps)	T (K)	P (Kbar)	#D $\#/\dot{A}^3$	-U (KJ/mol)	-Etot (KJ/mol)	MSD $\dot{A}^2$
1	0	0.0366	4.000	3.435	3.435	0.00000
9	800	-1.3982	3.686	3.400	3.293	0.00620
9	1420[a]	-1.1742	3.566	3.297	3.1139	0.012609
	1420[b]	-1.12	3.566	-	2.99	-

[a]present work; [b]Foiles (1985) [119]

where,

$$Z(R) = Z_o(1 + \beta(R)^\nu)e^{-\alpha R} \tag{4.13}$$

For copper the empirical parameters are $Z_o = 11$, $\nu = 2$, $\beta = 0.1609$, $\alpha = 1.7227$[120].

4.5 Validation of Bulk Copper

The computer code for MD simulation of metals using EAM was developed by K. S. Cheung for the simulation of crack-tip propagation in the α-Iron [121]. We modified this code for copper, by providing requisite potential parameters and potential energy versus pair-distance look-up table. For the code validation, thermodynamic (potential energy, total energy), structural, (G(r)) and elastic properties have been calculated and compared with the reported results available in the literature on copper.

4.5.1 Thermodynamic Properties of Copper

Thermodynamic properties of copper has been calculated for a simulation cell of 500 copper atoms at three temperatures 0K, 800K and 1420K (see Table 4.7).

4.5.2 Calculation of Radial Distribution Function of EAM Copper

The radial distribution function, G(r), provides a good test for the stability of the crystalline structure at low temperature (0K, 800K), and collapse of the lattice at liquid metal temperature (1420K). For this purpose we have calculated G(r) at 0K, 800K and 1420K. The G(r) at 0K, provides a check on the initial loading of the FCC structure. The G(r) at 800K provides check of stability of the crystalline structure, and the G(r) at 1440K is above melting temperature and, hence, provides necessary check for the collapse of the FCC structure at liquid metal temperature. Table 4.8 reports a comparison of the peak positions for FCC copper at three temperatures.

Table 4.8: Summary of G(r) Results (A) Peak Positions for Bulk Copper

Peak	I^{st} $(\dot{A})$	II^{nd} $(\dot{A})$	III^{rd} $(\dot{A})$	IV^{rd} $(\dot{A})$	T (K)
	2.60	3.68	4.50	5.15	0.0^a
	2.55	3.61	4.42	5.14	0.0^b
	2.67	3.73	4.57	5.29	800.0^a
	2.55	3.61	4.42	5.14	800.0^b
	2.70	-	4.67	7.0	1420^a
	2.68	-	4.65	6.9	1420^b

[a]present work; [b]Foils(1985) [119]

4.5.3 Calculation of Elastic Properties of the EAM Copper

For a system with cubic symmetry such as FCC copper, only three independent elastic constants remain from the generalized stiffness matrix, i.e., c11, c12 and c44. Using these three stiffness constants the stress, σ and strain, ϵ, can be related by following equations.

$$\sigma_{11} = c_{11}\epsilon_{11} + c_{12}\epsilon_{22} + c_{12}\epsilon_{33} \tag{4.14}$$

$$\sigma_{22} = c_{12}\epsilon_{11} + c_{11}\epsilon_{22} + c_{12}\epsilon_{33} \tag{4.15}$$

$$\sigma_{33} = c_{12}\epsilon_{11} + c_{12}\epsilon_{22} + c_{11}\epsilon_{33} \tag{4.16}$$

$$\sigma_{12} = c_{44}\gamma_{12} \tag{4.17}$$

$$\sigma_{13} = c_{44}\gamma_{13} \tag{4.18}$$

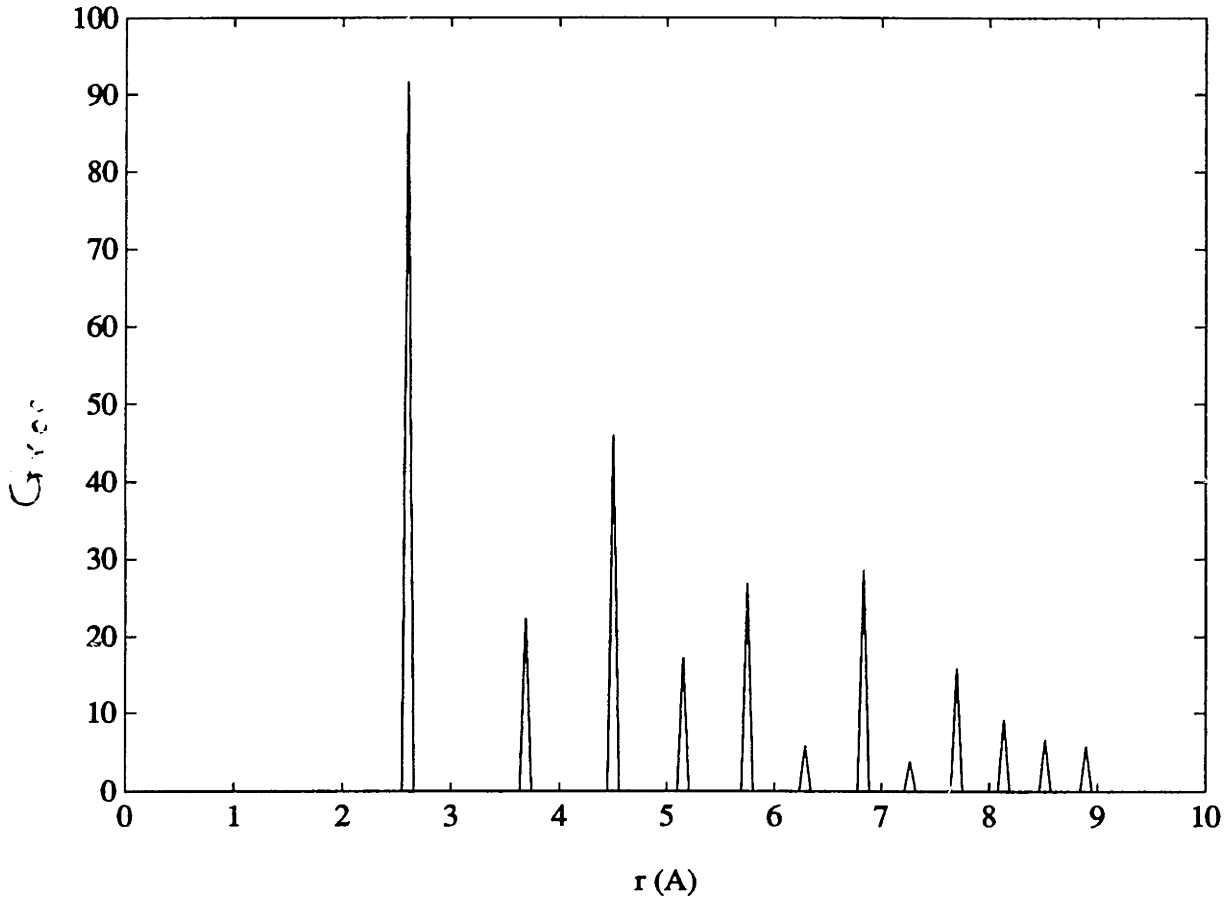

Figure 4-3: Radial distribution function of copper at 0K

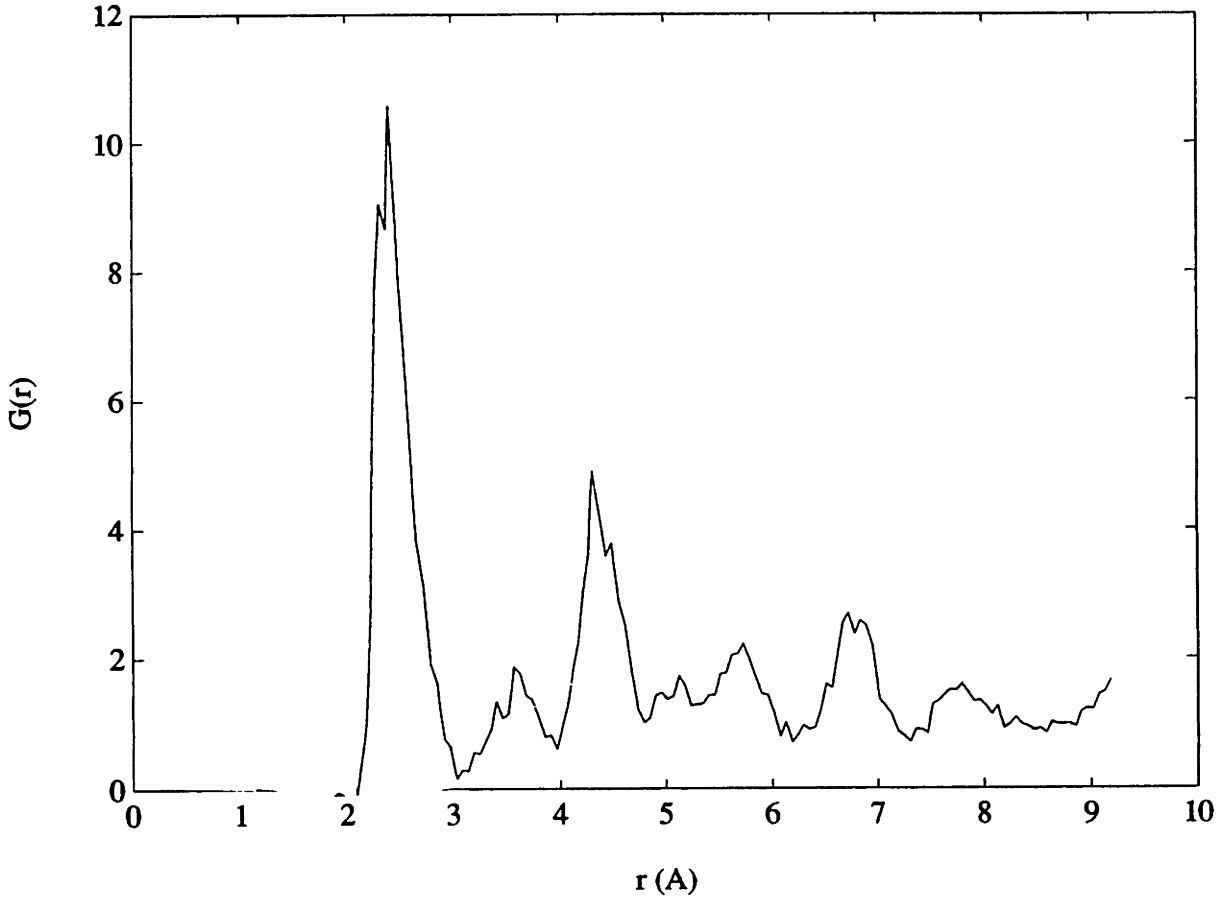

Figure 4-4: Radial distribution fuction of copper at 800K

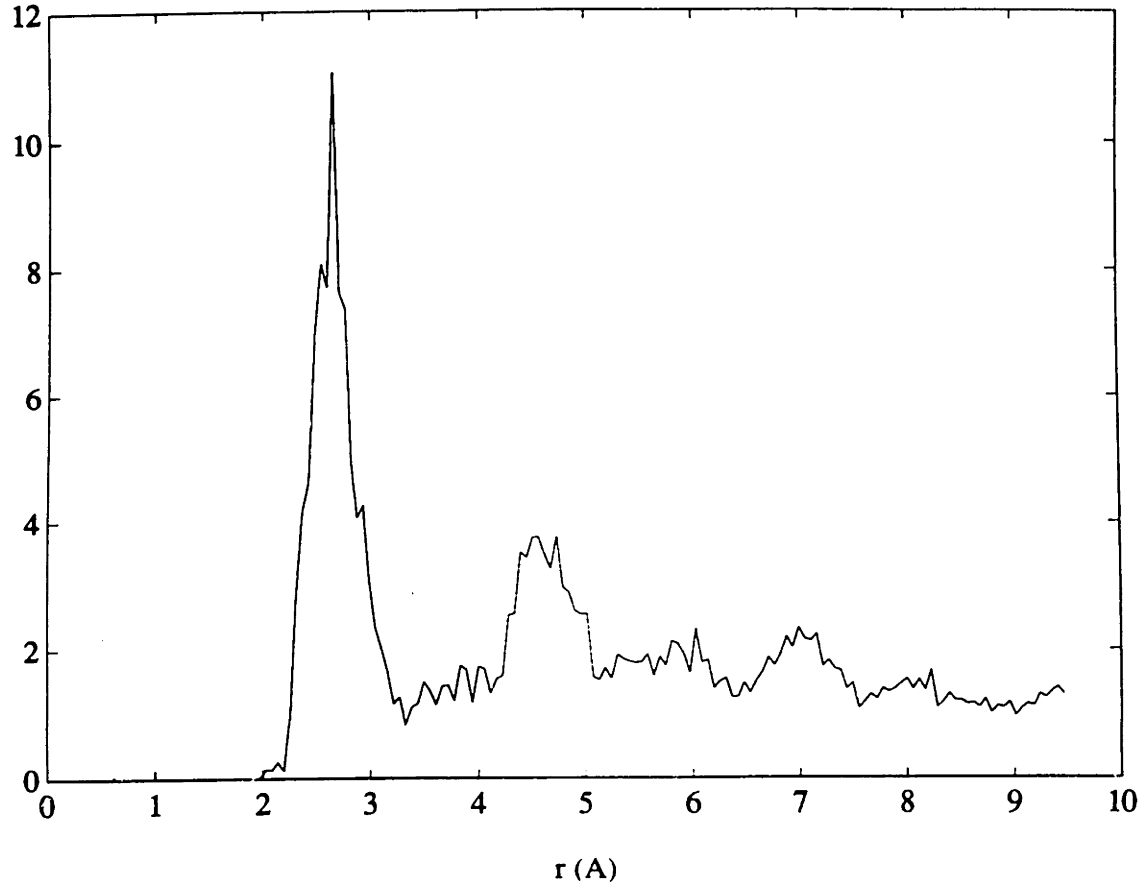

Figure 4-5: Radial distribution function of copper at 1420K

$$\sigma_{23} = c_{44}\gamma_{23} \tag{4.19}$$

The stress tensor of an atomistic system can be obtained from purely thermodynamic arguments by obtaining the derivative of the free energy with respect to strain. The Hamiltonian for the particles interacting via a pair potential function ϕ can be written as:

$$H = \sum_{i=1}^{N} \frac{P_i^2}{2m} + \sum_i \sum_{j>i} \phi(r_{(ij)}) \tag{4.20}$$

where P_i is the momentum for the particle i, m is mass, and r_{ij} is the distance between particles i and j. The stress tensor can be calculated using the expression:

$$\Omega\pi_{\alpha\beta} = \sum_{i=1}^{N} \frac{P_{i\alpha}P_{i\beta}}{m} - \sum_i \sum_{j>i} \frac{1}{r_{ij}} \frac{\partial\phi}{\partial r_{ij}} r_{ij\alpha} r_{ij\beta} \tag{4.21}$$

where Ω is the volume,$\pi_{\alpha\beta}$ is the $\alpha\beta$ commponent of the stress tensor, $P_{i\alpha}$ and $P_{i\beta}$ are the components of the momentum for the particle i, and $r_{ij\alpha}$ and $r_{ij\beta}$ are the $\alpha\beta$ components of the r_i - r_j, the relative position vector between particles i and j.

For the case of EAM potential, the embedding function term adds to the stress tensor expression:

$$\Omega\pi_{\alpha\beta} = \sum_{i=1}^{N} \frac{P_{i\alpha}P_{i\beta}}{m} - \sum_i \sum_{j>i} \frac{1}{r_{ij}} \frac{\partial\phi}{\partial r_{ij}} r_{ij\alpha} r_{ij\beta} - \sum_i \sum_{j>i} \frac{\partial F_i}{\partial \rho_i} \frac{\partial \rho_{ij}}{\partial r_{ij}} \frac{r_{ij\alpha} r_{ij\beta}}{r_{ij}} \tag{4.22}$$

The strain tensor ϵ of the given system can be computed from the change in the shape and size of the simulation cell described by a 3x3 matrix, h, with respect to size of a reference system h_o:

$$\epsilon = \frac{1}{2}(h^{t-1} h h_o^{-1} - 1) \tag{4.23}$$

where h is a 3x3 matrix whose column vectors define the three basis vectors that correspond to the shape and the size of the simulation cell, the superscript ^{t} and $^{-1}$ represent the transpose and the inverse of a matrix. For definition of h refer to [121].

4.5.4 The Stress-Strain Experiments on Bulk Copper

The first requirement to run a stress-strain experiment on a simulation cell with a fixed number of particle (T h N ensemble) is to find out a zero stress reference system dimensions h_o. This h_o matrix can be obtained by adjusting the cell density until the cell density with zero pressure is obtained.

The uniaxial strain experiments are run by fixing strain in any one of the principal directions, while keeping all other components zero. Thus in the elastic equations 4.10-4.15 only one term in the right side of equation remains, that explicitly defines the corresponding principal stress. By running the MD simulations for several fixed strains, a stress-strain curve can be obtained whose slope is the stiffness constant in the principal direction of the strain. Thus, by fixing ϵ_{11} over a range of strains we have obtain c_{11}.

The strain tensor can be fixed easily if the MD calculation is done in (T h N) ensemble by adjusting components in the cell's h matrix. The system studied here, consists 500 particles of FCC copper in 3-D periodic boundary conditions. The elastic constants are calculated at zero temperature. The run is made from 1 to 10 % strain and at each strain step the simulation is run for 200 time steps.

Table 4.9 reports the comparison of the elastic constants obtained by the stress-strain experiments with the data of Foiles et al. [120] and with the experimental of Simmons and Wang [122]. Figures 4-6,4-7 show the stress-strain plot for the experiment. The results show excellent agreement with the data of the Daw et al[8], which is not surprising since the EAM potential used in the present study uses the embedding function table that is supplied by Foiles [120].

Table 4.9: Comparison of Elastic Constant at 0K for an EAM-Copper

Reference	c_{11} erg/cm^3	c_{12} erg/cm^3	c_{44} erg/cm^3	E erg/cm^3	ν	K erg/cm^3
Foiles[b]	1.67	1.24	0.767	0.614	0.42	1.3865
Sonwalkar[a]	1.6716	1.241	0.768	0.614	0.42	1.3831
Experimet[c]	1.70	1.225	0.758	0.591	0.418	1.2148

[a]Present work,[b]Foiles et al.(1986) [120],[c]Simmons and Wang (1971) [122].

4.5.5 Simulation of [100] Free Surface of the EAM Copper

A FCC[100] surface of copper is modeled by removing the periodic boundary constraint in the z direction. The energy of a FCC[100] surface is calculated by obtaining difference between the potential energies of the FCC copper crystal, with and without, surface. The potential energy per particle for the periodic bulk copper at 0K is -3.539 eV, while for a solid with two free surfaces in z direction is -3.43494 eV. For a crystal with surface area of 326.70 $\dot{A}^2$ the surface energy predicted is 1279.59 ergs/cm2 which is in excellent agreement with the value of 1280 ergs/cm2 reported by Foiles et al.[120]. The metal surfaces show contraction in the inter layer distance between free surface and the adjacent layer in the case of bulk EAM copper. In our simulation, the contraction in the interlayer distance at 0K is 0.021 $\dot{A}$ to be compared with the value 0.026 $\dot{A}$ obtained by Foiles et al.[120] at zero temperature.

4.5.6 Summary of Results on Validation of EAM Copper Code

The thermodynamic, structural and elastic properties of the copper simulated using EAM potential show good agreement with existing simulation studies [119, 120] and experimental [122] data on copper in the solid and liquid phases. Therefore, the EAM potential formulation and the code developed for the simulation can be used for the ice-copper interface studies with some confidence.

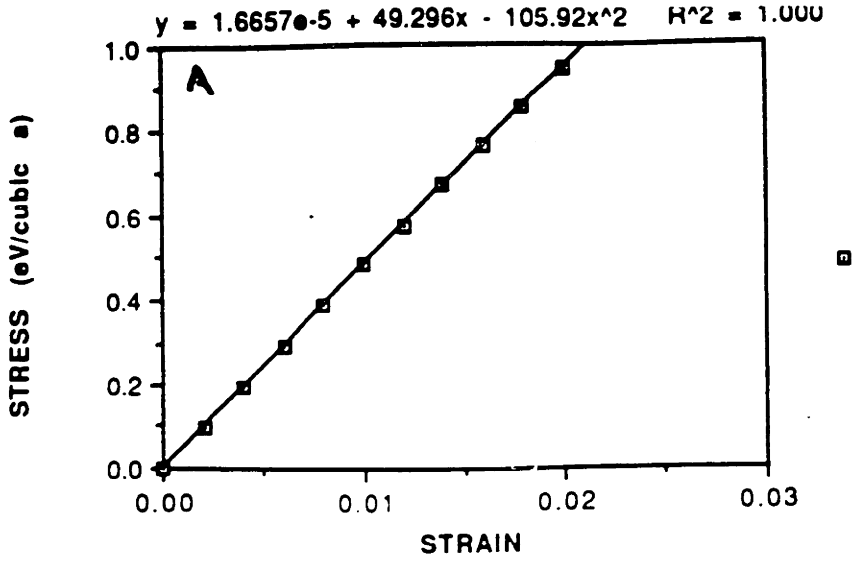

Figure 4-6: Stress-strain plot for c_{11} constant of copper at 0K

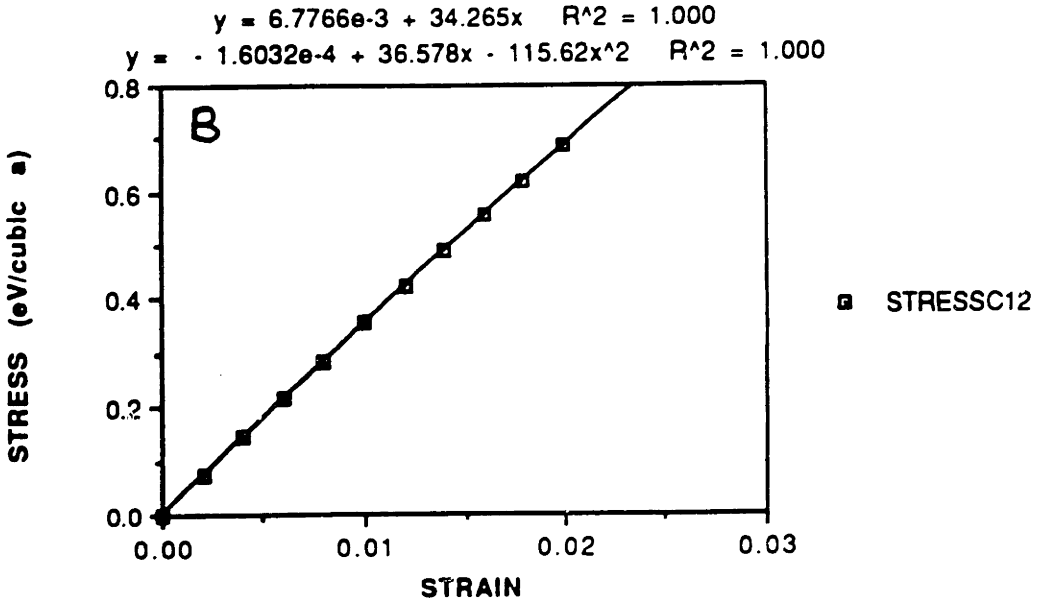

Figure 4-7: Stress-strain plot for c_{12} constant of copper 0K

Chapter 5

Molecular Dynamics Studies on Cubic Ice

This section reports the results of the molecular dynamics studies under different thermodynamic conditions. The main objective of these molecular dynamics studies is to gain the fundamental understanding on stability of the cubic crystal against the temperature induced disorder. The emphasis is on the dynamical properties that provide information about the vibrational modes. The temperature induced instability has been observed under both isochoric heating (where the volume of the simulation cell is maintained at a constant value) and under isobaric heating, (where the pressure in the simulation cell is maintained to a constant value by adjusting the volume). To resolve the structural sensitivity of the MD simulation of cubic ice, a comparison in the static and dynamic properties is made for simple and diamond cubic ice. Simulation of a film of diamond cubic ice is performed to assess the stability of an inhomogeneous system under long range electrostatic forces.

5.1 Melting of Simple Cubic Ice Under Isochoric Heating

The melting of ice under pressure is a phenomenon of considerable importance in understanding the phase behavior of ice. The well-known increase in the density of water during phase transition from solid to liquid phase suggests that external pressure on the ice should cause a decrease in the melting temperature [18, 17]. Therefore, the melting of ice under pressure has been used to test the validity of an effective pair potential designed to simulate ice. However, so far no study has been conducted for SPC potential model to verigy the pressure melting and to identify the mechanism that causes ice to melt under pressure.

In this regard, Weber and Stillinger for the ST2 [91] potential model and Tse and Klein for TIP4P [123] potential model, have demonstrated the validity of effective pair potentials in capturing the phase behavior of ice. However, studies so far have been focused on a few static properties, such as G(r), and have concerned themselves with the agreement of simulated results to the experimental phase-transition behavior. These studies did not provide plausible explanations about the mechanism responsible for pressure melting.

A study based on the systematic changes in the dynamic properties, such as molecular center of mass mean-squared displacement (MSD), hydrogen atom velocity-autocorrelation function (VACF), the vibrational spectra in translational vibration and O-H stretching region, with increase in temperature, can provide valuable information on the atomic motions responsible for the induction of instability in the presence of large internal pressure.

In the present study, a systematic heating of SPC ice subjected to tension, arranged in a cubic geometry, at a range of temperature covering between 70K and 350K has been performed. To assess the mechanism of phase transition static properties (e.g., potential energy and pressure, coordination number, density profile and diffraction pattern) and dynamic properties (e.g., mean-squared displacement of the molecular center-of-mass, velocity autocorrelation function for hydrogen atoms, and

generalized vibrational spectra) are obtained at each temperature step.

The results indicate that due to isochoric heating under excessive negative pressure (tension), the disorder in ice crystal starts much below melting temperature (230K). A structural transition is observed between 230K and 240K, which seems to be the underlying precursor of melting. The analysis of the property data suggests a partial breaking of the hydrogen bond in the crystal lattice prior to melting, as a mechanism of that leads to the melting transition. The partial breaking of the hydrogen bond couples the bending vibrations with the rotational vibrations, bringing the crystalline solid into a temporary instability that shakes the crystal into fragmented solid ready to melt with the addition of thermal energy.

5.1.1 Application of Computer Melting Experiment

Molecular dynamics (MD) simulation technique is now well established for the calculation of the dynamics properties of the molecular systems. In particular, extensive history exists on the determination of static and dynamic properties of water using potential models such as ST2 [86], TIPS [98, 124], MCY [95] and SPC [37] potential. However, not much data are reported on the calculation of pressure-induced disorder that causes the phase transition in ice.

The P-V-T diagram of ice-Ih [40] at 70K shows a molar volume of 19.291 cm^3/mol. The molar volume increases linearly to 19.655 cm^3/mol up to 273 K temperature (see Figure 5-2), reproduced from reference [18]). With the phase transition to liquid state, the volume drops to 18.0182 cm^3/mol. This behavior suggests that the bond length of water molecule increases with temperature up to 273 K. Above 273K, the breaking of hydrogen bonds leads to the collapse of the lattice structure and a drop in volume is observed. To observe phase transition in ice under negative pressure with a microcanonical ensemble (N,E,V), we choose to perform the isochoric heating of ice with a constant molar volume corresponding to that at 70K. The constant volume correponding to the density at 70K ice essentially provides negative pressure due to

expanded volume (reduced density 0.934). The melting under positive hydrostatic pressure has been studied using MD simulation [123], however, the isochoric heating offers opportunity to assess the effect of negative pressure on the process of thermal disorder.

Moreover, perfect crystal with 3-D periodic boundary conditions, having no external surface defect, is expected to melt at a temperature higher than the thermodynamic melting temperature [125]. Therefore, under 3-D periodic boundary conditions, if there is decrease in the melting temperature, caused by negetive pressure, it will be observed in computer melting experiment. This experiment is performed by systematic heating of cubic ice crystal in the range of 70K to 350K.

5.1.2 The Potential Model

The simple point charge (SPC) model of water proposed by Berendsen et. al [37] consists of tetrahedral geometry with equilibrium O-H bond length 1 $\dot{A}$, with point charges put on oxygen and hydrogen atoms of -0.82 and +0.41 e respectively. The intermolecular interactions between oxygen atoms are modeled as Lennard-Jones 6-12 potential functional, and the charge interaction by Coulomb potential. In the present simulation study, the flexible SPC model proposed by Toukan and Rahman is used.[9] In this version of the SPC model, the intramolecular interactions are modeled explicitly in terms of the O-H bond stretching and the H-O-H bond bending along with the cross terms for the stretch-stretch and stretch-bend contributions. An anharmonic Morse potential is used for O-H bond stretches and harmonic potentials are used for modeling other interactions. A few studies have been reported on the use of SPC potential in modeling ice [102, 92, 126, 94].

5.1.3 Property Calculations of Simple Cubic Ice

The molecular dynamics runs are made under microcanonical (NVE) conditions with 125 water molecules arranged into a simple cubic structure. The system is equilibrated at 70K for 10,000 time steps (4 ps) by constantly rescaling velocity to kee temperature constant. The properties are accumulated over the next 10,000 time steps. The temperature is raised by velocity rescaling. The procedure is repeated for each temperature. The volume of the simulation cell is kept constant at all temperatures corresponding to a density of 0.934 gm/cc.

The static and the dynamic properties are calculated using classical statistical mechanical ensemble averaging under the ergodic hypothesis[11].

Thermodynamic Properties

The potential energy depends on the configuration of the system under a given potential function.

$$U = \langle \sum_{i<J}^{N} U(r_{ij}) \rangle \tag{5.1}$$

where, r_{ij} is the radial distance between particle i and j and the brackets $\langle\rangle$ denote time average.

The pressure is calculated using virial theorem. The pressure of the molecular system with internal degree of freedom is defined as the ensemble average of the virial pressure [34].

$$P = \frac{1}{3\Omega} \langle \sum_{i=1}^{N} (m_i v_i . v_i + r_i . fi) \rangle \tag{5.2}$$

where, m_i, r_i, v_i, fi are mass, position, velocity, and force for i^{th} atom.

Structural Properties

To assess the particle distribution in the simulation cell we also plot the density profile. The density profile is obtained by dividing the simulation cell into 50 layers and counting the particles in each layer (or bin). The plot of density variation over 50 layers shows the distribution of particles in the simulation cell.

The diffraction pattern can be obtained by calculating static structure factor $S(\underline{k})$ for a prescribed range of wave vectors $\underline{k}$. The diffraction pattern corresponds to the direction dependent structural order for the given coordinates of atom positions.

Dynamic Properties

The mean-squared displacement of the particles from their initial positions, $\underline{r}(0)$, over time τ, provides a measure of the mobility in the MD system.

$$MSD = \langle |\underline{r}(\tau) - \underline{r}(0)|^2 \rangle \tag{5.3}$$

The dynamic properties of the atoms in the simulation cell can be calculated using time correlation functions. In this regard, the velocity-auto-correlation function (VACF) provides the necessary information about atomic motion (with respect to the time for a particular atom). The Fourier transform of the VACF function provides the power spectrum of the atoms which is essentially a generalized vibrational spectrum.

In general, if a(t) is a real dynamic property, i.e., velocity in the present case, then the time correlation function for velocity can be defined by an ensemble average:

$$c(t) = \langle a(0)a(t) \rangle \tag{5.4}$$

which leads to the limit of VACF:

$$= \lim_{\tau \to \infty} (1/\tau) \int_0^{\tau} dt' a(t')(at + t') \tag{5.5}$$

The power spectrum is calculated by the Fourier transform of the VACF:

$$\phi(\omega) = \int_0^\infty c(t)cos(\omega t)dt \tag{5.6}$$

5.1.4 Results of Isochoric Heating of Simple Cubic Ice

Results are reported as two series of runs. Series Run # 1 essentially covers the range between 70K and 350K in steps of 70K. The results of this series show a change in the slope of potential energy versus temperature plot in the region 210K-280K. Then, a second series is made, Series # 2, where the temperature range is from 210K to 270K is raised in steps of 10K. Simulation of each temperature step performed for 20,000 time steps.

Potential Energy

The results of the thermodynamic properties are listed in Table 5.1. The variation of the time-averaged potential energy with temperature shows that there is a change in the slope of potential energy verses temperature plot between 210K and 280K. A change in the slope of potential energy verses temperature signifies a change in the system configuration from either an ordered state to a disordered state or from one ordered structure to another ordered structure.

Table 5.2 lists the results of the thermodynamic properties obtained for the Series # 2. Figure 5-3 plots the variation of potential energy over the 210 to 270K temperature range in steps of 10K. The potential energy shows an increase up to 230K, but at 240K energy drops to a lower value. At subsequent values of temperatures the potential energy rises again. This behavior suggests that either the configuration of the system has changed into a new ordered state with lower potential energy, or it has become disordered with a lower potential energy than the ordered state at 230 K. In normal circumstances, such as phase transition of Lennard-Jones solids, the disordered state (liquid) has a higher PE than the ordered state. Nevertheless, the

drop in PE suggests a change in the configuration of the system. As reported in Table 5-3, we observe similar behavior in the behavior of pressure and total energy.

Pressure

The variation in pressure with temperature also shows a sudden change between 210K and 280K (see Table 5.1). The interpretation of the pressure change is not so simple in the present case. Hence, we refer to the experimental phase diagram of bulk ice at the solid-to-liquid phase transition as shown in Figure 5-2, and compare the pressure data reported in Table 5.2 (Figure 5-4). According to the phase diagram, the volume of the crystal linearly increases with the temperature up to the melting point. In the present MD experiment the constant volume (isochore) is chosen from the experimental value of cubic ice at 70K, which is 19.291 cm^3/mol. The SPC ice single crystal at that volume, however, is under considerable internal negative pressure (tension) caused by the stretching in the O-H atoms that are hydrogen bonded in the lattice structure. The decrease in interatomic distance, as the particles move faster with the temperature increase, causes a reduction in the existing tension and so a decrease in the pressure is observed (see Table 5.1).

The MD system is initially at a pressure of -17 Kbar at 70K, the increase in temperature causes internal pressure to increase at 230K to -9.943 Kbar, at 240K an increase in tension is observed. The sudden increase in tension may be attributed to the partial breakage of the hydrogen bonds. By virtue of this assumption the interatomic distance r_{ij} between atoms increases as the bonded O-H atoms become free (those having a large value of r_{ij}), causing a partial increase in the tensile forces. The average bond length 1.0071 $\dot{A}$ increases to 1.0074 $\dot{A}$ at 240K (see Table 5.9).

Coordination Number

The coordination number, defined as the number of atoms in the first coordination shell in the radial distribution function, is a quantity which is sensitive to the changes

in the local environment around an atom. The coordination number of simple-cubic system is four for the perfect lattice. At higher temperatures, when the radial distribution function no longer goes to zero between the first and second neighbor shells the average coordination number is no longer an integer. Figure 5-5 plots the variation of the coordination number with temperature for the range of 210K to 270K. We observe a sudden change in the coordination number from 5.50 at 230K to 6.40 at 240K. The higher coordination number indicates a change in the average nearest neighbor environment of an atom. Again, this change can either be due to a new ordered phase that cuses change in the short range order or a disordered state, which does not have short range ordered. However, comparison of time averaged G(r) at 230 and 240K shows no apparent change in the structure other than broadening of the peaks. This suggests an absence of a new-ordered phase (such as mertensitic phase transitions) that can cause a higher coordination number.

Density Profile and Diffraction Patterns

The comparison of the density profiles and the visual display of the time-averaged particle positions for 210K, 230K, 240K (Figures 5-65A-5C) shows that the density of the particles over the simulation cell is not uniform at 230K and 240K. At 230K we observe cavitation in the system. The system shows the existence of a local density variation. At 240K the system seems to collapse from cavity formation. This suggests that the network structure of the hydrogen-bonded solid may have experienced a mechanical instability because of the breaking of the hydrogen bonds that stabilize the crystalline system.

To investigate the system density at 230K and 240K we examined the time-averaged particle positions obtained over 20,000 time steps, collected at each 1,000 time steps. The particle positions are displayed on 3-D advanced visualization facility on the graphics workstation. Visualization of the crystal apparently shows a plane of splitting in the crystal and local congregation of the molecules, indicating a local density variation at 240K.

Figures 5-7(A-D) report the diffraction pattern of average oxygen positions at 0K, 210K, 230K, and 240K. We observe considerable disorder in the diffraction pattern present even at 210K. Comparison of the diffraction patterns, for the orientationally disordered oxygen at 230K and 240K seems to show larger circular clustering of the oxygen atoms at 230K and 240K as compared to long thin clusters found at 210K.

Mean-Squared Displacement and Diffusion

The MSD for all temperatures in Series #1 are shown in Figure 5-8(A-E) from 70K to 350K, respectively. The molecular center-of-mass MSD shows the mobility of one molecule with respect to its initial position. To evaluate the mobility of the molecular system, we calculate the average distance traveled by the center-of-mass during the run.

The criterion used to assess melting using MSD values is suggested by Lindemann's [127] which states that the amplitude of the molecular vibration greater than 13% of its lattice constant is an indication of the liquid state. In the present case, at 210K the oxygen atoms move by an average amplitude of 0.374 $\dot{A}$ from their lattice positions, which is 12% of the O-O distance.

The MSD does not show much difference in the characteristics of the displacement for all the temperatures in Series #2 in the range of 210K to 270K. This suggests that the transition at 230K and 240K may not be a phase transition but rather a structural disorder which is observed in the coordination number.

Vibrational Spectra

Table 5.3 lists the variation in peak positions of the averaged vibrational spectrum with increase in temperature. This vibrational spectrum is known as generalized vibrational frequency spectrum of hydrogen. The term "generalized" means

that the density of states is weighted by the square of vibrational amplitudes. The implicit assumption in this calculation is that all hydrogen atoms in the ice network are dynamically equivalent. Therefore the calculation of velocity-auto-correlation is averaged over all hydrogen atoms.

The hydrogen atom power spectrum has four prominent peaks, each representing a particular kind of vibrational motion as shown in Figures 5-9(A-D). The first peak at about 60 cm−1 represents translational motions. The second peak, relatively broad at 468 cm^{-1}, represents hindered molecular rotation (libration). The third peak at 1800 is associated with the H-O-H bond-bending vibrations, and the fourth broad peak has two vibrational modes overlapping at 3346 cm^{-1} and 3462 cm^{-1}, representing symmetric and asymmetric O-H stretching vibrations.

Figures 5-10(A-C) plot the O-H stretching frequency region ν_1 for 210K, 240K, and 280K. There is a clear upshift at 240K in both ν_1 and ν_3 frequencies. The increase in the O-H stretching region is attributed to the loss of coupling between the symmetric and asymmetric vibrations. The coupling is primarily caused by the hydrogen bond on O-H-O sites. The shifts at 240K are quite marked on both the frequencies. This may be explained by the partial breakage of the hydrogen bonds, which leads to the significantly disordered state. At 280K the spectrum covers a broader range of frequencies, which is indicative of a significant loss of hydrogen bond. The animation of the MD trjectories of the particles shows that the distorted molecules break away themselves from the partially connected hydrogen bond and become free to vibrate at their normal vibrational frequencies.

The variation in the vibrational peaks with temperature (Table 5.3, Figures 5-1110A-10C) shows that at temperatures 70K, 140K, and 210K a single sharp peak corresponding to the longitudinal acoustic (LA branch of the phonon dispersion) exists at about 60 cm^{-1}. At 240K the LA peak shifts to 82 cm^{-1} and an additional peak is observed at 128 cm^{-1}, which corresponds to the transvers acoustic branch (TA) of the phonon dispersion. The shifts in the LA and the origin of the TA peak can be attributed to the disorder in the lattice, which causes additional modes to become active. The disorder in the lattice is evident in the broadening of the lattice

modes.

At the same temperature, we also observe a shift of about 500 cm^{-1} in the rotational peak with a broadening and mixing of the librational modes with that of the bending vibrational mode (ν_2) at 1700 cm^{-1}. The mixing of the bending and rotational vibrations is possible if the hydrogen bonds which align the intermolecular rotational vibrations become distorted. In the presence of well-formed hydrogen bonds the Coulomb interaction between the neighboring molecules restricts the mixing of rotational modes with the bending. However, in the case of partial breakage of the hydrogen bond in a lattice, remaining bonds become distorted and are either stretched or compressed. As a result there is a mixing in the rotational and bending frequencies. This is evident from Table 5.9, where the bond angle of 106.134° at 230K changes to 106.057°. In this cavitated distorted solid, the intermolecular coupling becomes soft, causing an increase in the (ν_1) and (ν_3) modes.

At 280 K the translational peaks completely vanish, indicating a loss of order in the lattice. A significant number of the hydrogen bonds, responsible for the lattice structure, break and change the local environment. In this disordered environment the molecules are significantly free from the intermolecular coupling. Hence, in the liquid-like state, the mixing between the rotation and bending is lost and the two frequencies become separate. The softening of the intermolecular hydrogen bonding causes O-H stretching frequencies to cover a wider range of the frequencies.

Vibrational Force Field

A force field model based on the simple mechanistic model of the H_2O molecule, as derived by Landau and Lifshitz[17] is summarized in Table 5.9. The forces are calculated using the O-H stretching frequencies (ν_1, ν_3) and the angle-bending frequency (ν_2) obtained by the MD simulations (Table 5.3). This simplistic force field model shows that at 70K and 140K the symmetric stretching force constants are close to zero value. At 210K, the force K_{rr} shows tension on the hydrogen bond (negative sign), and the tension increases to a large negative value -0.1073 mdyn/a at 240K. At 280K,

a large positive value of 0.1522 mdyn/$\dot{A}$ represents compression in the force field. This behavior of the K_{rr} force may be explained as follows.

The stretch in the hydrogen bond initially causes tension. The tension becomes significantly larger when the hydrogen bonds partially break up, causing significant distortion in the local lattice structure. However, a significant breakage of the hydrogen bond at 280K causes the lattice structure to collapse and results in a compressive force field. This ccmpressive force field goes to tensile force at room temperature for water because of thermal agitation. The asymmetric force and the angle-bending force both show increase in compression at 240K that can be tentatively attributed to the coupling between the two harmonic O-H oscillators. The K_r and K_θ show a corresponding increase in the compression, which is caused by increase in the tension in the K_{rr} force. The force field argument also supports the notion of the partial breakage of the hydrogen bond at 240K.

5.1.5 Normal Mode Analysis of Vibrational Modes

The conventional normal mode analysis of the polyatomic molecules is described in the execellent book by Wilson et al. [128]. The normal mode analysis is carried out by solving the secular determinant that is formed by the F (force constant) and G (geometry) matrices. In the present case, however, we have carried out normal mode analysis on a nine atom system that represents a water molecule surrounded by the four nearest neighbors that constitute the tetrahedral coordination (See Figure 5-1). In this unconventional analysis, the particle positions of the distorted lattice are obtained by the simulations. These particle positions are obtained at the end of 20,000 time steps run made at 210K and 240K. The average particle positions are used as an input for evaluation of the G matrix. The solution of the secular determinant for results in eigenvalues representing the vibrational frequencies and eigenvectors representing the direction of the vibrations and their coupling according to the distribution of the displacement field. The nine atom system results in 27 normal frequencies and 27 eigenvectors for the 27 degrees of the freedom.

The calculations of the F and G matrices and the calculation of the secular equa-

tion [F - G λ] = 0 by the diagonalization of the determinant is obtained following the method described in Wilson et al. [128]. Table 5.5 shows the eigenvalue solution for the frequencies and their mode assignments, and the Table 5.6 eigen vector matrix for the corresponding displacements. A comparison between the Table 5.6 and Table 5.8 shows the distribution of the normalized displacement vectors for the Δr and the $\Delta\phi$ that are the stretching and bending, and rotational angles. At 210K the stretching and rotational angles keep the symmetry relation between the rotational and the bending vibrations. There are no couplings between the rotational displacements $\Delta\phi_1$,$\Delta\phi_2$ and $\Delta\phi_1$ and the bending displacements. However, at 240K the is clear coupling in the bending and rotational displacement. The stretching displacements show decrease in the displacement vector but do not show any coupling.

5.1.6 Conclusions from the Isochoric Heating of Simple Cubic Ice

The MD study shows that a partial disorder takes place between 230K and 240K. The uniform solid phase transforms to a fragmented solid (cavities) as a result of the partial breaking up of hydrogen bonds in the lattice network structure. The system undergoes this transition at 240K because of the temperature and tension in the isochoric system. The lower energy of the disordered state is due to an increase in the local density resulting from the cavitation.

The distortion of the hydrogen bonds below the melting temperature is initiated by the partial breakage of the hydrogen bond. This in turn causes a local density fluctuation leading to a higher coordination number at 240K. The higher coordination number solid gives rise to strong rotational modes mixed with the bending mode. The mixed rotational and bending modes with the increase in temperature shake the remaining lattice structure and finally break the solid into a disordered phase.

These results indicate that prior to melting there is a structural transition which involves a partial breakage of the hydrogen bond. This causes the initiation of microcavities in the lattice. Therefore, the perfect crystalline solid transforms into a high-defect-density crystalline solid before melting can occur.

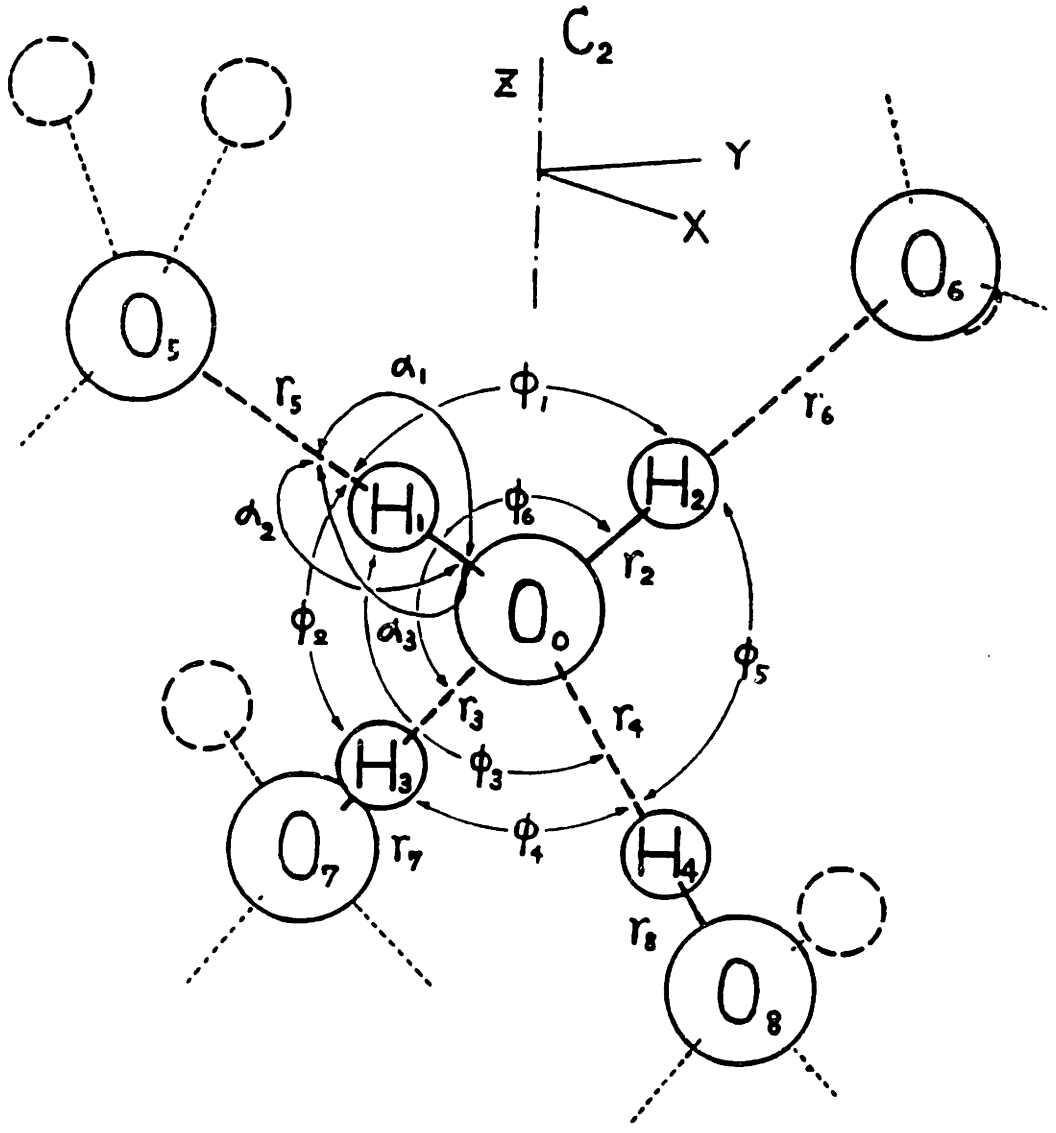

Figure 5-1: The nine atom system of the ice molecule for the normal mode analysis

Table 5.1: Summary of Thermodynamic Properties from 70K to 350K

Time (ps)	T (K)	U (KJ/mol)	P (Kbar)	-Etot (KJ/mol)	Uintra (KJ/mol)	Uinter (KJ/mol)	Coord# #
8	70	-31.89	-17.61	-31.59	0.33	-32.22	4.50
8	140	-31.59	-16.08	-31.01	0.41	-32.00	4.60
8	210	-31.09	-14.93	-30.20	0.58	-31.597	5.15
8	280	-30.79	-11.337	-29.62	0.63	- 31.37	6.78
8	350	-30.266	-9.192	-28.81	0.65	-30.92	7.04

where T is temperature, U configurational energy, P, pressure, Etot, total energy, Uintra, intramolecuar potential energy, Uinter, intermolecular potential energy, and Co-ord #, average coordination number of oxygen atoms.

Table 5.2: Summary of Thermodynamic Properties from 210K to 270K

Time (ps)	T (K)	U (KJ/mol)	P (Kbar)	-Etot (KJ/mol)	Uintra (KJ/mol)	Uinter (KJ/mol)	Coord # #
8	210	-31.097	-11.858	-30.240	0.468	-31.588	5.15
8	220	-31.028	-11.781	-30.145	0.448	-31.498	5.30
8	230	-30.898	- 9.943	-29.920	0.493	-31.449	5.50
8	240	-30.951	-10.456	-29.979	0.488	-31.489	6.40
8	250	-30.812	-11.092	-29.786	0.569	-31.359	6.38
8	260	-30.768	-10.333	-29.732	0.537	-31.278	6.62
8	270	-30.673	- 9.560	-29.584	0.497	-31.211	6.80

where T is temperature, U configurational energy, P, pressure, Etot, total energy, Uintra, intramolecuar potential energy, Uinter, intermolecular potential energy, and Co-ord #, average coordination number of oxygen atoms.

Table 5.3: Variation of Power Spectra with Temperature

T K	Peaks	I^{st}	II^{nd}	III^{rd} (all in cm^{-1})	IV^{th}	V^{th}
70		58	470,528	1804	3346	3462
140		52	480,570	1792	3334	3484
210		56	458,512	1794	3366	3472
240		82,128	962,1030	1180	3602	3670
280		-	432,520	1778	3422	3632

Peak I represents the hindered translational vibrations; Peak II represents the rotational vibrations; Peak III represents the angle-bending vibrations; Peak IV represents the O-H symmetric and asymmetric stretching vibrations.

Table 5.4: Temperature Variation of the Vibrational Force Field

T K	K_r md/a	K_{rr} md/a	K_θ md-a/rad
70	6.4701	-0.0034	0.5964
140	6.5525	0.0568	0.6098
210	6.5074	-0.0221	0.6039
240	7.2735	-0.1073	0.8276
280	7.1115	0.1522	0.7282

K_r represents the 0-H asymmetric stretching force constant; K_{rr} represents the O-H asymmetric stretching force constant; K_θ represents the H-O-H angle bending force constant.

Table 5.5: Normal Mode Vibrational Frequencies of Ice

T K	Peaks	I^{st}	II^{nd}	III^{rd} (all in cm^{-1})	IV^{th}	V^{th}
0		36	667	1733	3225	3317
210		84	781	1638	3153	3248
240		72,135	998	1323	3250	3348

Peak I represents the hindered translational vibrations; Peak II represents rotaitonal vibrations; Peak III represents the angle-bending vibrations; Peak IV the represents O-H symmetric and asymmetric stretching vibrations.

Table 5.6: Eigenvector Analysis of the Normal Modes 0K

Q	Peaks	I^{st}	II^{nd}	III^{rd}	IV^{th}	V^{th}
Δr_1		-0.01	00.0	-0.03	-0.72	00.73
Δr_2		00.01	00.0	-0.03	-0.72	-0.73
Δr_3		00.0	00.0	-0.04	00.02	00.0
Δr_4		00.0	00.0	-0.04	00.02	00.0
$\Delta \phi_1$		00.0	00.0	-1.46	00.14	00.0
$\Delta \phi_2$		00.05	-0.70	00.86	-0.05	-0.06
$\Delta \phi_3$		00.05	00.70	00.86	-0.05	-0.06
$\Delta \phi_4$		00.0	00.0	00.05	-0.05	00.0
$\Delta \phi_5$		-0.05	-0.70	00.86	-0.05	-0.06
$\Delta \phi_6$		-0.05	00.70	00.86	-0.05	-0.06
Δr_5		-0.25	00.0	00.06	00.69	-0.69
Δr_6		00.25	00.0	00.06	00.69	00.68
Δr_7		00.0	00.0	-0.00	00.02	00.0
Δr_8		00.0	00.0	-0.00	00.02	00.0

Table 5.7: Eigenvector Analysis of the Normal Modes 210K

Q	Peaks	I^{st}	II^{nd}	III^{rd}	IV^{th}	V^{th}
Δr_1		-0.03	00.0	-0.07	-0.82	00.83
Δr_2		00.03	00.0	-0.07	-0.82	-0.83
Δr_3		00.0	00.0	-0.08	00.02	00.0
Δr_4		00.0	00.0	-0.08	00.02	00.0
$\Delta \phi_1$		00.0	00.0	-1.46	00.14	00.0
$\Delta \phi_2$		00.08	-1.40	00.96	-0.07	-0.07
$\Delta \phi_3$		00.08	1.40	00.96	-0.07	-0.07
$\Delta \phi_4$		00.0	00.0	00.09	-0.05	00.0
$\Delta \phi_5$		-0.05	-1.40	00.86	-0.08	-0.08
$\Delta \phi_6$		-0.05	1.40	00.86	-0.08	-0.08
Δr_5		-0.50	00.0	00.07	00.89	-0.89
Δr_6		00.50	00.0	00.07	00.89	00.88
Δr_7		00.0	00.0	-0.00	00.02	00.0
Δr_8		00.0	00.0	-0.00	00.02	00.0

Table 5.8: Eigen vector Analysis of the Normal Modes 240K

Q	Peaks	I^{st}	II^{nd}	III^{rd}	IV^{th}	V^{th}
Δr_1		-0.04	00.03	-0.03	-0.55	00.55
Δr_2		00.04	00.03	-0.03	-0.55	-0.55
Δr_3		00.0	00.0	-0.04	00.04	00.02
Δr_4		00.0	00.0	-0.04	00.04	00.02
$\Delta \phi_1$		00.0	00.0	-1.46	00.18	00.07
$\Delta \phi_2$		00.09	-1.25	00.96	-0.15	-0.16
$\Delta \phi_3$		00.09	00.89	-1.25	-0.15	-0.16
$\Delta \phi_4$		1.08	00.81	00.05	-0.12	0.0
$\Delta \phi_5$		-0.09	-0.05	00.96	-0.12	-0.11
$\Delta \phi_6$		-0.05	00.09	00.76	-0.15	-0.15
Δr_5		-0.25	00.28	00.21	00.33	-0.33
Δr_6		00.25	-0.21	00.21	00.33	00.33
Δr_7		00.0	00.0	-0.00	00.12	00.0
Δr_8		00.0	00.0	-0.00	00.02	00.0

Table 5.9: Temperature Variation of Vibrational Force Field

T K	K_r md/a	K_{rr} md/a	K_θ md-a/rad
70	6.4701	-0.0034	0.5964
140	6.5525	00.0568	0.6098
210	6.5074	-0.0221	0.6039
240	7.2735	-0.1073	0.8276
280	7.1115	00.1522	0.7282

K_r represents the 0-H asymmetric stretching force constant; K_{rr} represents the O-H asymmetric stretching force constant hindered; K_θ represents the H-O-H angle bending force constant

Table 5.10: Temperature Variation of Bond Angle and Bond Length

Time (ps)	T (K)	r_{O-H} ($\dot{A}$)	θ_{HOH} (Degree)
8	210	1.0068	106.088
8	220	1.0072	106.123
8	230	1.0071	106.134
8	240	1.0074	106.057
8	250	1.0076	106.150
8	260	1.0073	106.203
8	270	1.0072	106.213

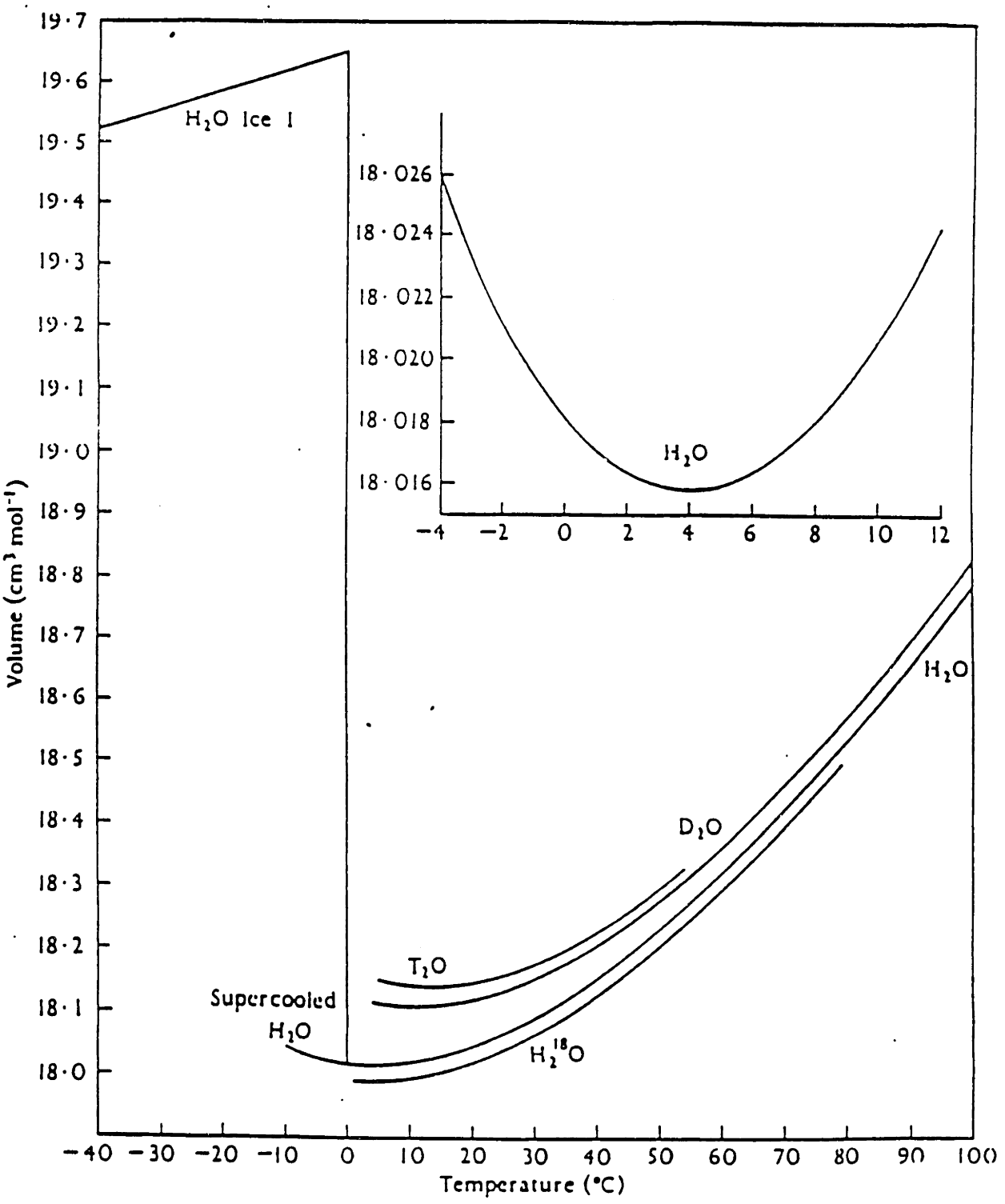

Figure 5-2: The molar volume of ice Ih at 1 bar pressure (Fletcher,1970).

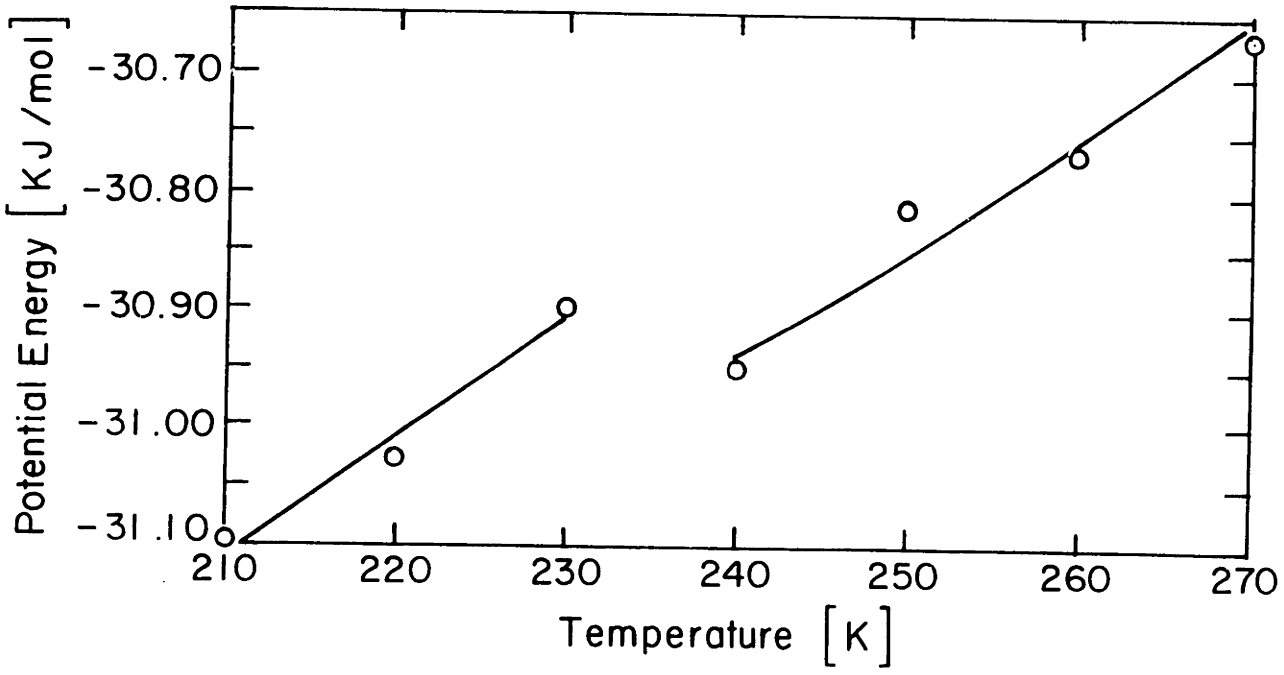

Figure 5-3: Temperature variation of potential energy.

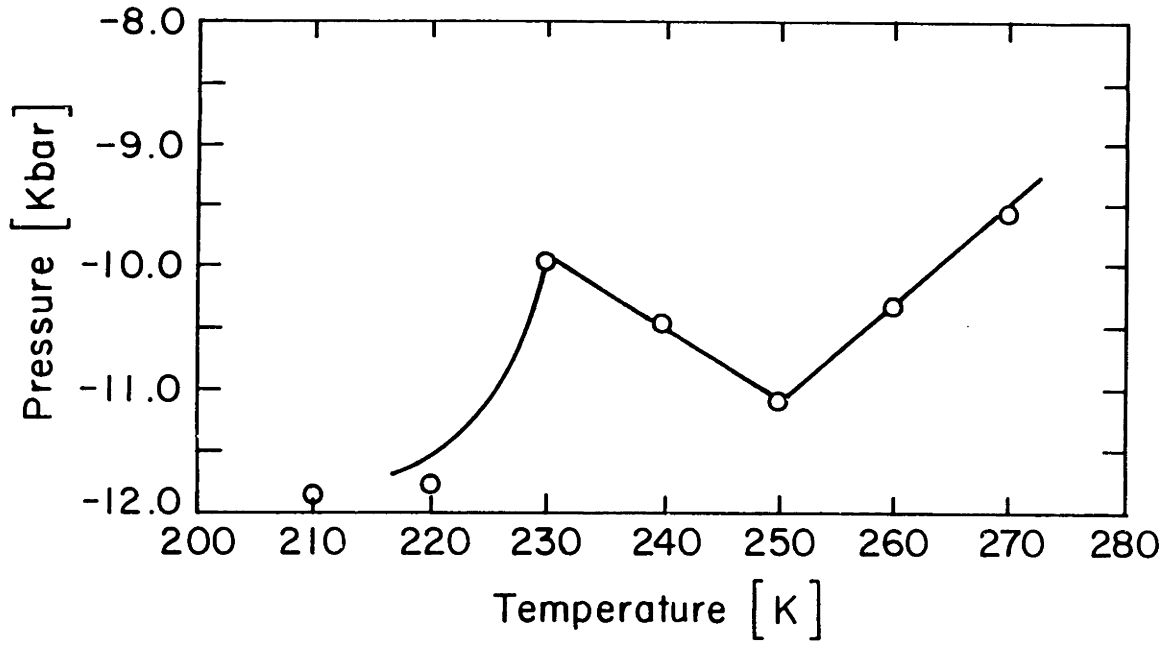

Figure 5-4: Temperature variation of pressure.

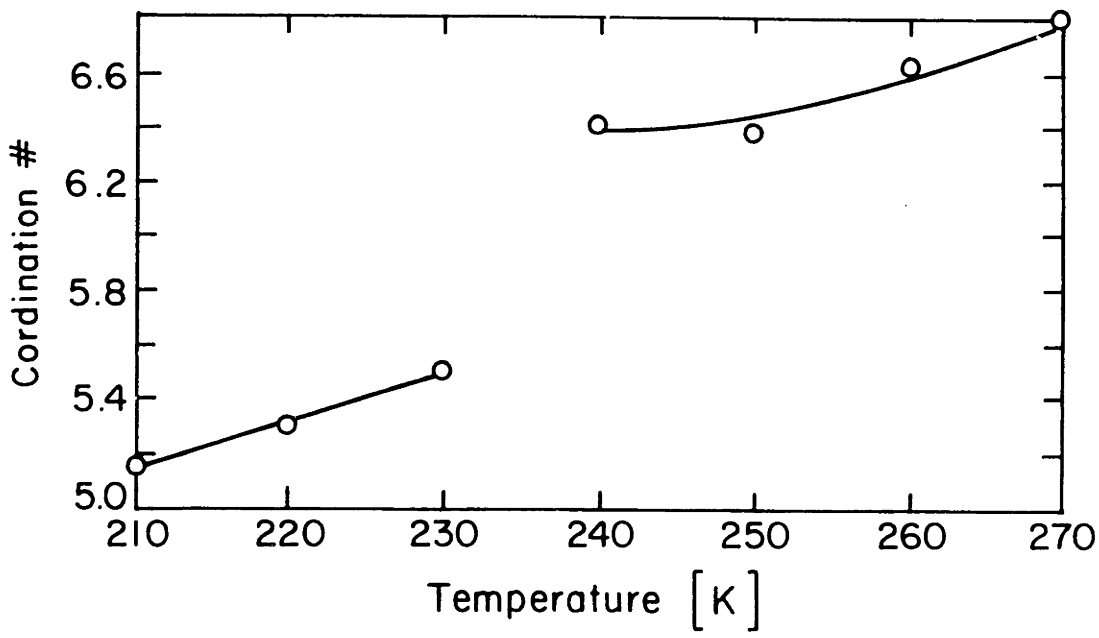

Figure 5-5: Variation in the coordination number with temperature.

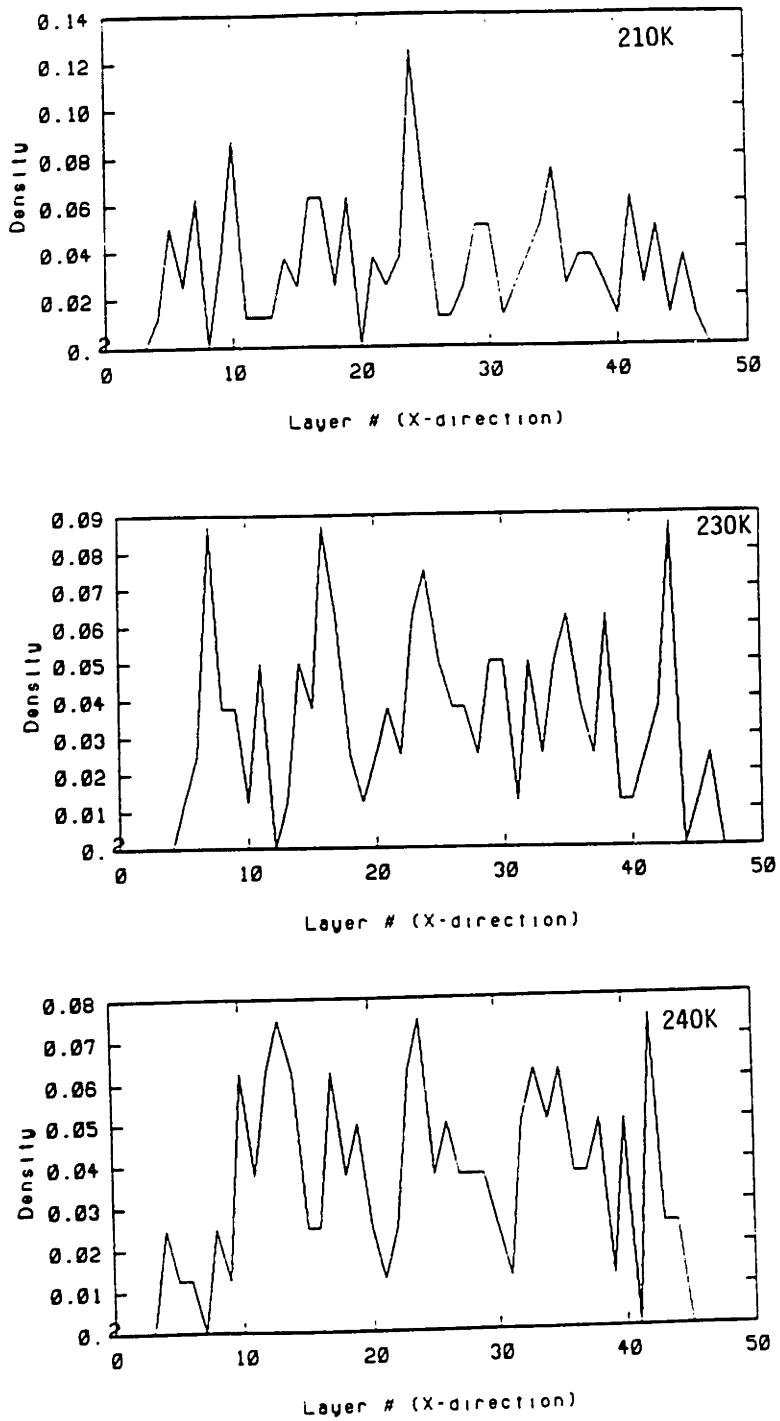

Figure 5-6: Variation in the density profile with temperature.

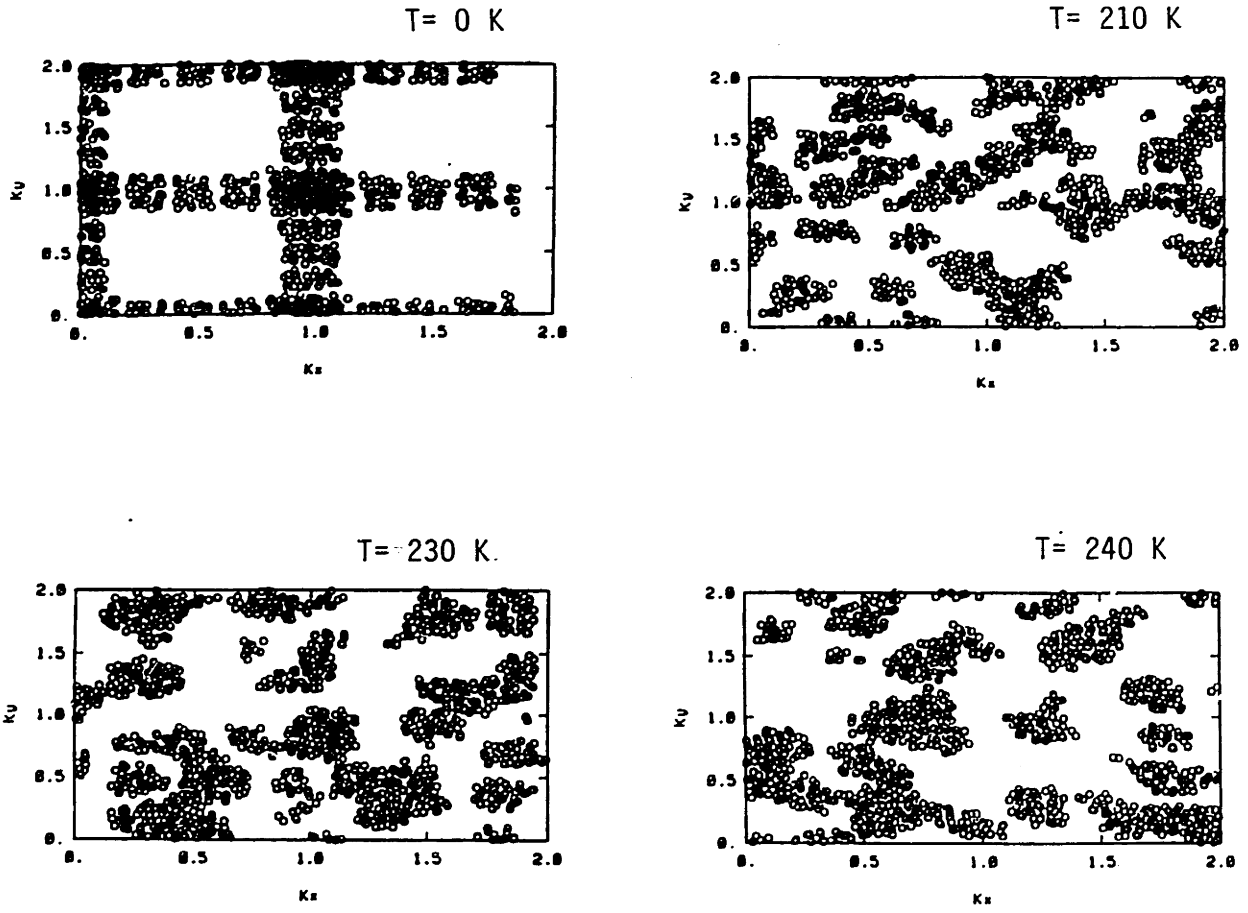

Figure 5-7: Temperature variations in the diffraction patterns.

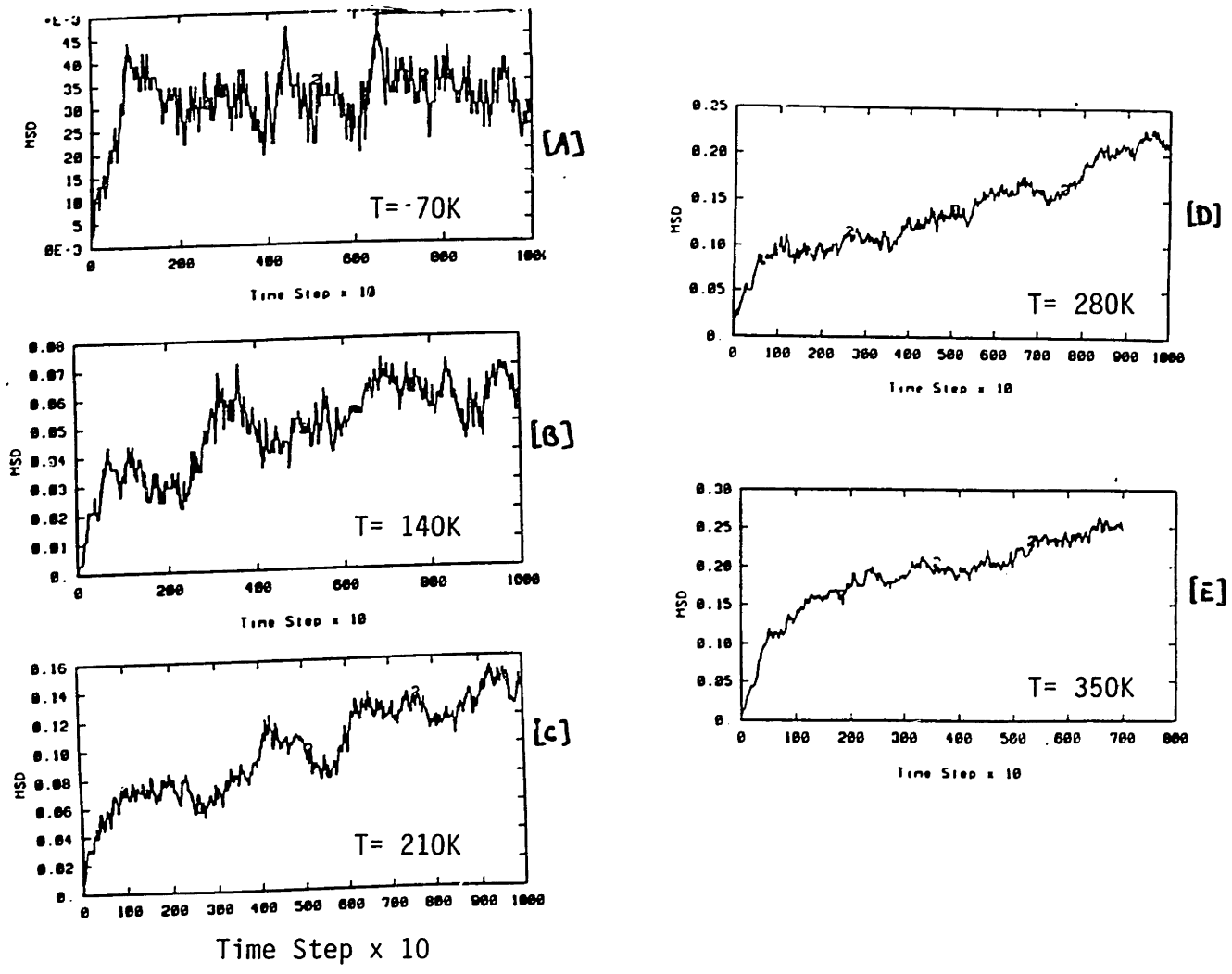

Figure 5-8: Time evolution of center-of-mass mean-squared displacements at different temperatures.

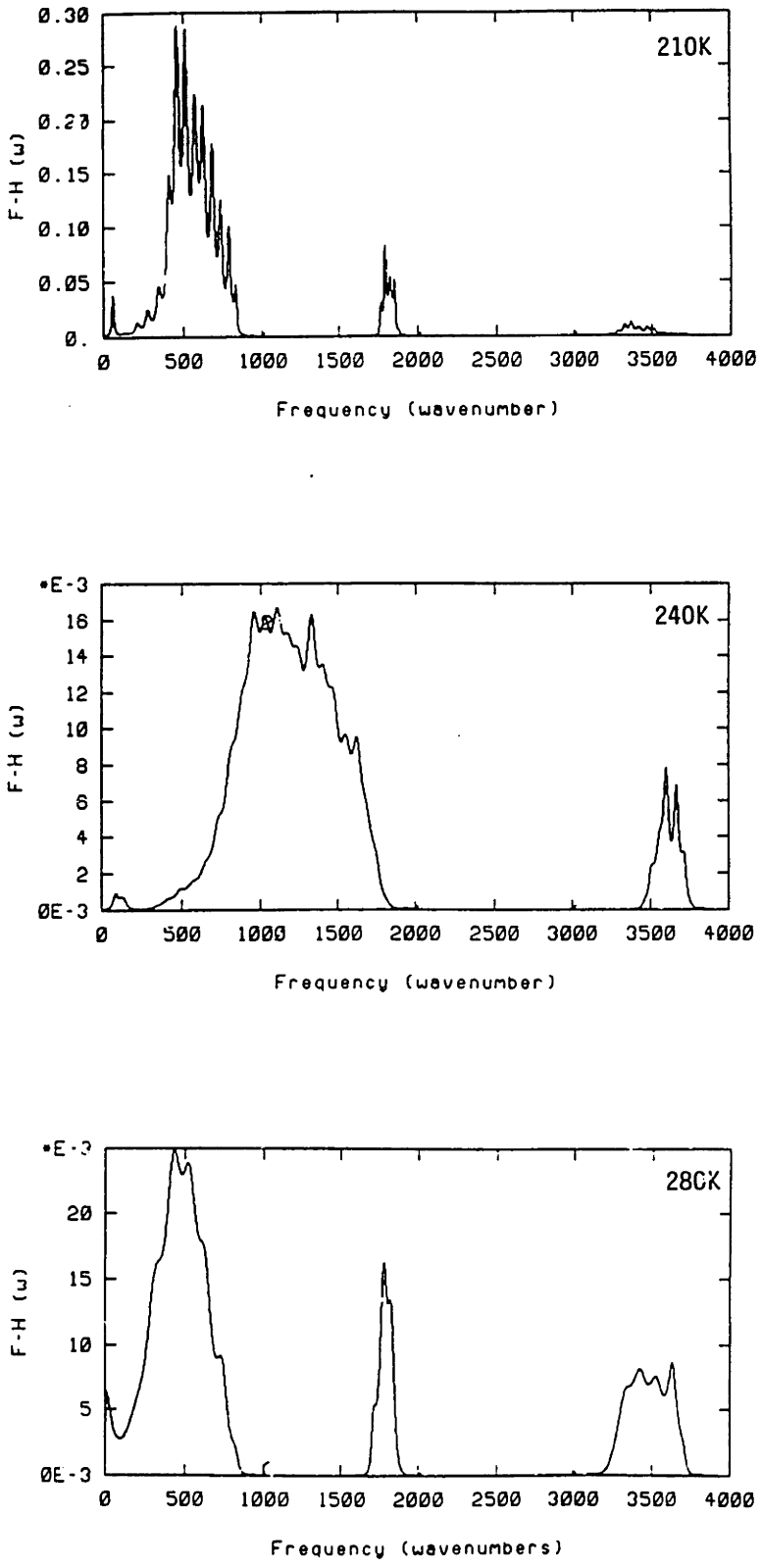

Figure 5-9: Temperature variations in power spectra of ice.

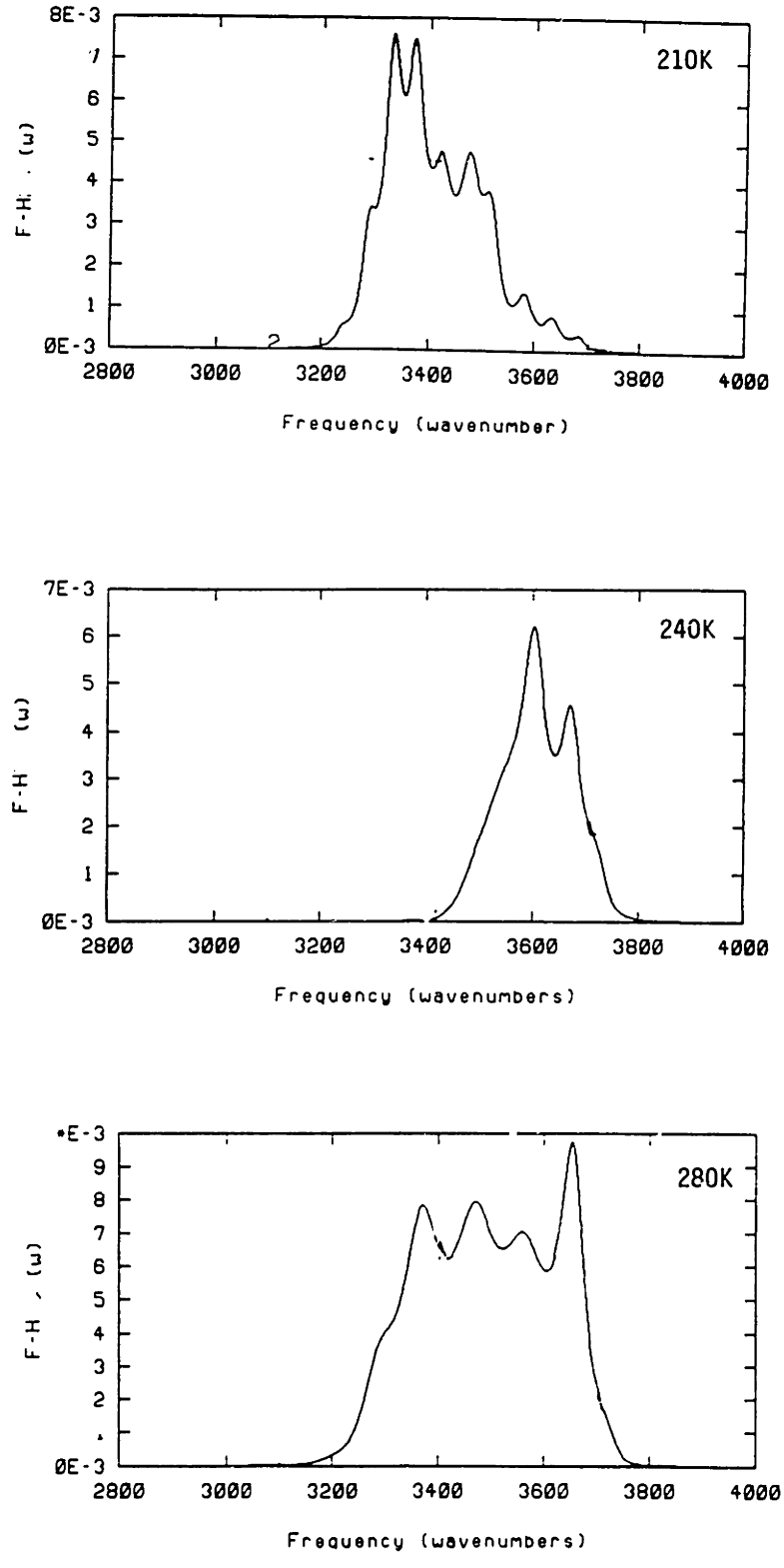

Figure 5-10: Temperature variations in power spectra of ice in the O-H stretching region.

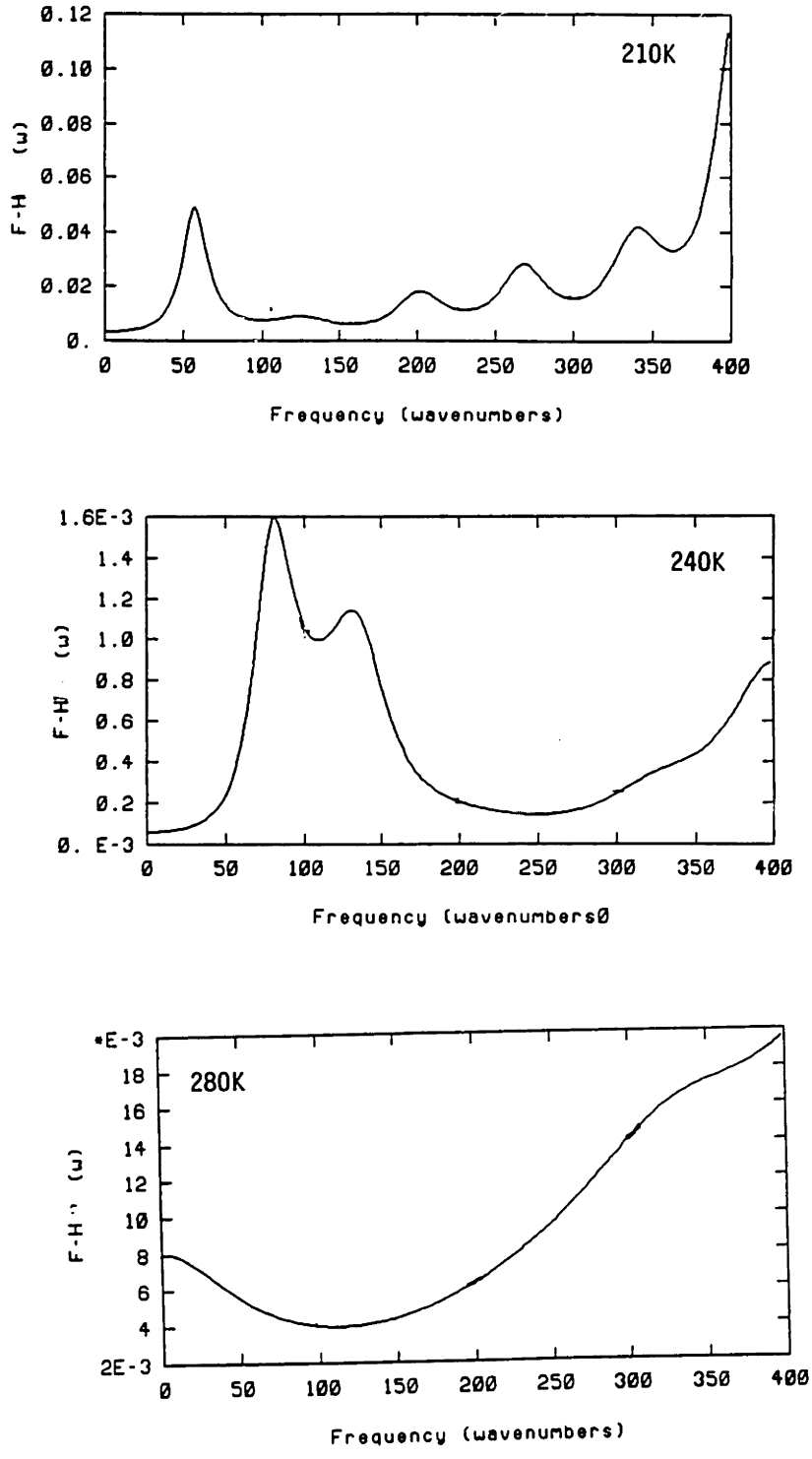

Figure 5-11: Temperature variations in power spectra of ice in the lattice vibrational region.

5.2.2 Results on the Isochoric Heating of Diamond Cubic Ice

A detailed discussion on the definition and significance of the properties listed here has been given in the preceding section. The present discussion concentrates on the observed features and comparison between simple cubic ice and diamond cubic ice.

Table 5.11 reports the thermodynamic data for the heating experiment conducted on the diamond cubic ice. As reported in the table, data are collected from a run made over eight pico-second (i.e., 20,000 timesteps).

The variation in the potential energy for the run made between 210-270 K are plotted in Figure 5-12. The temperature variation of potential energy shows a sudden change in the potential energy between 250K to 260K. A change in potential energy is indicative of the change in the configuration of an ice structure. The temperature variation of the co-ordination number is shown in Figure 5-13. This shows a sudden change from coordination number 5.4 to 6.35 at 250K and 260K temperatures. The co-ordination number represents the local environment of the nearest neighbors. The higher co-ordination number is observed in the case of either structural change or of disorder. The MSD variations are plotted in the Figure 5-14. The variations in the MSD show an increase in the mobility of the system with the increase in temperature, but they are not conclusive about the phase transition in the present case.

To assess the changes in the local density caused by heating, variation in the density profile with temperature are plotted in Figure 5-15. For comparison, the average oxygen positions (in x-direction) at the end of the corresponding temperature runs are plotted along with the density profile. The density profile variations between 250K and 260K show that there is a splitting in the crystal structure similar to that observed in the case of simple cubic ice at 230K temperature. The particle positions show a local density variation resulting from the splitting.

The variations in the bond length and bond angle with the increase in temperature are reported in Table 5.12. The observed data indicate the bond length at 260K is larger than that at 250K. However, the bond angle does not show any change between

250K and 260K.

5.2.3 Comparison of Simple and Diamond Cubic Ice

The radial distribution functions of the simple cubic ice and diamond cubic ice are quite different at zero temperature. However, at higher temperature (220K) they show the same features and are almost identical. The comparison based on the data on potential energy and coordination change shows that both simple and diamond cubic ice structures undergoes similar disordering process below the thermodynamic melting temperature. However, the temperatures at which this change is observed is 240K in simple cubic ice and at 260K in the diamond cubic ice. It is important to note that in the case of simple cubic ice, the heating is carried out under tension, while in the case of diamond cubic ice, heating is done under low (1.6 bars approx.) pressure. The data suggest that tension in the case of the simple cubic ice lowers the temperature of the partial breakage of the hydrogen bonds prior to melting. This phenomenon initiates the disintegration in the crystalline SPC ice.

5.2.4 Conclusions from the Isobaric Heating of Diamond Cubic Ice

Detailed calculations are performed in the case of simple cubic ice to gain an understanding of the structural disorder responsible for the potential energy and coordination changes below the melting transitions. The similarity in the molecular dynamic behavior of the SPC ice in case of diamond cubic ice allows us to state that within the limits of the simulation parameters, the properties of cubic ice are relatively insensitive to the type of cubic structure. Therefore, the results obtained from the simple cubic ice calculations are applicable to a cubic ice system irrespective of its structure.

Table 5.11: Summary of Thermodynamic Properties of Diamond Cubic Ice

Time (ps)	T (K)	U (KJ/mol)	P (Kbar)	-Etot (KJ/mol)	Uintra (KJ/mol)	Uinter (KJ/mol)	Co-ord # #
8	210	-36.120	1.584	-35.272	0.507	-36.641	5.00
8	220	-36.058	1.484	-35.730	0.502	-36.542	5.15
8	230	-36.400	1.616	-35.164	0.496	-36.542	5.20
8	240	-35.923	1.644	-34.989	0.489	-36.399	5.40
8	250	-35.793	1.524	-34.778	0.569	-36.340	5.40
8	260	-35.555	1.505	-34.401	0.550	-36.089	6.35
8	270	-35.519	1.527	-34.379	0.650	-36.251	6.40

where T is temperature, U configurational energy, P, pressure, Etot, total energy, Uintra, intramolecuar potential energy, Uinter, intermolecular potential energy, and Co-ord #, average coordination number of oxygen atoms.

Table 5.12: Variation of Bond Angle and Bond Length with Temperature for Diamond Cubic Ice

Time (ps)	T (K)	r_{O-H} ($\dot{A}$)	θ_{HOH} (Degree)
8	210	1.0089	106.437
8	220	1.0078	106.521
8	230	1.0078	106.442
8	240	1.0077	106.486
8	250	1.0076	106.592
8	260	1.0076	106.612
8	270	1.0076	106.619

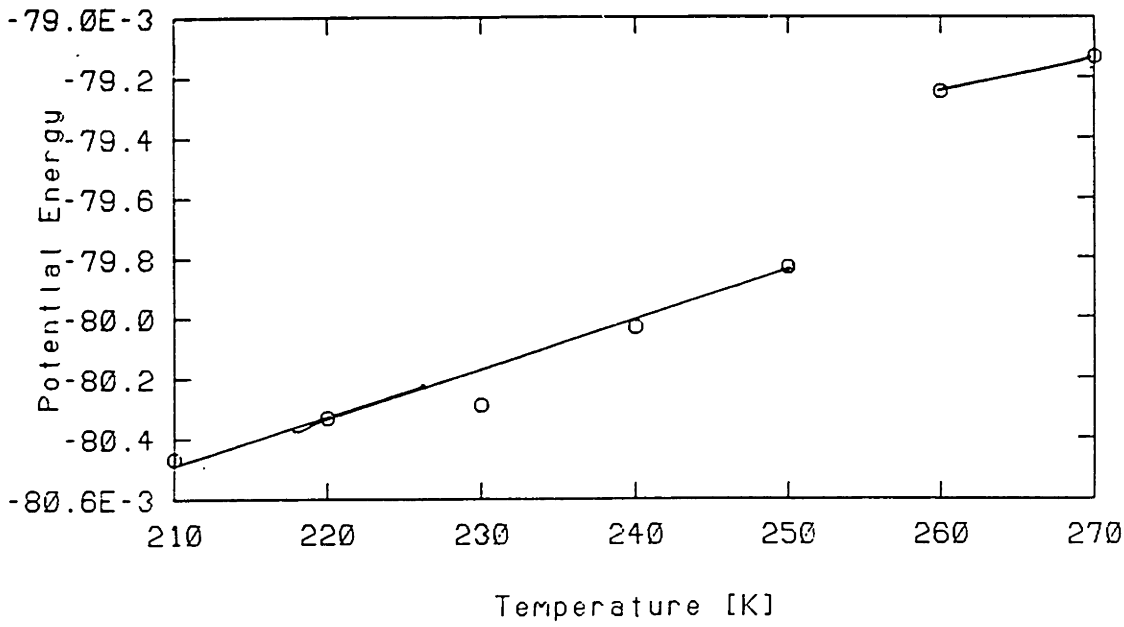

Figure 5-12: Temperature variation of potential energy.

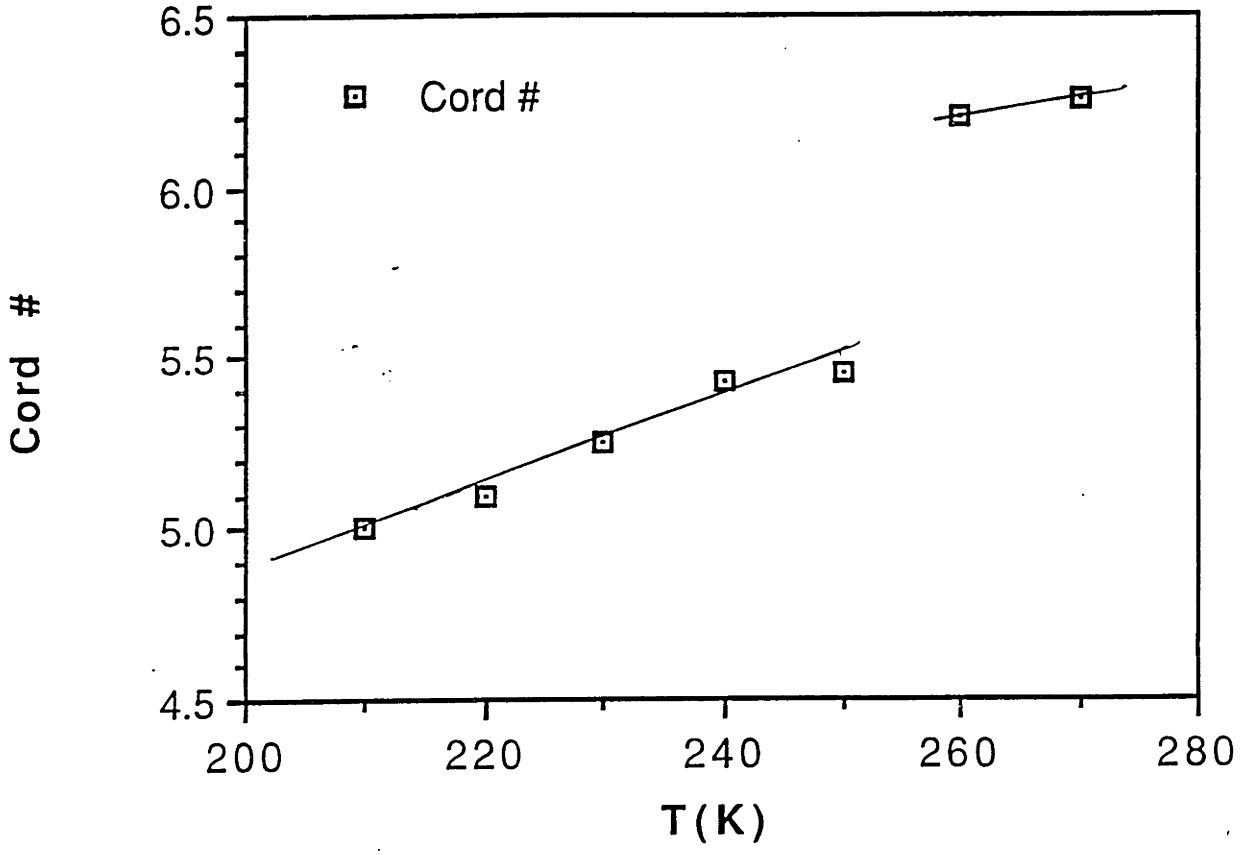

Figure 5-13: Variation in the coordination number with temperature.

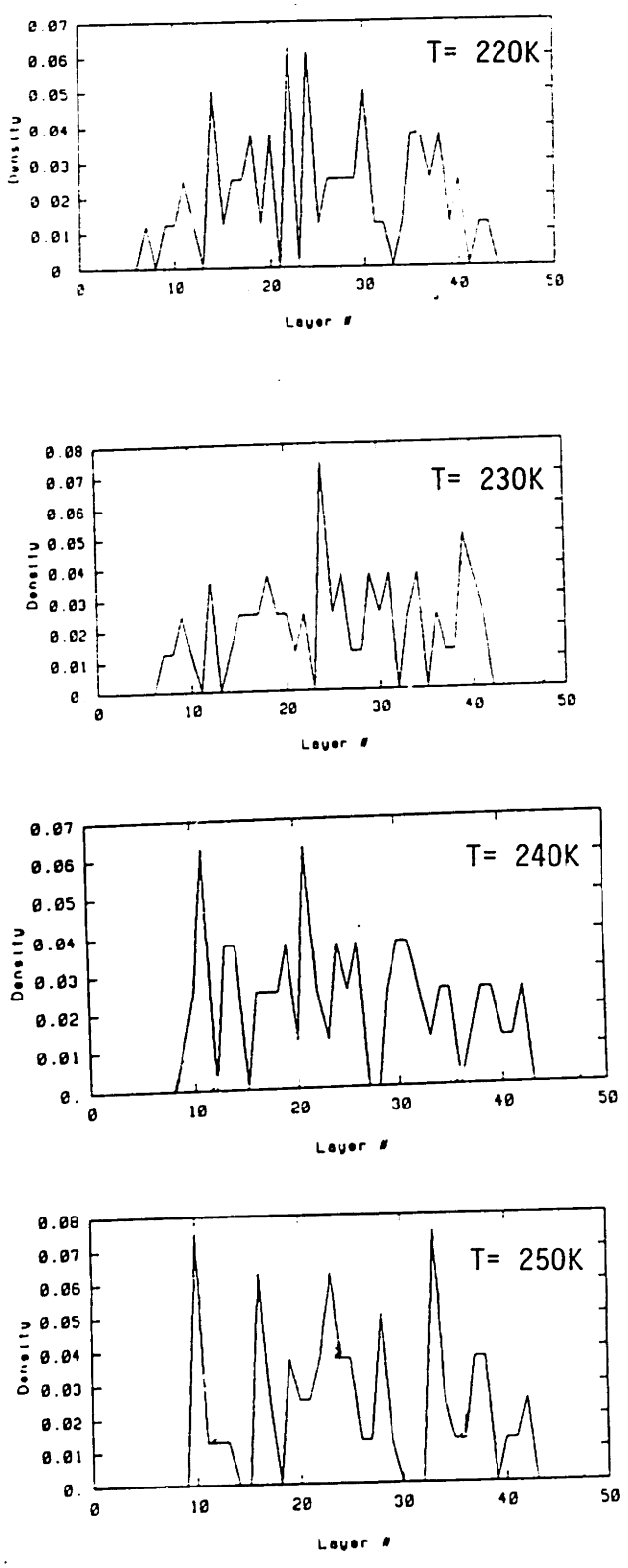

Figure 5-14: Variation in the density profile with temperature.

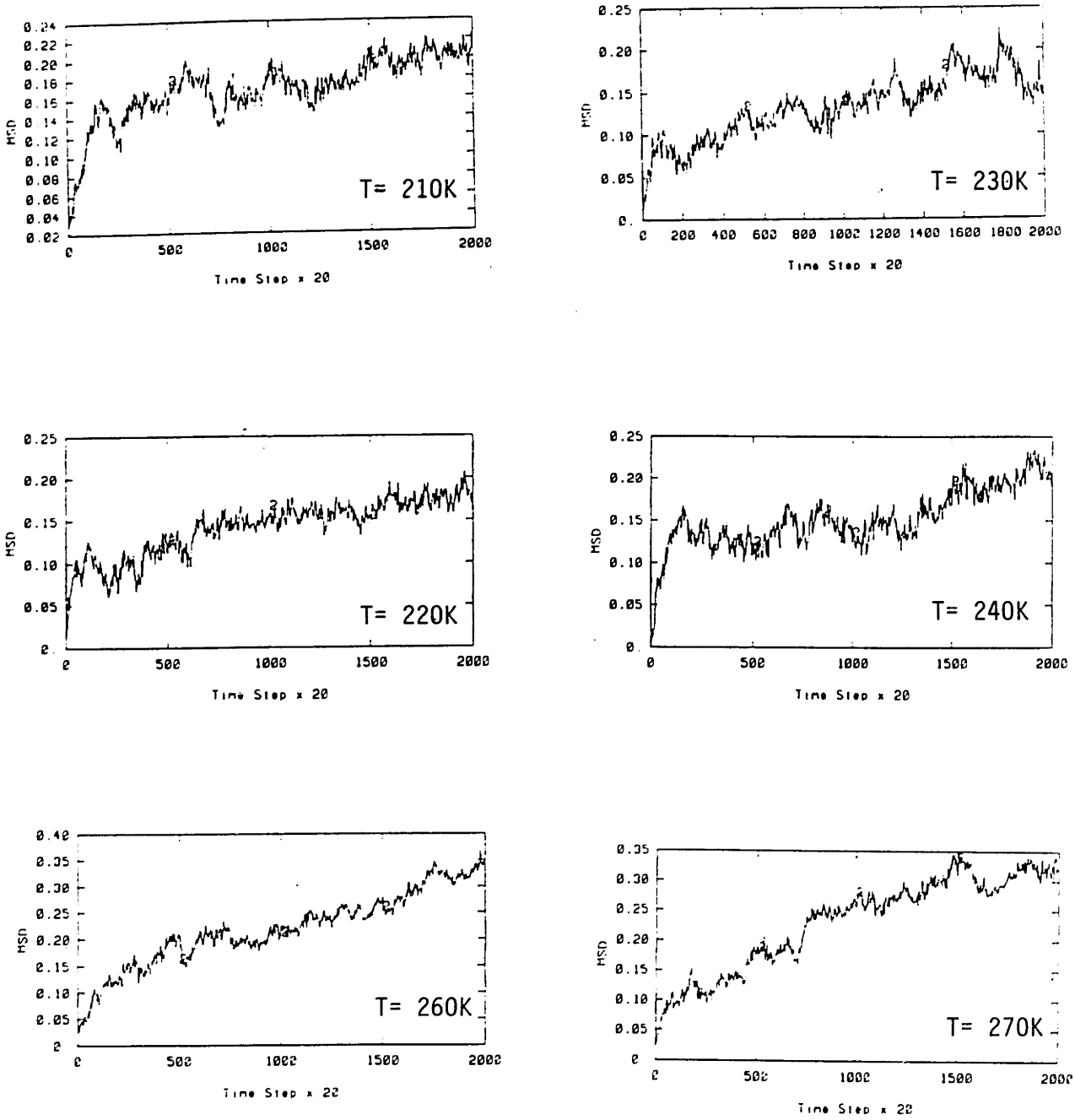

Figure 5-15: Time evolution of center-of-mass mean-squared displacements at different temperatures.

5.2.5 Simulation of Diamond Cubic Film

In order to assess the stability of the diamond cubic ice crystal under electrostatic forces, we have performed simulation of FCC(100) film with 64 water molecules arranged in a film configuration. The film is created by removing the periodic boundary constraints in the z direction. The film with eight layers of the eight water molecule is studied for its thermodynamic, structural and dynamic properties. The potential model used is SPC, and the 192 atoms in the diamond cubic structure provides film thickness of 12.703 Angstroms.

The film is simulated at zero temperature for 20,000 time steps with the last 10,000 time steps used in the property calculations. The simulation results discussed in the following section reveal that the electrostatic interaction makes the film to warp and twist and thus becomes deformed over time.

5.2.6 Results from the Simulation of an Ice Film

The a few thermodynamic, structural and dynamic properties are plotted with time(see Figure 5-16 to 5-20). The comparison is made with the starting configuration obtained at the end of the run. Figure 5-16 shows the variation of the potential energy over 10000 time steps. The variation indicates that the potential energy is conserved with some flectuation at the end. The variation in the mean squared displacement with temperature at 0K with time is shown in Figure 5-17. The variation shows that the film remains as solid throughout the run, though there is an increase in the mobility of the particles with time.

The variation in the radial distribution obtained at the end of 10000 time steps as compared to the initial radial distribution function at 0 time step, shows (Figure 5-18) the particle positions change even at zero temperature. This spread in the peaks of the G(r) can be attributed to the local change in the positions of the particles during the run.

The variations in the film density profile of the film at the end of run, as compared to the density profile at the beginning of the run, shows that in the x and y directions

there is clear evidence of motion of particles that breaks the symmetry of the crystal. The variation in the x and y directions indicates that there is a considerable twisting of the ice layers in the X-Y plane even at zero temperature.

The diffraction pattern of the diamond cubic at the begining of the run is compared with the diffraction pattern at the end of the run (see Figure 5-19). The diffraction patterns clearly show that even at zero temperature there is considerable displacement in the particle positions over 20,000 time steps as compared to the initial diamond cubic structure.

5.2.7 Conclusions from Simulation of Diamond Cubic Film

The displacements in the atomic positions in case of the diamond cubic film are quite significant. The layers that make interface with the vacuum seems to warp and twist owing to the instability caused by the internal forces. The forces that may cause this instability are primarily electrostatic in nature. The electrostatic forces are obtained by summing the Coulomb force in the real and the reciprocal space (Ewald sum procedure). In the present study, the Ewald sum in the reciprocal space for the z direction is suppressed to account for the discontinuity created by the vacuum [34]. This is the only difference in the force calculation as compared to the 3-D periodic diamond cubic ice. The 3-D periodic diamond cubic ice is quite stable in density profile up to 70K. Therefore, we conclude that the suppression of the Ewald summation in the z direction is causing the electrostatic instability that results in the considerable twisting and turning of the film of ice at zero temperature.

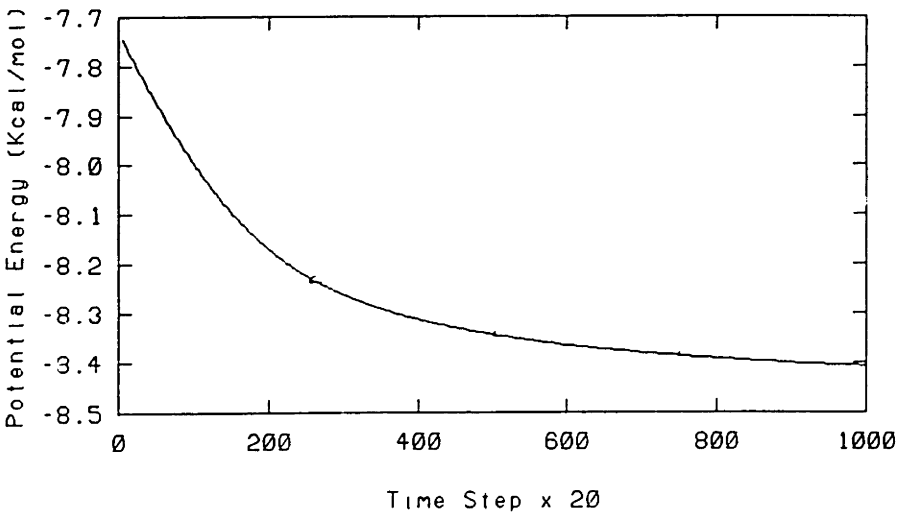

Figure 5-16: Variation of potential energy with time.

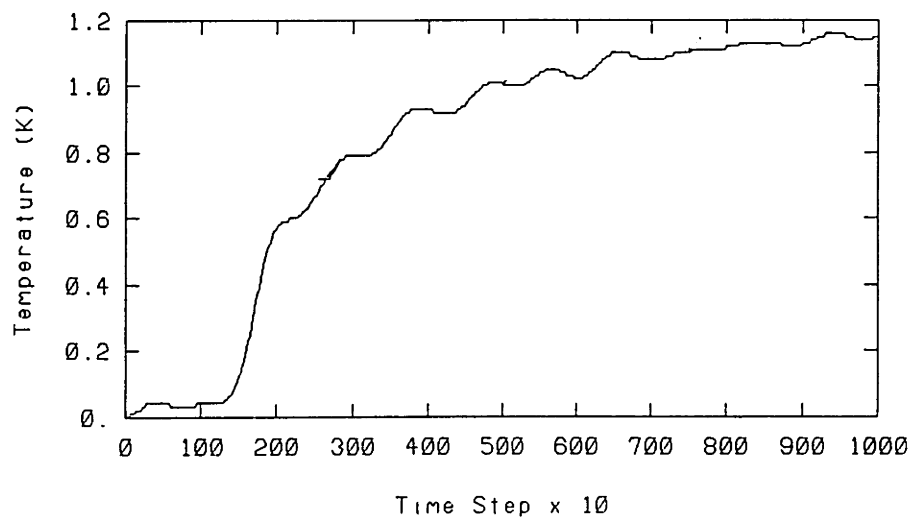

Figure 5-17: Time evolution of center-of-mass mean-squared displacements at zero temperature.

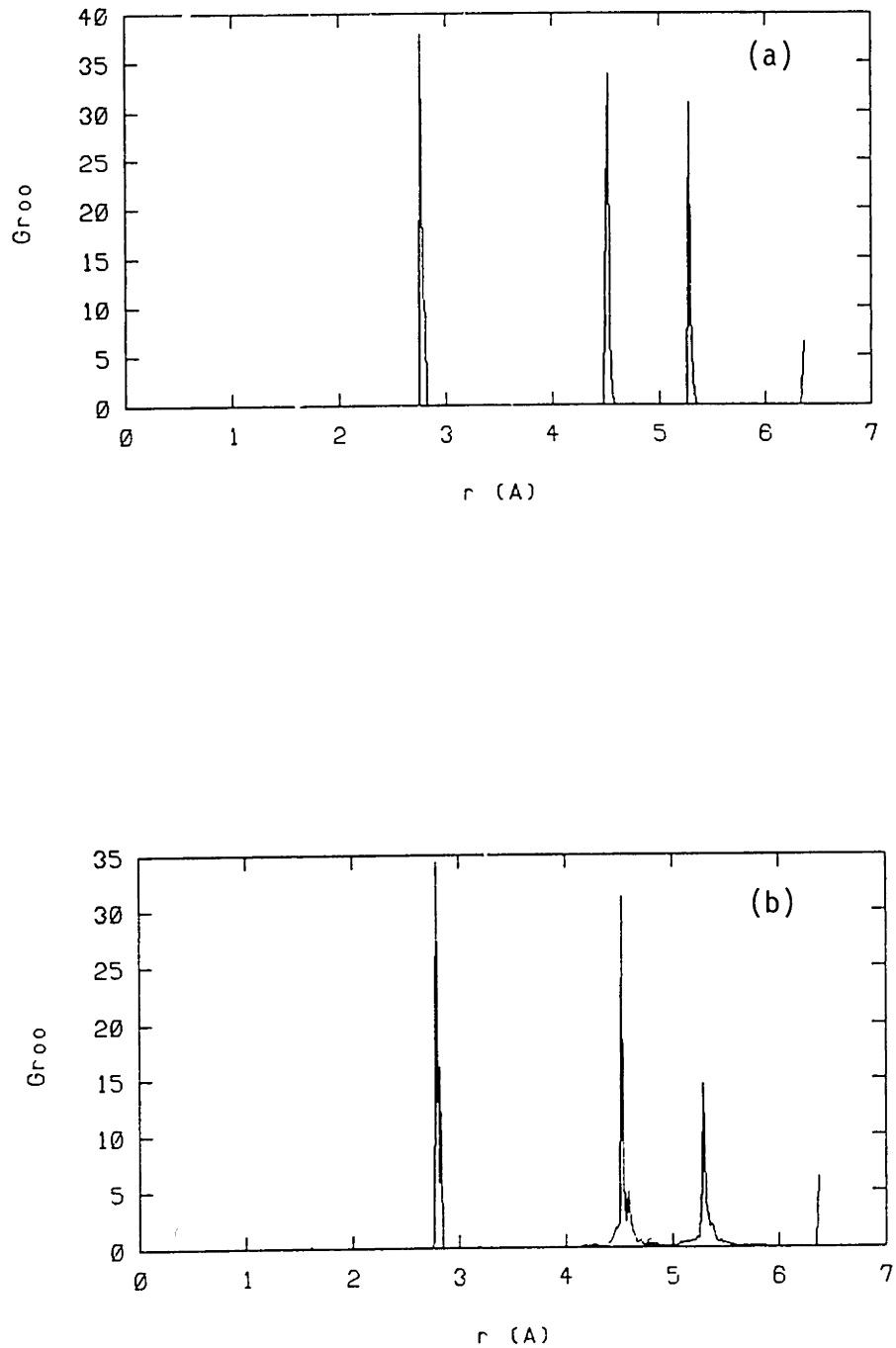

Figure 5-18: The O-O radial distribution function; (a) for initial structure; (b)for structure at the end of run.

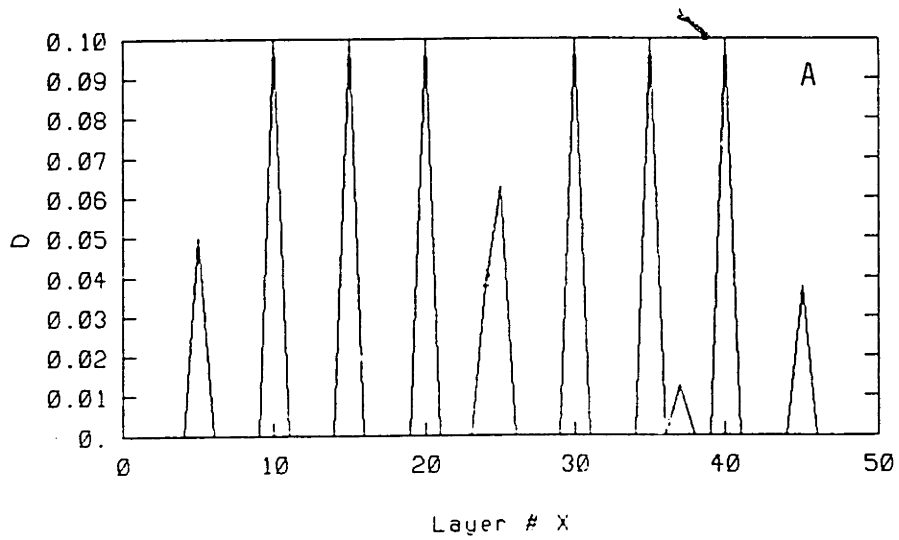

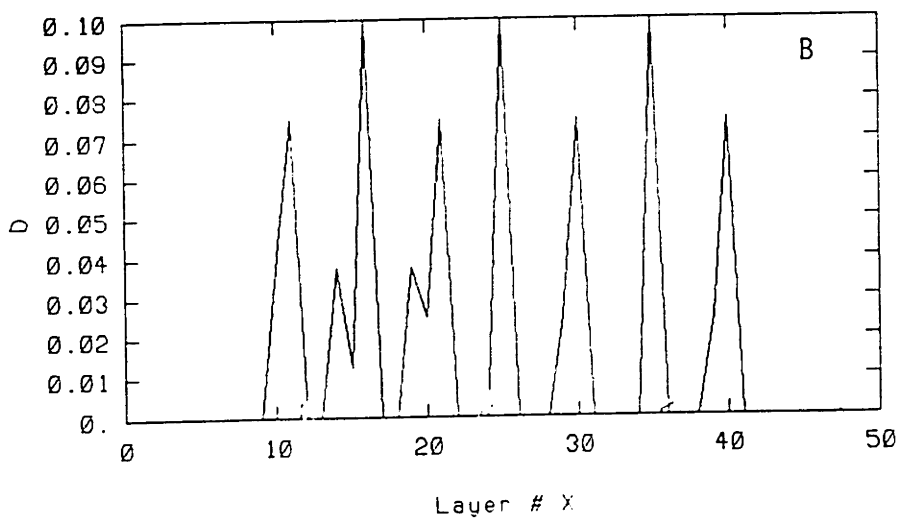

Figure 5-19: Variation in density profile with temperature. A. X-profile the begining; B. X-profile at the end of run

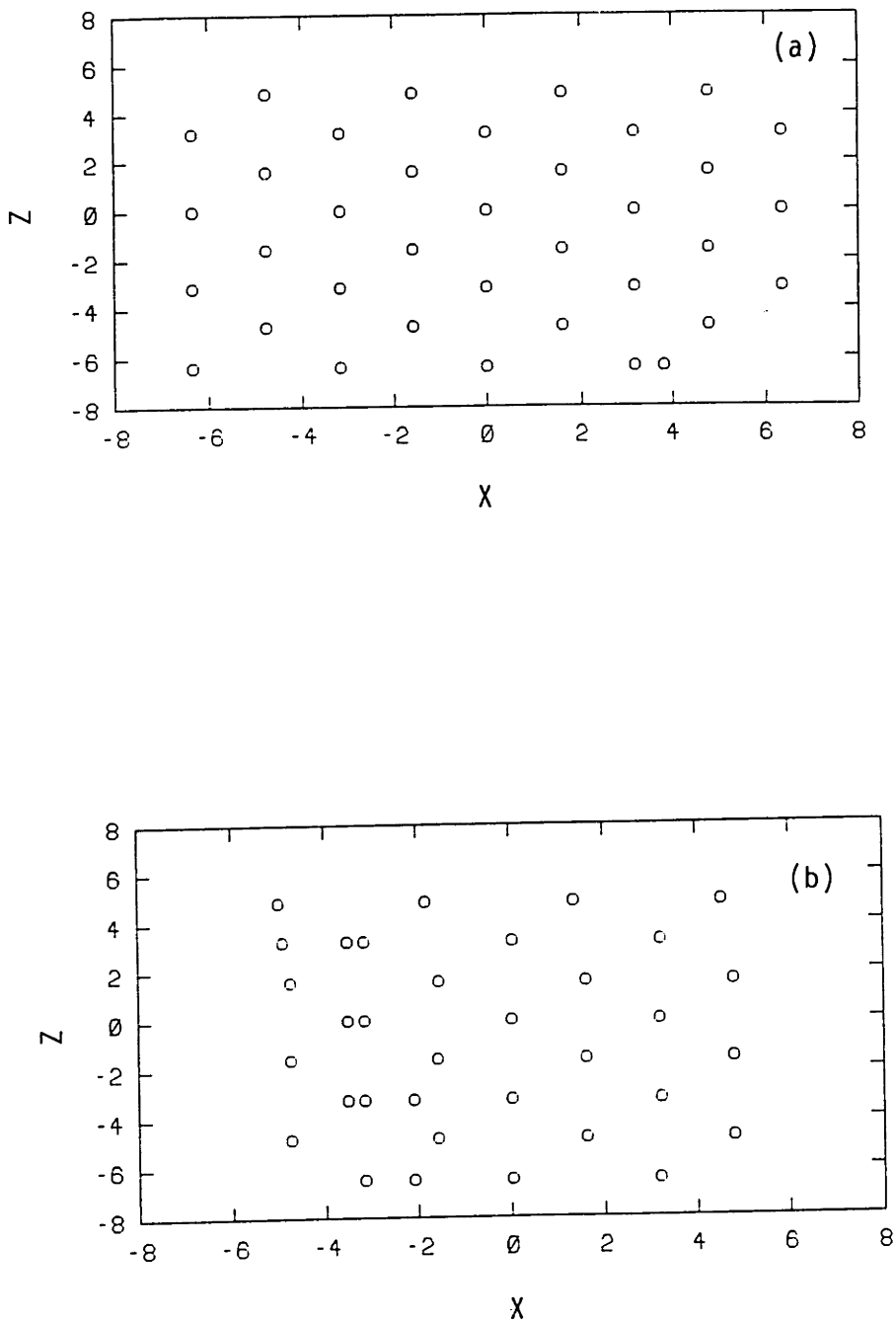

Figure 5-20: The change in particle positions. (a) initial position (b) positions at the end of run

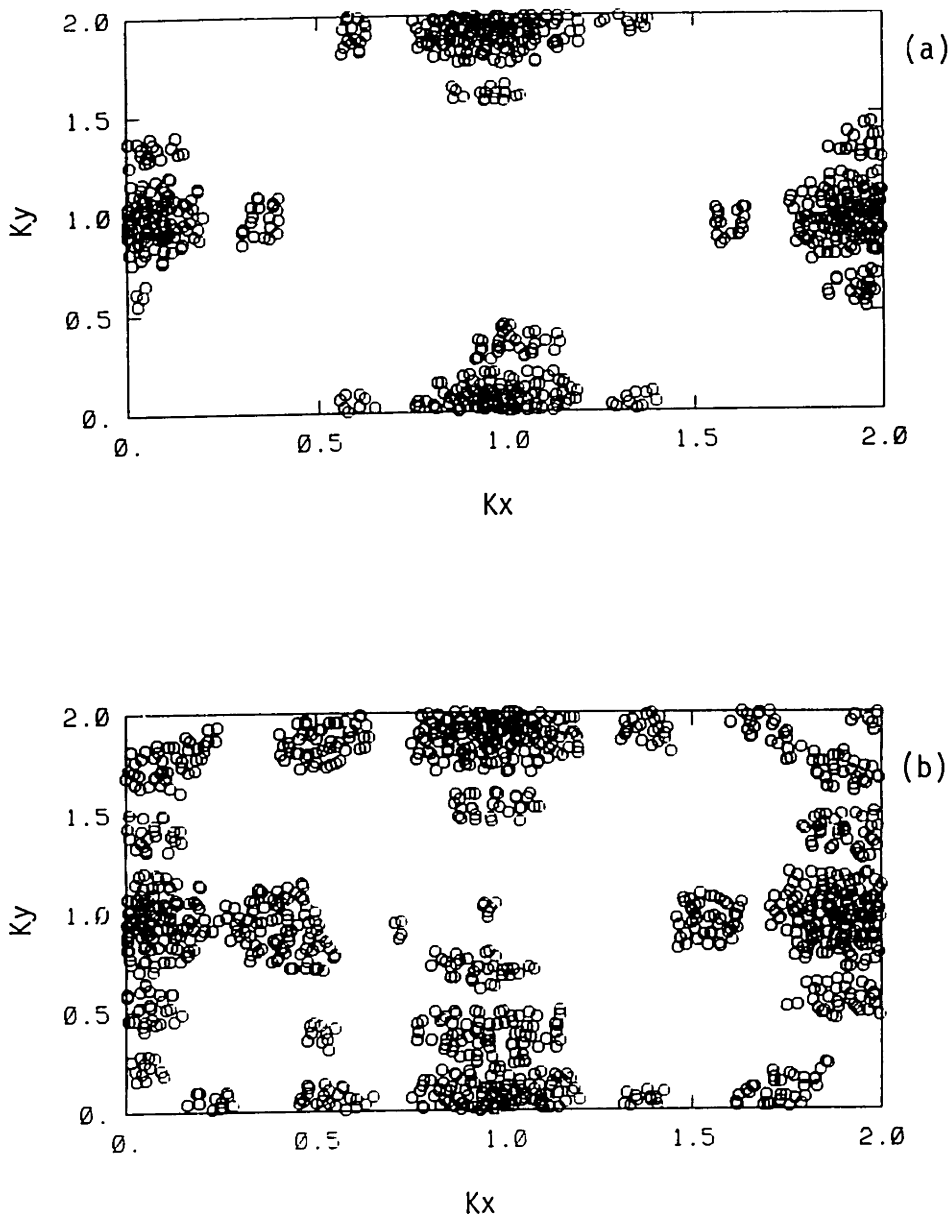

Figure 5-21: The change in diffraction pattern. (a) initial diamond cubic structure; (b) structure at the end of run.

Chapter 6

Molecular Dynamics of Ice-Copper Interface

Icing on solids is a problem involving bi-material interface. The properties of the interface governs the adhesive strength of a composite. Therefore, an understanding of the ice-solid interface is of primary importance for gaining valuable insight in solving the adhesion problems involving ice. In the simulation of a bi-material interface, the most important issue is the design of a cross-interaction potential model that adequately describes the atomic interaction between two different materials at the interface. This chapter deals with the simulation of an ice-copper interface. The results obtained from a few simulation runs are discussed in the following sections.

6.1 Simulation of a Bi-material Interface

The problem of simulating a water-wall bi-material interfaces has received increasing interest in recent years [129], [130, 131]; [132]; [133]. Interested reader are referred to the excellent reviews made by Spohr and Heinzinger, [134] and Heinzinger [135] for a detailed survey of the water-wall interface simulation methodologies and their comparison. All of them include a potential for water (e.g., ST2 [35], TIPS2 [98], MCY [95]), a potential describing metal wall, and a cross-interaction potential between metal-water interface.

The success of a bi-material interface primarily depends on the cross-interaction potential that describes the water-wall or water-metal interactions. In this regard, Valleau and Gardner, (1987) [136] performed the Monte Carlo (MC) simulation of the water-wall using non-polar hard-walls that can be described by a purely repulsive force or by a purely Lennard-Jones potential [136]. These potential models are justified only for studying the structure of water molecules adjacent to an inert surface. However, even in the case of inert walls, the convergence of long range forces present in the water, under a heterogeneous environment, was a difficult task. The anisotropy of the dipole distributions in water made these studies rather unreliable. It was recognized in the study of the Valleau and Gardner (1987) [136] that the problem of estimating long-ranged contributions to the potential energy of the water-wall interface is quite difficult. However, approximation of a molecular system in terms of a group of dipole sheets that lead to the vanishing of the total dipole moment, was found to yield reasonable results on the electrostatic forces.

In the case of the charged walls that imitate an ionic double layer near a charged electrode, the region next to wall is described by a smooth charge distribution approximated by the Guoy-Chapman theory [137] by Gardner and Valleau (1987) [132]. The Guoy-Chapman theory provides a mean electrostatic potential and an ionic distribution for the electrical double layer existing at the water-metal interface. The water molecules described by potential TIPS2, interact with the charges of the electrical double layer with its nearest-image box. The long-ranged charge distribution is evaluated outside the central box using a dipole sheet approximation [132].

Unlike the electrical double layers near electrode, Gardner and Valleau [132] showed that the metal surfaces are highly polarizable. The metallic walls, in the classical electrodynamics theory, are approximated by an infinite dielectric constant [137]. The surface of the metal wall is polarized by the charge within the model system, and as a result, observes change in the electrical field. The resulting fields can be obtained by adding the image charges that are equal to, but opposite in sign, to the particles interacting with the self-potential of the wall. The charges interacts with all the image-charges in the infinite dielectric medium of metal wall and also

with the self-image that gives rise to attraction of each charge towards surface. The potential energy of the interaction of polar molecule (such as water) with uncharged metallic wall having infinite dielectric constant can, therefore, be described by the interaction of the charge q_i on one of the particle with the electrostatic images of all the charged q_j on all particles including its own charge:

$$\phi_c = -q_i \sum_j q_j e^2 / 2r_{ij} \tag{6.1}$$

where r_{ij} is the distance between q_i and image charges q_j, and e is the charge on each particle. This procedure of calculating electrostatic potential energy is known as the "image charge method" [132].

Personage and Nicholson (1986) [130] indicated that the use of image charge method, can be modified according to a particular situations, such as, the actual structure of the metal surface needs to be considered for the description of the first chemisorbed or physisorbed layer. The image potential changes according to the type of surface exposed to the polar medium, e.g., low-index faces (smooth) show decrease in binding energy as compared to the high-index faces, which are rougher. The validity of the image law is limited to a certain distance from the wall. In cases of very short and long distances, the application of the image potential is doubtful. However, MC studies done by Personage and Nicholson [131] use image potential along with a LJ 9-3 potential to describe the water-metal potential. The Lennrd-Jones parameters σ and ϵ for the cross interaction are defined by the combining rules that are based on the assumption that the cross-interaction can be defined as the geometric mean of the two interacting potentials [138]. Personage and Nicholoson [130] use an approximate reaction-field method to describe the long-range Coulomb interaction between the charged particles. The MC studies carried out by the Personage and Nicholson [131] on the water-copper system showed limited success in obtaining preferential ordering of the dipoles to have their negative (oxygen) pointing at surface that is consistent with the results of low energy electron diffraction (LEED) experiments.

The first MD study on water-platinum performed by Spohr and Heinzinger (1986)

[129] following a similar approach as Personage and Nicholson [130] and Gardner and Valleau [132], used an image charge method to account for the electrostatic forces and a LJ 12-6 potentials for the cross-interaction between O-O of ST2 water and a LJ platinum atoms. The cross-interaction LJ potential was obtained using the combining rules. This simulation was able to capture the essence of the surface induced modifications caused by the uncharged platinum wall on the water molecule. But it was unable to give satisfactory interface geometry or capture the reduction in surface work function as a result of water adsorption on the metal surface.

These earlier developments of the water-metal potential were purely empirical based on the combining rules to obtain Lennard-Jones(12-6) or (9-3) parameters along with image charge potential for the electrostatic interaction. Therefore, they did not realistically capture the essence of the interface geometry, as the interface geometry showed preference of oxygen atom towards a hollow site, which is not consistent with the molecular orbital calculations. Recent experiments also showed a reduction in the work function as a result of the adsorption of water molecules on the transition-metal surfaces, that is not captured by the conventional Lennard-Jones water-metal potentials.

Regarding the geometry of the metal-water interface, molecular orbital calculations of Holloway and Bennemann (1980) [139] for water molecule interacting with five atom platinum FCC[100] surface were quite important. In this work, linear combination of atomic orbital (LCAO) method using extended Huckel scheme was employed to describe the substrate-adsorbate electronic interaction[140]. They calculated a variation in the chemisorption energy of water molecule for two cases: (a) on-top geometry, in which oxygen atom of water molecule sits right on-top of the central Pt atom; (b) oxygen atom with dipole pointing upwards site on a hollow site the middle of a five-atom Pt cluster. These calculations along with the experimental results of electron stimulated desorption ion angular distribution [ESDIAD] [141], show that the on-top sites between Pt atom and oxygen of water molecule is a preferred configuration to the positioning of the oxygen atom in a hollow site that result from a four-fold Pt cluster on a Pt[100] surface.

Based on the experimental and theoretical information known about the water-metal interface, a water-metal interaction potential function should result into: (a) a correct adsorption energy consistent with the value obtained from the quantum mechanical calculations; (b) a correct local configuration of the water molecules adjacent to the metal surface, and (c) a negative work function of the surface as a result of the water adsorption.

Recently Spohr (1989) [142] has obtained a pairwise additive interaction potential for water-metal potential based on extended Huckel molecular orbital calculations of a water molecule on top of a five-atom platinum cluster. The pair potential is fitted to a set of exponential functions.

Spohr (1989,1990) [142, 143] also used a flexible potential for water and jellium model for the platinum interactions. The studies conducted with this interface model provide satisfactory results on the geometry of the interface and the vibrational properties at the interface when compared with the experimental results of electron energy loss spectroscopy (EELS).

6.1.1 Design of Ice/Copper Interface Potential

In the present MD study of ice-copper bi-material interface, we have investigated two approaches (a) cross-interaction LJ(12-6) potential obtained from the combining rules, and (b) cross-interaction obtained by fitting the exponential functions suggested by Spohr (1990) [142], to electronic cluster calculations of the Ribarsky et al. (1985) [144]. The ice model used here is SPC and the copper model is derived from EAM potential model.

6.1.2 Ice/Copper Potential Using the Combining Rules

The design of ice/copper cross-interaction potential consists of two distinct terms: (a) the Lennard-Jones contribution arising from pairwise summation of the interactions between the oxygen and copper atoms and, (b) the electrostatic interaction calculated by treating the interface as a dielectric discontinuity.

The Lennard-Jones part (ϕ_{LJ}) is expressed in the standard 12-6 potential form as:

$$\phi_{LJ} = \sum_{k} 4\epsilon[(\sigma/r_k)^{12} - (\sigma/r_k)^6) \tag{6.2}$$

where r_k is the distance between the oxygen atom of the water molecule and copper atom k, and the summation is over all Cu atoms inside a cut-off radius of $L_x/2$, where L_x is the length of the simulation box in the x direction.

The electrostatic potential part is given by the Coulomb potential as:

$$\phi_c = -\sum_{\alpha=1}^{4} \sum_{\beta} q_\alpha q_\beta / r_{\alpha\beta} \tag{6.3}$$

The first summation includes the charges of water molecules of interest and the second summation is over all image charges inside the cut-off sphere. The radial distance $r_{\alpha\beta}$ describe distance between the charge q_α and its image charge q_β.

Calculation of Lennard-Jones Parameters for Cu/H_2O System

Determination of the Lennard-Jones parameters ϵ (dissociation energy at 0K) and σ (atomic spacing at zero potential energy) for the cross interaction of the ice and copper atoms is made by applying the combining rules suggested by Kong (1973) [138]. The combining rules are only applicable to effective pair potentials. In this regard the pair potentials are described in terms of attractive and repulsive parts.

$$\phi_R = \phi^{rep}(R) + \phi^{att}(R) \tag{6.4}$$

For the potential function of Lennard Jones type the combining rules for repulsive (term with power of 12) and attractive parts (term with the power of six) are given as follows:

$$\phi_R = 4\epsilon[(\sigma/R)^{12} - (\sigma/R)^6] \tag{6.5}$$

$$\epsilon_{ab}\sigma_{ab}^{12} = (\epsilon_{aa}\sigma_{aa}^{1}2/2^{13})[1 + (\epsilon_{bb}\sigma_{bb}^{12}/\epsilon_{aa}\sigma_{aa}^{12})^{1/13}]]^{13} \tag{6.6}$$

$$\epsilon_{ab}\sigma_{ab}^{6} = [(\epsilon_{aa}\sigma_{aa})^{6}(\epsilon_{bb}\sigma_{bb}^{6})]^{0}.5 \tag{6.7}$$

where subscripts aa refer to atoms in material a and bb refers to atoms in materials b, and ab refers to the cross interaction terms.

The SPC potential model of water has been already described in chapter-IV. The effective potential part of the copper is derived from the EAM potential.

6.1.3 Derivation of Pairwise Representation of EAM Copper Potential

In the case of EAM potentials, the potential energy for a system of N atoms is represented in terms of embedding energy and pairwise core-core repulsion energy.

$$E_{tot} = F_i(\rho_i) + \frac{1}{2}\sum_{j\neq i}\phi_{ij}(r_{ij}) \tag{6.8}$$

$$\rho_i = \sum_{j\neq i} f_j(r_{ij}) \tag{6.9}$$

where $F_i(\rho_i)$ represents the embedding energy for atom i, in the electron density of ρ_i; $f_j(r_{ij})$ is the electron density contribution to atom i from atom j at a distance r_{ij} apart, and the $\phi_{ij}(r_{ij})$ is the core-core repulsion energy between atoms i and j.

In order to derive an effective pair potential we need to obtain the variation of the potential energy with the distance r for a pair of atoms. To achieve this objective we consider a defect-free homogeneous solid with a number density such that each atomic site experiences the same background electronic contribution from the surrounding particles. Now we tag a particular atom i in this perfect lattice solid and introduce an additional test-particle j in the system, and now by changing the interatomic distance between the tagged particle and particle j the variation of potential energy versus radial distance is obtained. The incremental contribution to E_i by the extra

test particle is what is being defined as the effective pairwise potential $\phi_{eff}(r_{ij})$, and this definition of the pairwise potential is unique and centrally-symmetric for a given density. The effective pair potential, therefore, can be described as [121]:

$$\phi_{eff}(r_{ij}) = \phi(r_{ij}) + F(\sum_{l \neq i} f(r_{ij}) + f(r_{ij})) - F(\sum_{l \neq i} f(r_{ij})) \tag{6.10}$$

where subscript i represents the tagged particle and j represents the extra test particle introduced in to the system, subscript l represents all the atoms in the original system. The effective pair potential is obtained for the surface atoms because atoms on the Cu[100] surface are the ones that will interact with the water molecules.

The calculation is done for the EAM FCC copper at its normal density and zero temperature. Figure 6-2 shows the plot of $\phi_{eff}(r_{ij})$ versus radial distace, r. The potential energy curve so obtained is used to get the depth of the potential well ϵ and the interparticle distance at zero potential energy σ. Figure 6-1 to 6-4 show the plot of Lennard-Jones potential energy for copper surface atom, oxygen-oxygen pair potential for SPC water, copper atom effective pair potential, and copper-oxygen cross pair potential functions.

The Lennard-Jones functions for the the three potentials are:

Oxygen-oxygen pair potential

$$\phi_{r_{O-O}} = 4 * 0.6640[(3.16/r_{O-O})^{12} - (3.16/r_{O-O})^{6}] \tag{6.11}$$

Copper-copper pair potential

$$\phi_{r_{Cu-Cu}} = 4 * 5.5970[(2.67/r_{Cu-Cu})^{12} - (2.67/r_{Cu-Cu})^{6}] \tag{6.12}$$

Copper-oxygen cross-pair potential

$$\phi_{r_{Cu-O}} = 4 * 1.9275[(2.90/r_{Cu-O})^{12} - (2.90/r_{Cu-O})^{6}] \tag{6.13}$$

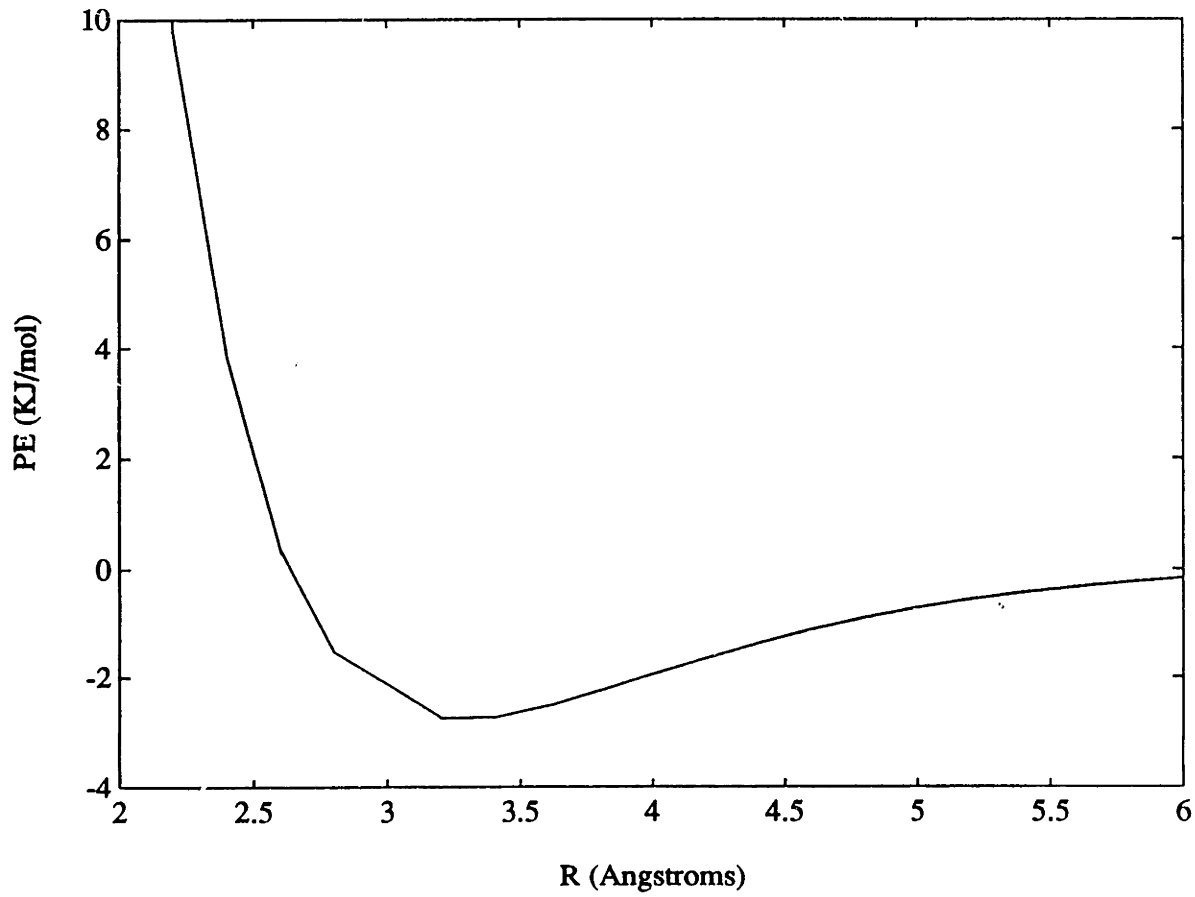

Figure 6-1: The Lennard-Jones function for atom at the Copper surface

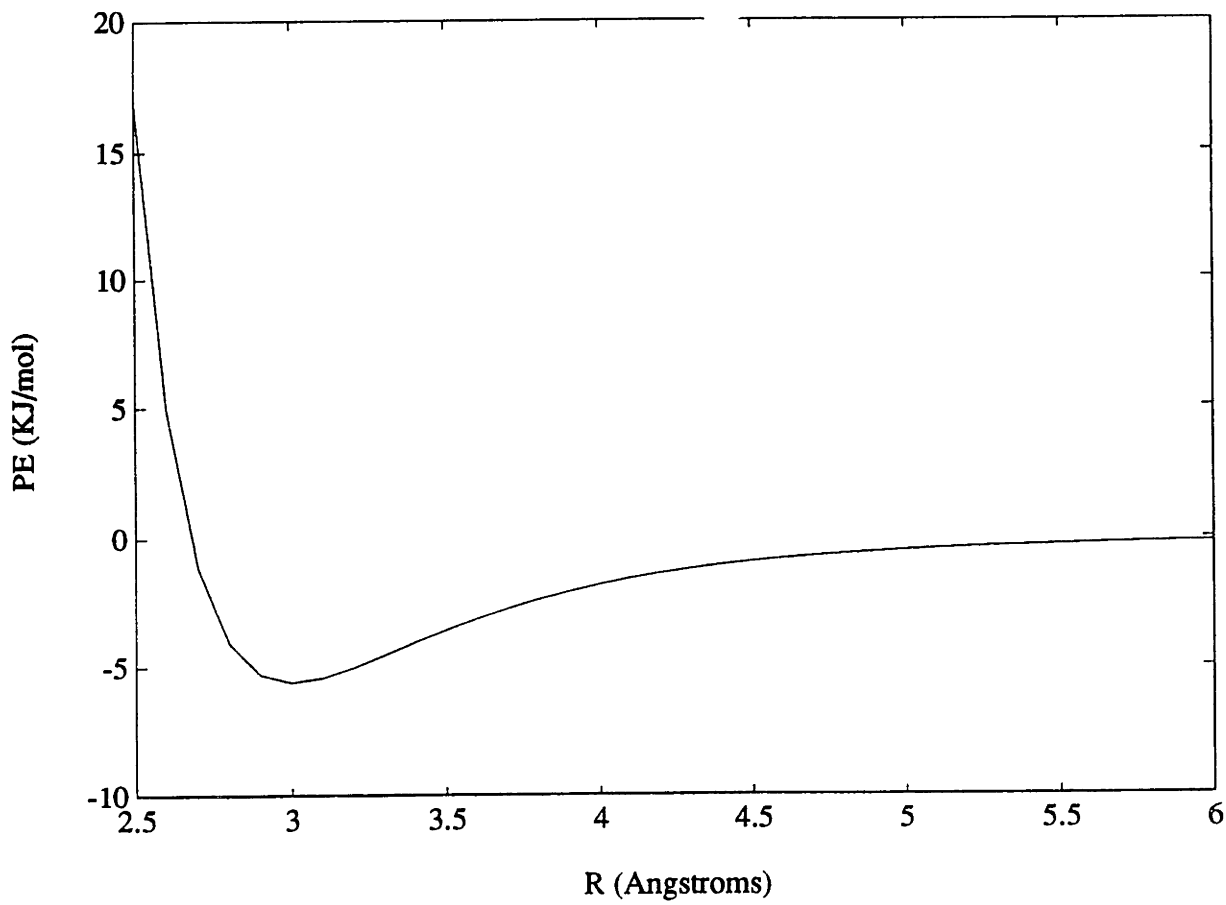

Figure 6-2: The effective pair-potential function of copper

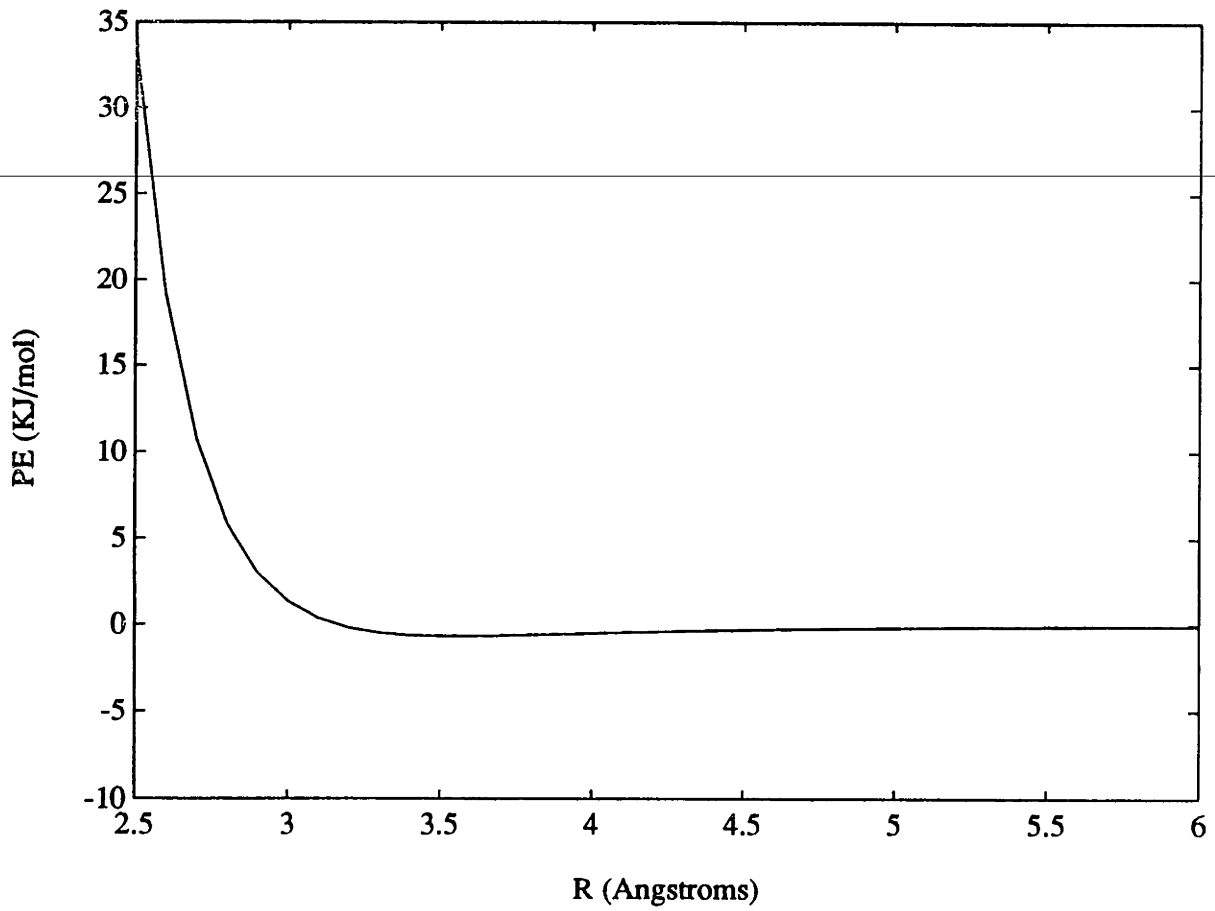

Figure 6-3: The oxygen atom pair-potential function for ice

6.1.4 Ice/Copper Potential Using Cluster Calculations

The electronic structure of water interacting with a Cu_5 atomic cluster is obtained by Ribarsky et al. (1985), using extended basis set spin-unrestricted self-consistant-field linear-combination-of-atomic orbitals method (SCF-LCAO) [144]. These calculations provide variation in the binding energy of the oxygen atom on-top of the copper atom with distance. The ground state binding energy, determined via systematic mapping of the potential energy surface is $E_b(H_2O\text{-}Cu_5)$ = 36.6 kJ/mol. The ground state energy and the variation of the potential energy is fitted to exponential functional set proposed by Spohr (1989) [142].

For the computational convenience the water-copper potential obtained by MO calculations is divided into a number of pairwise additive interactions between oxygen-metal and hydrogen-metal interactions. For a water-copper interaction the potential function is described as:

$$\phi_{W-Pt} = \phi_{O-Pt}(r_{O-Pt}, \rho_{O-Pt}) + \phi_{H-Pt}(r_{H_1-Pt}) + \phi_{H-pt}(r_{H_2-Pt}) \tag{6.14}$$

where

$$\phi_{O-Pt} = (1721.5exp(-1.1004r) - 1988.3exp(-2.082r)]f(\rho) + 10^6 exp(-6.3122r)[1-f(\rho)) \tag{6.15}$$

and

$$\phi_{H-Pt} = 1.5243exp(-1.3889r) \tag{6.16}$$

with

$$f(\rho) = exp(0.4322\rho^2) \tag{6.17}$$

where r and ρ are site-site distance and projection of the distance vector on the surface plane. (The energy units are in joules and length units are in angstroms.) Figure 6-4 shows the potential function obtained by the fitting.

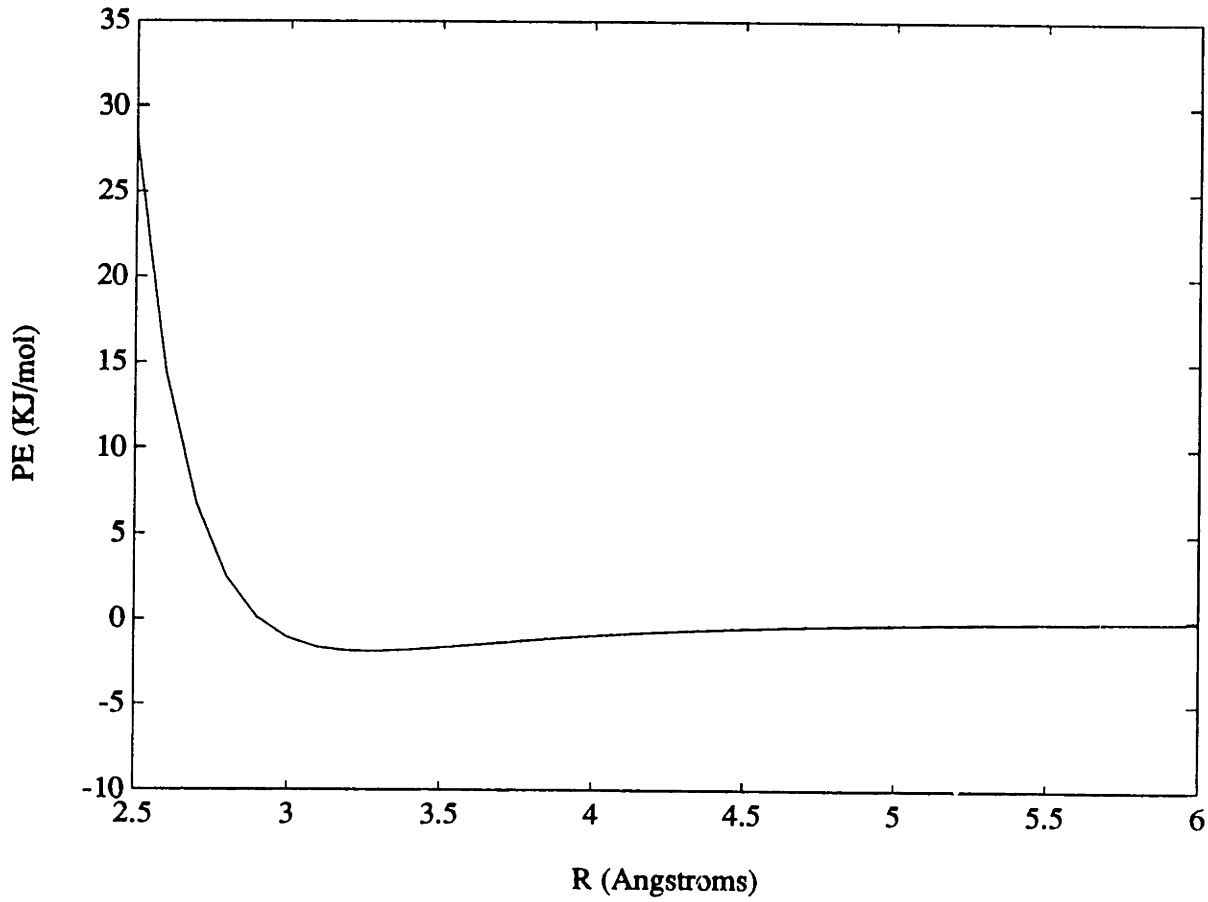

Figure 6-4: The cross-interaction Lennard-Jones Potential function for the ice-copper interface

6.1.5 MD Results on Lennard-Jones Interface Model

The interface potential derived on the basis of purely Lennard-Jones model are used to simulate an interface. This is obtained by joining two FCC blocks of 108 atoms each, representing water and copper respectively. Purpose of this study is toobtain preliminary insight in the development of a bi-material interface. A few runs made at zero temperature reveal that the binding energy and the geometry obtained by the Lennard-Jones cross-interaction potential do not agree with the experimental values. The experimental value of the adsorption energy for the adsorption of water on copper obtained by Ribarsky et al. [144] is 36.6 KJ/mol. The binding energy for a Lennard-Jones potentials is of the order 13.11 KJ/mol, obtained by finding the difference of the interface ice layer potential energy from the bulk copper potential energy. The runs made with the 108 water oxygen atoms and 108 copper atoms at zero temperature show that the oxygen atom of the ice molecule prefers hollow sites to the on-top sites. These results are in disagreement with the known simulation and experimental results. Therefore, we did not pursue these simulations further.

6.1.6 MD Studies on the Cluster Potential Model

The testing of the cluster potential model for the interface is done on the basis of two criteria: (a) calculated interface geometry should be in agreement with the experimental observations and, (b) calculated adsorption energy of the water molecules on the metal surface should be in agreement with that obtained by the cluster calculations. Table 6.1 shows the layer-by-layer variation of the thermodynamic parameters in the eight layer SPC ice on the copper surface. On the basis of the potential energy of the interface and the potential energy of the copper surface obtained in the chapter-4, the value of the adsorption energy is 30.3 KJ/mol, which is within 16% of the reported adsorption energy 36.6 kJ/mol in the case of water-copper interface [144].

The interface geometry is generated by putting a diamond cubic SPC ice (64 molecules) on top of FCC copper (108 atoms) as shown in Figure 6-5. The average

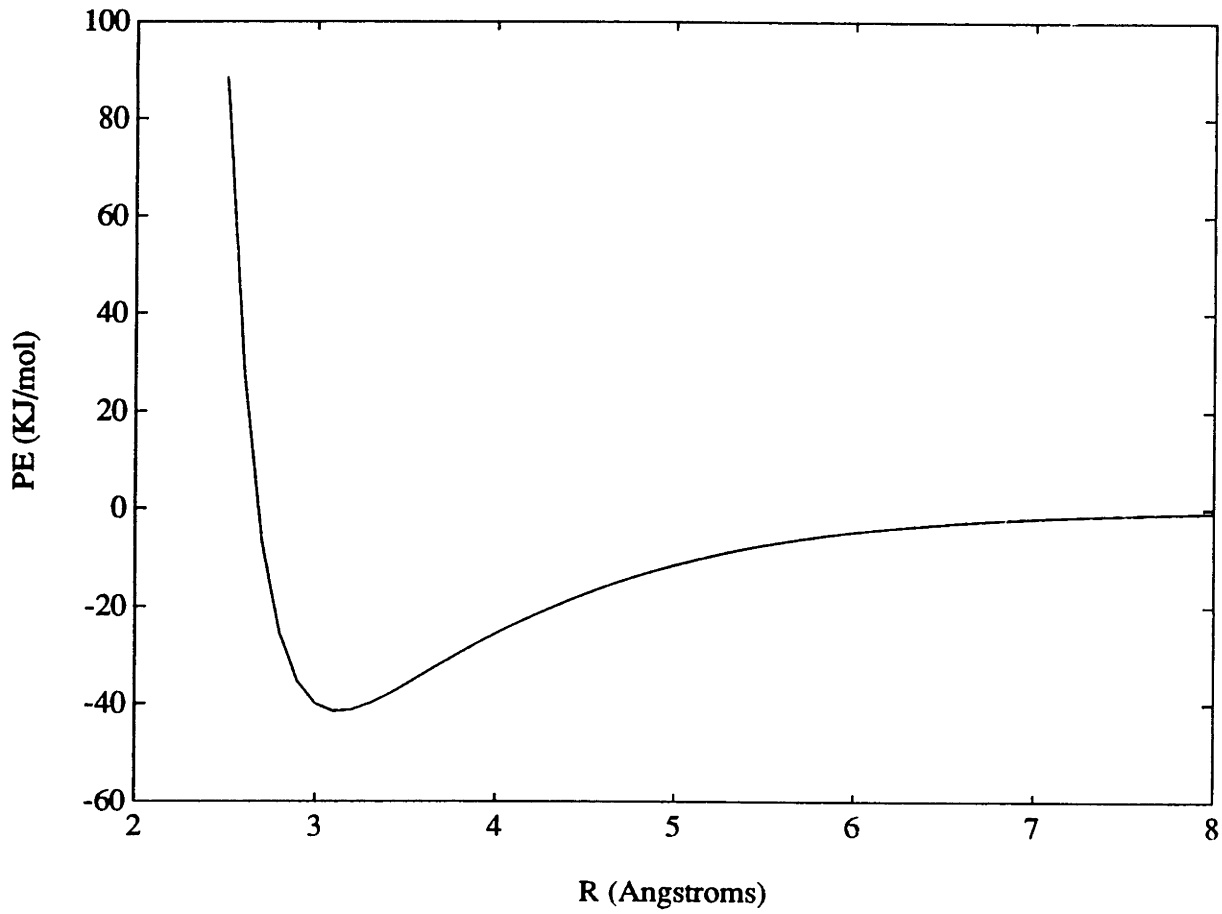

Figure 6-5: The cross-interaction potential function for ice-copper interface

particle positions are obtained at the end of a 20,000 time step run and the local configuration of the ice molecules on the copper surface is determined. As shown in the Figure 6-7, the oxygen atoms that are not commensurate with the copper lattice, move towards the commensurate sites. The hydroxil group finds an on-top site for the adsorption on the copper surface.

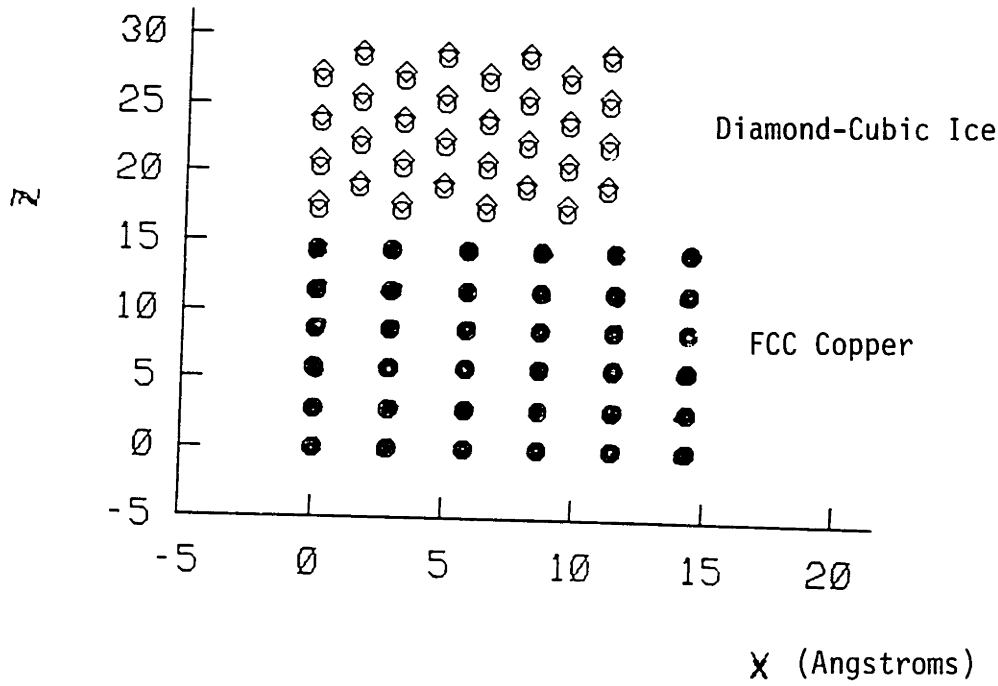

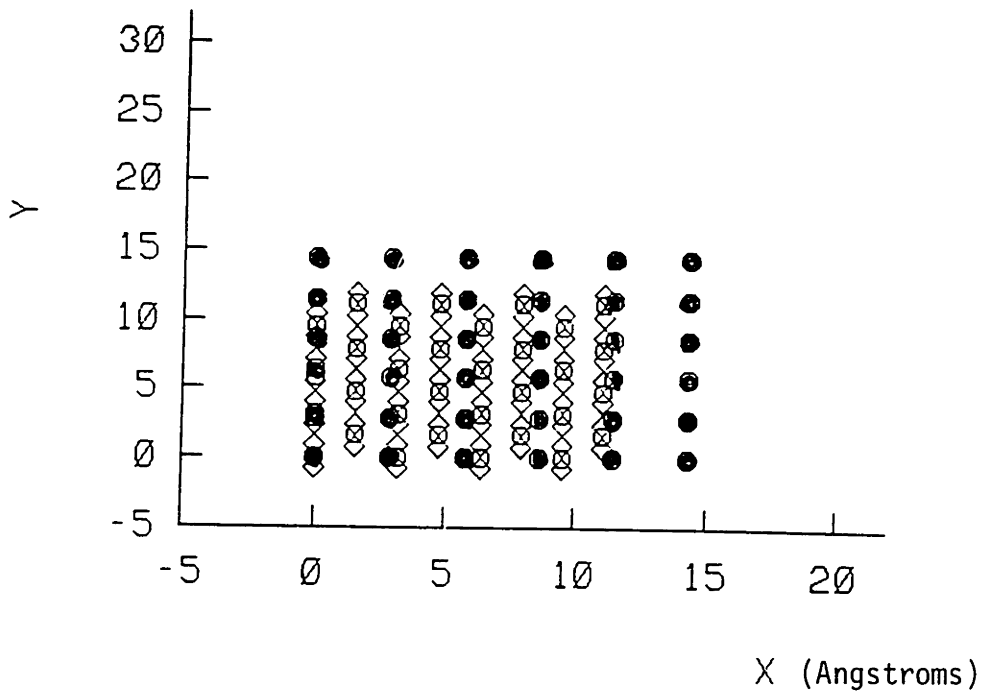

Figure 6-6: The initial geometry of the ice-copper interface

6.1.7 Comparison of Vibrational Spectrum with Raman Experiments

The vibrational spectrum of the diamond cubic ice layer on the copper FCC[100] surface has been calculated layer-by-layer on the copper surface. The copper block is made of 108 atoms while the diamond cubic ice block is made of 64 water molecules. The ice block is made of eight layers of eight ice molecules. The velocity autocorrelation and the power spectra of the eight layers are obtained at the end of 20000 time step run. The velocity-autocorrelation of the hydrogen atoms in each layer is obtained on the basis of the data collected for the last 10000 time steps.

The comparison of the vibrational spectra of ice layer on the copper surface obtained by Raman spectroscopy and computed using the velocity autocorrelation function is shown in Figure 6-8. The spectra of the interface layer is denoted by layer # 8. is compared with the Raman spectra of obtained for the thick and thin layer of ice on copper surface reported in the chapter 2 (see Figure 2-5).

The comparison is made on the vibrational spectra obtained in the O-H stretching region. The vibrational spectra for the interface ice layer #8 shows broad band width and three peaks. This is representative of the disorder in the ice lattice adjacent to the copper surface. The peak at about 3300 cm^{-1} becomes sharper and resembles the bulk ice for the surface layer.

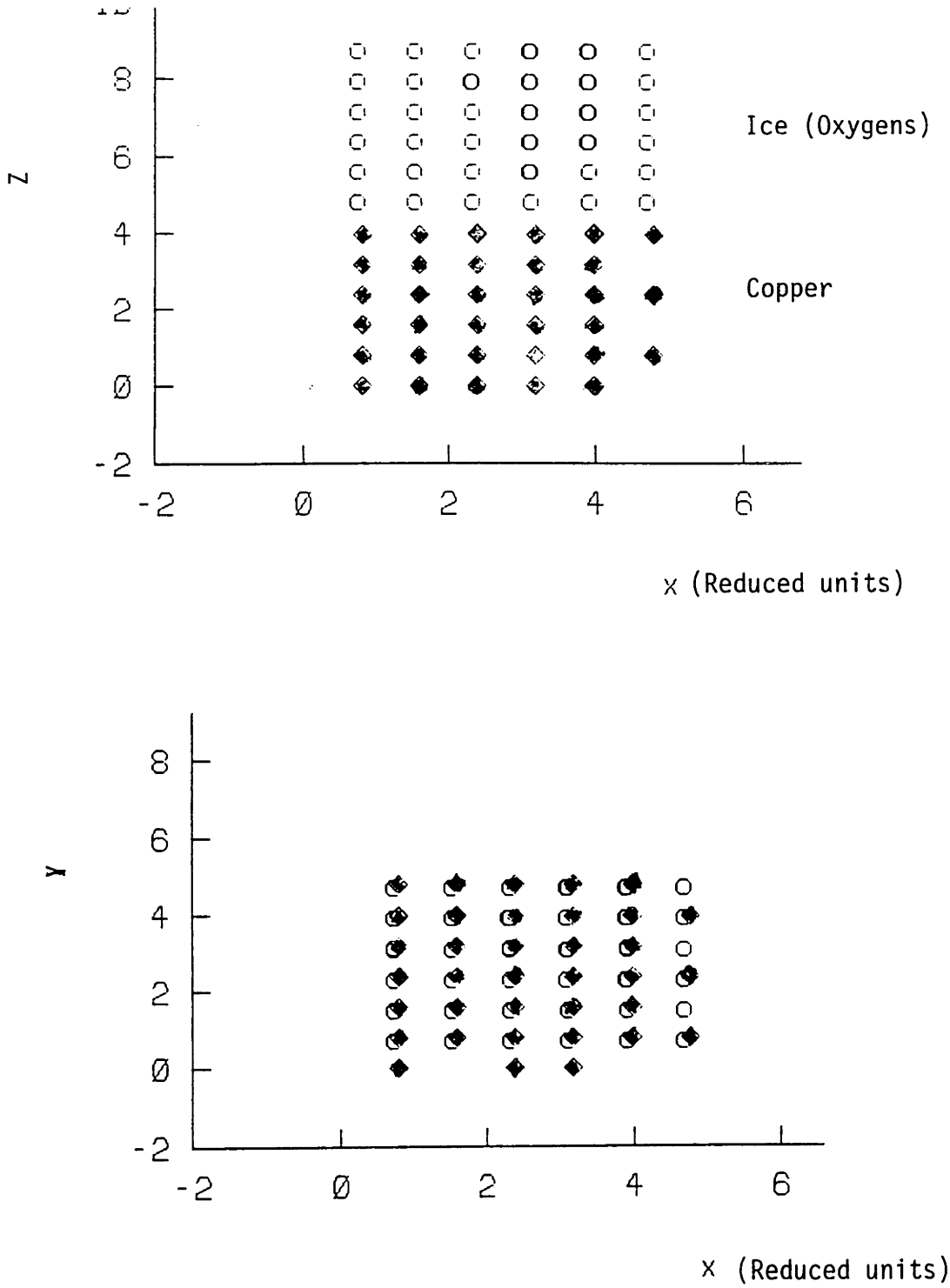

Figure 6-7: The average oxygen atom positions on the copper surface at 70K

Table 6.1: Summary of Thermodynamic Properties at 70K for ice layers on the Copper Surface

Layer# #	T (K)	U (KJ/mol)	P (Kbar)
1	70	-36.99	0.92
2	70	-35.32	-0.92
3	70	-35.12	-0.93
4	70	-34.92	-0.83
5	70	-33.78	-0.92
6	70	-32.12	-0.92
7	70	-31.34	-0.89
8	70	-30.29	-0.92

where U is the potential energy/particle of a layer and P, the pressure of the layer.

6.1.8 Results and Discussions

The results of the preliminary study on the ice-copper interface show that the cross-interaction potential obtained by fitting the exponential functions to electronic cluster calculation gives the adsorption energy to within 16% of the value reported by Ribarsky et al. [144]. The computed vibrational spectra of the interface ice layers at 70K on the copper surfaces, based on the layer-by-layer variation of the O-H stretching frequency band-width, show a larger disorder in the ice layer adjacent to copper surface as compared to the bulk ice. This result agrees with our experimental Raman measurements for thick and thin ice layers. The geometry of the ice-copper interface, obtained by plotting the time-averaged particle positions, shows that the adsorption of the oxygen atom occurs at the atomic sites of the copper lattice.

The results obtained from the laser Raman microprobe shear studies described in chapter 3, section 3.3, reveal that the adhesive strength of the ice/metal bond on a metal with a lattice spacing commensurate with the O-O spacing of ice lattice is higher than that for incommensurate substrates. Therefore, the adsorption of the hydroxil group on the atomic sites is an important mechanism of adhesive bond

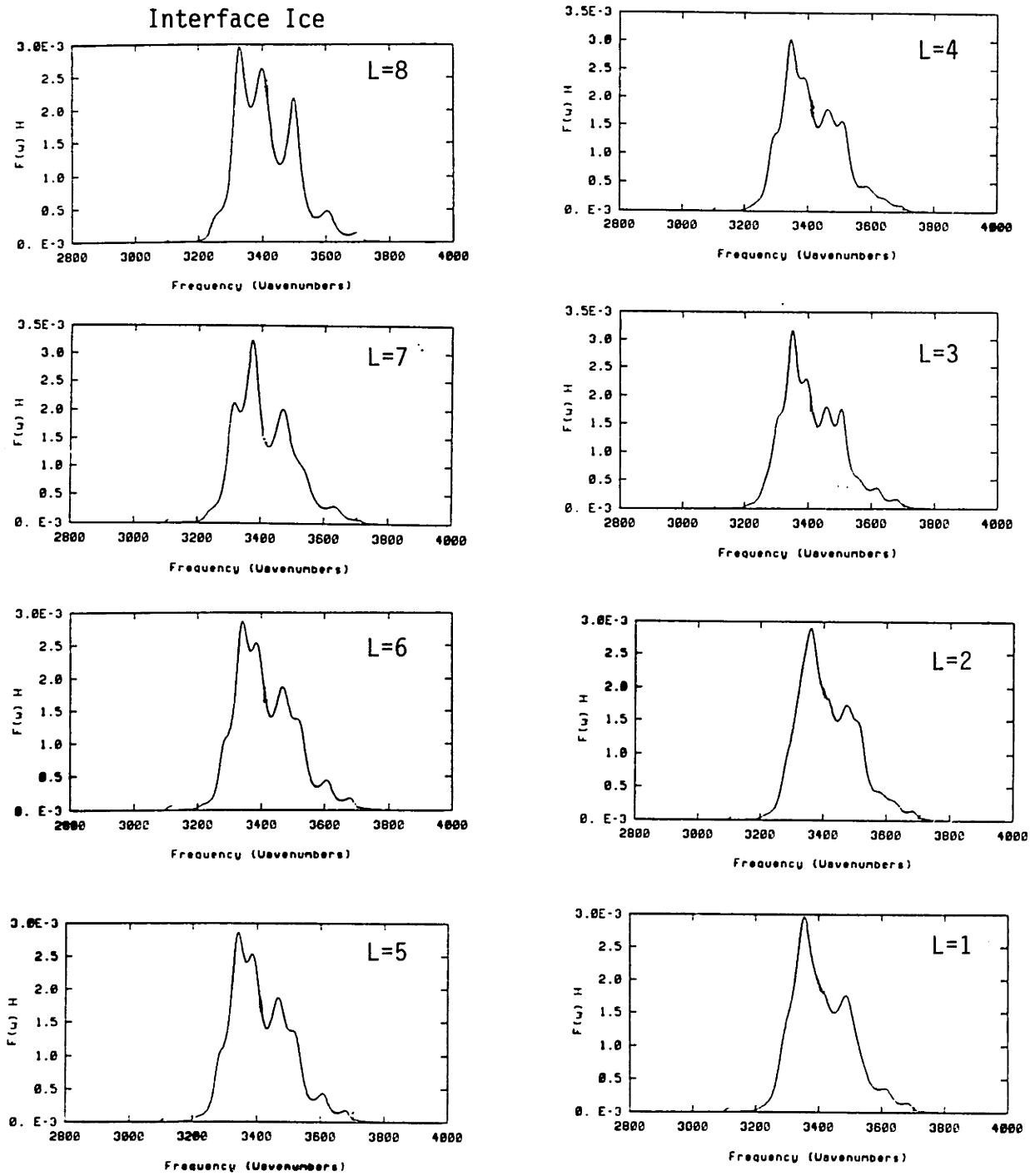

Figure 6-8: Vibrational spectra of ice layers on copper surface in the 0-H stretching region

formation. The result of the MD study confirms the preference of the oxygen atoms to be commensurate with the copper atoms. This observation supports our primary finding that the adsorption of the hydroxil group is commensurate with the lattice structure of substrate surface.

Chapter 7

Conclusions and Recommendations

The goal of this dissertation was to gain fundamental understanding on the formation and growth of ice-solid interface bond. In this regard, the research goals of this dissertation were: (a) to investigate influence of the microscopic physical-chemical parameters on the adhesion of ice, (b) to investigate the physical mechanisms responsible for the lower adhesive shear strength of an ice-solid bond compared to the tensile strength, and (c) to develop criteria that can be used in the rational design of de-icing coatings and materials.

The effects of the microscopic physical-chemical parameters on the adhesion of ice were studied with laser Raman microprobe shear apparatus. This apparatus was specially designed and fabricated to perform pure shear experiments on an ice-solid interface while simultaneously making Raman spectroscopic and video microscopic observations. In the experimental studies, the structure of ice layers forming on solid surfaces has been studied with laser Raman microprobe spectroscopy. The phenomena of the nucleation and the growth of ice on solid surfaces were investigated using both *in-situ* video and confocal microscopy.

In the computational studies, using molecular dynamics (MD) simulations, the instability of cubic ice induced by heating, under constant pressure and constant volume conditions, was investigated. The temperature induced variations in the structural

and dynamical properties were calculated in the range of 70K to 300K. The emphasis of the study was on the dynamical (vibrational) properties, which can be compared with the Raman experiments. Further, an ice-copper cross interaction potential was derived from the electronic cluster calculations to investigate the adsorption energy and structure of the ice-copper interface. The interface was studied layer-by-layer to investigate local variations in the dynamical properties. The O-H stretching peaks of the computed vibrational spectra of cubic ice were compared with the the O-H stretching peaks obtained from the Raman spectroscopy of ice layers on the copper substrate.

On the issue of lower shear strength of ice-solid bond, laser Raman spectroscopic studies on the solid surfaces were conducted. These studies indicated that the broken network structure of the high defect density polycrystalline ice is responsible for the lower shear strength.

The research findings of the experimental and MD studies are used to develop *a set of criteria* for the rational design of the de-icing coatings and materials.

The experimental and computational studies conducted to achieve this objective lead to the following specific findings:

7.1 Conclusions of Experimental Studies

1. Variations in Raman peaks positions and bandwidth in the O-H stretching and lattice vibrational regions are obtained with the use of *in-situ* laser Raman microprobe spectroscopy on several metal surfaces and electrical transmission line samples. The results show that the vapor deposited ice layer formed initially on the cold metal substrate (below 150K) possesses a low-density amorphous structure. This layer changes into high defect density polycrystalline ice above 150K temperature. *The broken network structure of the polycrystalline ice is responsible for the low shear strength of the ice-solid bond.*

2. The video and confocal microscopy of the nucleation and growth of ice formed by the condensation of atmospheric vapor on solid surfaces kept at -20 °C tempera-

ture (titanium, copper, aluminum, stainless, steel, glass and teflon) clearly show that the phase transition on the high energy surfaces is dominated by dropwise condensation, while on the low energy surface it has sheet-like condensation. The critical size of the ice embryo on the solids is inversely proportional to the surface free energy (obtained by the contact angle measurements). The work of adhesion calculated on the basis of contact angle measurements is inversely proportional to the critical embryo size. *The embryo shape and the density of droplet perimeter per unit area are primarily responsible in the growth and the strength of the ice-solid interface bond.*

3. The slice-by-slice observations of the growth process on the solid substrate show that there are three spacial regions, which constitute the formation: (i) the condensate region, where the pattern of the ice embryos is preserved; (ii) the faceted cross-linked region, where the ice embryos form the facets between them; (iii) crystal growth region, where the crystals grow out of the cross-linked facets. *The condensate region and the faceted cross-link regions are primarily responsible for the adhesive strength of the interface.*

4. The variations in the Raman spectra of the ice layers before and after shearing in the laser Raman microprobe shear apparatus, based on the peak positions of the O-H stretching frequencies and band widths, shows that the out-of-phase frequency (ν_3) has a large shift that results from the breakage of the hydrogen bonds. The in-phase vibrational frequency (ν_1) remains unchanged. The increase in the band width of the ν_3 frequency shows a disorder in unbonded hydrogen. *These observations indicate that the adhesive bond is formed by the adsorption of the hydroxil group on the metal surface.* The oxygen atoms are adsorbed primarily on the atomic sites of the metal surface. As a result, the ice-solid bond is strong for solids that have good match with the lattice of the ice (i.e., commensurate interfaces) and weak for mis-matched surfaces (i.e., incommensurate interfaces).

The results of the shear strength test show that the adhesive strength of the

ice-metal bond is sensitive to the applied strain-rate, while for the ice-teflon bond the failure is insensitive to strain-rate. The failure in an ice-metal bond occurs within the ice layer and is cohesive in nature, while in the case of the ice-teflon bond the failure is interfacial.

7.2 Conclusions of Molecular Dynamics Studies

1. The results from the isochoric and isobaric melting of simple cubic and diamond cubic, simple point charge (SPC) ice show a considerable increase and spread in the calculated rotational vibrations (frequency at about 600 cm^{-1}) towards the bending vibrations (located about 1700 cm^{-1} frequency). *This increase indicates a coupling and mixing of the rotational (torsional) vibrations with the bending vibration. This coupling and mixing of vibrations rotational and bending vibrations, precursor to melting is an important mechanism that leads to the disintegration of crystalline SPC ice.*

2. The sudden change in the coordination number, reduction in the potential energy, and an increase in the O-H stretching frequencies at 240K indicate that the coupling leads to a *partial breakage of the hydrogen bond.* This breakage results in the *formation of cavities in the crystal, which are essential for melting to commence.*

3. The diamond cubic film of ice formed with eight layers (15 angstrom thickness) is structurally unstable in the molecular dynamics simulations. The instability results primarily from the calculation of the long-range electrostatic forces by the summation of two unconditionally converging series. In the case of inhomogeneous systems, the asymmetry in the charge distribution results in surfaces with infinite dipole moments, prohibiting the convergence of the electrostatic forces both in the finite and reciprocal spaces.

4. The first attempt to simulate an ice-copper interface using a cross-interaction potential, obtained by fitting exponential functions to an electronic cluster cal-

culation, is found to be reasonable in describing the ice-copper interface geometry as well as the binding energy. The computed vibrational spectra of ice layers on the copper surface show larger disorder in the case of ice layer adjacent to the copper surface as compared to bulk ice. This observation agrees with our experimental Raman measurements on the ice layers on a copper substrate. The geometry of the simulated ice-copper interface shows that the adsorption of the oxygen atom occurs at the atomic sites of the copper lattice. *This observation strongly supports our primary experimental finding that the adsorption of the hydroxil group is commensurate with the lattice structure of the substrate.*

7.3 Recommendations for De-icing Problem

1. In the design of de-ice coatings or surfactants, the adsorption of the hydroxil (OH) group of water vapor should be prevented by selecting a nonpolar surface.

2. The adsorption of the water molecule is followed by the formation of the hydrogen bond between water molecules that is responsible for the stability of ice lattice. A coating with receptor radicles that react with the unbonded hydrogen of the adsorbed water molecules will effectively disrupt the lattice formation by breaking the hydrogen bond.

3. Ice formed on the surface is initially a low density polycrystalline ice which turns into a high density polycrystalline (faceted cross-linked region) ice due to recrystallization and provides strength to the ice-solid bond. De-icing chemicals or coatings should be designed to prevent this recrystallization by controlling the diffusion at the solid surface.

4. Solid surfaces with the lattice parameters that matches (i.e., commensurate) with the lattice of ice develops a strong coherent interface. An amorphous polymer coating that has a mis-match (incommensurate) with the ice lattice disrupts the coherency and results in a weak interface.

5. The work of adhesion depends on the size and shape of the droplet embryo formed at the cold substrate. Therefore, the surface of the conductor or coating needs modification in such a way that the condensation takes place with a large droplet size that maintains large contact angle. A surface modification or a coating that will produce a large contact angle is desirable for this purpose.

6. The formation of droplets is followed by the coalescence that is responsible for the equilibrium shape of the droplet embryo prior to phase transition. A coating that helps the coalescence via a hopping mechanism of droplets will result in a large embryo size and a weak adhesive bond.

7. The mechanical interlocking caused by surface pits contributes significantly to the adhesive strength. For high energy surfaces, it is important to control surface roughness. A coating that provides a smooth finish to the metal surface will be effective in reducing the adhesive strength.

The conclusions in this study provide a fundamental understanding of the formation and growth of ice-solid interface bonds: The adsorption of the 0-H group of ice on the atomic sites of the substrate is primarily responsible for the interface bonding, the importance of droplet perimeter and the coupling between rotational and bending vibrations is a mechnism of disintegration of ice prior to melting. This fundamental understanding has resulted in several important recommendations that provide a rational basis for the design of de-ice coatings and materials.

7.4 Future Research Directions

The current experimental studies provide information regarding the ice-solid interface at the scale of several microns. To make direct comparison with the MD simulations at a scale of about 20 angstroms, the resolution of the experimental set-up needs to be improved. A possible means to achieve such a resolution would be to use high resolution confocal Raman spectroscopy along with waveguide integrated optics. The

inclusion of waveguide in a confocal Raman experiment will provide a resolution that is adequate to investigate monolayer assemblies of ice layers on solid surfaces [30, 33].

The present work has estabilished the preliminary validity of the ice-copper interface potential model. The validity of interface model needs to be tested over the range of temperatures and pressures where phase transition in ice is observed. The calculation of the elastic properties of the interface will be essential to explore the structural stability and strength of the anisotropic interface. Several investigations and computer experiments on the interface models remain to be carried out. In this regard, the influence of the microscopic parameters, such as surface geometry (FCC[100], FCC[110] and FCC[111]), the degree of disregistry and surface enrgy, on interface adhesion needs to be quantified.

The present study has not looked into the mechanisms of decohesion of ice-solid interface using MD simulations. Future research, therefore, could be directed towards the atomistic study of the decohesion processes.

The next logical step would be to develop coatings and materials using the recommendations provided in this study. A possible coating can be developed using a combination of a durable block-copolymer substrate attached with a low energy surfactant. With the methodology developed in this study, the infrastructure and expertise for further experiments in this direction are already in place. This means a product developmental effort following the recommendations would be cost-effective at this stage. The products so developed would be an effective solution to the icing problems we mentioned at the begining of this study.

.1 Appandix A: Property Calculations

In order to validate the MD simulation model the thermodynamic, structural and dynamic properties are calculated. In the MD simulation the properties are in general calculated by the hypothesis of ergodicity, i.e., the statistical mechanical ensemble average is equivalent to the time average. Hence if a property $A(r_i)$ is dependent on the system configuration r_i then the equilibrium value of the property can be calculated by the time average

$$\langle A \rangle = \frac{1}{J} \sum_{J=1}^{M} A(r_i(t_j)) \tag{.1}$$

The following sections describe the procedure to some of the properties which are used to monitor and validate the SPC model.

Temperature

A temperature for the simulated system is defined by the total kinetic energy by equipartition of the velocity on each particles. The average temperature of the system is calculated by obtaining the total kinetic energy.

$$T = \frac{1}{3NK_b} \langle \sum_{i=1}^{N} m_i v_i . v_i \rangle \tag{.2}$$

where N is the number of particles in the simulation cell and K_b is the Boltzmann constant.

Potential Energy

The potential energy depends on the configuration of the system under a given potential function.

$$U = \langle \sum_{i<J}^{N} U(r_{ij} \rangle \tag{.3}$$

Pressure

The pressure is calculated using virial theorem. The pressure of the molecular system with internal degree of freedom is defined as the ensemble average of the virial pressure.

$$P = \frac{1}{3\omega}\langle\sum_{i=1}^{N} m_i v_i.v_i + r_i.fi\rangle \tag{.4}$$

Mean Squared Displacement

The square of the displacement of the particles from their initial positions averaged over time provides a measure of the diffusion in the MD system. The long time limit of the mean squared displacement can be used to calculate self diffusion using famous Einstein's relation.

$$MSD = \langle|\underline{r}(\tau) - \underline{r}(0)|^2\rangle \tag{.5}$$

Self-Diffusion

$$D_s = \frac{1}{3}\lim_{\tau\to\infty}\frac{1}{2\tau}MSD \tag{.6}$$

Radial Distribution Function

The spatial correlation between site α and β belonging to different molecules i and j can be calculated by following equation:

$$G_{\alpha\beta}(r) = \frac{1}{\rho_{alpha\beta} 4\pi r^2 dr} \langle \sum_{i \neq j}^{N} \delta(r - |\underline{r}_{\alpha i} - \underline{r}_{\beta j}|) \rangle \qquad (.7)$$

This function defines ratio of local number density to the bulk number density and is a measure of probability of finding sites α and β a distance r apart.

Velocity Autocorrelation Function and Power Spectra

The dynamic properties of the atoms in the simulation cell can be calculated using time correlation functions. In this regard velocity autocorrelation function provides necessary information about the atomic motion with time of a particular atom. The Fourier transform of the velocity autocorrelation function provide the power spectrum of the atoms which is equivalent to a generalized vibrational spectrum.

In general, if a(t) is real dynamic property then the time correlation function can be defined by an ensemble average':

$$c(t) = \langle a(0)a(t) \rangle \qquad (.8)$$

which is equivalent to

$$= \lim \tau \rightarrow \infty (1/\tau) \int_0^{\tau} dt' a(t')(at + t')$$

the statistical error can arise in the calculation of the time correlation function due to finite time averaging. The estimation of the error can be made on the basis of relaxation time $\tau_a$and total time τ as:

$$\varepsilon = \pm \sqrt{\frac{2\tau_a}{\tau}} (1 - c(t)) \qquad (.9)$$

The c(t) is the single-particle time correlation function which is averaged over N particle in the system to get an ensemble average of the dynamic property.

Bibliography

[1] H.H.G. Jellinek. *J. of Colloid Sc.*, 14:268, 1959.

[2] W.D. Bascom, R.L. Cottington and and C.R. Singleterry. *J. Adhesion*, 1:246, 1969.

[3] L. E. Raraty and D. Tabor. *Proc. Roy. Soc.*, 245A:184, 1968.

[4] J. C. Pohlman and P. Landers. *IEEE Trans.*, PAS-101(6):1497, 1982.

[5] J. J. Reinmann, R. J. Shaw and W. A. Olsen. *U.S. Army Cold Regions Res. Engrg. Lab, Hanover, NH.*, Sp. Rep. 83-17:103, 1983.

[6] S. C. Dunn and R. V. Schenk. Fhwa-rd-79-109. Technical report, Federal Highway Administration, 1980.

[7] D. L. Minsk. *U.S. Army Cold Regions Res. Engrg. Lab, Hanover, NH.*, Sp. Rep. 83-17:93, 1983.

[8] W. B. Bendel and D. Paton. *J. Appl. Meteor.*, 20:1445, 1981.

[9] J. G. Havard and J. C. Pohlman. *IEEE Trans.*, PAS-103(2):318, 1984.

[10] S.E. Trost,J.H. Frank and E.L. Cussler. *J. Transportation Eng.*, 113:15, 1987.

[11] H. H. G. Jellinek. *U.S. Army Cold Regions Res. Engrg. Lab, Hanover, NH.*, Sp. Rep. 83-17:97, 1983.

[12] H. H. G. Jellinek. *U.S. Army Cold Regions Res. Engrg. Lab, Hanover, NH.*, Sp. Rep. 115:46, 1970.

[13] K. Itagaki. *J. Colloid Interface Sci.*, 25:218, 1967.

[14] A. J. Kinloch. *Adhesion and Adhesives.* Chapman Hall, London, 1987.

[15] A. W. Adamson. *Physical Chemistry of Surfaces.* John Wiley and Sons, New York, 1982.

[16] A. Zangwill. *Physics at Surfaces.* Cambridge University Press,Cambridge, 1988.

[17] P. V. Hobbs. *Physics and Chemistry of Ice.* MIT Press, Cambridge, MA,, 1954.

[18] N. H. Fletcher. *The Chemical Physics of Ice.* Cambridge University Press, London, 1970.

[19] T. C. Sivakumar, D. Schuh, M. G. Sceats, and S. A. Rice. *Chem. Phys. Lett.*, 48:212, 1977.

[20] J. R. Scherer, M. K. Go, and S. Kint. *J. Chem. Phys.*, 78:1304, 1974.

[21] G. P. Johari and T. C. Sivakumar. *J. Chem. Phys.*, 69:5557, 1978.

[22] D. D. Klug, O. Mishima, and E. Whalley. *J. Chem. Phys.*, 86:5323, 1987.

[23] T. Englert, G. Abstreiter, and J. Pontcharra. *Solid State Electronics*, 237:31, 1980.

[24] A. Erbil, G. Dresselhaus, and M. S. Dresselhaus. *Solid State Commn.*, 25:5451, 1982.

[25] C. Underhill, S. Y. Leung, G. Dresselhaus, and M. S. Dresselhaus. *Phys. Rev. B*, 29:769, 1979.

[26] T. Nishioka, Y. Shinoda, and Y. Ohamachi. *J. Appl. Phys.*, 57(2):276, 1985.

[27] H. Atwater. PhD thesis, Electrical Engg., MIT, 1987.

[28] D. R. Tallant and K. L. Higgens. *Proc. of ICALEO, Laser Institute of America.*, 42:12, 1983.

[29] D. R. Clark and F. Adar. *in Advances in Material Characterization*, 57(2):276, 1985.

[30] J. F. Rabolt and J. D. Swalen. Research report, # 5414. Technical report, IBM San Jose, CA., 1986.

[31] A. Ishitani, H. Ishida, G. Katagiri, and S. Tomita. *Proc. of First Intl. Conf. on Composite Interfaces, (Cleveland, OH).* Academic Press, New York, 1986.

[32] R. W. W. van Resandt, H.J.B. Marsman, R. Kaplan, J. Davoust, E.H.K. Stelzer and R. Strickler. *J. Microsc.*, 138:27, 1985.

[33] R. Tabaksblat, R.J. Meier and B. J. Kip. *Applied Spectroscopy*, 46:60, 1992.

[34] M. P. Allen and D. J. Tildesley. *Computer simulation of liquids.* Clarendon Press, Oxford, 1987.

[35] A. Rahman. *Phys. Rev.*, 136:A405–A411, 1964.

[36] C. L. Briant and J.J. Burton. *J. Chem. Phys.*, 63:3327, 1975.

[37] H.J.C. Berendsen, J.P.M. Postma, W.V. van Gunsteren, and J. Hermans. *in Intermolecular Forces.* Reidel, Dordrecht, 1981.

[38] K. Toukan and A. Rahman. *Phys. Rev. B*, 31:2643, 1985.

[39] J. J. Anderson. PhD thesis, Nuclear Engg., MIT, 1986.

[40] D. Eisenberg and W. Kauzmann. *The Structures and Properties of Water.* Oxford University Press, 1966.

[41] S. H. Frank. *Science*, 169(3946):635, 1970.

[42] M. Daw and M. I. Baskes. *Phys. Rev. B*, 29:6443, 1984.

[43] H.R. Baker, W.D. Bascom, and C.R. Singleterry. *J. Colloid Sc.*, 17:477, 1962.

[44] S. K. Sharma, H. K. Mao, P. M. Bell, and J. A. Xu. *J. Raman Spectrosc.*, 16:350, 1985.

[45] J. E. Bertie and E. Whalley. *J. Chem. Phys.*, 46:1271, 1967.

[46] J. L. Viovy, G. M. Searby, F. Fried, M. J. Vellutini, and P. Sixou. *Mol. Phys.*, 38:1275, 1979.

[47] J. R. Scherer and R. G. Snyder. *J. Chem. Phys.*, 67:4794, 1977.

[48] S. R. J. Bruek, B-Y Tsaur, C. C. F. John, D. V. Murphy, T. F. Deutsch, and D. J. Silverman. *Appl. Phys. Lett*, 40(10):895, 1982.

[49] K. Kakimoto and T. Katoda. *Appl. Phys. Lett*, 40(9):836, 1982.

[50] C. G. Venkatesh and S. A. Rice. *J. Chem. Phys.*, 63:1065, 1975.

[51] T. C. Sivakumar, S. A. Rice, and M. G. Seats. *J. Chem. Phys.*, 69:3468, 1978.

[52] E. Whalley. Personal communications, 1984.

[53] Z. A. Gabrichidze. *Opt. and Spectrosc*, 19:319, 1965.

[54] D. C. Cross, J. Burnham, and P. A. Leighton. *J. Am. Chem. Soc.*, 59:1134, 1937.

[55] S.F. Ackley and M.K. Templeton. *U.S. Army Cold Regions Res. Engrg. Lab, Hanover, NH.*, Rep. 79-4, 1979.

[56] P. McComber. *U.S. Army Cold Regions Res. Engrg. Lab, Hanover, NH.*, Sp. Rep. 83-17:51, 1983.

[57] E. P. Lozowski , J. R. Stallabrass and P. F. Hearty. *J. Climate and Appl. Meterology*, 22:2053, 1983.

[58] L. Makkonen. *J. Climate and Appl. Meterology*, 23:929, 1984.

[59] K. F. Jones and K. Z. Egelhofer. *U.S. Army Cold Regions Res. Engrg. Lab, Hanover, NH.*, Rep. 91-3, 1991.

[60] N. Sonwalkar, S. Shyam Sunder and S. K. Sharma. *J. Raman Spectrosc*, 22:551, 1991.

[61] P. T. T. Wong and E. Whalley. *J. Chem. Phys.*, 62:2418, 1975.

[62] D.S. Olander and S. A. Rice. *Proc. Nat. Acad. Sci. USA*, 69:98, 1972.

[63] H. Kroemer. *J. Crystal Growth*, 81:193, 1987.

[64] K. Klier and A. C. Zettlemoyer. *J. Colloid Interface Sci.*, 58:193, 1977.

[65] J. Q. Broughton and G. H. Gilmer. *J. Chem. Phys.*, 84:5759, 1986.

[66] W. D. Kingery. *Ice and Snow: Properties, Processes and Applications.* MIT Press, Cambridge, MA,, 1963.

[67] W. A. Zisman. *Advances in Chemistry Series*, 43:1, 1964.

[68] A-M. Cazabat. *Contemp. Phys.*, 28:347, 1987.

[69] U. Nakaya. *Snow Crystals: Natural and Artificial.* Harvard University Press,Cambridge, MA, 1954.

[70] J. Hallett and B.J. Mason. *Proc. Roy. Soc. London, A*, 247:440, 1958.

[71] T. Kuroda and R. Lacmann. *J. Crystal Growth*, 56:189, 1982.

[72] M. Mellor, G.F.N. Cox, H. Bosworth. *U.S. Army Cold Regions Res. Engrg. Lab, Hanover, NH.*, Report 84-8:13, 1984.

[73] M. Isai, M. Ohshita, J. Beerens, J. D. N. Cheeke. *Rev. Sci. Instrum*, 61:1556, 1990.

[74] J. P. Hirth and K. L. Moazed. *Fundamental Phenomenon in Materials Sciences,*, 3:63, 1966.

[75] T. Kobayashi. *in Physics of Snow and Ice.* Proc. Int. Conf. Low Temp. Sci., 1967.

[76] W. M. Ketcham and P.V. Hobbs. *Philos. Mag.*, A19:1161, 1969.

[77] R. Smith-Johannsen. *GE Report# 5539*, page 149, 1946.

[78] H. H. G. Jellinek. *ACS Symp. Ser.*, 8:248, 1975.

[79] E. H. Andrews and N. A. Lockington. *J. Material Sci.*, 18:1455, 1983.

[80] H. H. G. Jellinek, H. Kachi, S. Kittaka, M. Lee and R. Yokata. *Colloid and Polymer Sc.*, 8:544, 1978.

[81] N. Sonwalkar, S. Shyam Sunder and S.K. Sharma. *accepted in Applied Spectroscopy.*

[82] N. Sonwalkar, S. Shyam Sunder and S.K. Sharma. *to be published in J. Crystal Growth.*

[83] M. Landy and A. Freiberger. *J. Colloid. and Interface Sci.*, 25:231, 1967.

[84] D. D. Klug and E. Whalley. *J. Chem. Phys*, 81:1220, 1984.

[85] D. Beysens, A. Steyer and P. Goenoun. *Phase Transition*, 31:219, 1991.

[86] A. Rahman and F. H. Stillinger. *J. Chem. Phys.*, 55:3336, 1971.

[87] F. H. Stillinger and A. Rahman. *J. Chem. Phys.*, 60:1545, 1974.

[88] J. Anderson, J.J. Ullo and S. Yip. *J. Chem. Phys.*, 87:1726, 1987.

[89] H.J.C. Berendsen, J.R. Grigera and T.P. Straatsma. *J. Phys. Chem.*, 91:6269, 1987.

[90] M. Prevost, D.V. Belle, G. Lippens and S. Wodak. *Mol. Phys.*, 71:587, 1990.

[91] T. A. Weber and F.A. Stillinger. *J. Chem. Phys.*, 81:438, 1984.

[92] J.S. Tse, M. L. Klein and I. R. McDonald. *J. Chem. Phys.*, 81:612, 1984.

[93] O. A. Karim and A. D. J. Haymet. *Chem. Phys. Lett.*, 138:531, 1987.

[94] O. A. Karim, P.A. Kay and A. D. J. Haymet. *J. Chem. Phys.*, 92:4634, 1990.

[95] O. Matsuoka, E. Clementi and M. Yoshimine. *J. Chem. Phys.*, 64:1351, 1976.

[96] F. H. Stillinger and C. W. Devid. *J. Chem. Phys.*, 69:1473, 1978.

[97] J.S. Rowlinson. *Trans. Faraday Soc.*, 47:120, 1951.

[98] W. L. Jorgensen. *J. Am. Chem. Soc.*, 103:335, 1981.

[99] H. L. Lamberg and F.H. Stillinger. *J. Chem. Phys.*, 62:1677, 1975.

[100] W. L. Jorgensen, J. Chandrasekher, J. Madura, R.W. Impey and M.L. Klein. *J. Chem. Phys.*, 79:926, 1983.

[101] R. Bansil, T. Berger, K. Toukan, M.A. Ricci and S.H. Chen. *Chem. Phys. Lett.*, 132:165, 1986.

[102] R.W. Impey, M.L. Klein and I.R. McDonald. *J. Chem. Phys.*, 74:647, 1981.

[103] B. Kamb. *Trans. Am. Cryst. Assoc.*, 5:61, 1969.

[104] G. Honjo, N. Kitamura, K. Shimaoka and K. Mihama. *J. Phys. Soc. Japan*, 11:527, 1956.

[105] S.W. Peterson and H. A. Levy. *Acta Cryst.*, 10:70, 1957.

[106] J.D. Bernal and R.W. Fowler. *J. Chem. Phys.*, 1:515, 1933.

[107] L. Pauling. *J. Am. Chem. Soc.*, 57:2680, 1935.

[108] P.P. Ewald. *Ann. PhysiK*, 64:253, 1921.

[109] M. J. L. Sangster and M. Dixon. *Advances in Physics*, 25:247, 1976.

[110] H.M. Evjan. *Phys. Rev.*, 39:675, 1932.

[111] N. Bjerrum. *Science*, 115:385, 1952.

[112] K. Krynicki, C. D. Green, and D. W. Sawyer. *Faraday Discuss. Chem. Soc.*, 66:771, 1978.

[113] L. D. Landau and E. M. Lifshitz. *Mechanics.* Pergamon Press, New York, 1960.

[114] W. A. Harrison. *Pseudo potentials in the Theory of Metals.* Benjamin, New York, 1966.

[115] R. A. Johnson. *Phys. Rev. B*, 6:2094, 1972.

[116] M. W. Finnis and J. E. Sinclair. *Philos. Mag. A*, 50:45, 1984.

[117] M. Daw and M. I. Baskes. *Phys. Rev. Lett.*, 50:1285, 1983.

[118] D. J. Oh and R. A. Johnson. *J. Mater. Res.*, 3:471, 1988.

[119] S. M. Foiles. *Phys. Rev., B*, 32:3409, 1985.

[120] S. M. Foiles, M. I. Baskes, and M. S. Daw. *Phys. Rev., B*, 33:7983, 1986.

[121] K. Cheung. *Atomistic study of dislocation nucleation at a crack tip.* PhD thesis, Department of Nuclear Engineering, MIT, 1990.

[122] G. Simmons and H. Wang. *Single Crystal Elastic Constants and Calculated Aggregate Properties : A Handbook.* (MIT Press, Cambridge), 1971.

[123] J. S. Tse and M. L. Klein. *Phys. Rev. Lett.*, 58:1672, 1987.

[124] J.R. Reimers, R.O. Watts, and M.L. Klein. *Chem. Phys.*, 64:95, 1982.

[125] S. R. Phillpot, J.F. Lutsko, D. Wolf and S. Yip. *Phys. Rev. B,*, 40:2831, 1989.

[126] O. A. Karim and A. D. J. Haymet. *J. Chem. Phys.*, 89:6889, 1988.

[127] F.A., Lindemann. *Phys. Zeit*, 11:609, 1910.

[128] E.B. Wilson, J.C. Decius and P.C. Cross. *Molecular Vibrations.* Dover, New York, 1955.

[129] E. Spohr and K. Heinzinger. *Chem. Phys. Leti.*, 123:218, 1986.

[130] N. G. Personage and D. Nicholson. *J. Chem. Soc., Faraday Trans.*, 82:1521, 1986.

[131] N. G. Personage and D. Nicholson. *J. Chem. Soc., Faraday Trans.*, 83:663, 1987.

[132] A. A. Gardner and J. P. Valleau. *J. Chem. Phys.*, 86:4162, 1987.

[133] C. W. Bauschlicher. *J. Chem. Phys.*, 83:3129, 1985.

[134] E. Spohr and K. Heinzinger. *Electrochemca Acta.*, 33:1211, 1988.

[135] K. Heinzinger. *Pure & Appl. Chem.*, 63:1733, 1991.

[136] J. P. Valleau and A. A. Gardner. *J. Chem. Phys.*, 86:4162, 1987.

[137] D.Handerson, L. Blum, and M. Lozada-cassou. *J. Electroanal. Chem.*, 150:291, 1983.

[138] C. L. Kong. *J. Chem. Phys.*, 59:2464, 1973.

[139] S. Holloway and K. H. Bennemann. *Surf. Sci.*, 101:327, 1980.

[140] D. Bullett. *Solid State Physics.* Academic Press, New York, 1980.

[141] T. E. Madey and J. T. Yates. *Surf. Sci.*, 51:77, 1977.

[142] E. Spohr. *J. Phys. Chem.*, 93:1617, 1989.

[143] E. Spohr. *Chem. Phys.*, 141:87, 1990.

[144] M.W. Ribarsky, W.D. Luedtke, and U. Landman. *Phys. Rev. B*, 63:1733, 1991.